Pharmaceutical Applications of Layered Double Hydroxides

By

Henry Alexander Fisher



A thesis submitted in partial fulfilment of the requirement for the degree of Doctor of Philosophy at the University of Oxford

Hertford College

Oxford

July 2016

The work described in this thesis was carried out in the Chemistry Research Laboratory, Mansfield Road, Oxford between January 2011 and July 2016 under the supervision of Professor Dermot O'Hare. All the work is my own unless otherwise stated to the contrary, and has not been submitted for any degree at this or any other university.

Henry Alexander Fisher
July 2016

Abstract

Pharmaceutical Applications of Layered Double Hydroxides

Henry Fisher — Hertford College

D.Phil Thesis — Michaelmas Term 2015

The principle aims of this thesis are to investigate the synthesis of layered double hydroxides (LDHs) for use as drug delivery systems, and to explore the potential of these compounds to provide solutions to typical pharmaceutical problems.

In **Chapter 1**, background information on pharmaceutics and drug delivery is given. LDHs are introduced and their structure, synthesis and general applications described. The biomedical and pharmaceutical applications of LDHs are reviewed.

Chapter 2 presents the intercalation of the GABAergic drugs gabapentin and pregabalin into an LDH using the coassembly method. The optimum conditions for the restacking process are investigated, an improved method of anhydrous restacking in ethanol at reduced temperatures is described, and a mechanism is suggested. The stabilising effect of LDH intercalation on the drug ions is measured.

Chapter 3 explores the potential for LDHs to stabilise and deliver catecholamine drugs levodopa, carbidopa and methyldopa. The ability of a range of LDHs to intercalate and stabilise these drugs against racemisation and oxidative decomposition across a variety of conditions is reported.

In **Chapter 4**, the potential for LDHs to deliver neutral hydrophobic and cationic drugs through the intercalation of cyclodextrin–drug inclusion complexes is investigated. A range of partially substituted anionic cyclodextrins are synthesised and intercalated into an LDH. Cyclodextrin–drug inclusion complexes are intercalated, their interlayer orientation is suggested and drug release measured.

In **Chapter 5**, the potential of polymer–LDH composites for drug delivery is explored. A selection of drug intercalated LDHs from Chapters 2 and 3 are encapsulated in several enteric polymers typically used for drug delivery. The release profiles and stabilising effects of the composites are measured.

Chapter 6 details the experimental procedures and analytical instruments used throughout this thesis. The **Appendices** contain supplementary characterisation and analytical data that are referred to in the main text.

Acknowledgements

First and foremost, I would like to thank Professor Dermot O'Hare for giving me the opportunity to work in his research group, first when conducting my Part II project, then as a research assistant, and then finally to conduct my D.Phil project, and I am grateful for all his ample advice and guidance along the way.

Secondly, I would like to thank the postdocs from the group who have provided me with much direction and support over the years and helped to keep me on the (fairly broad and winding) straight and narrow. Thanks to Dr. Gareth Williams for teaching me the dark art of LDH synthesis and starting me down the path to which this thesis has been the conclusion. Thanks to Dr. Jean-Charles Buffet for proofreading this entire thesis and for providing words of wisdom throughout the years, particularly whenever I chose to attempt any particularly daring practical chemistry. Thanks also to Drs. Chunping Chen, Zoe Turner and Nick Rees for fielding my many questions and for performing emergency microscopy, 2D and solid-state NMR respectively.

Next I would like to thank the two members of the O'Hare Group that have remained a constant for nearly the whole of my time, and have both made the leap from D.Phil student to postdoc status, Drs. Mark Chadwick and Robert 'Coops' Cooper. Thanks for providing plenty of entertainment both in an out of the lab, lending an ear whenever things got tough, usually over a pint, and for always being on hand to suggest an early trip to the Uni Club at the end of the week.

Thank you to all those others in the O'Hare group who have passed or are still passing through with me, my fellow D.Phil students: Tom for all your food and wine knowledge, Hannah for suffering an LDH project alongside me, Sam for your wonderful baking, Charles for being there at the beginning, Anchalee, Joyce, Saul, Dave and your pioneering sense of style, Chris, Golf and Duncan. Most recently, thanks also to Drs. Yue Wu and Sandy Kilpatrick for providing light relief during the write-up process.

To all the many Part II students that have come and gone, it has been great to meet you and you have provided endless amusement for those of us that are slightly older, wiser and more jaded. In particular, thanks to Chloe for being an excellent student, and for conducting some initial experiments with sulfobutylether cyclodextrins and investigating decarbonation. Thanks also to Little Jack for conducting a few forays into cyclodextrin chemistry under my guidance, even if they were ultimately ill-fated. Also thanks to my fellow Part II students Rich, Tom and Chio way back when. Also to my first Part II student, Emily, well done for suffering the project through to the

end. To all I have forgotten to mention, thanks to you too, it has been a ball.

Outside of the group, thank you to those in the department and at Hertford that have kept everything running, in particular to Aga and Hazel, who have always made sure the correct forms were signed and chemicals ordered. Thanks to all those in stores and elsewhere that have played some integral part, great or small, directly in the completion of this work, and to Oxford Pharmascience for the funding. Thanks also to my wonderful housemates over the years, with whom I have always had great fun and occasional calls from the Council, if also the occasional disagreement: Sarah (still best housemate ever), Tim, Carly, Anna, and last but certainly not least Waney, who has provided an ocean of calm during my write-up, and without whom this last year and a bit would have been immeasurably more challenging.

Thanks to all my friends, both new and old, for putting up with me. The Pugh Crew for endless nostalgia and giving me something to aim for when I get a proper job, in particular Helen, Dan, Lisa and Jess for perking me up. All those from OUDC with whom I have chasséd over the years, in particular Em, Nik, Colleen, Haz, Dean, Dan, Helen, Flo and so many others (but most of all DHoF), you have kept me sane (although sometimes it hasn't felt that way), given me an excuse to escape the lab and a true passion that I will always keep with me.

A special thank you to those I have loved and that have loved me along the way. Two people deserve very special mention, Milou and Zoë, you have broken my heart and I have broken yours, and in between we have shared some of the most treasured moments and memories of our lives. You have seen me at my worst and best, picked me up and held me and filled me with life. We have argued, and made up, and danced (especially danced), and cried, and I will never regret a single moment I spent with either of you, for opening my eyes to totally new worlds, although I know you will both be furious that I put you both in the same sentence. Thanks to Charlie, you have jumped in rather at the sharp end of things, but made these last few months worth toiling through, and I very much look forward to enjoying a few more with you at least, and then who knows? And a nod to everyone else that has put a certain smile on my face at some point or other: Caroline, Liz, Jenny, Asya, Anya, Haz, Jamie, Sophia, Josie and all those whose names I have forgotten or never learnt. Oh, and thanks to Mandy, you're amazing.

Finally, thanks to my family, to Mum, Dad and Bibs. I really could not have done any of this without you three by my side every step of the way and always at the other end of the phone when I needed to talk, or rant, or someone organise my life for me, and no one else could possibly do. You have always been there when I have felt lost.

Five years unhappy labor
22 to 27 working
Not a dime in the bank
To show for it anyway

Excerpt from *My Alba*
Alan Ginsberg

Contents

1 Introduction **1**

1.1 Overview 1

1.2 Background in pharmaceutics 2

1.2.1 Pharmaceutical formulation 3

1.2.2 Controlled release 5

1.2.3 Kinetic models for drug release 8

1.2.3.1 The Avrami–Erofe'ev model 8

1.2.3.2 The Elovich model 9

1.2.3.3 The simple first order model 9

1.2.3.4 The modified Freundlich model 10

1.2.3.5 The parabolic diffusion model 11

1.3 Layered double hydroxides 12

1.3.1 Structure of layered double hydroxides 12

1.3.2 Synthesis of layered double hydroxides 17

1.3.2.1 Coprecipitation 17

1.3.2.2 Salt–oxide method 18

1.3.2.3 Ion-exchange 19

1.3.2.4 Calcination–reconstruction 19

1.3.2.5 Decarbonation 20

1.3.2.6 Delamination–restacking 21

1.3.3 General applications of layered double hydroxides 22

1.3.4 Pharmaceutical applications of layered double hydroxides . . . 23

1.3.4.1 Biocompatible layered double hydroxides 24

1.3.4.2 Topical drug delivery 25

1.3.4.3 Oral drug delivery 26

1.3.4.4 Parenteral drug delivery 31
1.3.5 Other biomedical applications of layered double hydroxides . . 33
1.3.5.1 Biosensors 34
1.3.5.2 Vaccine adjuvants 34
1.4 Aims of this thesis 35
1.5 References 37

2 Intercalation of Unstable Drugs Gabapentin and Pregabalin Through an Improved Coassembly Route 49
2.1 Introduction 49
2.1.1 Scope of this Chapter 51
2.2 Synthesis and characterisation of nanohybrids 51
2.2.1 Delamination of MgAl-NO_3 LDH 52
2.2.2 Restacking synthesis of nanohybrids 53
2.2.3 Powder X-ray diffraction 54
2.2.4 Fourier transform infrared spectroscopy 58
2.2.5 Solid state ^{13}C NMR spectroscopy 60
2.2.6 Deintercalation experiments 62
2.2.7 Thermogravimetric analysis 62
2.2.8 Elemental analysis and drug content 62
2.2.9 Scanning electron microscopy 64
2.2.10 Transmission electron microscopy 65
2.3 Effects of restacking conditions 66
2.3.1 Restacking solvent 66
2.3.1.1 Restacking mechanism 68
2.3.2 Water presence in restacking 70
2.3.3 Restacking temperature 71
2.4 Release behaviour 73
2.4.1 Kinetic analysis 74
2.5 Effect on drug stability 76
2.5.1 Stability studies 76
2.5.1.1 NMR spectroscopy decomposition studies 78
2.6 Future work 79

2.7 Conclusion 79
2.8 References 81

3 Studies on the stability of catecholamine drugs intercalated into layered double hydroxides 84

3.1 Introduction 84
3.1.1 Catecholamine drugs 85
3.1.2 Attempts to stabilise catecholamine drugs 87
3.1.3 Scope of this Chapter 89
3.2 Synthesis of MgAl-drug LDH nanohybrids 90
3.2.1 Powder X-ray diffraction 90
3.2.2 Fourier transform infrared spectroscopy 95
3.2.3 Solid state ^{13}C NMR spectroscopy 98
3.2.4 Dissolution experiments 100
3.2.5 Thermogravimetric analysis 101
3.2.6 Elemental analysis and drug content 104
3.2.7 Scanning electron microscopy 105
3.2.8 Discussion 106
3.3 LDH precursors containing Fe^{2+} 106
3.3.1 Powder X-ray diffraction 108
3.3.2 Fourier transform infrared spectrosopy 111
3.3.3 Thermogravimetric and elemental analysis 111
3.3.4 Scanning electron microscopy 114
3.4 Intercalation of L-DOPA into LDHs containing Fe^{2+} 115
3.4.1 Powder X-ray diffraction 116
3.4.2 Fourier transform infrared spectroscopy 117
3.4.3 Solid state ^{13}C NMR spectroscopy 118
3.4.4 Dissolution experiments 119
3.4.5 Thermogravimetric and elemental analysis 120
3.4.6 Scanning electron microscopy 121
3.5 Nanohybrid release behaviour 121
3.5.1 Kinetic analysis 123
3.6 Decomposition studies 126

3.6.1 Stability in dry conditions . . . 126
3.6.2 Stability in wet conditions . . . 131
3.6.3 Discussion . . . 133
3.7 Conclusion . . . 134
3.8 References . . . 135

4 Drug storage and delivery using layered double hydroxide–cyclodextrin nanohybrids 137
4.1 Introduction . . . 137
4.1.1 Scope of this chapter . . . 139
4.2 Functionalisation of β-cyclodextrin . . . 140
4.2.1 Nuclear magnetic resonance spectroscopy . . . 140
4.2.2 Fourier transform infrared spectroscopy . . . 145
4.2.3 Elemental analysis . . . 146
4.3 Intercalation of substituted β-cyclodextrins . . . 147
4.3.1 Powder X-ray diffraction . . . 147
4.3.2 Fourier transform infrared spectroscopy . . . 152
4.3.3 Solid-state nuclear magnetic resonance spectroscopy . . . 154
4.3.4 Formulae calculations . . . 156
4.3.4.1 Energy dispersive X-Ray spectroscopy . . . 156
4.3.4.2 Thermogravimetric analysis . . . 156
4.3.4.3 Elemental analysis . . . 156
4.3.5 Scanning electron microscopy . . . 159
4.4 Intercalation of β-cyclodextrin–drug complexes . . . 160
4.4.1 Model drugs . . . 161
4.4.2 Powder X-ray diffraction . . . 163
4.4.3 Fourier transform infrared spectroscopy . . . 166
4.4.4 Nuclear magnetic resonance spectroscopy . . . 168
4.4.5 Elemental analysis . . . 169
4.4.6 Scanning electron microscopy . . . 170
4.5 Proposed orientation of guest species . . . 171
4.6 Release studies . . . 176
4.6.1 Kinetic models . . . 181

4.6.2 Discussion . . . 183
4.7 Conclusion . . . 184
4.8 References . . . 186

5 An investigation of enteric polymer–layered double hydroxide composites for drug delivery 188
5.1 Introduction . . . 188
5.1.1 Scope of this Chapter . . . 191
5.2 Synthesis of polymer–nanohybrid composites . . . 191
5.2.1 Eudragit®–nanohybrid composites . . . 192
5.2.2 Alginate–nanohybrid beads . . . 192
5.2.3 Powder X-ray diffraction . . . 193
5.2.4 Fourier transform infrared spectroscopy . . . 194
5.2.5 Drug content . . . 196
5.2.6 Energy dispersive X-ray spectroscopy . . . 198
5.2.7 Scanning electron microscopy . . . 199
5.3 Release studies . . . 201
5.3.1 Release of GBP and PGB . . . 201
5.3.2 Release of L-DOPA . . . 203
5.3.3 Release kinetics . . . 205
5.3.4 Discussion . . . 207
5.4 Stability studies . . . 209
5.4.1 GBP and PGB stability . . . 209
5.4.2 L-DOPA stability . . . 209
5.5 Conclusion . . . 212
5.6 References . . . 214

6 Experimental details 216
6.1 Analytical techniques . . . 216
6.1.1 Powder X-ray diffraction . . . 216
6.1.2 Fourier transform infrared spectroscopy . . . 216
6.1.3 Solid state NMR spectroscopy . . . 216
6.1.4 Solution phase NMR spectroscopy . . . 217

6.1.5 Scanning electron microscopy and energy dispersive X-ray spectroscopy . . . 217
6.1.6 Transmission electron microscopy . . . 218
6.1.7 Elemental analysis . . . 218
6.1.8 Thermogravimetric analysis . . . 218
6.1.9 Fluorescence spectroscopy . . . 218
6.1.10 Circular dichroism . . . 218
6.1.11 Ultraviolet spectroscopy . . . 219
6.2 General experimental procedures . . . 219
6.2.1 Synthesis of highly crystalline MgAl-NO_3 LDH . . . 219
6.2.2 Preparation of HCl-glycine and phosphate buffers . . . 220
6.2.3 Determination of drug concentration from ultraviolet spectroscopy . . . 220
6.2.4 Determination of aggregated concentrations of catecholamine decomposition products from ultraviolet spectroscopy . . . 221
6.2.5 Fluorospectroscopic determination of drug concentration . . . 221
6.3 Materials . . . 222
6.4 Experimental procedures from Chapter 2 . . . 222
6.4.1 Delamination of MgAl-NO_3 LDH . . . 222
6.4.2 Synthesis of MgAl-drug nanohybrids . . . 223
6.4.3 Comparison of restacking solvent . . . 223
6.4.4 Investigation of water presence in restacking . . . 223
6.4.5 Investigation of restacking temperature . . . 224
6.4.6 Release studies . . . 224
6.4.7 Aqueous stability studies . . . 225
6.5 Experimental procedures from Chapter 3 . . . 225
6.5.1 General synthesis methods . . . 225
6.5.2 Synthesis of MgAl-drug nanohybrids . . . 226
6.5.2.1 Ion-exchange . . . 226
6.5.2.2 Coprecipitation . . . 226
6.5.3 Synthesis of Fe^{II} containing precursor LDHs . . . 226
6.5.4 Synthesis of Fe^{II} containing LDH–drug nanohybrids . . . 227
6.5.5 Release studies . . . 228

6.5.6 Dry stability studies . . . 228
6.5.7 Aqueous stability studies . . . 229
6.6 Experimental procedures from Chapter 4 . . . 229
6.6.1 β-Cyclodextrin substitution . . . 229
6.6.1.1 Non-selective carboxymethylation . . . 229
6.6.1.2 C2 selective carboxymethylation . . . 230
6.6.1.3 Sulfobutylation . . . 231
6.6.2 Intercalation of substituted β-cyclodextrins . . . 231
6.6.3 Intercalation of β-cyclodextrin–drug complexes . . . 232
6.6.4 Calculation of drug content of nanohybrids . . . 233
6.6.5 Release studies . . . 233
6.7 Experimental procedures from Chapter 5 . . . 233
6.7.1 General synthesis methods . . . 233
6.7.2 Eudragit® composites . . . 234
6.7.3 Synthesis of alginate composites . . . 234
6.7.4 Determination of composite drug content . . . 235
6.7.5 Release studies . . . 235
6.7.6 GBP and PGB composite stability studies . . . 236
6.7.7 L-DOPA composite dry stability studies . . . 236
6.7.8 L-DOPA composite aqueous stability studies . . . 237
6.8 References . . . 238

7 Summary **239**

Appendix **241**
A Supporting data for Chapter 2 . . . 241
A.1 Gabapentin and pregabalin elemental analysis data . . . 241
A.2 Gabapentin and pregabalin nanohybrid decomposition plots . 242
B Supporting data for Chapter 3 . . . 243
B.1 Catecholamine nanohybrid elemental analysis data . . . 243
B.2 Catecholamine decomposition plots . . . 244
C Supporting data for Chapter 4 . . . 258
C.1 Lattice parameters and interlayer distances for all nanohybrids containing β-cyclodextrins and β-cyclodextrin–drug complexes 258

C.2 Correlation coefficients of modelled drug release kinetics of β-cyclodextrin–drug containing nanohybrids 260
C.3 Rate constants for drug release from β-cyclodextrin–drug containing nanohybrids 262
D Supporting data for Chapter 5 264
D.1 FTIR spectra of composites 264
D.2 Correlation coefficients of kinetic models fitted to drug release profiles of composites 265
D.3 Reaction parameters for drug release from composites, obtained from kinetic models 266
D.4 Decomposition plots of composites containing L-DOPA 268

List of abbreviations

[A]	Concentration of A, in moldm^{-3}
2D	Two-dimensional
a.u.	Arbitary units
AACD	Aromatic L-amino acid decarboxylase
ACE	Angiotensin-converting-enzyme
Alg	Alginate
AMI	Amitriptyline
anhyd	Anhydrous
α_{obs}	Observed optical rotation
ATR	Attenuated total reflection
C-DOPA	Carbidopa
CD	Cyclodextrin
CFA	Cefuroxime axetil
CIN	Cinnarizine
CMCD	Carboxymethyl cyclodextrin
COMT	Catechol-O-methyl transferase
CP	Cross-polarisation (NMR); Coprecipitation (synthesis)
CPZ	Chlorpromazine
δ	Chemical shift
DCM	Dichloromethane
d_{hkl}	D-spacing of the plane with Miller indices hkl
DMF	Dimethylformamide
DNA	Deoxyribonucleic acid
ε_r	Relative permittivity
EA	Elemental analysis
EDX	Energy dispersive X-ray spectroscopy
EDXRD	Energy dispersive X-ray diffraction
EE	Encapsulation efficiency
Eud L	Eudragit® L 100
Eud S	Eudragit® S 100
FTIR	Fourier transform infrared spectroscopy
FITC	Fluorescein isothiocyanate
FWHM	Full width at half maximum
GABA	γ-Aminobutyric acid
GBP	Gabapentin
GI	Gastrointestinal
h	Hour(s)
hkl	Miller indices of a crystal lattice
HMBC	Heteronuclear multiple bond correlation
HMT	Hexamethylenetetramine
$h\nu$	Ultraviolet radiation
IE	Ion-exchange

IMI	Imipramine
JEEP	Join Engineering, Environmental and Processing
k_{obs}	Observed reaction rate constant
L-DOPA	Levodopa
LDH	Layered double hydroxide
LDO	Layered Metal Oxide
M-DOPA	Methyldopa
MAS	Magic angle spinning
MgAl-NO_3	$[Mg_2Al(OH)_6]NO_3 \cdot yH_2O$
min	Minute(s)
NMR	Nuclear magnetic resonance
NSAID	Nonsteroidal anti-inflammatory drug
PGB	Pregabalin
PMZ	Promethazine
ppm	Parts per million
PTFE	Polytetrafluoroethylene
PXRD	Powder X-ray diffraction
r^2	The coefficient of determination of a linear regression line (correlation coefficient)
RNA	Ribonucleic acid
rpm	Revolutions per minute
s	Second(s)
SBECD	Sulfobutylether cyclodextrin
SEM	Scanning electron microscopy
SKIE	Solvent kinetic isotope effect
SS	Solid state
θ	Angle of incidence
t	Time
T	Temperature
t_{50}	Time at which 50% release occurs
t_{90}	Time at which 90% release occurs
TEM	Transmission electron microscopy
TGA	Thermogravimetric analysis
THF	Tetrahydrofuran
UV	Ultraviolet
W/W	Weight by weight
XRD	X-ray diffraction

1. Introduction

1.1 Overview

Since the rise of the modern pharmaceutical industry in the mid nineteenth century, a core pillar of research has revolved around the study of the delivery of drugs into the body and the optimisation of this process through the evolution of improved drug formulations, with the aim of increasing the utility, efficacy, precision, or scope of drugs.[1] Whilst drug discovery is often seen as the first step in finding a pharmacological treatment for a given condition, the role of pharmaceutics (dosage form design), is often vital in advancing a potential drug into an effective treatment. The chemistry, pharmacology or pharmacokinetics of a drug can limit its functionality, either in general or with a particular patient demographic, and it is often only through the development of an appropriate delivery method and formulation that such obstacles can be overcome.[2]

The methods used to deliver drugs vary widely and encompass both physical and chemical techniques, depending on the route of delivery, and the aims and requirements of the drug treatment in question. Inorganic species are an important and broad family of compounds used for drug delivery, encompassing silicas, metal oxide nanoparticles, nanotubes and layered materials, amongst others.[3–6] The pharmaceutical applications that inorganic species have been investigated for are equally wide ranging, from acting as storage vehicles for controlled release through to providing targeted delivery to regions of the body that are otherwise inaccessible.[7] In particular, layered double hydroxides have been investigated extensively in recent years for their potential in drug delivery, due to their ability to reversibly intercalate anionic drug species, alongside other desirable characteristics such as their easily tunable

composition, size and morphology.[8] The potential applications of layered double hydroxides in drug delivery are continually developing as our chemical knowledge of this family of compounds increases, and is applied to more varied and challenging problems within pharmaceutics.

1.2 Background in pharmaceutics

Pharmaceutics is an umbrella term for a family of diverse subject areas, with a common focus on the stages and processes involved in developing a drug into a final dosage form, once it has been discovered and tested for pharmacological and toxicological effects. Most simply, *"pharmaceutics converts a drug into a medicine."*[9] Pharmaceutics encompasses physical pharmaceutics – physical chemical considerations relating to the effective design of dosage forms, biopharmaceutics – the understanding of the relevant physiological systems affected by a drug and how physiological systems affect the arrival of a drug at its site of action, pharmaceutical formulation – the design and formulation of medicines, manufacture – processing involved and scale up of medicine production, pharmaceutical microbiology – the avoidance of microorganisms in medicines and their sterilisation, and performance testing – dissolution, stability and drug release testing.[9]

A medicine can be thought of as a drug delivery system – it has a primary purpose of delivering a drug compound to the body in a safe, effective, accurate, efficient, reproducible and convenient manner.[9] The mode of delivery is essential to the success of a potential medicine, and there are three main considerations that must be taken into account across all areas of pharmaceutics during the design of dosage forms:[9,10] physiochemical considerations of the drug itself and its excipients, such as solubility and chemical stability; biopharmaceutical considerations, such as how the route of administration may affect the bioavailability of a drug; and therapeutic considerations, such as how the needs of patient may influence which route of administration is most appropriate, and whether the condition being treated may present further complications that may be overcome by application of a particular dosage form.

1.2.1 Pharmaceutical formulation

Whilst all the subjects involved in pharmaceutics are interrelated, the areas most relevant to this thesis are pharmaceutical formulation and performance testing, as these relate to the chemical considerations and adverse characteristics that must be addressed when attempting to formulate a given drug compound, such as its aqueous stability, and to the increased functionality that can be conferred upon a drug by a given formulation, through attributes like controlled release.[10]

Pure drug compounds are crystalline or amorphous powders, and it has been the role of pharmaceutics since the advent of modern pharmacy to incorporate these raw powders into more practical and effective dosage forms. The range of dosage forms that have been developed is vast, from solid oral dosage forms such as tablets and capsules,[11] liquid parenteral formulations designed for intravenous or intramuscular injection,[12] topical formulations such as gels, ointments and dermal patches,[13] and inhalational formulations such as nebulisers and inhalers,[14] through to complex formulations such as gastroretentive systems for sustained release,[15,16] subcutaneous implant systems designed for long-term release,[17,18] injectable nanoparticles for targeted delivery,[19–21] combination drug systems,[22] and delayed onset dosage forms.[23,24]

The development of a new dosage form for a given drug presents a series of challenges that are particular to the drug and dosage form being considered. For example, the combination of excipients needed for the formulation of an oral tablet will, amongst other requirements, need to produce an effectively compounded tablet that will not disintegrate prior to administration, yet will disintegrate once reaching the desired section of the gastrointestinal (GI) tract.[11] The taste masking of a tablet may simply require a polymer or sugar coating. However, if the dosage form is an orally administered liquid, such as a syrup, the requirements for masking the taste of a drug will be much greater and more challenging, and may affect the maximum drug concentration of the dosage form. The list of possible requirements and considerations for different dosage forms is myriad, but those of most relevance to this thesis are those affecting oral administration of drug species in either solid or liquid formulations; these are detailed below.

Many drugs have an unpleasant taste, which can range from disagreeable but

still palatable, through to unpalatable to the extent that the taste may induce retching. In all cases, taste masking of the drug is required.[25] This may involve the use of sweeteners or flavourings,[26] complexation with cyclodextrins or ion exchange resins,[27–29] polymer coating,[30] formation of drug salts,[31,32] or compacting with viscous agents that prevent oral diffusion,[33,34] amongst other methods.[35] The simplest dosage form for taste masking is as a solid tablet or capsule that is swallowed whole, although this may be inconvenient for children or elderly patients, for whom chewable or liquid formulations are more appropriate, and so much work has been conducted into developing taste masking drugs for these formulations.[36,37] In more extreme cases, the drug compound may be an irritant, particularly to soft tissues such as mucous membranes. These drugs may require the same treatment as deeply unpleasant tasting drugs with complexation or encapsulation, although the consequences of drug leaching prior to the intended gut section are more severe.[38,39]

A factor that is of relevance to all drug formulations is drug stability, although in the case of orally administered drugs, in addition to drug stability during storage, the drug stability once it reaches the stomach, or once it has passed through the stomach if it is absorbed at a later stage of the GI tract is of relevance.[40,41] Drug stability can be a particular issue for liquid dosage forms.[42] This is both because many drugs are more susceptible to reaction when in solution, and also because liquid dosage forms are more prone to contamination in comparison to individually sealed tablets or capsules. Liquid dosage forms may require pH buffering agents or antioxidants,[43] or if the liquid dosage is in the form of a suspension, leaching of the drug from the solid particles may be kept under a certain threshold through manipulation of the morphology or size of the particles.[44]

To prevent the drug ions decomposing in the stomach or elsewhere in the GI tract, or to improve absorption or extend release time, dosage forms may be given an enteric coating, or the drug species may be contained within an enteric polymer matrix.[45–47] These materials will only dissolve or release their contents above specific pH level, and so preventing release within the acidic conditions of the stomach, or they may consist of materials that are enzyme-responsive and so release in a specific area of the GI tract.[48] Common enteric coating and polymer matrix materials are calcium alginate, which consists of chains of the anionic polymer alginate crosslinked by

calcium ions, which swells and diffuses in neutral and basic pH environments,[49] and the commercial preparation Eudragit®, which is the block copolymer poly(methyl methacrylate-co-methacrylic acid), which dissolves above a specific pH, that can be tailored by altering the ratios of poly(methyl methacrylate) and poly(methacrylic acid) within the sample.[50] The methods by which drug particles may be coated can also vary widely, and have a great influence of the release rate of the drug.[51]

Bioavailability is defined as the fraction of an administered dose that reaches the bloodstream unchanged. Increasing the bioavailability of a drug is another central aim to many oral dosage forms, as this allows smaller dosages of drugs to be given. Poor bioavailability may even prevent oral dosages of a drug from being effective at all, and so providing a solution to this may open up possibilities for new dosage forms for certain drugs.[52] Many factors affect the bioavailability of a given drug, from simple effects like aqueous solubility, particularly in acidic or neutral conditions, lypophilicity, through to effects like the health of the GI tract (which is affected by age), gastric emptying rate, whether food is consumed before, alongside, or after drug administration, poor hepatic or renal function, and enzyme induction or inhibition. Dosage form solutions to these issues are wide ranging.[53–56]

Active site targeting is not generally an area of relevance regarding oral dosage forms, but its importance for inorganic nanoparticle dosage forms merits its inclusion here. Active site targeting dosage forms may be injected into the bloodstream, only releasing their contents at a specific location, either through triggering by an enzyme or substrate,[48,57] or some external influence such as a magnetic field or electromagnetic radiation of a specific wavelength.[58–60] Active site targeting allows a much lower drug dose to be used, and can significantly reduce unwanted side effects from the action of the drug at unwanted sites. The dosage form may even transport the drug into cells or across membranes that the drug cannot cross otherwise, greatly increasing their efficacy and potential to treat different conditions.[61,62]

1.2.2 Controlled release

The controlled release of drugs through dosage form design is one of the most active areas of pharmaceutics.[63] The controlled release of drugs is concerned with

manipulating the speed with which drugs are absorbed into and remain in the body, and incorporates sustained release, accelerated release and delayed onset dosage forms.[64] Controlled release may be employed to counter many drawbacks of the drug being administered, such as poor bioavailability,[65] to prevent side effects from the drug overdose range, simply for convenience to reduce the dosage frequency needed, or may be necessary to allow a patient to stay dosed for a sufficient period time to allow them to sleep through the night.[66–68] Unwanted side effects have also been observed when the blood concentration of some drugs changes rapidly, and controlled release dosage formed may be designed to counter these effects.[69] Combined drug dosage forms may also be designed whereby a first drug is release before another, particularly when the first drug prevents or slows the metabolism of the second drug, or allows its effects to be focused on one part of the body.[70–72] Gastroretentive formulations control the release of drugs by remaining in the stomach or intestines for an extended period, which is of use for drugs which need to be absorbed in a specific section of the GI tract.[16,73,74]

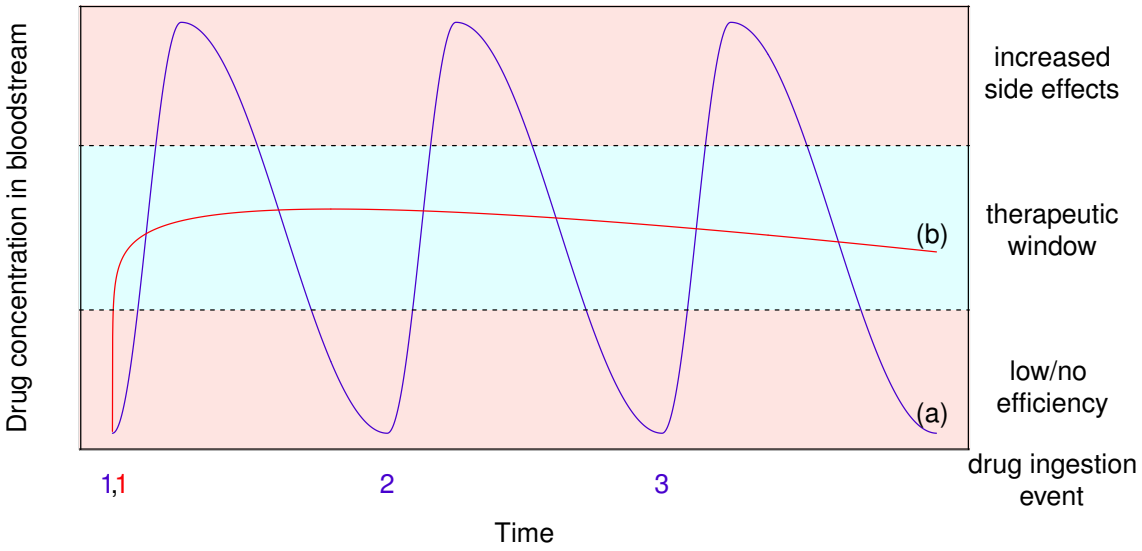


Figure 1.1: Typical blood concentration profiles of a drug species over time after administering in (a) conventional release formulation and (b) a controlled release formulation.

The range of drug blood concentrations in which a drug is considered effective is called the therapeutic window. If the drug blood concentration lies above this window, increased and unwanted side effects may occur, whilst if it falls below this window, the concentration is not sufficient for the drug to have its intended effects.[75]

Figure 1.1 depicts typical blood concentration profiles of a drug after administration of conventional and controlled release formulations. After administration of the conventional release dosage form, there is a short lag while the dosage form is disintegrated (if it is an oral tablet or capsule) and absorbed, at which point all the administered dose is absorbed rapidly and the drug blood concentration quickly peaks at its maximum level. This can often fall above the therapeutic window and lead to negative side effects. The amount of time the drug blood concentration spends within the therapeutic window is entirely dependent on the rate at which the drug is metabolised or excreted, and consequently if the drug is metabolised quickly, regular dosing will be necessary to avoid the drug blood concentration falling below the effective range.[64]

In comparison, controlled release aims to maintain the drug blood concentration within the therapeutic window for a designated amount of time, usually for as long as possible.[64] The most simple sustained release systems may achieve this by gradually leaching or diffusing their contents over time, for example as they move through the GI tract.[46,76] More sophisticated controlled release systems may aim to release an initial burst, or even attempt to accelerate the initial absorption of a drug, such as by increasing its solubility, to reach the therapeutic more rapidly.[77,78] Beside a direct therapeutic benefit, this may cause the patient to feel as though the medicine is more effective, as the rapid change in concentration will be more noticeable, as in rapid release pain medication.[78]

The initial burst of drug release may then be combined with a tapered, gradual release to maintain the drug blood concentration within the therapeutic window. The two-phase release profile has been achieved through many methods, including core-shell systems,[79] polymer matrices with varying density or solubility,[80] layered or coated compounds,[81,82] drug-chelate or drug-complex systems,[83] or simply by using release systems that naturally exhibit a two-stage release profile, such as those that rely on a mixture of rapid dissolution and slow diffusion, as with layered inorganic compounds.[84–86]

1.2.3 Kinetic models for drug release

There are many kinetic models that have been used to model the release of drug species from solid dosage forms, and more broadly, the release of any target species into solution from a solid matrix. Such models can typically be used to calculate mechanistic data, such as the activation energy of release reaction, and the rate constants of release. Most generally, models of release follow a sigmoidal curved plot, whereby there in an initiation phase to the release, an acceleratory growth phase, and a decay period, although in different models some of these phases may be negligible or absent. Of these models, there are five that have typically been found to be suitable for modelling release from two dimensional layered solids, and in particular layered double hydroxides, the family of compounds that are the subject of this thesis: the Avrami–Erofe'ev, Elovich, simple first order, modified Freundlich and parabolic diffusion models.[87]

1.2.3.1 The Avrami–Erofe'ev model

The Avrami-Erofe'ev model, created by Avrami in 1939 from Johnson-Mehl-Avrami-Kolmogorov kinetics and later modified by Erofe'ev, has been applied to several areas of solid state kinetics including phase transformation, decomposition, and intercalation.[88–90] The model can be used to determine sigmoidal kinetic characteristics of many common solid state reactions. The general form of the model is expressed in Equation 1.1 in its exponential form and in Equation 1.2 in its logarithmic form.

$$\alpha = 1 - \mathrm{e}^{-kt^n} \qquad \textbf{Equation 1.1}$$

$$-\ln(1-\alpha) = kt^n \qquad \textbf{Equation 1.2}$$

Where α is the reaction progress calculated from the ratio between the concentration of drug released at time, t, and the theoretical drug concentration upon complete drug release, k is the reaction constant, and n is the exponent. Taking logarithms of Equation 1.2 returns Equation 1.3,

$$\ln(-\ln(1-\alpha)) = n\ln k + n\ln t \qquad \textbf{Equation 1.3}$$

which, when plotted, allows n and k to be calculated.

1.2.3.2 The Elovich model

The Elovich model was first applied to gas sorption reactions, later being modified by Elovich *et al.* It has subsequently been applied to release processes from host matrices and desorption processes.[91,92] Equation 1.4 gives the general form of this model, used for sorption processes:

$$\frac{\mathrm{d}\alpha}{\mathrm{d}t} = m\mathrm{e}^{-n\alpha} \qquad \textbf{Equation 1.4}$$

Where α represents reaction progress, and m and n are constants. This model was modified to describe phosphate release from soils to:

$$1 - \alpha = n\ln t + m \qquad \textbf{Equation 1.5}$$

The reaction constants n and m are arbitrary and have not been shown to have physical, chemical, or mechanistic significance.

1.2.3.3 The simple first order model

The simple first order model expresses a simple logarithmic relationship between the reaction progress, α, and reaction time, t. The first order model for the release of a drug, A, with concentration C_A is given by Equation 1.6.[93]

$$\frac{\mathrm{d}C_\mathrm{A}}{\mathrm{d}t} = -kC_\mathrm{A} \qquad \textbf{Equation 1.6}$$

Rearrangement and subsequent integration gives Equation 1.8,

$$\frac{\mathrm{d}C_\mathrm{A}}{C_\mathrm{A}} = -k\mathrm{d}t \qquad \textbf{Equation 1.7}$$

$$\ln C_\mathrm{A} = -kt + c \qquad \textbf{Equation 1.8}$$

At $t = 0$, $c = \ln C_{\mathrm{A}}^{0}$, where C_{A}^{0} is the initial concentration of A, and so Equation 1.8 can be expressed as:

$$\ln C_{\mathrm{A}} = -kt + \ln C_{\mathrm{A}}^{0} \qquad \textbf{Equation 1.9}$$

Which rearranges to:

$$\ln\left(\frac{C_{\mathrm{A}}}{C_{\mathrm{A}}^{0}}\right) = -kt \qquad \textbf{Equation 1.10}$$

The reaction progress, α, can be expressed in terms of $C_{\mathrm{A}}/C_{\mathrm{A}}^{0}$,

$$\alpha = 1 - \frac{C_{\mathrm{A}}}{C_{\mathrm{A}}^{0}} \qquad \textbf{Equation 1.11}$$

And so the simple first order model can be expressed by Equation 1.12.

$$\ln(1 - \alpha) = -kt \qquad \textbf{Equation 1.12}$$

This allows the rate constant, k, to be calculated.[91,93]

1.2.3.4 The modified Freundlich model

The modified Freundlich model is commonly employed for studying ion-exchange kinetics in zeolites, clays and layered materials, as it describes diffusion-controlled desorption from heterogeneous surfaces. It is expressed in Equation 1.13 in its original form using the two parameter Freundlich isotherm, where K_{F} is the Freundlich constant, C_{e} is the concentration of the adsorbant at equilibrium, and n is a dimensionless parameter that varies between 0 and 1.[91,94]

$$\alpha = k_{\mathrm{F}} C_{\mathrm{e}}^{1/n} \qquad \textbf{Equation 1.13}$$

Kuo and Lotse modified the Freundlich equation in 1973 to model the kinetics of phosphate adsorption and desorption on hematite and gibbsite, expressing the isotherm in a time-dependent form, as in Equation 1.14.[95]

$$\alpha = k_{\mathrm{F}} t^{n} \qquad \textbf{Equation 1.14}$$

This can be expressed as a linear plot like so,

$$\ln\alpha = \ln k_{\mathrm{F}} + n\ln t \qquad \textbf{Equation 1.15}$$

In this case, k_{F} denotes the rate constant.

1.2.3.5 The parabolic diffusion model

The parabolic diffusion model is used to model the kinetics of both ion-exchange and adsorption reactions, and assumes that the rate limiting phenomena of these processes are diffusion controlled. It is derived from calculations for the rate of radial diffusion in cylinders, whereby diffusion in perpendicular directions is negligible. The formula for such a diffusion controlled process is expressed in Equation 1.16:

$$\alpha = \frac{4}{\sqrt{\pi}}\sqrt{\frac{Dt}{r^2}} - \frac{Dt}{r^2} \qquad \textbf{Equation 1.16}$$

Where r represents the radius of the cylinder, D corresponds to the apparent diffusion constant, α corresponds to the reaction progression and t corresponds to the reaction time. Division by t returns:

$$\frac{\alpha}{t} = \frac{4}{\sqrt{\pi}}\left(\sqrt{\frac{D}{r^2}}\right)\frac{1}{\sqrt{t}} - \frac{D}{r^2} \qquad \textbf{Equation 1.17}$$

Which can be written as:

$$\frac{\alpha}{t} = \frac{m}{\sqrt{t}} - n \qquad \textbf{Equation 1.18}$$

where $m = \frac{4}{\sqrt{\pi}}\sqrt{\frac{D}{r^2}}$ and $n = -\frac{D}{r^2}$.

A linear plot of α/t against $1/\sqrt{t}$ then allows the values of the constants to be determined.[96]

1.3 Layered double hydroxides

1.3.1 Structure of layered double hydroxides

Layered double hydroxides (LDHs) are a widely studied family of layered ionic compounds which can be expressed by the general formula $[M^{z}_{1-x}M^{III}_{x}(OH)_2]^{a+}A^{n-}_{a/n} \cdot mH_2O$, where M^z is a mono or divalent metal cation such as Li^+, Mg^{2+}, Ca^{2+}, Fe^{2+}, Co^{2+}, Ni^{2+}, Cu^{2+}, Zn^{2+}, etc., M^{III} is a trivalent metal cation such as Al^{3+}, Ga^{3+}, Fe^{3+}, Co^{3+}, Cr^{3+}, etc., and A^{n-} is an n-valent anion. Most commonly, $z = 2$, and consequently $a = x$. The structure of LDHs can be thought of as a modified brucite $Mg(OH)_2$ structure, which consists of infinite sheets of edge-sharing $Mg(OH)_6$ octahedra, but with some fraction of the Mg^{2+} ions replaced by M^{3+} ions, as Figure 1.2 illustrates. This substitution results in a net positive charge on the metal hydroxide layers, which is balanced by the inclusion of labile interlayer anions, along with co-intercalated water molecules.[97,98] Co-intercalation and surface absorption of other protic and organic solvents has also been observed in LDHs, although generally water is preferentially intercalated.[99–101]

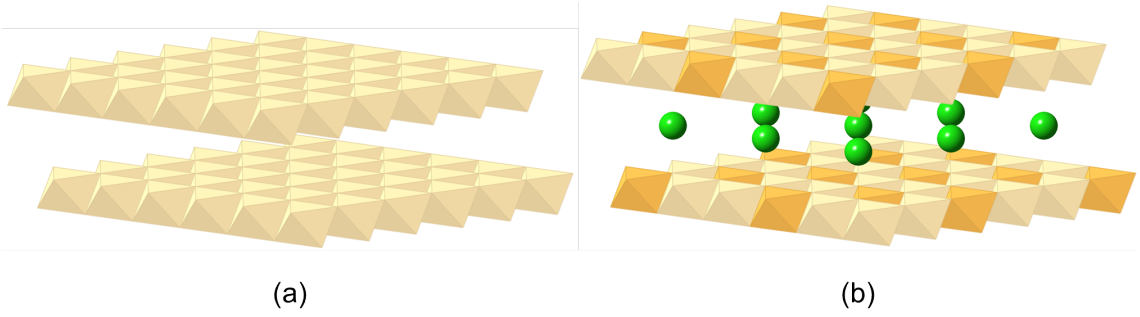


Figure 1.2: The structure of (a) brucite, $Mg(OH)_2$, and (b) an LDH, $Mg_2Al(OH)_6Cl$. $Mg(OH)_6$ octahedra are depicted in cream, $Al(OH)_6$ are depicted in yellow, and Cl^- ions are depicted as green spheres.

Also known are a class of LDHs based on the gibbsite γ-$Al(OH)_3$ structure, whereby M^{III} is Al^{3+} and M^{z+} is typically Li^+, Co^{2+}, Ni^{2+}, Cu^{2+} or Zn^{2+}.[102,103] In contrast with the majority of the previously described families of LDHs, this group shows substantial cation ordering; the Li^+ ions are found regularly ordered in one third of the octahedral sites of the $Al(OH)_3$ layers, or in the case of divalent cations, one sixth of the octahedral sites, leaving another sixth of these sites vacant, resulting

in the general formulae $[LiAl_2(OH)_6]^+A^- \cdot mH_2O$ and $[M^{II}Al_4(OH)_{12}]^{2+}A_2^- \cdot mH_2O$. Additionally, ternary LDHs of this form containing combinations of the M^{II} ions have been prepared.[104] The metal hydroxide layers stack in eclipsed hexagonal (*aba*) or rhombohedral (*abca*) sequences, as with the polymorphs of $Al(OH)_3$, being gibbsite, bayerite and nordstrandite.[105]

Generally, pure LDH structures only form within the range $0.20 \leq x \leq 0.33$ with metal hydroxide impurities growing in beyond these limits, although pure LDH phases have been identified within the range $0.07 \leq x \leq 0.50$.[106,107] The metal hydroxide layers are typically stacked hexagonally (*aba* sequence) or rhombohedrally (*abca* sequence), producing unit cells two or three sheets thick respectively, as illustrated in Figure 1.3. Alongside these principle stacking sequences, other less common stacking sequences are possible, and all possible polytypes resulting from different stacking combinations have been described in the literature.[108,109] In practice, LDH samples may incorporate multiple stacking sequences and polytypes within individual particles and crystalline regions. Additionally, stacking faults and turbostratic disorder are commonly observed, particularly in samples synthesised though coprecipitation.[110–112] The prevalence of such stacking faults and disorder in a given LDH sample manifests in the degree of Warren-type anisotopy observed in the Bragg reflections of the X-ray diffraction patterns of the LDHs, exempting the basal, $(00l)$ reflections, which do not typically exhibit any significant anisotropy.[113,114]

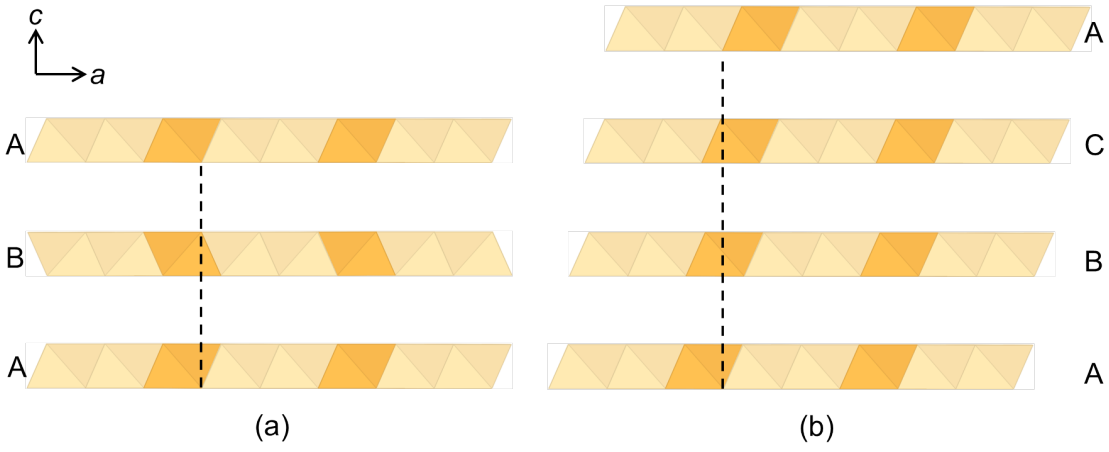


Figure 1.3: The stacking sequence of (a) a hexagonally stacked LDH, (2H), and (b) a rhombohedrally stacked LDH, (3R).

Over forty naturally occurring LDH species have been identified, including hydro-

talcite ($Mg_6Al_2(OH)_{16}CO_3 \cdot 4\,H_2O$), quintinite ($Mg_4Al_2(OH)_{12}CO_3 \cdot H_2O$), takovite ($Ni_6Al_2(OH)_{16}CO_3 \cdot 4\,H_2O$) and fougèrite ($Fe_4^{2+}Fe_2^{3+}(OH)_{12}CO_3 \cdot 3\,H_2O$), and artificially synthesised LDH species are also commonly referred to as pseudohydrotalcites in acknowledgement of the structural similarity between these species.[115,116] LDHs are notable in comparison to many other clay materials for consisting of cationic metal hydroxide layers with interlayer anions, whereas clay materials consisting of anionic layers with intercalated cations are much more common, as in montmorillonite and kaolinite.[117] Hydrotalcite was first identified in 1842 by Hochstetter, and the first artificially synthesised LDH samples were reported by Feitknecht in the 1930s.[118–120] The crystal structure (determined by a single crystal diffraction study) of an LDH, sjögrenite, was first obtained by Allmann and Lohse in 1966, shortly followed by that of pyroaurite by Allmann in 1968, both LDHs being different polytypes of $Mg_6Fe_2(OH)_{12}CO_3 \cdot 4\,H_2O$, and illustrating the relationship between different stacking sequences that give rise to the hexagonal and rhombohedral polytypes.[121,122]

Another attractive property of LDHs is the ability to closely control the ratios and identities of the metal cations within the metal hydroxide layers, which in turn influences many physical and chemical characteristics of the resulting LDHs. Certain characteristics can be more finely tuned through the synthesis of ternary and quaternary LDHs, some of which also display novel features not present in binary LDHs.[123]

The intercalation chemistry of LDHs with anions is extensive, with intercalated species ranging from small inorganic anions such as nitrate and halides, through to organic anions such as drugs, agrochemicals, carboxylates and anionic surfactants, and large complex species such as polyoxometalate anions, polymers, porphyrins, calixarenes, metallocenes, C_{60} and DNA.[124–137] Many smaller anions can be intercalated directly though coprecipitation from basic solution, whereas larger, more complex species may be intercalated by using a variety of methods detailed in Section 1.3.2. The breadth of LDH synthesis and intercalation techniques available allows the intercalation of a target anion into LDH particles of a particular intended size or morphology.[138]

The powder X-ray diffraction patterns of LDHs are distinctive, and exhibit intense basal Bragg reflections which index as $(00l)$ with systematic absences. These can be explained with reference to the structure factors, F_{hkl}, of the two predominant

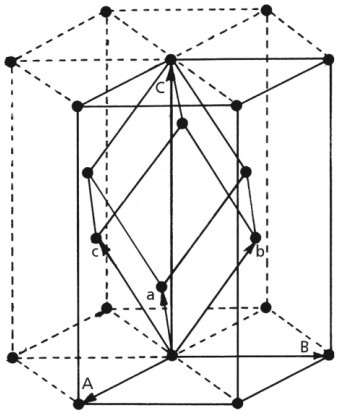


Figure 1.4: The relationship between the rhombohedral R unit cell, with lattice vectors a, b and c, and the triple hexagonal cell, with lattice vectors A, B and C.[139]

polytypes, rhombohedral and hexagonal.[113] By considering rhombohedral polytypes in terms of a triple hexagonal unit cell, as illustrated in Figure 1.4, both of the predominant polytypes can be indexed using the equation for a hexagonal lattice, Equation 1.19.

$$\frac{1}{d^2} = \frac{4}{3}\frac{h^2 + hk + k^2}{a^2} + \frac{l^2}{c^2} \qquad \textbf{Equation 1.19}$$

The structure factor, F_{hkl}, for the Bragg reflections seen in the diffraction patterns of the rhombohedral and hexagonal polytypes, can be calculated from the Miller indices, h, k and l, and help to explain the absences seen in the LDH diffraction patterns, with interlayer species being ignored. Briefly, in rhombohedral polytypes, when $h = k = 0$ and $l \neq 3N$ (where N is an integer), $F_{hkl} = 0$, explaining why basal Bragg reflections are only seen at hkl values of (003), (006), (009), ... (00$3\underline{n}$). Similarly, in hexagonal polytypes, when $h = k = 0$ and $l \neq 2N$, $F_{hkl} = 0$, resulting in basal Bragg reflections at hkl values of only (002), (004), (006), ... (00$2\underline{n}$). Similar extinction coefficients can be calculated for the Bragg reflections of each polytype when $h = 0$ and $k = 1$, with rhombohedral polytypes only exhibiting reflections when $l = 3N + 2$, *e.g.* (012), (015), (018), *etc.* and hexagonal polytypes given no restrictions and all (01l) allowed. Similarly, when $h = k = 1$, rhombohedral polytypes only exhibit Bragg reflections when $l = 3N$, *e.g.* (110), (113), (116), *etc.* and hexagonal polytypes only exhibit Bragg reflections when $l = 2N$, *e.g.* (110), (112), (114), *etc.*

As the c lattice parameter runs parallel to the stacking direction of the LDH layers, the basal (00l) reflections allow for facile determination of the size of the interlayer space. The d-spacing of the (003) reflection in rhombohedral polytypes, and the (002)

reflection in hexagonal polytypes, equals the thickness of a single metal hydroxide sheet plus the interlayer distance. The thickness of the metal hydroxide sheets varies very little, and is typically around 4.8 Å.[140] As the size of the interlayer space is directly related to the identity of the interlayer anions, the success of intercalation reactions can be obtained quickly from powder X-ray diffraction analysis, although different interlayer anions that produce the same interlayer distances cannot be discerned through this analytical technique alone. Additionally, the progress of intercalation reactions can be monitored readily through *in situ* energy dispersive X-ray diffraction (EDXRD) reactions.[141–143]

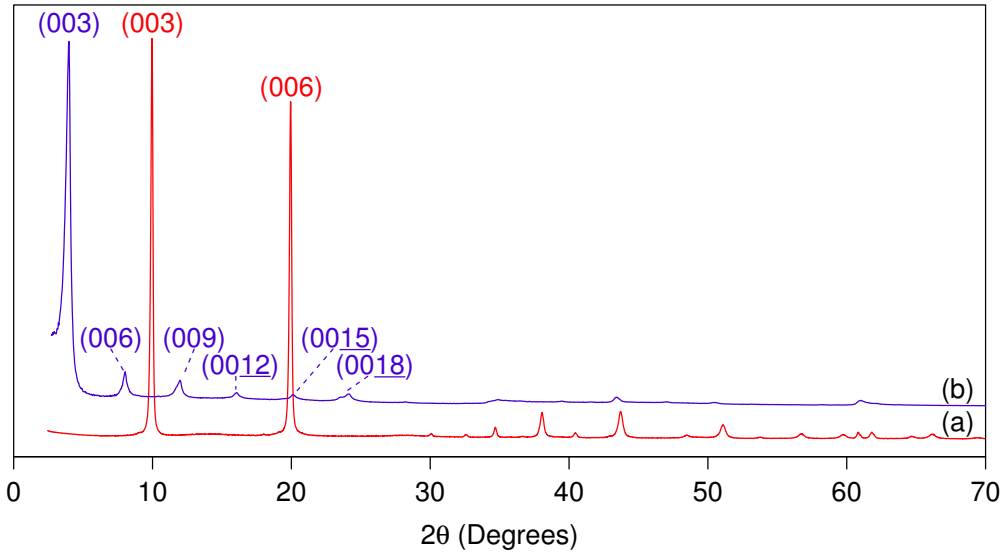


Figure 1.5: X-ray diffraction patterns of (a) a $[Mg_2Al(OH)_6]NO_3$ LDH and (b) a $[Mg_2Al(OH)_6]$ibuprofen LDH, illustrating the difference in the positions of the basal $(00l)$ Bragg reflections.

It is common for surfactant anions or other anions that due to their structure may act like surfactants, to form bilayers within the interlayer region with charged, hydrophilic groups facing the metal hydroxide sheets, and hydrophobic groups facing towards each other.[144] Ibuprofen is one such anion that forms bilayers, and Figure 1.5 illustrates the difference in positions of basal $(00l)$ Bragg reflections between an LDH intercalated with a bilayer of ibuprofen ions, causing an interlayer distance of 17.3 Å, and an analogous LDH intercalated with nitrate ions, causing an interlayer distance of 4.07 Å.[124]

1.3.2 Synthesis of layered double hydroxides

LDHs have been synthesised through a multitude of methods.[145] The major synthesis routes, and those relevant to this thesis, are detailed below, although other synthesis routes have been reported for specific cases, such as mechanochemical methods or routes using alternative reagents such as epoxides.[142,146,147]

1.3.2.1 Coprecipitation

Coprecipitation forms the desired LDH from the gradual addition of a solution of mixed metal salts, typically metal nitrates or metal chlorides, and the interlayer anion to a basic solution with vigorous stirring. The LDH precipitates out of solution as the metal hydroxide layers aggregate *in situ* around the interlayer anion.[145] Coprecipitation may be performed under conditions of 'high supersaturation' or 'low supersaturation', the former consisting of the gradual addition of a concentrated metal salt solution directly to the basic solution also containing the intended guest ion, typically forming small particles, and the latter consisting of simultaneous addition of the metal salt and basic solutions to a third solution containing the intended guest ion, typically forming larger, more crystalline particles.[106,148,149] A wide range of anions may be intercalated through this method, although it is generally more effective with smaller anions such as chloride, nitrate, carbonate, or simple organic carboxylates.[150] The resultant LDH can often be poorly crystalline, although this can be improved upon by hydrothermal treatment of either the reactant mixture during synthesis, or of the resulting LDH subsequently.[151–153]

Highly crystalline particles can also be generated by the method known as homogeneous coprecipitation, whereby instead of the addition of a separate basic reagent, the basicity of the reaction mixture is mediated by the gradual hydrolysis of urea or a similar reagent such as hexamethylenetetramine or formamide, often under refluxing or hydrothermal conditions.[154–158] Whilst this generates large ($> 1\,\mu m$ diameter) platelets, it is often only possible to produce LDH particles that contain carbonate as the interlayer anions, as the carbonate ions are formed *in situ* during the hydrolysis process. Advances have been made, however, to synthesise highly crystalline LDHs containing other interlayer anions through this method, including

buffering the reactant mixture using ammonium nitrate to produce nitrate containing LDHs, and adding surfactant anions to the reaction mixture to intercalate long chain alkyl carboxylates and sulfonates.[159,160]

Conversely, coprecipitation using the reverse microemulsion method, whereby water solvated reactants form colloidal dispersions in oil in which the reaction proceeds, leads to the formation of small, (< 40 nm diameter) poorly crystalline nanoparticles, with precise and controllable sizes.[161–163]

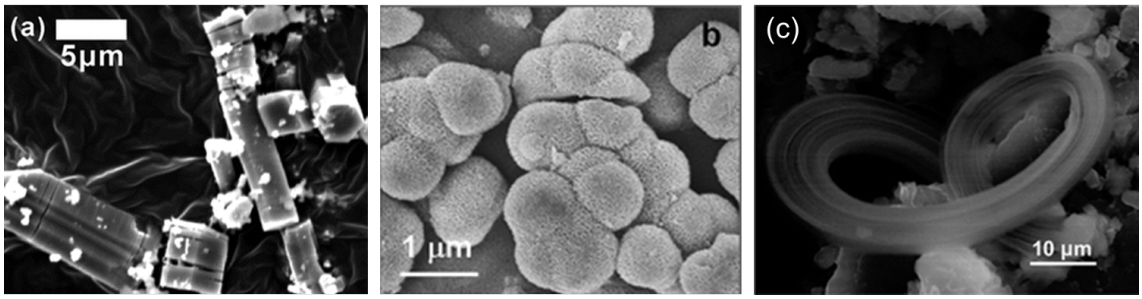


Figure 1.6: A selection of LDHs exhibiting unusual morphologies: (a) $LiAl_2(OH)_6Br$ exhibiting rod-like morphology, formed by a salt–oxide method,[164] (b) $Mg_2Al(OH)_6$4-biphenylacetate exhibiting coral-like morphology, formed by a coprecipitation method,[138] and (c) $Mg_2Al(OH)_6$dodecyl sulfate exhibiting belt-like morphology, formed by a coprecipitation method.[161]

An advantage of coprecipitation synthesis is the breadth of controllable particle sizes and morphologies that is possible by altering the synthesis conditions. In particular the temperature, speed, concentration, ageing time or pH of the reaction mixture have all been studied extensively, although new morphologies are still being discovered, as can be seen from examples in Figure 1.6.[138,165–167] Sonication and microwave irradiation during the ageing process have also been investigated.[168] Additionally, when performed in the presence of an appropriate template, such as a silica or magnetite nanoparticles, or platinum or carbon rods, the coprecipitation method allows the formation of composite materials, such as core-shell type structures, or coated electrodes.[169–173]

1.3.2.2 Salt–oxide method

The salt–oxide method consists of heterogeneous reaction of a metal (II) oxide or hydroxide suspended in a concentrated aqueous solution of a metal (III) salt, often

at elevated temperatures or under hydrothermal conditions. This relies on the interaction between the basic metal oxide and acidic metal salt close to the surface of the metal oxide particles, creating a local environment within the desired basic pH range for seeding and growth of the LDH crystals. Several LDHs, in particular those containing Cu^{2+} or Cr^{3+} ions, can be synthesised via the salt–oxide method, where coprecipitation routes towards the same species are difficult or impossible.[174–177]

1.3.2.3 Ion-exchange

Ion-exchange reactions are the principle method of exchanging the intercalated ions in LDHs and have been studied in depth, most notably using *in situ* energy dispersive X-ray diffraction (EDXRD), to reveal varied mechanistic pathways, with both direct reaction from precursor to product LDH, and mechanistic pathways containing an intermediate phase being observed.[141,143] Typically, an LDH which has been synthesised with a labile interlayer anion, such as nitrate or chloride, is suspended in a concentrated solution of the desired guest anion.[145,150] In comparison, small polyvalent anions such as carbonate, phosphate and sulphate are much less labile, to the extent where direct ion-exchange reactions to remove carbonate ions from LDHs are generally considered impossible.[178–180] Elevated temperatures or long reaction times may be needed to reach high intercalation percentages, especially if the desired guest anion has a high mass:charge ratio, although it has been observed that at high temperature intercalation can be hindered.[145,181,182] If the target anion is particularly large and does not intercalate readily into an LDH with a small precursor anion, the LDH is 'pillared', whereby a labile, intermediate-sized anion, such as dodecylsulfate or other surfactant-type anion is intercalated prior to intercalation of the larger species.[144,183] This increases the interlayer distance in stages, as the significant disparity in interlayer spacing from starting material to finished product hinders one-step ion exchange.

1.3.2.4 Calcination–reconstruction

Calcination–reconstruction is a technique used on carbonate intercalated LDHs, as these LDHs often form readily and carbonate ions cannot be replaced through

ion-exchange. The LDH is flash calcined at approximately 500 °C, which removes the interlayer carbonate as carbon dioxide, along with any cointercalated water molecules, forming a layered double oxide (LDO). The LDO is then subsequently rehydrated in a concentrated solution of the chosen anion, which is intercalated into the LDH as it reforms, retaining its original structure due to a phenomenon known as the 'memory effect' that is often observed when calcining layered materials.[184–186] This method has been used to intercalate many varied species, in particular large guest species such as dye anions, and has also been utilised to intercalate neutral guests such as pentose and hexose sugars.[187–190] Drawbacks of this synthesis method are that intercalation of the desired guest is often accompanied by intercalation of carbonate or other readily intercalated anions, and that the crystallinity of the resulting LDH is generally greatly reduced in comparison to the precursor carbonate LDH.[191]

1.3.2.5 Decarbonation

An alternative method of functionalising carbonate intercalated LDHs is through decarbonation. In this process, the carbonate is removed through reaction with a dilute solution of a strong acid in the presence of an intended guest ion to produce an LDH with either labile interlayer anions ready for further reaction, or another intended guest anion. However, due to the restrictions on the reaction relating to pH, the type of guest ions that can be directly intercalated by this method is limited. Decarbonation was first demonstrated by Costantino *et al.*[180] by passing a flow of gaseous HCl over carbonate LDH at 150 °C, although the more practical solution phase method was developed and further refined by Iyi *et al.*[156,192–194]

Several variations of the solution phase method have been developed. In the salt-acid method, the carbonate LDH is suspended in a solution containing approximately two equivalents of a strong acid, typically hydrochloric, hydrobromic, nitric or perchloric, to each equivalent of intercalated carbonate anions, alongside salts of the intended guest anions at high concentration. The salt-acetate buffer method replaces the strong acid by an acetic acid-sodium acetate buffer, requiring a lower concentration of the guest ion salt.[194–196] Other variations are the acid-alcohol method, which consists of suspending the carbonate LDH in a dilute solution of acid in methanol or ethanol, without the requirement of any additional salt in the reaction mixture,[197]

and the ammonium salt-acid method, which uses acidic ammonium salts in place of the dilute acid.[198] This method of functionalising carbonate LDHs has the advantage of retaining morphology and degree of crystallinity of the precursor LDH.

1.3.2.6 Delamination–restacking

Delamination of LDH sheets has been achieved in a number of conditions of varying extremity, including refluxing in butanol at 120 °C for 16 h,[199] heating to 70 °C in polar acrylates with vigorous agitation,[200] in hydrophobic solvents toluene and CCl_4,[201,202] in a DMF-ethanol mixture,[203] in water,[204] and in formamide with agitation.[205,206] The identity of the interlayer anion is often vital when delaminating via different methods. For example, delamination in butanol, toluene and CCl_4 has only been possible when dodecylsulfate is the interlayer anion, whilst the method of delamination in water relies on the interlayer anion being lactate.[204,207] Delamination using formamide has been demonstrated with samples containing various interlayer species, including several amino acids and nitrate ions, although it has been noted that other interlayer ions, such as carbonate, lactate and oleate, do not facilitate delamination with formamide, or facilitate only partial delamination, as is the case with chloride, perchlorate and acetate.[208–210] When delaminated, the individual LDH sheets do not exhibit X-ray diffraction patterns typical of LDHs, and consequently their characterisation has relied on other techniques.[211] Delaminated LDH sheets are desirable for a number of reasons, including their high surface area and facile synthesis, which indicate their potential use in thin film coatings, as catalyst supports, as electrode surfaces, as composites with polymer matrices, or as catalysts for water splitting, amongst other uses.[212,213]

Besides the direct applications of delaminated LDH sheets, the delaminated layers can be reassembled into larger LDH particles again through a restacking process which, when conducted in the presence of a desired guest anion, provides another route of intercalation. The restacking process is most commonly achieved by the addition of LDH suspensions that have delaminated in formamide to a solution of either water or ethanol containing the desired guest anion, although direct addition of the intended guest species to the formamide suspension has also been successful.[210,214] The restacking method has been used to intercalate a range of species, from simple

carbonate ions through to micelles consisting of cholate anions encapsulating neutral camptothecin.[215–217] Despite its potential for intercalation of species that cannot be intercalated through other means, the restacking process has not been studied in depth for optimisation or elucidation of its mechanism.

1.3.3 General applications of layered double hydroxides

Besides biomedical applications, which are addressed separately below, LDHs have found applications in a wealth of areas.[218,219] There is much interest in the use of LDHs in catalysis, with examples of both the metal hydroxide layers and interlayer guest species acting as effective catalysts.[220–222] In the cases of the interlayer anions acting as catalysts, LDH intercalation allows facile recovery of the catalyst, whilst also reducing the prevalence of unwanted reactions.[221] The metal hydroxide layers themselves, due to their local basic environment, have been found to catalyse aldol condensations,[223,224] oxidation of methane,[225] phenols[226] and olefins,[220] synthesis of gold nanoparticles,[227] and splitting of water.[213] Additionally, LDHs have been used as precursors for catalyst materials, as the LDOs produced from calcination of LDHs have been found to catalyse oxidation of methanol, aldol condensations, the Henry reaction, and others.[222,228–231] Additionally, both LDHs and LDOs have found uses at catalyst supports.[232–236]

The selective separation of anions from solution has also been explored as a possible application of LDHs, due to their high capacity for anion uptake, ease of separation from solution and ability to selectively intercalate specific anions in preference to others.[237] This principle has been applied to waste management to extract oxoanions,[238–241] reactive dyes,[242,243] chlorinated organic species[244] and other pollutants from waste streams using both LDHs and LDOs through their reconstruction into LDHs, and even LDH/graphene oxide nanocomposites.[245–247] LDHs have been used to separate both amino acids and nucleosides,[248,249] as well as structural isomers of benzenedicarboxylate and napthalenedicarboxylate.[237,250]

The storage and release of guest anions has received much attention, and the breadth of anions that have been intercalated into LDHs has already been mentioned in Section 1.3.1, with many of these species finding specific applications. Areas

that have received particular interest include the intercalation of herbicides and pesticides for their use as controlled release vectors in agriculture,[126,251–253] the intercalation of vitamins, food additives and flavouring compounds for use in food production,[87,130,254,255] and surfactants for use in the synthesis of polymer–LDH composites.[128,256]

1.3.4 Pharmaceutical applications of layered double hydroxides

Several properties of LDHs make then particularly suitable as drug delivery systems. The biocompatibility of LDHs is discussed specifically below, but beyond this, the ability of LDHs to reversibly intercalate guest anions make LDHs excellent candidates for the controlled release of drug species, and this potential has been explored in multiple routes of administration, including topical, oral and parenteral drug delivery. The facile, inexpensive synthesis of LDHs, coupled with the well-documented and diverse range of compositions, particle sizes and morphologies available, provides for controlled release dosage forms that can be tailored to suit different drugs, purposes, and release rates.[145] The typical release profile of an LDH follows the two-phase shape of a burst followed by gradual release, which is often desired in controlled release formulations.[86]

The ability of LDHs to stabilise their interlayer guest ions has led to their investigation for stabilising unstable drugs, such as retinoic acid, cefazolin, levodopa and L-alanyl-glutamine, as well as their release.[257–260] For drugs that may have stability issues relating to their long term storage, due potentially to their hygroscopic nature or thermal instability, intercalation with LDHs provides a method of stable long-term storage.[261,262]

The ability of LDHs to act as drug storage materials has led to much interest in their use in polymer composites, particularly with enteric polymers, which may allow LDH particles to pass through the stomach, where they would otherwise be dissolved, and for their controlled release properties to be utilised in delivering drugs to the lower GI tract.[263–268] This may increase the bioavailability of the drug species being delivered, particularly as LDHs promote the delivery of drug species in their anionic

form, which can increase their solubility and may in some cases lead to greater absorption.[269–271] It should be noted, however, that due to the basic nature of LDHs, drugs that favour absorption in strongly acidic conditions may actually be absorbed less well.

Whilst LDHs have not been investigated extensively for their ability to mask the taste of drugs, interest has recently been growing in this area due to their neutral 'chalky' taste, which can be easily incorporated into solid chewable or liquid suspension dosage forms, and treatment of LDH particles to minimise initial leaching of intercalated drug when in the mouth indicated their potential in this area.[272] The taste masking abilities of similar layered clay materials has also been established.[273]

Parenteral delivery of drugs through LDH systems has also received significant interest, due to the ability of LDHs to act as active targeting systems, particularly when coupled with other inorganic compounds such as magnetite.[274] Increased efficacy of drugs has been observed and investigated, due to the LDH particles carrying drugs through cell membranes.[275]

The pharmaceutical applications of LDHs have been reviewed extensively in recent years, but the areas that have received most interest and show most potential are detailed here.[8,276–281]

1.3.4.1 Biocompatible layered double hydroxides

Although the combinations of metal ions that can be used to form LDH layers are extensive, when the requirement of biocompatibility is factored in, the variety of options available is limited to LDHs with layers predominantly comprising the ions Mg^{2+}, Ca^{2+}, Zn^{2+} and Al^{3+}.[280,282] Minor contributions to the LDH sheets, in the form of ternary ions, may be acceptable from some ions, including Li^{+}, Fe^{2+}, Fe^{3+} and Cr^{3+}, particularly when these ions impart a some kind of functionality to the LDH, such as a stabilising or synergistic effect,[283] or as a radiolabelling agent, as with $^{57}Co^{2+}$ and $^{67}Ga^{3+}$,[284,285] or fluorescence agent, as with several reported lanthanide-doped LDHs.[286–289]

Clay-like materials, of which LDH materials are a subset, have been used in pharmaceutics for decades, in part due to their low toxicity and high biocompatibility,

although generally those used for biomedical and pharmaceutical applications have been cationic clays, due to their greater prevalence in comparison to anionic clays such as LDHs.[282,290] When considering the biocompatibility of an LDH material, as with other inorganic and organic drug delivery systems, the material must fulfil certain chemical, physical and toxicological requirements. Chemical requirements include stability, purity and chemical inertness; physical requirements may be water content, particle size and morphology; toxicological requirements are that it is non-toxic, at least within the predicted dose and for the intended mode of use, and that it is microbiologically pure.[282,291–293] Many LDH materials can therefore, when made with the already stipulated selection of metal cations, be generally considered to be highly biocompatible, as the extensive study of LDH materials means the level to which LDH materials meet all of the chemical, physical and toxicological requirements is well known, and LDHs generally lie well within safe toxicity limits.[294–298]

1.3.4.2 Topical drug delivery

The first investigations into the use of LDHs as drug delivery systems focussed on the delivery of sunscreen agents in topical dosage forms,[299,300] and later research into this application has found that LDH particles, whilst also preventing leaching of the sunscreen agents away from the skin surface and preventing their photodegradation,[301–303] may act synergistically to absorb sunlight in a similar manner to zinc oxide particles used in sunblock.[304,305] In preventing leaching of sunscreen agents into the skin, LDH compounds have been shown to significantly reduce their toxicity.

Topical delivery of other drugs using LDHs has been limited, as LDH particles are not absorbed through the skin and drug delivery via ion-exchange or dissolution generally requires the LDHs to be in an aqueous environment. However, formulations such as transdermal patches and other topical formulations have been investigated for the nonsteroidal anti-inflammatory drugs (NSAID) diclofenac, ketoprofen and flurbiprofen, aspirin, and ascorbic acid.[306–310]

Whilst not strictly topical delivery, an unusual form of drug delivery involving LDHs has been reported by Tamaro *et al.* for the antifibrinolytic drug tranexamic acid, whereby the drug-intercalated LDH has been encapsulated with poly(ε-caprolactone)

to form a polymer–LDH composite, with the suggestion that this material could be used as suture threads or medicated scaffolds.[311] Another novel drug delivery application has been the use of LDH coatings for the release of antibiotics on titanium implants.[312]

1.3.4.3 Oral drug delivery

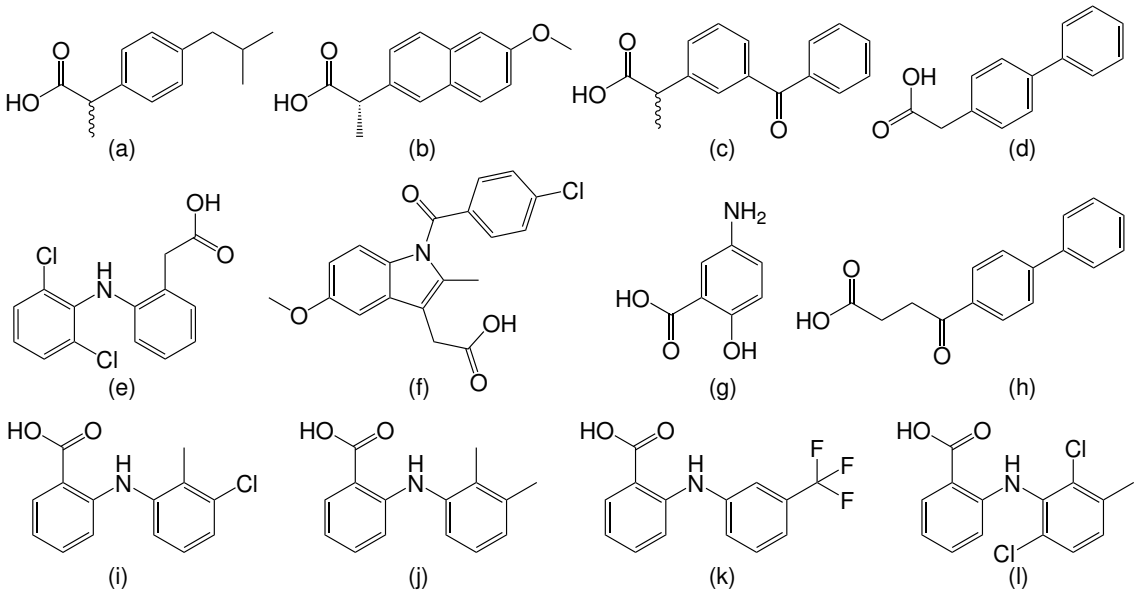


Figure 1.7: The structures of some commonly intercalated NSAIDs, (a) ibuprofen, (b) naproxen, (c) ketoprofen, (d) felbinac, (e) diclofenac, (f) indomethacin, (g) mesalazine, (h) fenbufen, (i) tolfenamic acid, (j) mefenamic acid, (k) flufenamic acid and (l) meclofenamic acid.

The most extensively investigated pharmaceutical application of LDHs is as oral drug delivery systems. Within this area of research, three treatment classes of drugs have received particular attention: nonsteroidal anti-inflammatory drugs (NSAIDs), cardiovascular drugs and antibiotics, although individual cases of research with other drugs of interest also exist. Of these classes, intercalation and delivery of NSAIDs has been most widely studied and reported on.[278] NSAIDS were some of the first drugs intercalated into LDHs for oral delivery.[124,313–316] Due to their stability, cost, and facile intercalation, they have quickly become model drugs for demonstrating the pharmaceutical potential of new LDH morphologies, compositions and composites, with ibuprofen, diclofenac and naproxen being used most commonly.[85,138,170,268,317–324] This has also allowed comparisons between the quality of products from different

synthesis methods, greatly advancing insights into the optimum conditions for synthesising drug-containing LDHs.

The pharmaceutical reasons for intercalating NSAIDs into LDHs include their poor aqueous solubility, which may severely limit their absorption, and also their propensity to cause irritation to the GI tract when delivered in their pristine state. The increased solubility and absorption of NSAIDs upon release from LDHs has been demonstrated.[269,315,325,326] GI irritation has even prevented the oral administration of some NSAIDs, such as fenbufen, although such irritation can be reduced through controlled release.[327] Additionally, the antacid properties of LDHs have been shown to reduce ulceration in the GI tract caused by NSAIDs.[325,328] Consequently, the range of NSAID drugs that have been intercalated is extensive, and has included fenamic acids (tolfenamic, mefenamic, flufenamic and meclofenamic acid), salicylates (salicylic acid, mesalazine), propionic acid derivatives (ibuprofen, naproxen, ketoprofen, fenbufen, flurbiprofen, dexketoprofen) and acetic acid derivatives (felbinac, diclofenac, aceclofenac, indomethacin), the most common of which are displayed in Figure 1.7.[124,270,326,328–333]

The release kinetics of NSAID-intercalated LDHs have been studied extensively. Comparisons between different morphologies, particle sizes, particle interactions, metal cation combinations and drug species with differing levels of hydrophobicity have all been investigated, and kinetic modelling has indicated the importance of the speed with which drug ions may diffuse through LDH layers.[86,334–338] The positive effects of delivery through LDH systems on NSAIDs have been demonstrated with *in vivo* studies in mice.[306,325] NSAIDs are the only drug that have been investigated with LDHs for taste-masking purposes, as ibuprofen has a notably bitter taste that prevents its formulation in concentrated liquid formulations.[272]

Cardiovascular drugs are the second family that have received attention for oral delivery within LDHs, and examples are displayed in Figure 1.8. Within this broad grouping are statins, Figure 1.8(a) and (b),[261,339] ACE inhibitors, Figure 1.8(c) and (d),[340,341] and fibrates, Figure 1.8(e), (f) and (g).[124,342] In comparison to NSAIDs, these drugs have significantly different functions, sites of action and requirements regarding their delivery in oral dosage forms.

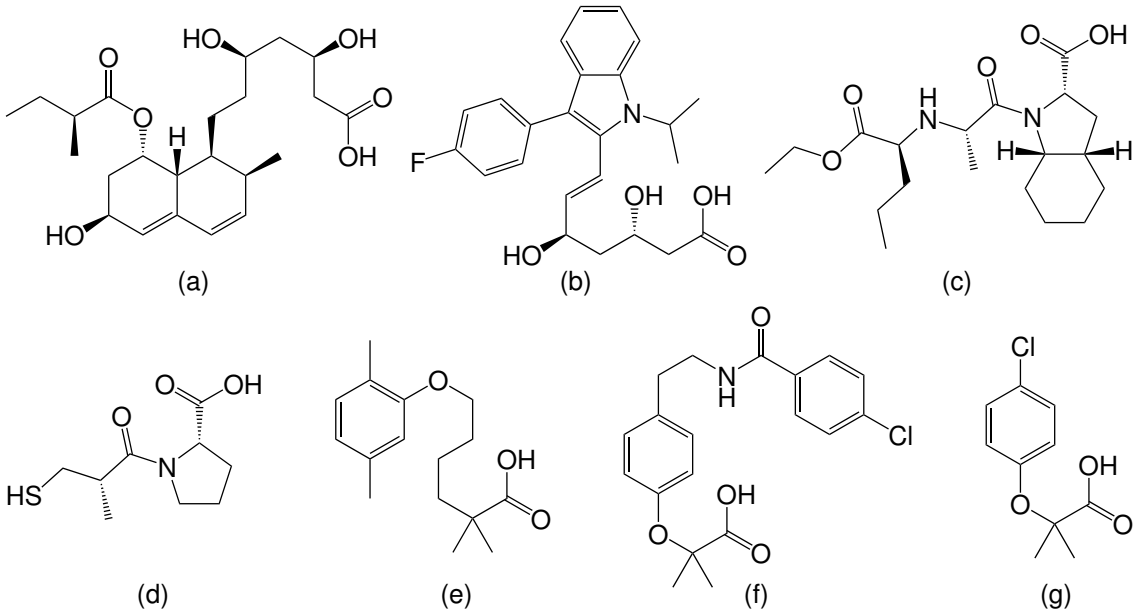


Figure 1.8: The structures of some commonly intercalated cardiovascular drugs, (a) pravastatin, (b) fluvastatin, (c) perindopril, (d) captopril, (e) gemfibrozil, (f) bezafibrate and (g) clofibric acid.

Statins are 3-hydroxy-3-methyl glutaryl-coenzyme A (HMG-CoA) reductase inhibitors, used as effective cholesterol lowering drugs, primarily prescribed to reduce the risk of cardiovacular disease. When formulated as pharmaceutically acceptable pristine salts, statins exhibit conformational instability caused by their hygroscopic nature, which in turn has an adverse effect on their aqueous solubility and, consequently, their bioavailability. Additionally, statins are prone to lactamisation during storage, which renders them inactive, and unstable in acidic conditions. Panda *et al.* reported the intercalation of two statins, pravastatin and fluvastatin, with the aim of creating chemically stable and highly bioavailable dosage forms of these drugs, with controlled release capabilities. Both drugs were found to be chemically stable within the LDH layers and exhibited practicable release profiles, although differences in the hydrophobicity of each drug led to significant differences in release rate and the percentage of total drug release achieved.[261]

Angiotensin-converting-enzyme (ACE) inhibitors are antihypertensive drugs used in the treatment of congestive heart failure. Zhang *et al.* first reported the intercalation of the ACE inhibitor captopril,[340] which was followed by the intercalation of enalpril, lisinopril, captopril and ramipril by Xia *et al.*[341] Both reported increased thermal stability of the drugs upon intercalation, and favourable release profiles. Subsequently,

Al Ali *et al.* have reported the intercalation of perindopril erbumine into both magnesium–aluminium and zinc–aluminium LDHs and compared the ACE inhibiting efficacy of both formulations on cell lines.[343,344]

Fibrates are hypercholesterolemia drugs that are typically administered orally and absorbed in the duodenum, although poor solubility, sensitivity to oxidation and a capacity to cause GI tract irritation are drawbacks that have all been reported with the delivery of these drugs. The first intercalation of a fibrate drug was by Khan *et al.* with gemfibrozil, and subsequently Berber *et al.* have reported the intercalation of bezafibrate and clofibric acid. In both reports, improved drug solubility and practicable release profiles were reported.[124,342]

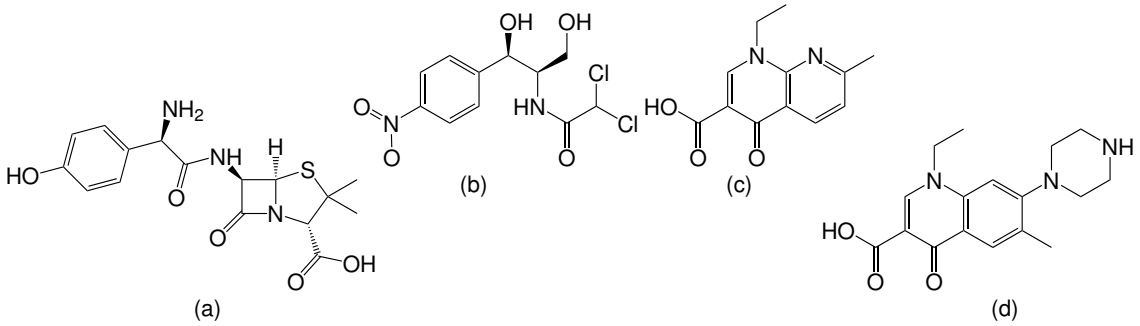


Figure 1.9: The structures of some intercalated antibiotics, (a) amoxicillin, (b) chloramphenicol, (c) nalidixic acid and (d) norfloxacin.

Several antibiotics have been intercalated into LDHs, either as model drugs to demonstrate the intercalation of different classes of antibiotics, or to counter their poor solubility. Trikeriotis and Ghanotakis demonstrated the intercalation of four antibiotics of diverse stuctures: the hydrophilic ampicillin and nalidixic acid, which could be intercalated directly as anions with high loading percentages recorded, and the hydrophobic gramicidin and amphotericin B, which were intercalated within cholate micelles, although low loading percentages were observed. The controlled release profiles of all four antibiotics were also recorded.[345]

Amoxicillin, a member of the penicillin family of antibiotics, was intercalated by Wang *et al.*[286,346] into two functionalised LDH–magnetite structures, one of which was also doped with lanthanide ions. It has also been intercalated into poly(ε-caprolactone)-LDH composites which exhibited a favourable two-step sustained release profile.[347]

Chloramphenicol has been intercalated into several LDHs, and the encapsulation of some of these LDHs with polymers has also been demonstrated, with release profiles having been measured for both the LDH and polymer–LDH composite systems.[331,348,349] The LDH intercalation of norfloxacin and ciprofloxacin have also been demonstrated and their release profiles measured.[350,351]

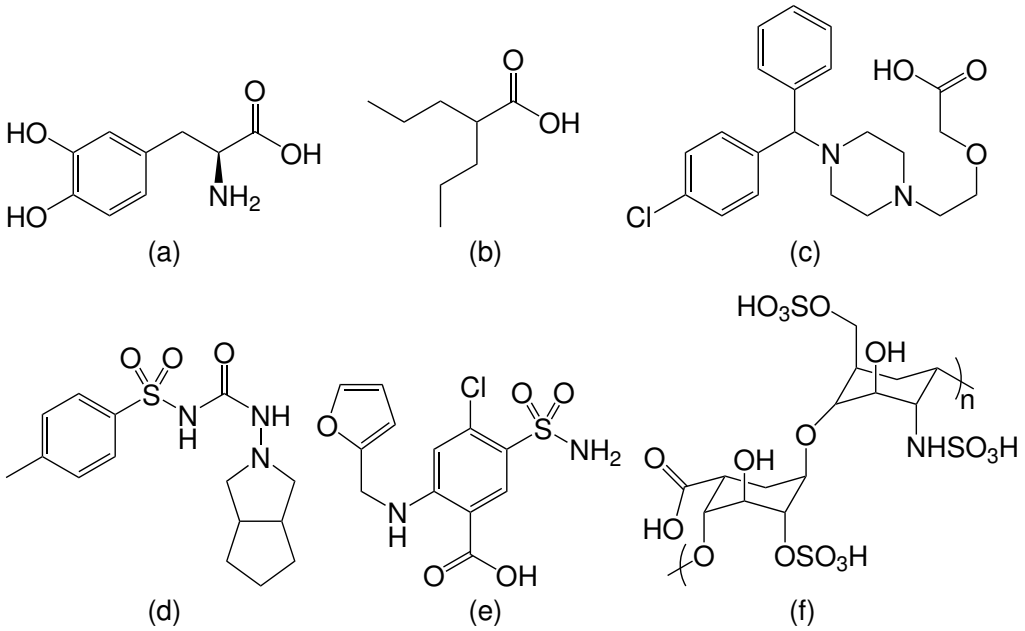


Figure 1.10: The structures of some other intercalated drugs of interest, (a) levodopa, (b) valproic acid, (c) cetirizine, (d) gliclazide, (e) furosemide and (f) heparin.

Besides the classes of drugs already mentioned, several other assorted drugs have been intercalated into LDHs, such as the examples displayed in Figure 1.10. These drugs have generally been chosen because they are anionic, and so are chemically suitable for intercalation, and because they have some specific pharmaceutical characteristic that makes them desirable candidates, such as poor stability or solubility, whilst also acting as models for the intercalation of different classes of drugs. These have included levodopa, an antiparkinsons drug of the catecholamine family that exhibits poor stability with respect to oxidative decomposition. Upon LDH intercalation, levodopa demonstrated improved thermal stability and stability with respect to racemisation.[258,352] Valproic acid, an antiepileptic drug also used to treat bipolar disorder, was first intercalated by Khan *et al.* due to its simplicity and stability as an anion, and has since been intercalated with the aim of developing a sustained release formulation, and to protect it from moisture, as it is hygroscopic when formulated

as the pure sodium salt.[124,353–355]

The antihistamine cetirizine has been intercalated into magnesium–aluminium and zinc–aluminium LDHs, exhibiting improved thermal stability upon intercalation. Cetirizine was found to form a bilayer when intercalated, due to the presence of both highly hydrophilic and hydrophobic regions. The LDH compounds showed sustained drug release and inhibition of histamine release when tested on cell lines.[356] Gliclazide is an antidiabetic drug of the sulfonylurea class that demonstrated poor solubility and gastric uptake. It has been intercalated into a ternary zinc–aluminium–chromium LDH, with the aim of producing a dosage form that both improved gliclazide bioavailability, whilst also providing nutrients (Zn and Cr) which are directly involved in the physiology of insulin; a marked improvement in the solubility of gliclazide in acid buffers was observed upon intercalation.[283] Furosemide is a loop diuretic drug that has exhibited poor solubility and gastric uptake. It has been intercalated into two LDH systems by Peroli *et al.* who subsequently formulated the intercalation compound into oral tablets, and tested for improved gastric uptake of the drug from these dosage forms *in vivo* and on *ex vivo* mucus membranes. It was found LDH intercalation improves furosemide bioavailability.[271,357,358]

Despite having received much interest and shown much potential, the realisation of practicable controlled release oral dose forms involving LDHs has not yet arrived. Indeed, Rives concludes in a review on LDH–NSAID delivery systems that further insights are still required for effective controlled release oral delivery systems involving LDHs to be developed, and these will necessarily require enteric coatings or polymer–nanoparticle matrices, as the introduction of LDHs to the stomach unprotected results in rapid dissolution, removing any opportunity for controlled release.[278]

1.3.4.4 Parenteral drug delivery

The low toxicity of LDH particles has led to their investigation as parenteral drug delivery systems. Much work has focussed on the interaction of LDH particles of different sizes with cells, as uptake of smaller LDH particles by cells may be used as a route for drugs species that are not usually absorbed to gain access to cells, and as a means of active site targeting.[359–361] Anticancer drugs have received the most

interest for this purpose, and examples are detailed in Figure 1.11, although another focus has been on the delivery of DNA and RNA sections for gene therapy.[8,362–369] Cointercalation of fluorescent dyes such as fluorescein isothiocyanate (FITC) onto LDH particles has also been reported, as this has allowed the positions of LDH particles in relation to cells to be observed through fluorescence microscopy.[370–373] LDHs radiolabelled with radioactive metal cations have also been used for this purpose.[284,285] Additionally, individual examples of other parenterally administered drugs exists, such as intercalation of the anticoagulant drug heparin.[289,374,375]

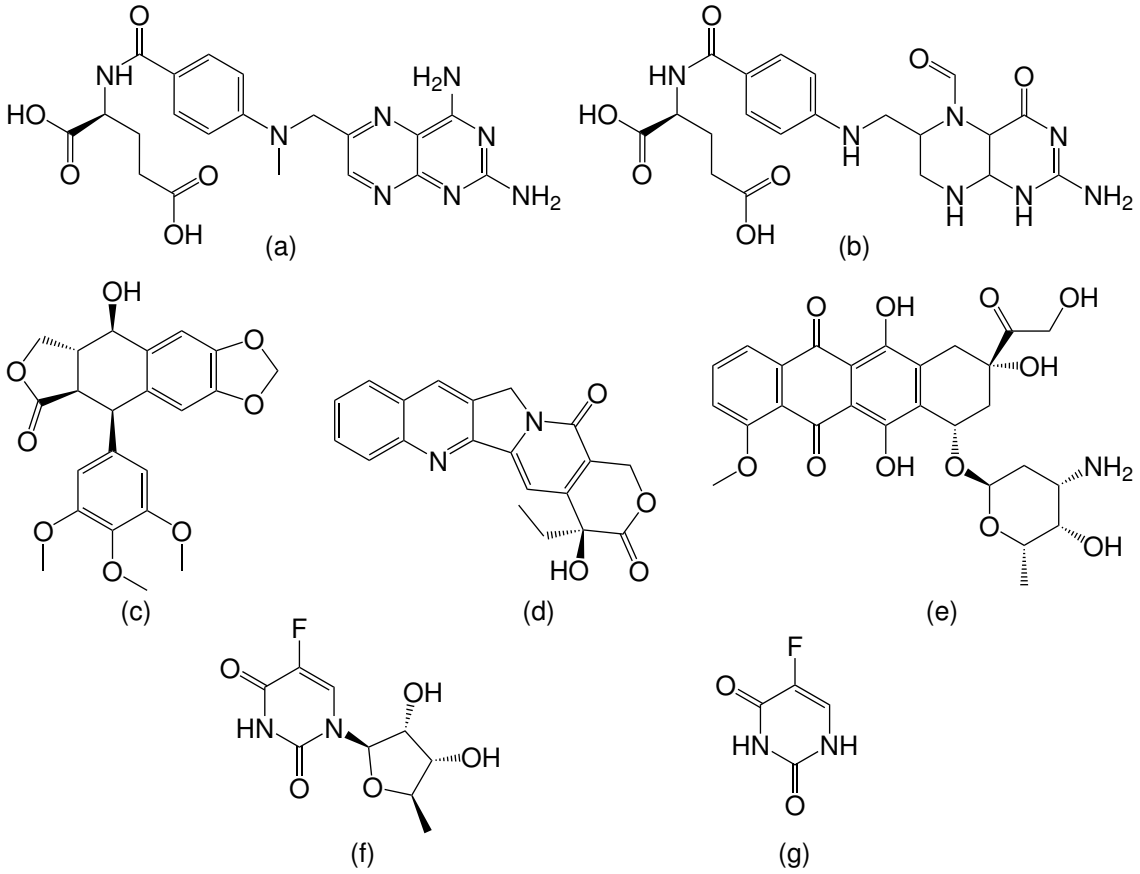


Figure 1.11: The structures of some commonly intercalated anticancer drugs, (a) methotrexate, (b) folinic acid, (c) podophyllotoxin, (d) camptothecin, (e) doxorubicin, (f) doxifluridine and (g) fluorouracil.

Of the anticancer drugs that have been investigated for parenteral delivery within LDHs, by far the most studied example is methotrexate, which has come to be used as a model drug for comparing the suitability of LDH systems for parenteral delivery, due the extent to which it has been studied.[62,376,377] Methotrexate is a folinic acid derived anticancer agent, and folinic acid itself has also been intercalated.[262]

Methotrexate has received particular attention as it has been observed that delivery within LDH particles leads to a significant improvement in both the efficacy and duration of the drug at its site of action within the body. This could allow for lower dosages to be administered, reducing the marked negative side effects of the drug.[62] The considerable improvement in the drug function has been attributed to uptake of the LDH–drug particles into tumour cells through a clathrin-mediated pathway, and also through the LDH particles preventing the drug from diffusing away from the site of action.[275,370,378]

Following from the success of LDH intercalation with methotrexate, other anticancer drugs that have been trialled include fluorouracil, which has both been intercalated on its own and as a cyclodextrin inclusion complex,[379–382] prazosin, as a cyclodextrin inclusion complex,[383] doxifluridine, into LDH particles and LDH–magnetite hybrids for targeted delivery,[384,385] podophyllotoxin,[386] doxorubicin,[387] and camptothecin, which has been intercalated using cholate and dodecylsulfate micelles, as well as directly.[216,388–390] Cell line efficacy studies with fluorouracil, podophyllotoxin and doxorubicin intercalated LDHs have shown generally positive results regarding improved cytotoxicity towards tumour cells.[378,382,386,387]

Another recent development in the use of LDHs with anticancer agents has been the coating of LDH particles with polyethylene glycolylated phospholipids or albumin, which improves uptake of LDH particles into cells, facilitating improved drug delivery.[373,391]

1.3.5 Other biomedical applications of layered double hydroxides

Besides their application in pharmaceutics, LDHs are used or are being investigated for several other biomedical applications. The most simple and oldest of these is the use of hydrotalcite as an antacid, as the basicity of both the metal hydroxide layers and intercalated carbonate ions reduce stomach acidity upon dissolution, similarly to how brucite ($Mg(OH)_2$) is used in Milk of Magnesia.[392–394] Hydrotalcite has been commercialised as an antacid in two formulations, Altacite® and Talcid®. Recently, hydrotalcite-like compounds containing zinc ions have been investigated for

treating stomach ulcers.[395,396] LDHs containing iron cations have been investigated as potential treatments for iron deficiency,[397] LDHs containing calcium have been investigated for use as calcium supplements,[297] whilst hydrotalcite has also been investigated as a potential adsorbent of intestinal phosphates.[398]

1.3.5.1 Biosensors

Due to their ability to adsorb both small organic anions and large biological species, LDH particles and thin films have been investigated for use in several biosensors.[399] By immobilising enzymes such as tyrosinase,[400] glucose oxidase,[401,402] polyphenol oxidase,[403,404] acetylcholinesterase,[405] urease,[406–408] trypsin[409] and horseradish peroxidase[410,411] on LDH particles, materials have been developed for detecting a range of species, including transketolase, glucose, polyphenols, organophosphates, urea, cyanide and hydrogen peroxide.[173,412] Besides enzymes, other species including haemoglobin,[413–415] myoglobin[416] and the fluorescence agent 8-amino-1,3,6-naphthalenetrisulfonate[417] have been adsorbed onto LDHs and used for sensing small molecules such as catechols,[418] trichloroacetic acid, aspirin,[419] and dextran. Examples have been shown to exhibit good selectivity for their target molecules, even in the presence of other similar compounds.[417] The biosensors typically rely on electrochemical methods for detection, either by coating an electrode with the LDH particles, or by monitoring changes in current of electrochemical cells containing the LDH particles, when exposed to their target sensing molecules.

1.3.5.2 Vaccine adjuvants

Recently, the potential of LDHs as vaccine adjuvants has been investigated, due to their structural and chemical similarity to the inorganic compounds that are the predominant adjuvants in use worldwide today. These commercial 'alum' adjuvants are based on aluminium hydroxide compounds such as the layered aluminium oxyhydroxide boehmite. The potential advantages of LDHs over alum compounds as adjuvants are derived from the much greater variation that can be achieved with LDH compounds, both in the chemistry of the metal hydroxide layers and the interlayer anions, and in the morphology and size of the particles. The variation in the chem-

istry and morphology of LDH particles allows for the tailoring of different adjuvants to produce greater, and more specific immune responses for different vaccines. Immunological responses generated by LDH particles have been observed both *in vitro* and *in vivo*.[420,421] It is even anticipated that an understanding of the relationship between the physiochemical properties of LDHs and the immunological responses generated may lead to the design of bespoke adjuvants *in silico*.[422] Additionally, the intercalation chemistry of LDHs provides for the potential of hybrid adjuvants, whereby organic adjuvants are intercalated into the LDH layers.

1.4 Aims of this thesis

The aim of this thesis is to explore the potential of LDHs as drug delivery systems. This aim is approached from several perspectives. The general objective of using LDHs to solve or lessen problems relating to the delivery and use of common, important or model drug species is tackled across all chapters. Attempts are made to expand the range of drugs that can be delivered effectively using LDHs. In particular, the intercalation of GABAergic drugs gabapentin and pregabalin, which cannot be intercalated into LDHs using more established synthesis methods, is attempted in Chapter 2 by the delamination–restacking method, and the intercalation of neutral hydrophobic and cationic drug species is attempted in Chapter 4 through the use of cyclodextrin inclusion complexes.

The potential of LDHs to chemically stabilise different drugs is investigated, with the aim of allowing the formulation of drugs in previously impractical dosage forms. Composites containing LDHs which increase the utility and functionality of LDHs as drug delivery systems are investigated and compared. The potential of several properties of LDHs that have previously been reported in the literature is tested systematically, such as their ability to stabilise or usefully control the release of drug species, so as to either confirm or refute previous claims, and to provide a more detailed understanding of these properties so that they can be applied practically in a therapeutic setting.

Overall, it is hoped that the research conducted and reported here will provide a link

between current academic understanding and real-world applications, and lead to the development and use of LDHs in practicable solutions to current pharmaceutical challenges.

1.5 References

(1) Lund, W., *The Pharmaceutical Codex: Principles and Practice of Pharmaceutics*; The pharmaceutical codex; Pharmaceutical Press: 1994.
(2) Banker, G. S.; Siepmann, J.; Rhodes, C., *Modern Pharmaceutics, Fourth Edition*; Drugs and the Pharmaceutical Sciences; CRC Press: 2002.
(3) Xu, Z. P.; Zeng, Q. H.; Lu, G. Q.; Yu, A. B. *Chem. Eng. Sci.* **2005**, *61*, 1027–1040.
(4) Murakami, K. T.; Tatsuya Recent Advances in Inorganic Nanoparticle-Based Drug Delivery Systems., 2008.
(5) Rotello, V. M. *Adv. Drug Deliv. Rev.* **2008**, *60*, 1225.
(6) Zhang, L.; Li, Y.; Yu, J. C. *J. Mater. Chem. B* **2014**, *2*, 452–470.
(7) Zhang, X.; Cresswell, M., *Inorganic Controlled Release Technology: Materials and Concepts for Advanced Drug Formulation*; Elsevier Science: 2015.
(8) Kuthati, Y.; Kankala, R. K.; Lee, C.-H. *Appl. Clay Sci.* **2015**, *112–113*, 100–116.
(9) Aulton, M. E.; Taylor, K. M. G., *Aulton's Pharmaceutics: The Design and Manufacture of Medicines*; Elsevier Health Sciences UK: 2013.
(10) Troy, D. B.; Remington, J. P.; Beringer, P., *Remington: The Science and Practice of Pharmacy*; Lippincott Williams & Wilkins: 2006, pp 939–964.
(11) Conway, B. R. *Pharm. Manuf. Handb. Prod. Process.* **2008**, 233–265.
(12) Birrer, G. A.; Murthy, S. S.; Liu, J.; Estrada, J. *Handb. Mod. Pharm. Anal.* **2001**, *3*, 269.
(13) Mahalingam, R.; Li, X.; Jasti, B. R. In *Pharm. Sci. Encycl.* John Wiley & Sons, Inc.: 2010.
(14) Smyth, H. D. C.; Hickey, A. J., *Controlled Pulmonary Drug Delivery*; Advances in Delivery Science and Technology; Springer New York: 2011.
(15) Arora, S.; Ali, J.; Ahuja, A.; Khar, R. K.; Baboota, S. *Aaps PharmSciTech* **2005**, *6*, 372–390.
(16) Nayak, A. K.; Malakar, J.; Sen, K. K. *J Pharm Educ Res* **2010**, *1*, 1–10.
(17) Dash, A.; Cudworth II, G. *J. Pharmacol. Toxicol. Methods* **1998**, *40*, 1–12.
(18) Tao, S. L.; Desai, T. A. *Adv. Drug Deliv. Rev.* **2003**, *55*, 315–328.
(19) LaVan, D. A.; McGuire, T.; Langer, R. *Nat Biotech* **2003**, *21*, 1184–1191.
(20) Xu, Z. P.; Zeng, Q. H.; Lu, G. Q.; Yu, A. B. *Chem. Eng. Sci.* **2006**, *61*, 1027–1040.
(21) Anderson, J. M.; Shive, M. S. *Adv. Drug Deliv. Rev.* **2012**, *64*, 72–82.
(22) Oster, J. R.; Epstein, M. eng *J. Clin. Hypertens.* **1987**, *3*, 278–293.
(23) Cleary, G. W.; Colley, K. J.; Miranda, J. Transdermal delivery device having delayed onset. US 5271940 A., 1993.
(24) Sangalli, M. E.; Maroni, A.; Zema, L.; Busetti, C.; Giordano, F.; Gazzaniga, A. *J. Control. Release* **2001**, *73*, 103–110.
(25) Sohi, H.; Sultana, Y.; Khar, R. K. *Drug Dev. Ind. Pharm.* **2004**, *30*, 429–448.
(26) Lankpord, B. L.; Becker, C. H. *J. Am. Pharm. Assoc.* **1951**, *40*, 77–82.
(27) Manek, S. P.; Kamat, V. S. *Indian J. Pharm. Sci* **1981**, *43*, 209–212.
(28) Szejtli, J.; Szente, L. *Eur. J. Pharm. Biopharm.* **2005**, *61*, 115–125.
(29) Zhou, J.; Ritter, H. *Polym. Chem.* **2010**, *1*, 1552–1559.
(30) Lu, M.-y. F.; Borodkin, S.; Woodward, L.; Li, P.; Diesner, C.; Hernandez, L.; Vadnere, M. *Pharm. Res.* **1991**, *8*, 706–712.
(31) Nanda, A.; Kandarapu, R.; Garg, S. *Indian J. Pharm. Sci.* **2002**, *64*, 10–17.
(32) Dhakane, K. *Asian J. Biomed. Pharm. Sci.* **2012**, *1*, 16–21.
(33) Skrabanja, A. T. P.; Tully, R. E. Oral liquid antidepressant solution. US 6114324 A., 2000.
(34) Pradeep, S.; Tulshi, C.; Akash, J.; Vipin, S. *Int. J. Pharm. Sci. Lett.* **2011**, *3*, 229–237.
(35) Douroumis, D. *Expert Opin. Drug Deliv.* **2007**, *4*, 417–426.
(36) Nahata, M. C. *Pediatrics* **1999**, *104*, 607–609.
(37) Ernest, T. B.; Elder, D. P.; Martini, L. G.; Roberts, M.; Ford, J. L. *J. Pharm. Pharmacol.* **2007**, *59*, 1043–1055.
(38) Yoo, M. K.; Choi, H. K.; Kim, T. H.; Choi, Y. J.; Akaike, T.; Shirakawa, M.; Cho, C. S. *Arch. Pharm. Res.* **2005**, *28*, 736–742.

(39) Tack, D. A.; Rogers, R. S. *Dermatol. Ther.* **2002**, *15*, 236–250.
(40) Erah, P. O.; Goddard, A. F.; Barrett, D. A.; Shaw, P. N.; Spiller, R. C. *J. Antimicrob. Chemother.* **1997**, *39*, 5–12.
(41) Shapira, A.; Davidson, I.; Avni, N.; Assaraf, Y. G.; Livney, Y. D. *Eur. J. Pharm. Biopharm.* **2012**, *80*, 298–305.
(42) Glass, B. D.; Haywood, A. *J. Pharm. Pharm. Sci.* **2006**, *9*, 398–426.
(43) Yoshioka, S.; Stella, V. J., *Stability of drugs and dosage forms*; Springer: 2000.
(44) Tang, B.; Cheng, G.; Gu, J.-C.; Xu, C.-H. *Drug Discov. Today* **2008**, *13*, 606–612.
(45) George, M.; Abraham, T. E. *J. Control. Release* **2006**, *114*, 1–14.
(46) Philip, A. K.; Philip, B. *Oman Med. J.* **2010**, *25*, 79–87.
(47) Nikam, V. K.; Kotade, K. B.; Gaware, V. M.; Dhamak, R.; Somwanshi, S. B.; Khadse, A. N. *Pharmacol. Online* **2011**, *1*, 152–164.
(48) Thornton, P. D.; Mart, R. J.; Ulijn, R. V. *Adv. Mater.* **2007**, *19*, 1252–1256.
(49) Tonnesen, H. H.; Karlsen, J. *Drug Dev. Ind. Pharm.* **2002**, *28*, 621–630.
(50) Mustafin, R. I. *Pharm. Chem. J.* **2011**, *45*, 285–295.
(51) Yu, D.-G.; Williams, G. R.; Wang, X.; Liu, X.-K.; Li, H.-L.; Bligh, S. W. A. *RSC Adv.* **2013**, *3*, 4652–4658.
(52) Chan, O. H.; Stewart, B. H. *Drug Discov. Today* **1996**, *1*, 461–473.
(53) Martinez, M. N.; Amidon, G. L. *J. Clin. Pharmacol.* **2002**, *42*, 620–643.
(54) Schmidt, L. E.; Dalhoff, K. *Drugs* **2002**, *62*, 1481–1502.
(55) Maher, S.; Leonard, T. W.; Jacobsen, J.; Brayden, D. J. *Adv. Drug Deliv. Rev.* **2009**, *61*, 1427–1449.
(56) Raghuvanshi, S.; Pathak, K. *J. Drug Deliv.* **2014**, *2014*, 479246.
(57) De La Rica, R.; Aili, D.; Stevens, M. M. *Adv. Drug Deliv. Rev.* **2012**, *64*, 967–978.
(58) Brazel, C. S. *Pharm. Res.* **2009**, *26*, 644–656.
(59) Hayashi, K.; Ono, K.; Suzuki, H.; Sawada, M.; Moriya, M.; Sakamoto, W.; Yogo, T. *ACS Appl. Mater. Interfaces* **2010**, *2*, 1903–1911.
(60) Jeyamohan, P.; Hasumura, T.; Nagaoka, Y.; Yoshida, Y.; Maekawa, T.; Kumar, D. S. *Int. J. Nanomedicine* **2013**, *8*, 2653–2667.
(61) Desai, N.; Trieu, V.; Yao, Z.; Louie, L.; Ci, S.; Yang, A.; Tao, C.; De, T.; Beals, B.; Dykes, D.; Noker, P.; Yao, R.; Labao, E.; Hawkins, M.; Soon-Shiong, P. *Clin. Cancer Res.* **2006**, *12*, 1317–1324.
(62) Chakraborty, J.; Roychowdhury, S.; Sengupta, S.; Ghosh, S. *Mater. Sci. Eng. C Mater. Biol. Appl.* **2013**, 2168–2174.
(63) Arafat, M. *Int. J. Pharm. Pharm. Sci.* **2015**, *7*, 16–21.
(64) Ratnaparkhi, M. P.; Gupta Jyoti, P. *Terminology* **2013**, *3*, 4.
(65) Amri, A.; Chaumeil, J. C.; Sfar, S.; Charrueau, C. *J. Control. Release* **2012**, *158*, 182–193.
(66) Allen, T. M.; Cullis, P. R. *Science (80-.).* **2004**, *303*, 1818–1822.
(67) Walker, S. L.; Fine, A.; Kryger, M. H. *Sleep* **1996**, *19*, 214–218.
(68) Wasdell, M. B.; Jan, J. E.; Bomben, M. M.; Freeman, R. D.; Rietveld, W. J.; Tai, J.; Hamilton, D.; Weiss, M. D. *J. Pineal Res.* **2008**, *44*, 57–64.
(69) Benet, L. Z.; Kroetz, D. L.; Sheiner, L. B.; Hardman, J. G.; Limbird, L. E. *Goodman Gilman's Pharmacol. Basis Ther.* **1996**, 3–27.
(70) Arica, B.; Kaş, H. S.; Moghdam, A.; Akalan, N.; Hincal, a. A. *J. Control. Release* **2005**, *102*, 689–97.
(71) Diener, H.-C.; Sacco, R.; Yusuf, S. *Cerebrovasc. Dis.* **2007**, *23*, 368–380.
(72) Hussein, M. Z.; Abdul Nor Shazlirah Shazlyn, R.; Sarijo, S. H.; Zainal, Z. *Appl. Clay Sci.* **2012**, *58*, 60–66.
(73) Tang, Y.-D.; Venkatraman, S. S.; Boey, F. Y. C.; Wang, L.-W. *Int. J. Pharm.* **2007**, *336*, 159–165.
(74) Chen, C.; Han, C.-H.; Sweeney, M.; Cowles, V. E. *J. Pharm. Sci.* **2013**, *102*, 1155–1164.
(75) Muller, P. Y.; Milton, M. N. *Nat. Rev. Drug Discov.* **2012**, *11*, 751–761.

(76) Bae, K. H.; Lee, F.; Xu, K.; Keng, C. T.; Tan, S. Y.; Tan, Y. J.; Chen, Q.; Kurisawa, M. *Biomaterials* **2015**, *63*, 146–157.
(77) Siddiqui, M. D. N.; Garg, G.; Sharma, P. K. *Adv. Biol. Res. (Rennes).* **2011**, *5*, 291–303.
(78) Huang, X.; Brazel, C. S. *J. Control. release* **2001**, *73*, 121–136.
(79) Bhattacharyya, S.; Wang, H.; Ducheyne, P. *Acta Biomater.* **2012**, *8*, 3429–3435.
(80) Narasimhan, B.; Langer, R. In *Abstr. Pap. 214st ACS Natl. Meet. Las Vegas 1997*, Amer. Chemical Soc. 1155 16th ST, NW, Washington, DC 20036: 1997; Vol. 213, pp 337–340.
(81) Rokhade, A. P.; Patil, S. A.; Aminabhavi, T. M. *Carbohydr. Polym.* **2007**, *67*, 605–613.
(82) Koppolu, B.; Rahimi, M.; Nattama, S.; Wadajkar, A.; Nguyen, K. T. *Nanomedicine Nanotechnology, Biol. Med.* **2010**, *6*, 355–361.
(83) Zhang, N.; Li, J.; Jiang, W.; Ren, C.; Li, J.; Xin, J.; Li, K. *Int. J. Pharm.* **2010**, *393*, 213–219.
(84) Siepmann, J.; Siepmann, F. *J. Control. Release* **2012**, *161*, 351–362.
(85) Huang, W.; Zhang, H.; Pan, D. *AIChE J.* **2011**, *57*, 1936–1946.
(86) Rojas, R.; Jimenez-Kairuz, A.; Manzo, R.; Giacomelli, C. *Colloids Surfaces A Physicochem. Eng. Asp.* **2014**, *463*, 37–43.
(87) Markland, C.; Williams, G. R.; O'Hare, D. *J. Mater. Chem.* **2011**, *21*, 17896–17903.
(88) Avrami, M. *J. Chem. Phys.* **1939**, *7*, 1103–1112.
(89) Avrami, M. *J. Chem. Phys.* **1940**, *8*, 212–224.
(90) Avrami, M. *J. Chem. Phys.* **1941**, *9*, 177–184.
(91) Aharoni, C.; Levinson, S.; Ravina, I.; Sparks, D. L. English *Soil Sci. Soc. Am. J.* **1991**, *55*, 1307–1312.
(92) Starcher, A. N.; Siebecker, M.; Li, W.; Elzinga, E.; Sparks, D. L. In *Abstr. Pap. 245th ACS Natl. Meet. Expo. New Orleans, LA, United States, April 7-11, 2013*, American Chemical Society: 2013, GEOC–75.
(93) Kodama, T.; Harada, Y.; Ueda, M.; Shimizu, K.; Shuto, K.; Komarneni, S. *Langmuir* **2001**, *17*, 4881–4886.
(94) Freundlich, H. *Zeitschrift fur Phys. Chemie* **1907**, *57*, 385–470.
(95) Kuo, S.; Lotse, E. G. *Soil Sci.* **1973**, *116*, 400–406.
(96) Crank, J., *The Mathematics of Diffusion*; Oxford science publications; Clarendon Press: 1979.
(97) Pesic, L.; Salipurovic, S.; Markovic, V.; Vucelic, D.; Kagunya, W.; Jones, W. *J. Mater. Chem.* **1992**, *2*, 1069–1073.
(98) Williams, G. R.; O'Hare, D. *Solid State Sci.* **2006**, *8*, 971–980.
(99) Yang, M.; McDermott, O.; Buffet, J.-C.; O'Hare, D. *RSC Adv.* **2014**, *4*, 51676–51682.
(100) Chen, C.; Yang, M.; Wang, Q.; Buffet, J.-C.; O'Hare, D. *J. Mater. Chem. A* **2014**, *2*, 15102–15110.
(101) Chen, C.; Byles, C. F. H.; Buffet, J.-C.; Rees, N. H.; Wu, Y.; O'Hare, D. *Chem. Sci.* **2016**.
(102) Poeppelmeier, K. R.; Hwu, S. J. *Inorg. Chem.* **1987**, *26*, 3297–3302.
(103) Fogg, A. M.; Williams, G. R.; Chester, R.; O'Hare, D. *J. Mater. Chem.* **2004**, *14*, 2369–2371.
(104) Williams, G. R.; Moorhouse, S. J.; Prior, T. J.; Fogg, A. M.; Rees, N. H.; O'Hare, D. *Dalt. Trans.* **2011**, *40*, 6012–6022.
(105) Fogg, A. M.; Freij, A. J.; Parkinson, G. M. *Chem. Mater.* **2002**, *14*, 232–234.
(106) Cavani, F.; Trifirò, F.; Vaccari, A. *Catal. Today* **1991**, *11*, 173–301.
(107) Atwood, J. L.; Lehn, J. M.; Alberti, G.; Bein, T. In *Compr. Supramol. Chem. Vol. 7,* Pergamon Press, New York: 1991.
(108) Bookin, A. S.; Drits, V. A. *Clays Clay Miner.* **1993**, *41*, 551–557.
(109) Bookin, A. S.; Cherkashin, V. I.; Drits, V. A. *Clays Clay Miner.* **1993**, *41*, 558–564.
(110) Radha, A. V.; Kamath, P. V.; Shivakumara, C. *J. Phys. Chem. B* **2007**, *111*, 3411–3418.
(111) Radha, A. V.; Kamath, P. V.; Shivakumara, C. *Acta Crystallogr. Sect. B Struct. Sci.* **2007**, *63*, 243–250.
(112) Koilraj, P.; Kannan, S. *J. Colloid Interface Sci.* **2010**, *341*, 289–297.

(113) Wang, C. J. Controlled Synthesis and Properties of Layered Double Hydroxides., D.Phil Thesis, University of Oxford, 2012.
(114) Aghdaee, S. R.; Soleimanian, V. *Powder Diffr.* **2009**, *24*, 228–233.
(115) De Roy, A.; Forano, C.; Malki, K.; Besse, J.-P. English In *Expand. Clays Other Microporous Solids SE - 7*, Occelli, M., Robson, H., Eds.; Springer US: 1992, pp 108–169.
(116) Mills, S. J.; Christy, A. G.; Genin, J.-M. R.; Kameda, T.; Colombo, F. *Mineral. Mag.* **2012**, *76*, 1289–1336.
(117) Evans, D. G.; Slade, R. C. T. In *Layer. double hydroxides*; Springer: 2006, pp 1–87.
(118) Phillips, W.; Alger, F., *An Elementary Treatise on Mineralogy, Fifth edition*, 1844, p 134.
(119) Feitknecht, W.; Fischer, G.; Helu, G. *Helv. Chim. Acta* **1935**, *18*, 555–569.
(120) Reichle, W. T. *Solid State Ionics* **1986**, *22*, 135–141.
(121) Allmann, R.; Lohse, H.-H. *Neues Jahrb. Miner. Monatsh.* **1966**, 161–181.
(122) Allmann, R. *Acta Crystallogr. Sect. B* **1968**, *24*, 972–977.
(123) Vulic, T.; Reitzmann, A.; Ranogajec, J.; Marinkovic-Neducin, R. *J. Therm. Anal. Calorim.* **2012**, *110*, 227–233.
(124) Khan, A. I.; Lei, L.; Norquist, A. J.; O'Hare, D. *Chem. Commun.* **2001**, *22*, 2342–2343.
(125) Khan, A. I.; Ragavan, A.; Fong, B.; Markland, C.; O'Brien, M.; Dunbar, T. G.; Williams, G. R.; O'Hare, D. *Ind. Eng. Chem. Res.* **2009**, *48*, 10196–10205.
(126) Cardoso, L. P.; Celis, R.; Cornejo, J.; Valim, J. B. *J. Agric. Food Chem.* **2006**, *54*, 5968–5975.
(127) Cui, W.; Jiao, Q.; Zhao, Y.; Zhou, M. *Micro Nano Lett.* **2011**, *6*, 832–835.
(128) Costa, F. R.; Leuteritz, A.; Wagenknecht, U.; Jehnichen, D.; Häußler, L.; Heinrich, G. *Appl. Clay Sci.* **2008**, *38*, 153–164.
(129) Wang, Z.-l.; Wang, E.-b.; Tian, S.-y.; Xiao, D.-r.; Gao, L.; Wang, L.; Xu, L. *Chem. Res. Chinese Univ.* **2005**, *21*, 492–495.
(130) Darder, M.; López-Blanco, M.; Aranda, P.; Leroux, F.; Ruiz-Hitzky, E. *Chem. Mater.* **2005**, *17*, 1969–1977.
(131) Barbosa, C. A. S.; Ferreira, A. M. D. C.; Constantino, V. R. L. *Eur. J. Inorg. Chem.* **2005**, 1577–1584.
(132) Kantonis, G.; Trikeriotis, M.; Ghanotakis, D. F. *J. Photochem. Photobiol. A Chem.* **2007**, *185*, 62–66.
(133) Sasaki, S.; Aisawa, S.; Hirahara, H.; Sasaki, A.; Narita, E. *Chem. Lett.* **2004**, *33*, 790–791.
(134) Mousty, C.; Forano, C.; Fleutot, S.; Dupin, J. *Electroanalysis* **2009**, *21*, 399–408.
(135) Tseng, W.-Y.; Lin, J.-T.; Mou, C.-Y.; Cheng, S.; Liu, S.-B.; Chu, P. P.; Liu, H.-W. *J. Am. Chem. Soc.* **1996**, *118*, 4411–4418.
(136) Medina, A.; Martinez, M.; Gonzalez, J. R.; Diaz, A.; Colon, J. L. In *Abstr. Pap. 232nd ACS Natl. Meet. San Fr. CA, United States*, American Chemical Society: 2006, MEDI–167.
(137) Choy, J.-H.; Park, J.-s.; Kwak, S.-Y.; Jeong, Y.-J.; Han, Y.-S. *Mol. Cryst. Liq. Cryst. Sci. Technol. Sect. A Mol. Cryst. Liq. Cryst.* **2000**, *341*, 425–429.
(138) Gunawan, P.; Xu, R. *J. Mater. Chem.* **2008**, *18*, 2112–2120.
(139) Hammond, C., *The Basics of Crystallography and Diffraction*; IUCr texts on crystallography; Oxford University Press: 2015, p 151.
(140) Allmann, R. *Chimica* **1970**, 99–108.
(141) Fogg, A. M.; Dunn, J. S.; O'Hare, D. *Chem. Mater.* **1998**, *10*, 356–360.
(142) Milanesio, M.; Conterosito, E.; Viterbo, D.; Perioli, L.; Croce, G. *Cryst. Growth Des.* **2010**, *10*, 4710–4712.
(143) Kaassis, A. Y. A.; Xu, S.-M.; Evans, D. G.; Williams, G. R.; Wei, M.; Duan, X. *J. Phys. Chem. C* **2015**, *119*, 18729–18740.
(144) You, Y.; Zhao, H.; Vance, G. F. *Colloids Surfaces A Physicochem. Eng. Asp.* **2002**, *205*, 161–172.
(145) He, J.; Wei, M.; Li, B.; Kang, Y.; Evans, D. G.; Duan, X., *Preparation of Layered Double Hydroxides*; Structure and Bonding, Vol. 119; Springer-Verlag: 2006, pp 89–119.
(146) Tongamp, W.; Zhang, Q.; Saito, F. *Powder Technol.* **2008**, *185*, 43–48.

(147) Oestreicher, V.; Jobbágy, M. *Langmuir* **2013**, *29*, 12104–12109.
(148) Zhang, W. H.; Guo, X. D.; He, J.; Qian, Z. Y. *J. Eur. Ceram. Soc.* **2008**, *28*, 1623–1629.
(149) Klemkaite, K.; Prosycevas, I.; Taraskevicius, R.; Khinsky, A.; Kareiva, A. English *Cent. Eur. J. Chem.* **2011**, *9*, 275–282.
(150) Meyn, M.; Beneke, K.; Lagaly, G. *Inorg. Chem.* **1990**, *29*, 5201–5207.
(151) Kloprogge, J. T.; Hickey, L.; Frost, R. L. *J. Solid State Chem.* **2004**, *177*, 4047–4057.
(152) Xu, Z. P.; Stevenson, G.; Lu, C.-Q.; Lu, G. Q. *J. Phys. Chem. B* **2006**, *110*, 16923–16929.
(153) Lu, G. Q.; Xu, Z. Preparations of suspensions. US 20100233286., 2010.
(154) Ogawa, M.; Kaiho, H. *Langmuir* **2002**, *18*, 4240–4242.
(155) Iyi, N.; Matsumoto, T.; Kaneko, Y.; Kitamura, K. *Chem. Lett.* **2004**, *33*, 1122–1123.
(156) Liu, Z.; Ma, R.; Ebina, Y.; Iyi, N.; Takada, K.; Sasaki, T. *Langmuir* **2006**, *23*, 861–867.
(157) Okamoto, K.; Iyi, N.; Sasaki, T. *Appl. Clay Sci.* **2007**, *37*, 23–31.
(158) Manohara, G. V.; Kunz, D. A.; Kamath, P. V.; Milius, W.; Breu, J. *Langmuir* **2010**, *26*, 15586–15591.
(159) Inayat, A.; Klumpp, M.; Schwieger, W. *Appl. Clay Sci.* **2011**, *51*, 452–459.
(160) Iyi, N.; Tamura, K.; Yamada, H. *J. Colloid Interface Sci.* **2009**, *340*, 67–73.
(161) Hu, G.; O'Hare, D. *J. Am. Chem. Soc.* **2005**, *127*, 17808–17813.
(162) Wang, C. J.; Wu, Y. A.; Jacobs, R. M. J.; Warner, J. H.; Williams, G. R.; O'Hare, D. *Chem. Mater.* **2011**, *23*, 171–180.
(163) Wongariyakawee, A.; Schaeffel, F.; Warner, J. H.; O'Hare, D. *J. Mater. Chem.* **2012**, *22*, 7751–7756.
(164) Wang, C. J.; O'Hare, D. *J. Mater. Chem.* **2012**, *22*, 23064–23070.
(165) Yun, S. K.; Pinnavaia, T. J. *Chem. Mater.* **1995**, *7*, 348–354.
(166) Chang, Z.; Evans, D. G.; Duan, X.; Vial, C.; Ghanbaja, J.; Prevot, V.; de Roy, M.; Forano, C. *J. Solid State Chem.* **2005**, *178*, 2766–2777.
(167) Wang, Q.; Tang, S. V. Y.; Lester, E.; O'Hare, D. *Nanoscale* **2013**, *5*, 114–117.
(168) Climent, M. J.; Corma, A.; Iborra, S.; Epping, K.; Velty, A. *J. Catal.* **2004**, *225*, 316–326.
(169) Ding, P.; Qu, B.; Shi, L.; Ge, C.; Yang, H. *Mater. Lett.* **2008**, *62*, 3815–3817.
(170) Bao, H.; Yang, J.; Huang, Y.; Xu, Z. P.; Hao, N.; Wu, Z.; Lu, G. Q. M.; Zhao, D. *Nanoscale* **2011**, *3*, 4069–4073.
(171) Shao, M.; Ning, F.; Zhao, J.; Wei, M.; Evans, D. G.; Duan, X. *J. Am. Chem. Soc.* **2012**, *134*, 1071–1077.
(172) Scavetta, E.; Ballarin, B.; Berrettoni, M.; Carpani, I.; Giorgetti, M.; Tonelli, D. *Electrochim. Acta* **2006**, *51*, 2129–2134.
(173) Shan, D.; Mousty, C.; Cosnier, S. *Anal. Chem.* **2004**, *76*, 178–183.
(174) Boehm, H.-P.; Steinle, J.; Vieweger, C. *Angew. Chemie* **1977**, *16*, 265–266.
(175) El Malki, K.; De Roy, A.; Besse, J. P. *Eur. J. solid state Inorg. Chem.* **1989**, *26*, 339–351.
(176) Zhouri, E.; Hajbi, A. E. *Ann. Chim. Sci. des Matériaux* **1999**, *24*, 57–62.
(177) Markland, C. Novel Apects of Layered Double Hydroxide Chemistry., D.Phil Thesis, University of Oxford, 2011.
(178) Miyata, S. *Clays Clay Miner.* **1983**, *31*, 305–311.
(179) Carlino, S. *Solid State Ionics* **1997**, *98*, 73–84.
(180) Costantino, U.; Marmottini, F.; Nocchetti, M.; Vivani, R. *Eur. J. Inorg. Chem.* **1998**, *1998*, 1439–1446.
(181) Desigaux, L.; Belkacem, M. B.; Richard, P.; Cellier, J.; Léone, P.; Cario, L.; Leroux, F.; Taviot-Guého, C.; Pitard, B. *Nano Lett.* **2006**, *6*, 199–204.
(182) José dos Reis, M.; Silvério, F.; Tronto, J.; Valim, J. B. *J. Phys. Chem. Solids* **2004**, *65*, 487–492.
(183) Yun, S. K.; Pinnavaia, T. J. *Inorg. Chem.* **1996**, *35*, 6853–6860.
(184) Chibwe, K.; Jones, W. *J. Chem. Soc., Chem. Commun.* **1989**, 926–927.
(185) Ulibarri, M. A.; Pavlovic, I.; Barriga, C.; Hermosin, M. C.; Cornejo, J. *Appl. Clay Sci.* **2001**, *18*, 17–27.
(186) Ogawa, M.; Inomata, K. *Chem. Lett.* **2005**, *34*, 810–811.

(187) Tagaya, H.; Ogata, A.; Kuwahara, T.; Ogata, S.; Karasu, M.; Kadokawa, J.-i.; Chiba, K. *Microporous Mater.* **1996**, *7*, 151–158.
(188) Nakayama, H.; Wada, N.; Tsuhako, M. *Int. J. Pharm.* **2004**, *269*, 469–478.
(189) Aisawa, S.; Hirahara, H.; Ishiyama, K.; Ogasawara, W.; Umetsu, Y.; Narita, E. *J. Solid State Chem.* **2003**, *174*, 342–348.
(190) Aisawa, S.; Hirahara, H.; Takahashi, S.; Umetsu, Y.; Narita, E. *Chem. Lett.* **2004**, *33*, 306–307.
(191) Rocha, J.; del Arco, M.; Rives, V.; A. Ulibarri, M. *J. Mater. Chem.* **1999**, *9*, 2499–2503.
(192) Iyi, N.; Matsumoto, T.; Kaneko, Y.; Kitamura, K. *Chem. Mater.* **2004**, *16*, 2926–2932.
(193) Iyi, N.; Okamoto, K.; Kaneko, Y.; Matsumoto, T. *Chem. Lett.* **2005**, *34*, 932–933.
(194) Iyi, N.; Sasaki, T. *Appl. Clay Sci.* **2008**, *42*, 246–251.
(195) Iyi, N.; Sasaki, T. *J. Colloid Interface Sci.* **2008**, *322*, 237–45.
(196) Iyi, N.; Yamada, H. *Chem. Lett.* **2010**, *39*, 591–593.
(197) Iyi, N.; Yamada, H.; Sasaki, T. *Appl. Clay Sci.* **2011**, *54*, 137–132.
(198) Iyi, N.; Yamada, H. *Appl. Clay Sci.* **2012**, *65-66*, 121–127.
(199) Adachi-Pagano, M.; Forano, C.; Besse, J.-P. *Chem. Commun.* **2000**, 91–92.
(200) O'Leary, S.; O'Hare, D.; Seeley, G. *Chem. Commun.* **2002**, 1506–1507.
(201) Jobbágy, M.; Regazzoni, A. E. *J. Colloid Interface Sci.* **2004**, *275*, 345–348.
(202) Naik, V. V.; Ramesh, T. N.; Vasudevan, S. *J. Phys. Chem. Lett.* **2011**, *2*, 1193–1198.
(203) Gordijo, C. R.; Leopoldo Constantino, V. R.; de Oliveira Silva, D. *J. Solid State Chem.* **2007**, *180*, 1967–1976.
(204) Hibino, T.; Kobayashi, M. *J. Mater. Chem.* **2005**, *15*, 653–656.
(205) Hibino, T.; Jones, W. *J. Mater. Chem.* **2001**, *11*, 1321–1323.
(206) Li, L.; Ma, R.; Ebina, Y.; Iyi, N.; Sasaki, T. *Chem. Mater.* **2005**, *17*, 4386–4391.
(207) Leroux, F.; Adachi-Pagano, M.; Intissar, M.; Chauviere, S.; Forano, C.; Besse, J.-P. *J. Mater. Chem.* **2001**, *11*, 105–112.
(208) Hibino, T. *Chem. Mater.* **2004**, *16*, 5482–5488.
(209) Wypych, F.; Bubniak, G. A.; Halma, M.; Nakagaki, S. *J. Colloid Interface Sci.* **2003**, *264*, 203–207.
(210) Liu, Z.; Ma, R.; Osada, M.; Iyi, N.; Ebina, Y.; Takada, K.; Sasaki, T. *J. Am. Chem. Soc.* **2006**, *128*, 4872–4880.
(211) Funnell, N. P.; Wang, Q.; Connor, L.; Tucker, M. G.; O'Hare, D.; Goodwin, A. L. *Nanoscale* **2014**, *6*, 8032–8036.
(212) Wang, Q.; O'Hare, D. *Chem. Rev.* **2012**, *112*, 4124–4155.
(213) Song, F.; Hu, X. *Nat. Commun.* **2014**, *5*, 4477.
(214) Huang, G.; Ma, S.; Zhao, X.; Yang, X.; Ooi, K. *Chem. Commun.* **2009**, *1*, 331–333.
(215) Wu, X.; Wang, S.; Du, N.; Zhang, R.; Hou, W. *J. Solid State Chem.* **2013**, *203*, 181–186.
(216) Wu, X.; Li, H.; Song, S.; Zhang, R.; Hou, W. *Int. J. Pharm.* **2013**, *454*, 453–61.
(217) Zhang, Y.; Song, M.; Yun, R.; Meng, Q.; Yan, D. *Chinese J. Chem.* **2014**, *32*, 859–864.
(218) Evans, D. G.; Duan, X. *Chem. Commun.* **2006**, 485–496.
(219) Li, F.; Duan, X. *Struct. Bond.* **2006**, *119*, 193–223.
(220) Gardner, E.; Pinnavaia, T. J. *Appl. Catal. A Gen.* **1998**, *167*, 65–74.
(221) Liu, P.; Wang, C.; Li, C. *J. Catal.* **2009**, *262*, 159–168.
(222) Xu, Z. P.; Zhang, J.; Adebajo, M. O.; Zhang, H.; Zhou, C. *Appl. Clay Sci.* **2011**, *53*, 139–150.
(223) Tichit, D.; Naciri Bennani, M.; Figueras, F.; Tessier, R.; Kervennal, J. *Appl. Clay Sci.* **1998**, *13*, 401–415.
(224) Lü, Z.; Zhang, F.; Lei, X.; Yang, L.; Xu, S.; Duan, X. *Chem. Eng. Sci.* **2008**, *63*, 4055–4062.
(225) Morioka, H.; Shimizu, Y.; Sukenobu, M.; Ito, K.; Tanabe, E.; Shishido, T.; Takehira, K. *Appl. Catal. A Gen.* **2001**, *215*, 11–19.
(226) Tong, Z.; Shichi, T.; Takagi, K. *Mater. Lett.* **2003**, *57*, 2258–2261.
(227) de Victoria Rodriguez, M.; Brunet, E.; Nocchetti, M.; Presciutti, F.; Costantino, F. *RSC Adv.* **2014**, *4*, 26912–26917.

(228) Zhang, H.; Qi, R.; Evans, D. G.; Duan, X. *J. Solid State Chem.* **2004**, *177*, 772–780.
(229) Kantam, M. L.; Ravindra, A.; Reddy, C. V.; Sreedhar, B.; Choudary, B. M. *Adv. Synth. Catal.* **2006**, *348*, 569–578.
(230) Abelló, S.; Dhir, S.; Colet, G.; Pérez-Ramírez, J. *Appl. Catal. A Gen.* **2007**, *325*, 121–129.
(231) Velu, S.; Suzuki, K.; Okazaki, M.; Kapoor, M. P.; Osaki, T.; Ohashi, F. *J. Catal.* **2000**, *194*, 373–384.
(232) Elena Pérez-Bernal, M.; Ruano-Casero, R.; Pinnavaia, T. J. *Catal. Letters* **1991**, *11*, 55–61.
(233) Choudary, B. M.; Madhi, S.; Chowdari, N. S.; Kantam, M. L.; Sreedhar, B. *J. Am. Chem. Soc.* **2002**, *124*, 14127–14136.
(234) Tsyganok, A. I.; Tsunoda, T.; Hamakawa, S.; Suzuki, K.; Takehira, K.; Hayakawa, T. *J. Catal.* **2003**, *213*, 191–203.
(235) Buffet, J.-C.; Arnold, T. A. Q.; Turner, Z. R.; Angpanitcharoen, P.; O'Hare, D. *RSC Adv.* **2015**, *5*, 87456–87464.
(236) Buffet, J.-C.; Wanna, N.; Arnold, T. A. Q.; Gibson, E. K.; Wells, P. P.; Wang, Q.; Tantirungrotechai, J.; O'Hare, D. *Chem. Mater.* **2015**, *27*, 1495–1501.
(237) Fogg, A. M.; Green, V. M.; Harvey, H. G.; O'Hare, D. *Adv. Mater.* **1999**, *11*, 1466–1469.
(238) Goh, K.-H.; Lim, T.-T.; Dong, Z. *Water Res.* **2008**, *42*, 1343–1368.
(239) Xu, Y.; Dai, Y.; Zhou, J.; Xu, Z. P.; Qian, G.; Lu, G. Q. M. *J. Mater. Chem.* **2010**, *20*, 4684–4691.
(240) Goh, K. H.; Lim, T. T.; Dong, Z. L. *Water Sci. Technol.* **2010**, *61*, 1411–1417.
(241) Mandel, K.; Drenkova-Tuhtan, A.; Hutter, F.; Gellermann, C.; Steinmetz, H.; Sextl, G. *J. Mater. Chem. A* **2013**, *1*, 1840–1848.
(242) Bin Hussein, M. Z.; Zainal, Z.; Yaziz, I.; Beng, T. C. *J. Environ. Sci. Heal. Part A* **2001**, *36*, 565–573.
(243) Saiah, F. B. D.; Su, B.-L.; Bettahar, N. *J. Hazard. Mater.* **2009**, *165*, 206–217.
(244) Chuang, Y. H.; Tzou, Y. M.; Wang, M. K.; Liu, C. H.; Chiang, P. N. *Ind. Eng. Chem. Res.* **2008**, *47*, 3813–3819.
(245) Morris, J. M.; Jin, S.; Cui, K. *Chem. Eng. J.* **2008**, *145*, 160–163.
(246) Cardoso, L. P.; Valim, J. B. *J. Phys. Chem. Solids* **2006**, *67*, 987–993.
(247) Lv, L.; He, J.; Wei, M.; Evans, D. G.; Duan, X. *J. Hazard. Mater.* **2006**, *133*, 119–128.
(248) Narita, E. *Nendo Kagaku* **2001**, *40*, 173–178.
(249) Jin, L.; Ni, X.; Liu, X.; Wei, M. *Chem. Eng. Technol.* **2010**, *33*, 82–88.
(250) Fogg, A. M.; Dunn, J. S.; Shyu, S.-G.; Cary, D. R.; O'Hare, D. *Chem. Mater.* **1998**, *10*, 351–355.
(251) Inacio, J.; Taviot-Gueho, C.; Forano, C.; Besse, J. P. *Appl. Clay Sci.* **2001**, *18*, 255–264.
(252) Cornejo, J.; Celis, R.; Pavlovic, I.; Ulibarri, M. A. *Clay Miner.* **2008**, *43*, 155–175.
(253) Touloupakis, E.; Margelou, A.; Ghanotakis, D. F. *Pest Manag. Sci.* **2011**, *67*, 837–841.
(254) Gasser, M. S. *Colloids Surfaces, B Biointerfaces* **2009**, *73*, 103–109.
(255) Zhao, H.-Z.; Chang, Y.-Y.; Yang, J.; Yang, Q.-Z. *Electron. Mater. Lett.* **2013**, *9*, 251–255.
(256) Fischer, H. *Mater. Sci. Eng. C* **2003**, *23*, 763–772.
(257) Choy, J.-H.; Park, T.; Kim, S.-T.; Son, Y.-H. Pharmaceutical composition for the treatment of cancer comprising LMH-RA complex. WO 2006091009 A1., 2006.
(258) Wei, M.; Pu, M.; Guo, J.; Han, J.; Li, F.; He, J.; Evans, D. G.; Duan, X. *Chem. Mater.* **2008**, *20*, 5169–5180.
(259) Ryu, S.-J.; Jung, H.; Oh, J.-M.; Lee, J.-K.; Choy, J.-H. *J. Phys. Chem. Solids* **2010**, *71*, 685–688.
(260) Wang, Y.; Wu, P.; Hou, Y.; Zhu, N.; Dang, Z. *Ind. Eng. Chem. Res.* **2012**, *51*, 11128–11136.
(261) Panda, H. S.; Srivastava, R.; Bahadur, D. *J. Phys. Chem. B* **2009**, *113*, 15090–100.
(262) Choy, J.-H.; Jung, J.-S.; Oh, J.-M.; Park, M.; Jeong, J.; Kang, Y.-K.; Han, O.-J. *Biomaterials* **2004**, *25*, 3059–3064.
(263) Li, B.; He, J.; Evans, D. G.; Duan, X. *Int. J. Pharm.* **2004**, *287*, 89–95.
(264) Ambrogi, V.; Perioli, L.; Ricci, M.; Pulcini, L.; Nocchetti, M.; Giovagnoli, S.; Rossi, C. *Microporous Mesoporous Mater.* **2008**, *115*, 405–415.

(265) Choi, G.; Lee, J.-H.; Oh, Y.-J.; Choy, Y. B.; Park, M. C.; Chang, H. C.; Choy, J.-H. *Int. J. Pharm.* **2010**, *402*, 117–122.
(266) Alcântara, A. C. S.; Aranda, P.; Darder, M.; Ruiz-Hitzky, E.; Alcantara, A. C. S.; Aranda, P.; Darder, M.; Ruiz-Hitzky, E. *J. Mater. Chem.* **2010**, *20*, 9495–9504.
(267) Del Arco, M.; Fernandez, A.; Martin, C.; Rives, V. *J. Solid State Chem.* **2010**, *183*, 3002–3009.
(268) Barkhordari, S.; Yadollahi, M.; Namazi, H. *J. Polym. Res.* **2014**, *21*, 1–9.
(269) Ambrogi, V.; Fardella, G.; Grandolini, G.; Nocchetti, M.; Perioli, L. *J. Pharm. Sci.* **2003**, *92*, 1407–1418.
(270) Perioli, L.; Ambrogi, V.; di Laura, N.; Nocchetti, M.; Rossi, C. *Appl. Clay Sci.* **2011**, *51*, 407–413.
(271) Perioli, L.; Ambrogi, V.; Nocchetti, M.; Sisani, M.; Pagano, C. *Appl. Clay Sci.* **2011**, *53*, 696–703.
(272) Thompson, C.; Bravo, C. M. L.; O'Hare, D. Layered double hydroxides. WO 2014053822 A1., 2014.
(273) Lee, J.-H.; Choi, G.; Oh, Y.-J.; Park, J. W.; Choy, Y. B.; Park, M. C.; Yoon, Y. J.; Lee, H. J.; Chang, H. C.; Choy, J.-H. *Int. J. Nanomedicine* **2012**, *7*, 1635–1649.
(274) Ay, A. N.; Konuk, D.; Zuemreoglu-Karan, B. *Mater. Sci. Eng. C Mater. Biol. Appl.* **2011**, *31*, 851–857.
(275) Choi, S.-J.; Choi, G. E.; Oh, J.-M.; Oh, Y.-J.; Park, M.-C.; Choy, J.-H. *J. Mater. Chem.* **2010**, *20*, 9463–9469.
(276) Choy, J.-H.; Oh, J.-M.; Park, D.-H. In *Low-Dimens. Solids*, John Wiley & Sons Ltd.: 2010, pp 163–187.
(277) Oh, J.-M.; Park, D.-H.; Choi, S.-J.; Choy, J.-H. *Recent Pat. Nanotechnol.* **2012**, *6*, 200–217.
(278) Rives, V.; del Arco, M.; Martín, C. *J. Control. Release* **2013**, *169*, 28–39.
(279) Rives, V.; del Arco, M.; Martín, C. *Appl. Clay Sci.* **2014**, *88*, 239–269.
(280) Bi, X.; Zhang, H.; Dou, L. *Pharmaceutics* **2014**, *6*, 298–332.
(281) Zhang, K.; Xu, Z. P.; Lu, J.; Tang, Z. Y.; Zhao, H. J.; Good, D. A.; Wei, M. Q. *Int. J. Mol. Sci.* **2014**, *15*, 7409–7428.
(282) Del Hoyo, C. *Appl. Clay Sci.* **2007**, *36*, 103–121.
(283) Ambrogi, V.; Perioli, L.; Ciarnelli, V.; Nocchetti, M.; Rossi, C. *Eur. J. Pharm. Biopharm.* **2009**, *73*, 285–291.
(284) Musumeci, A. W.; Schiller, T. L.; Xu, Z. P.; Minchin, R. F.; Martin, D. J.; Smith, S. V. *J. Phys. Chem. C* **2010**, *114*, 734–740.
(285) Smith, S. V.; Musumeci, A.; Pham, B.; Fong, N.; Mume, E.; Xu, Z.; Basu, S.; Gahan, L.; Minchin, R.; Martin, D. In *Pacifichem 2010, Int. Chem. Congr. Pacific Basin Soc. Honolulu, HI, United States, December 15-20, 2010*, American Chemical Society: 2010, HEALTH–507.
(286) Wang, J.; Liu, Q.; Zhong, C.; Li, Z.; Liu, Y.; Yang, P.; Jing, X.; Zhang, M. Sustained-release magnetic rare earth-doped amoxicillin anion-intercalated layered double hydroxides (LDHs)/ferrosoferric oxide with fluorescence property for targeted drug delivery, and its preparation by coprecipitation and calcination-rehydration. CN 1., 2009.
(287) Wang, J.; Zhou, J.; Li, Z.; Song, Y.; Liu, Q.; Jiang, Z.; Zhang, M. *Chem. Eur. J.* **2010**, *16*, 14404–14411.
(288) Wang, J.; Zhou, J.; Li, Z.; Liu, Q.; Yang, P.; Jing, X.; Zhang, M. *Mater. Res. Bull.* **2010**, *45*, 640–645.
(289) Wang, L.; Xing, H.; Zhang, S.; Ren, Q.; Pan, L.; Zhang, K.; Bu, W.; Zheng, X.; Zhou, L.; Peng, W.; Hua, Y.; Shi, J. *Biomaterials* **2013**, *34*, 3390–3401.
(290) Lopezgalindo, a.; Viseras, C.; Cerezo, P. *Appl. Clay Sci.* **2007**, *36*, 51–63.
(291) Aguzzi, C.; Cerezo, P.; Viseras, C.; Caramella, C. *Appl. Clay Sci.* **2007**, *36*, 22–36.
(292) Linkov, I.; Satterstrom, F. K.; Corey, L. M. *Nanomedicine Nanotechnology, Biol. Med.* **2008**, *4*, 167–171.
(293) Li, Y.; Liu, D.; Ai, H.; Chang, Q.; Liu, D.; Xia, Y.; Liu, S.; Peng, N.; Xi, Z.; Yang, X. *Nanotechnology* **2010**, *21*, 105101–105113.

(294) Vega-Villa, K. R.; Takemoto, J. K.; Yáñez, J. A.; Remsberg, C. M.; Forrest, M. L.; Davies, N. M. *Adv. Drug Deliv. Rev.* **2008**, *60*, 929–938.
(295) Choi, S.-J.; Choy, J.-H. *Nanomedicine* **2011**, *6*, 803–814.
(296) Kura, A. U.; Hussein, M. Z.; Fakurazi, S.; Arulselvan, P. *Chem. Cent. J.* **2014**, *8*, 47.
(297) Kim, T.-H.; Lee, J.-A.; Choi, S.-J.; Oh, J.-M. *Int. J. Mol. Sci.* **2014**, *15*, 22563–22579.
(298) Choi, S.-J.; Paek, H.-J.; Yu, J. *Int. J. Nanomedicine* **2015**, *10*, 3217–3229.
(299) Carr, S. W.; Franklin, K. R.; Nunn, C. C.; Pasternak, J. J.; Scott, I. R. Sunscreen agents containing layered double hydroxides. EP 557089 A1., 1993.
(300) Carr, S. W.; Franklin, K. R.; Nunn, C. C.; Pasternak, J. J.; Scott, I. R. Sunscreen agents based on layered double hydroxides. US 5474762 A., 1995.
(301) Perioli, L.; Ambrogi, V.; Rossi, C.; Latterini, L.; Nocchetti, M.; Costantino, U. *J. Phys. Chem. Solids* **2006**, *67*, 1079–1083.
(302) Perioli, L.; Ambrogi, V.; Bertini, B.; Ricci, M.; Nocchetti, M.; Latterini, L.; Rossi, C. *Eur. J. Pharm. Biopharm.* **2006**, *62*, 185–193.
(303) Sun, W.; He, Q.; Luo, Y. *Mater. Lett.* **2007**, *61*, 1881–1884.
(304) He, Q.-L.; Yin, S.; Sato, T. *Adv. Sci. Technol.* **2003**, *31*, 445–452.
(305) El-Toni, A. M.; Yin, S.; Sato, T. *J. Solid State Chem.* **2004**, *177*, 3197–3201.
(306) Bonina, F. P.; Giannossi, M. L.; Medici, L.; Puglia, C.; Summa, V.; Tateo, F. *Appl. Clay Sci.* **2008**, *41*, 165–171.
(307) Park, M.-C.; Kim, H.; Park, D.-H.; Yang, J.-H.; Choy, J.-H. *Bull. Korean Chem. Soc.* **2012**, *33*, 1827–1828.
(308) Kim, M. H.; Park, D.-H.; Yang, J.-H.; Choy, Y. B.; Choy, J.-H. *Int. J. Pharm.* **2013**, *444*, 120–127.
(309) Hong, C.; Qi-dan, L.; Wen-gong, Z.; Zheng-hua, L. *Chem. Eng. J.* **2012**, *185–186*, 358–365.
(310) Yang, J.-h.; Lee, S.-y.; Han, Y.-s.; Park, K.-c.; Choy, J.-h. **2003**, *24*, 499–503.
(311) Tammaro, L.; Costantino, U.; Nocchetti, M.; Vittoria, V. *Appl. Clay Sci.* **2009**, *43*, 350–356.
(312) Badar, M.; Rahim, M. I.; Kieke, M.; Ebel, T.; Rohde, M.; Hauser, H.; Behrens, P.; Mueller, P. P. *J. Biomed. Mater. Res. Part A* **2015**, *103*, 2141–2149.
(313) Fardella, G.; Perioli, L.; Costantino, U.; Nocchetti, M.; Ambrogi, V.; Grandolini, G. *Proc. Int. Symp. Control. Release Bioact. Mater.* **1997**, *24*, 1033–1034.
(314) Fardella, G.; Ambrogi, V.; Perioli, L.; Grandolini, G. *Proc. Int. Symp. Control. Release Bioact. Mater.* **1998**, *25*, 774–775.
(315) Ambrogi, V.; Fardella, G.; Grandolini, G.; Perioli, L. *Int. J. Pharm.* **2001**, *220*, 23–32.
(316) Hwang, S.-H.; Han, Y.-S.; Choy, J.-H. *Bull. Korean Chem. Soc.* **2001**, *22*, 1019–1022.
(317) Gordijo, C. R.; Barbosa, C. a. S.; Da Costa Ferreira, A. M.; Constantino, V. R. L.; de Oliveira Silva, D. *J. Pharm. Sci.* **2005**, *94*, 1135–48.
(318) Gunawan, P.; Xu, R. *J. Pharm. Sci.* **2008**, *97*, 4367–4378.
(319) Zhang, H.; Pan, D.; Zou, K.; He, J.; Duan, X. *J. Mater. Chem.* **2009**, *19*, 3069–3077.
(320) Miao, Y.-E.; Zhu, H.; Chen, D.; Wang, R.; Tjiu, W. W.; Liu, T. *Mater. Chem. Phys.* **2012**, *134*, 623–630.
(321) Lu, X.; Meng, L.; Li, H.; Du, N.; Zhang, R.; Hou, W. *Mater. Res. Bull.* **2013**, *48*, 1512–1517.
(322) Conterosito, E.; Van Wouter, B.; Palin, L.; Croce, G.; Perioli, L.; Viterbo, D.; Gatti, G.; Milanesio, M. *Cryst. Growth Des.* **2013**, *13*, 1162–1169.
(323) Nagaraj, V. J.; Sun, X.; Mehta, J.; Martin, M.; Ngo, T.; Dey, S. K. *J. Nanotechnol.* **2015**, *2015*.
(324) Arratia-Quijada, J.; Jiménez, C. S.; Gurinov, A.; Centeno, A. P.; Andrade, I. C.; Arízaga, G. G. C. *Mater. Sci. Eng. B* **2016**, *203*, 7–12.
(325) Del Arco, M.; Cebadera, E.; Gutierrez, S.; Martin, C.; Montero, M. J.; Rives, V.; Rocha, J.; Sevilla, M. A. *J. Pharm. Sci.* **2004**, *93*, 1649–1658.
(326) Del Arco, M.; Fernandez, A.; Martin, C.; Sayalero, M. L.; Rives, V. *Clay Miner.* **2008**, *43*, 255–265.
(327) Li, B.; He, J.; Evans, D. G.; Duan, X. *Appl. Clay Sci.* **2004**, *27*, 199–207.

(328) Cunha, V. R. R.; Guilherme, V. A.; de Paula, E.; de Araujo, D. R.; Silva, R. O.; Medeiros, J. V. R.; Leite, J. R. S. A.; Petersen, P. A. D.; Foldvari, M.; Petrilli, H. M. *Mater. Sci. Eng. C* **2016**, *58*, 629–638.
(329) Zhang, H.; Zou, K.; Sun, H.; Duan, X. *J. Solid State Chem.* **2005**, *178*, 3485–3493.
(330) Berber, M. R.; Minagawa, K.; Katoh, M.; Mori, T.; Tanaka, M. *Eur. J. Pharm. Sci.* **2008**, *35*, 354–360.
(331) San Roman, M. S.; Holgado, M. J.; Salinas, B.; Rives, V. *Appl. Clay Sci.* **2012**, *55*, 158–163.
(332) Silion, M.; Hritcu, D.; Jaba, I. M.; Tamba, B.; Ionescu, D.; Mungiu, O. C.; Popa, I. M. *J. Mater. Sci. Mater. Med.* **2010**, *21*, 3009–3018.
(333) San Román, S.; Almeida, G. N.; del Arco, M.; Martín, C. *Appl. Clay Sci.* **2016**, *121*, 9–16.
(334) Parello, M. L.; Rojas, R.; Giacomelli, C. E. *J. Colloid Interface Sci.* **2010**, *351*, 134–9.
(335) Del Arco, M.; Fernandez, A.; Martín, C.; Rives, V. *Appl. Clay Sci.* **2009**, *42*, 538–544.
(336) Mohanambe, L.; Vasudevan, S. *J. Phys. Chem. B* **2005**, *109*, 15651–15658.
(337) Silion, M.; Popa, M. I. *Stud. si Cercet. Stiint. Chim. si Ing. Chim. Biotehnol. Ind. Aliment.* **2008**, *9*, 465–472.
(338) Rojas, R.; Palena, M. C.; Jimenez-Kairuz, A. F.; Manzo, R. H.; Giacomelli, C. E. *Appl. Clay Sci.* **2012**, *62-63*, 15–20.
(339) Sekhar, P. H.; Rohit, S.; Dhirendra, B. A stable delivery system for statin drugs. IN 2008MU02093 A., 2010.
(340) Zhang, H.; Zou, K.; Guo, S.; Duan, X. *J. Solid State Chem.* **2006**, *179*, 1792–1801.
(341) Xia, S.-J.; Ni, Z.-M.; Xu, Q.; Hu, B.-X.; Hu, J. *J. Solid State Chem.* **2008**, *181*, 2610–2619.
(342) Berber, M. R.; Hafez, I. H.; Minagawa, K.; Mori, T.; Tanaka, M. *Pharm. Res.* **2010**, *27*, 2394–2401.
(343) Al Ali, S. H. H.; Al-Qubaisi, M.; Hussein, M. Z.; Ismail, M.; Zainal, Z.; Hakim, M. N. *Int J Nanomedicine* **2012**, *7*, 2129–2141.
(344) Al Ali, S. H. H.; Al-Qubaisi, M.; Hussein, M. Z.; Ismail, M.; Zainal, Z.; Hakim, M. N. *Int. J. Nanomedicine* **2012**, *7*, 4251.
(345) Trikeriotis, M.; Ghanotakis, D. F. *Int. J. Pharm.* **2007**, *332*, 176–184.
(346) Wang, J.; Liu, Q.; Zhang, G.; Li, Z.; Yang, P.; Jing, X.; Zhang, M.; Liu, T.; Jiang, Z. *Solid State Sci.* **2009**, *11*, 1597–1601.
(347) Valarezo, E.; Tammaro, L.; Gonzalez, S.; Malagon, O.; Vittoria, V. *Appl. Clay Sci.* **2013**, *72*, 104–109.
(348) Frunza, M.; Popa, I. M.; Carja, G. *Stud. si Cercet. Stiint. Chim. si Ing. Chim. Biotehnol. Ind. Aliment.* **2005**, *6*, 173–179.
(349) Tammaro, L.; Costantino, U.; Bolognese, A.; Sammartino, G.; Marenzi, G.; Calignano, A.; Tete, S.; Mastrangelo, F.; Califano, L.; Vittoria, V. *Int. J. Antimicrob. Agents* **2007**, *29*, 417–423.
(350) Li, Y.-H.; Xu, J.; Zhang, S.-J.; Li, D.-X.; Zheng, B.; Hou, W.-G. *Wuji Huaxue Xuebao* **2009**, *25*, 2124–2128.
(351) Rezvani, Z.; Shahbaei, M. *Polym. Compos.* **2014**, *36*, 1819–1825.
(352) Duan, X.; Wei, M.; Guo, J.; He, J. Preparation of levodopa chiral intercalated hydrotalcite for the treatment of Parkinson's disease. CN 1850275 A., 2006.
(353) Nakayama, H.; Akasaka, H.; Tsuhako, M. *J. Pharm. Sci.* **2009**, *98*, 46–49.
(354) Hayashi, A.; Nakayama, H. *Chem. Lett.* **2010**, *39*, 1060–1062.
(355) Du, B.; Wang, R. *Cailiao Daobao* **2011**, *25*, 58–61.
(356) Hussein-Al-Ali, S. H.; Al-Qubaisi, M.; Hussein, M. Z.; Ismail, M.; Zainal, Z.; Hakim, M. N. *Int. J. Mol. Sci.* **2012**, *13*, 5899–5916.
(357) Perioli, L.; D'Alba, G.; Pagano, C. *Eur. J. Pharm. Biopharm.* **2012**, *80*, 621–629.
(358) Perioli, L.; Mutascio, P.; Pagano, C. *Pharm. Res.* **2013**, *30*, 156–166.
(359) Choy, J.-H.; Kwak, S.-Y.; Park, J.-S.; Jeong, Y.-J. *J. Mater. Chem.* **2001**, *11*, 1671–1674.
(360) Oh, J.-M.; Park, D.-H.; Oh, Y.-J.; Choi, S.-J.; Park, M.-C.; Choy, J.-H. *Clay Sci.* **2011**, *15*, 111–115.

(361) Tanaka, M.; Aisawa, S.; Hirahara, H.; Narita, E.; Yin, S.; Sato, T. *Funct. Mater. Lett.* **2012**, *5*, 1260003–1260008.
(362) Kwak, S.-Y.; Jeong, Y.-J.; Park, J.-S.; Choy, J.-H. *Solid State Ionics* **2002**, *151*, 229–234.
(363) Tyner, K. M.; Roberson, M. S.; Berghorn, K. A.; Li, L.; Gilmour, R. F.; Batt, C. A.; Giannelis, E. P. *J. Control. Release* **2004**, *100*, 399–409.
(364) Ladewig, K.; Xu, Z. P.; Lu, G. Q. *Expert Opin. Drug Deliv.* **2009**, *6*, 907–922.
(365) Li, A.; Qin, L.; Wang, W.; Zhu, R.; Yu, Y.; Liu, H.; Wang, S. *Biomaterials* **2010**, *32*, 469–477.
(366) Zhao, Z.; Qi, Y.; Wei, M.; Zhang, F.; Xu, S. *Mater. Lett.* **2012**, *78*, 62–65.
(367) Wong, Y.; Cooper, H. M.; Zhang, K.; Chen, M.; Bartlett, P.; Xu, Z. P. *J. Colloid Interface Sci.* **2012**, *369*, 453–459.
(368) Hu, H.; Xiu, K. M.; Xu, S. L.; Yang, W. T.; Xu, F. J. *Bioconjug. Chem.* **2013**, *24*, 968–978.
(369) Li, L.; Gu, W.; Chen, J.; Chen, W.; Xu, Z. P. *Biomaterials* **2014**, *35*, 3331–3339.
(370) Oh, J.-M.; Choi, S.-J.; Kim, S.-T.; Choy, J.-H. *Bioconjug. Chem.* **2006**, *17*, 1411–1417.
(371) Xu, Z. P.; Niebert, M.; Porazik, K.; Walker, T. L.; Cooper, H. M.; Middelberg, A. P. J.; Gray, P. P.; Bartlett, P. F.; Lu, G. Q. *J. Control. Release* **2008**, *130*, 86–94.
(372) Musumeci, A. W.; Mortimer, G. M.; Butler, M. K.; Xu, Z. P.; Minchin, R. F.; Martin, D. J. *Appl. Clay Sci.* **2010**, *48*, 271–279.
(373) Gu, Z.; Zuo, H.; Li, L.; Wu, A.; Xu, Z. P. *J. Mater. Chem. B* **2015**, *3*, 3331–3339.
(374) Gu, Z.; Thomas, A. C.; Xu, Z. P.; Campbell, J. H.; Lu, G. Q. *Chem. Mater.* **2008**, *20*, 3715–3722.
(375) Gu, Z.; Rolfe, B. E.; Xu, Z.-P.; Thomas, A. C.; Campbell, J. H.; Lu, G.-Q. M. *Biomaterials* **2010**, *31*, 5455–5462.
(376) Tian, D.-Y.; Liu, Z.-L.; Li, S.-P.; Li, X.-D. *Mater. Sci. Eng. C* **2014**, *45*, 297–305.
(377) Alexa, I. F.; Pastravanu, C. G.; Ignat, M.; Popovici, E. *Colloids Surf. B. Biointerfaces* **2013**, *106*, 135–139.
(378) Choi, S.-J.; Oh, J.-M.; Choy, J.-H. *J. Nanosci. Nanotechnol.* **2010**, *10*, 2913–2916.
(379) Wang, Z.; Wang, E.; Gao, L.; Xu, L. *J. Solid State Chem.* **2005**, *178*, 736–741.
(380) Yasutake, A.; Aisawa, S.; Kobashi, N.; Takahashi, S.; Hirahara, H.; Narita, E. *Clay Sci.* **2008**, *14*, 49–54.
(381) Jin, L.; Liu, Q.; Sun, Z. Z.-Y.; Ni, X.-Y. X.; Wei, M. *Ind. Eng. Chem. Res.* **2010**, *49*, 11176–11181.
(382) Aisawa, S.; Yasutake, A.; Takahashi, S.; Hirahara, H.; Narita, E. *J. Soc. Inorg. Mater. Japan* **2012**, *19*, 230–236.
(383) Nakayama, H.; Kuwano, K.; Tsuhako, M. *J. Phys. Chem. Solids* **2007**, *69*, 1552–1555.
(384) Pan, D.; Zhang, H.; Zhang, T.; Duan, X. *Chem. Eng. Sci.* **2010**, *65*, 3762–3771.
(385) Pan, D.; Zhang, H.; Fan, T.; Chen, J.; Duan, X. *Chem. Commun.* **2011**, *47*, 908–910.
(386) Xue, Y. H.; Zhang, R.; Sun, X. Y.; Wang, S. L. *J. Mater. Sci. Mater. Med.* **2008**, *19*, 1197–1202.
(387) Choi, S.-J.; Oh, J.-M.; Choy, J.-H. *J. Phys. Chem. Solids* **2007**, *69*, 1528–1532.
(388) Tyner, K. M.; Schiffman, S. R.; Giannelis, E. P. *J. Control. Release* **2004**, *95*, 501–14.
(389) Dong, L.; Yan, L.; Hou, W.-G.; Liu, S.-J. *J. Solid State Chem.* **2010**, *183*, 1811–1816.
(390) Li, Y.; Du, N.; Hou, W.; Liu, S. English *Chem. Res. Chinese Univ.* **2014**, *30*, 137–143.
(391) Yan, M.; Zhang, Z.; Cui, S.; Lei, M.; Zeng, K.; Liao, Y.; Chu, W.; Deng, Y.; Zhao, C. *Int. J. Nanomedicine* **2014**, *9*, 4867–4878.
(392) Hara, S.; Hirayama, H.; Itabashi, H.; Sasaki, Y.; Matsushima, Y. *Zasshi. Tokyo Ika Daigaku* **1968**, *26*, 211–226.
(393) Katuyuki, H.; Norio, I.; Takeo, I.; Teruhiko, K.; Kimiaki, Y. Novel synthetic hydrotalcite and antacid comprising said synthetic hydrotalcite. US 3650704., 1972.
(394) Llewellyn, A. F.; Tomkin, G. H.; Murphy, G. M. *Pharm. Acta Helv.* **1977**, *52*, 1–5.
(395) Miyata, S. Zn hydrotalcites as antiulcer drugs. JP 2008120703 A., 2008.
(396) Katsuki, K.; Okada, A. Agent for treating ulcer. US 8372429., 2013.

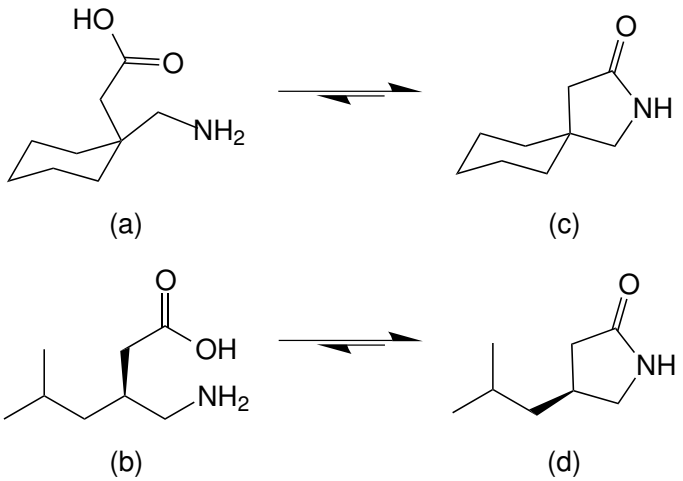
(397) Anabuki, H.; Miyata, S. Composition and method for treating iron deficiency syndrome. EP 61175 A1., 1982.
(398) Ookubo, A.; Ooi, K.; Hayashi, H. *J. Pharm. Sci.* **1992**, *81*, 1139–1140.
(399) Tonelli, D.; Scavetta, E.; Giorgetti, M. *Anal. Bioanal. Chem.* **2013**, *405*, 603–614.
(400) Sanchez-Paniagua Marta, L.; Charmantray, F.; Helaine, V.; Hecquet, L.; Mousty, C. *Biosens. Bioelectron.* **2010**, *26*, 139–143.
(401) Carja, G.; Ratoi, S.; Ciobanu, G.; Balasanian, I. *Environ. Eng. Manag. J.* **2009**, *8*, 55–58.
(402) Wei, M.; Rao, X.; Duan, X. Layered double hydroxide nanosheet-dual protein composite ultrathin film modified electrode and preparation method thereof based on electrostatic layer-by-layer assembly. CN 101839884 A., 2010.
(403) Shan, D.; Cosnier, S.; Mousty, C. *Anal. Chem.* **2003**, *75*, 3872–3879.
(404) Sanchez-Paniagua Marta, L.; Leroux, F.; Mousty, C. *Sensors Actuators, B Chem.* **2010**, *150*, 36–42.
(405) Gong, J.; Guan, Z.; Song, D. *Biosens. Bioelectron.* **2013**, *39*, 320–323.
(406) De Melo, J. V.; Cosnier, S.; Mousty, C.; Martelet, C.; Jaffrezic-Renault, N. *Anal. Chem.* **2002**, *74*, 4037–4043.
(407) Maaref, A.; Barhoumi, H.; Rammah, M.; Martelet, C.; Jaffrezic-Renault, N.; Mousty, C.; Cosnier, S. *Sensors Actuators, B Chem.* **2007**, *B123*, 671–679.
(408) Vial, S.; Prevot, V.; Leroux, F.; Forano, C. *Microporous Mesoporous Mater.* **2008**, *107*, 190–201.
(409) Mansouri, H.; Forano, C.; Prevot, V.; Jaffrezic-Renault, N.; Ben Abdesslem., H. A. *Sens. Lett.* **2009**, *7*, 888–895.
(410) Chen, X.; Fu, C.; Wang, Y.; Yang, W.; Evans, D. G. *Biosens. Bioelectron.* **2008**, *24*, 356–361.
(411) Li, M.; Ji, H.; Wang, Y.; Liu, L.; Gao, F. *Biosens. Bioelectron.* **2012**, *38*, 239–244.
(412) Forano, C.; Vial, S.; Mousty, C. *Curr. Nanosci.* **2006**, *2*, 283–294.
(413) Li, M.; Chen, S.; Ni, F.; Wang, Y.; Wang, L. *Electrochim. Acta* **2008**, *53*, 7255–7260.
(414) Charradi, K.; Forano, C.; Prevot, V.; Madern, D.; Ben Abdesslem, H. A.; Mousty, C. *Langmuir* **2010**, *26*, 9997–10004.
(415) Sun, W.; Guo, Y.; Lu, Y.; Hu, A.; Shi, F.; Li, T.; Sun, Z. *Electrochim. Acta* **2013**, *91*, 130–136.
(416) Zhan, T.; Guo, Y.; Xu, L.; Zhang, W.; Sun, W.; Hou, W. *Talanta* **2012**, *94*, 189–194.
(417) Jin, L.; Guo, Z.; Wang, T.; Wei, M. *Sensors Actuators, B Chem.* **2013**, *177*, 145–152.
(418) Kong, X.; Rao, X.; Han, J.; Wei, M.; Duan, X. *Biosens. Bioelectron.* **2010**, *26*, 549–554.
(419) Gualandi, I.; Scavetta, E.; Zappoli, S.; Tonelli, D. *Biosens. Bioelectron.* **2011**, *26*, 3200–3206.
(420) Williams, G. R.; Fierens, K.; Preston, S. G.; Lunn, D.; Rysnik, O.; De Prijck, S.; Kool, M.; Buckley, H. C.; Lambrecht, B. N.; O'Hare, D.; Austyn, J. M. *J. Exp. Med.* **2014**, *211*, 1019–1025.
(421) Buckley, H. C. Applications of Layered Double Hydroxides as Inorganic Adjuvants., D.Phil, University of Oxford, 2014.
(422) Maughan, C. N.; Preston, S. G.; Williams, G. R. *J. Pharm. Pharmacol.* **2015**, *67*, 426–449.

2. Intercalation of Unstable Drugs Gabapentin and Pregabalin Through an Improved Coassembly Route

2.1 Introduction

Gabapentin (1-(aminomethyl)cyclohexylacetic acid) and pregabalin ((*S*)-3-(aminomethyl)-5-methylhexanoic acid) are γ-aminobutyric acid (GABA) analogues and anticonvulsant drugs used in the treatment of epilepsy and neuropathic pain such as postherpetic neuralgia, as well as many off-label indications such as restless leg syndrome.[1–5] These drugs have high potential for use in treating paediatric patients, but their suitability is currently limited in this area by their poor aqueous stability and extremely bitter taste, which have prevented stable and palatable liquid dosage forms from being created.[6–8] This also limits their suitability for use by patients who have difficulty swallowing tablets, such as geriatric patients and those with limited muscle control.[9] The opportunity to investigate controlled release of these drugs, which are typically metabolised and excreted rapidly, is also of interest.[10–13]

Gabapentin (GBP) and pregabalin (PGB) undergo degradation in aqueous solution via intramolecular cyclisation to form lactam analogues 2-aza-spiro[4,5]decan-3-one and (*S*)-4-isobutyl-2-pyrrolidinone, shown in Scheme 2.1. Lactamisation proceeds through both acid and base catalysed mechanisms, and attempts to stabilise GBP through complexation to cyclodextrin compounds have proved unsuccessful, complexation actually increasing the rate of lactamisation through restricting the drug in more reactive conformers.[14–16] Furthermore, the gabapentin lactam decomposition



Scheme 2.1: The structures of (a) gabapentin, (b) pregabalin, and their lactam decomposition products (c) 2-aza-spiro[4,5]decan-3-one and (d) (*S*)-4-isobutyl-2-pyrrolidinone.

product has been shown to exhibit a sufficiently high toxicity that its presence in pharmaceutical preparations of GBP must be kept to a minimum.[17,18]

Intercalation within LDH layers has been shown to successfully stabilise unstable and metastable anions, particularly those in which negatively charged functional groups are the cause of instability.[19–21] Electrostatic interactions between the negatively charged groups and the positive metal hydroxide layers, coupled with restricted movement from immobilisation within the interlayer region, leads to the increased stability of intercalated anions. The ability of LDHs to mask the taste of their intercalated anions, and to provide sustained release functionality, provides additional benefits applicable to these drugs.[22,23]

The unstable nature of GBP and PGB in aqueous, and in particular basic, solution precludes the use of many traditional LDH intercalation methods, such as coprecipitation, ion-exchange, calcination–rehydration and hydrothermal synthesis, all of which were attempted under various conditions, but with no success. The delamination–restacking, or coassembly, method of LDH intercalation has received considerable interest in recent years, and it has been shown to be effective for intercalating anions and other species that have resisted more traditional methods.[24–29] Some aspects of the coassembly method have been scrutinised, particularly those affecting delamination, such as the effect of the delamination solvent by Hibino and Jones, the effect of interlayer anion by Hibino and then Liu *et al.*, and the possible mechanism

for delamination by Ma *et al.* and Liu *et al.*[30–33] However, many aspects of the procedure, especially regarding the restacking process and its mechanism, remain underexplored, and as such there is significant potential for further investigation and optimisation, which would increase the utility of the coassembly method.

2.1.1 Scope of this Chapter

The intercalation of gabapentin and pregabalin into a magnesium–aluminium layered double hydroxide by the coassembly, or delamination–restacking method to form inorganic-drug nanohybrids is reported. The parameters (reaction solvent, temperature, water presence) of the restacking process were investigated, finding that drug loading, purity and crystallinity of the nanohybrid products were all significantly increased by performing the restacking procedure in ethanol, anhydrously, and at reduced temperatures as low as −40 °C. To explain these findings, a possible mechanism to the restacking process is proposed. The drug release profiles of the nanohybrids were recorded and fitted to kinetic models. The nanohybrids were suspended in water and the stabilities of the drug ions measured, with regard to decomposition through lactamisation. Their stabilities were found to increase by a factor of at least 15, when compared to solutions of the pristine drugs. The improved coassembly method resulted in nanohybrids of sufficient quality and stability to be usable in pharmaceutical suspensions and other wet formulations.

2.2 Synthesis and characterisation of nanohybrids

The synthesis of the LDH–drug nanohybrids was adapted from the delamination–restacking method reported by Wu *et al.*[34] A highly crystalline precursor LDH, $Mg_2Al(OH)_6NO_3$, referred to herein as MgAl-NO_3, was delaminated through sonication in formamide. The synthesis of the nanohybrids by the restacking process was then investigated under a range of conditions, detailed in full in Section 6.4, following the same general method whereby the delaminated MgAl-NO_3 LDH nanosheet suspension in formamide was added to a solution containing either GBP or PGB alongside simultaneous addition of a basic solution; the resulting nanohybrids are

referred to herein as MgAl-GBP and MgAl-PGB.

2.2.1 Delamination of MgAl-NO_3 LDH

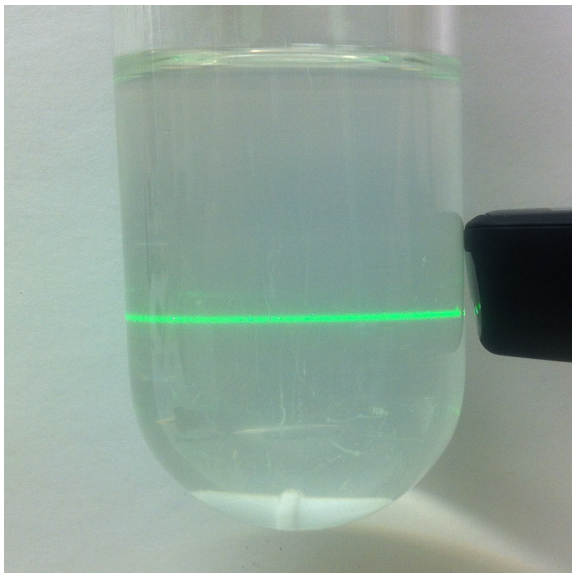


Figure 2.1: The suspension of delaminated MgAl-NO_3 in formamide exhibiting the Tyndall effect.

The delaminated LDH suspension exhibited a Tyndall effect, as seen in Figure 2.1 confirming formation of a colloidal suspension, rather than dissolution of the precursor LDH particles. The XRD pattern of the suspension, seen in Figure 2.2, shows the complete absence of any reflections relating to the (00l) reflections found in the precursor LDH, however a small reflection at $2\theta = 60.5^{\circ}$ relates to the (110) reflection of the precursor, indicating complete delamination to 2D sheets of the metal hydroxide layers, whilst a broad shoulder in the baseline around $2\theta = 26^{\circ}$ can be attributed to scattering by liquid formamide, as seen in other delamination studies.[32,34] Samples of precursor LDH that had been dried under high vacuum prior to delamination took longer to fully delaminate than samples of precursor LDH that had not been dried under vacuum. This is presumably due to slower proliferation of formamide between the LDH layers, caused by stronger interlayer forces resulting from a lack of cointercalated water.

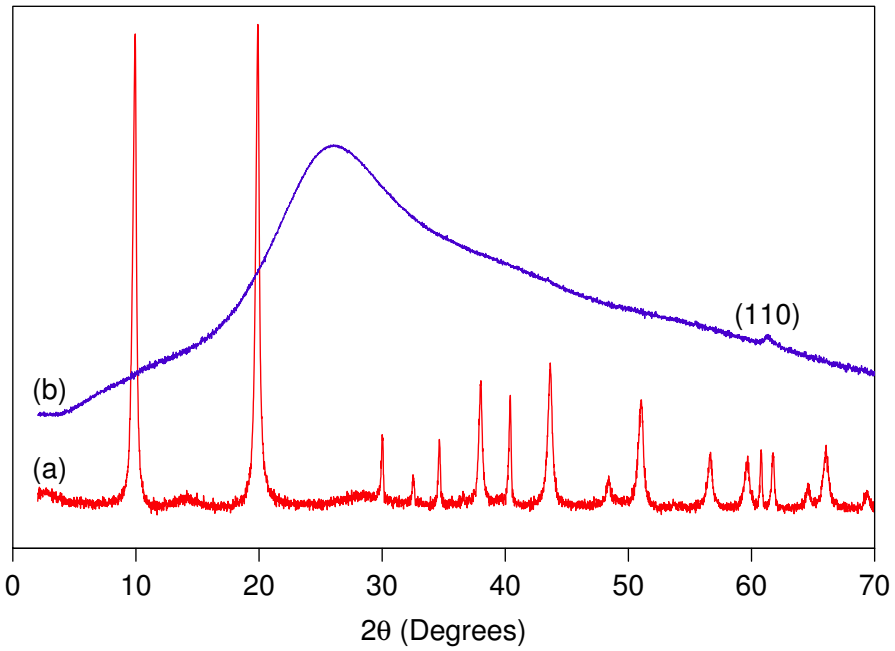


Figure 2.2: The XRD patterns of MgAl-NO_3 (a) before delamination and (b) delaminated in formamide.

2.2.2 Restacking synthesis of nanohybrids

The restacking process was conducted using both water and ethanol as the solvent, and in case of ethanol, was conducted in both hydrous and anhydrous conditions. Nanohybrids containing GBP were synthesised in all three conditions, although nanohybrids containing PGB were only synthesised in anhydrous ethanolic conditions; the different samples are referred to as MgAl-GBP_{water}, MgAl-$GBP_{ethanol}$, MgAl-GBP_{anhyd} and MgAl-PGB_{anhyd}.

The restacking procedure was initially performed at room temperature (20 °C). An attempt at increasing the crystallinity of the nanohybrids was made by performing the restacking procedure at elevated temperatures of 40 and 80 °C. When this was found to have a detrimental effect on the crystallinity and purity of the resulting nanohybrids, the restacking procedure was performed at reduced temperatures of 0, −20 and −40 °C. Samples are denoted by their synthesis temperature, T, like so MgAl-$\langle drug \rangle_{\langle solvent \rangle,\langle T \rangle}$. For example, MgAl-$GBP_{ethanol,40}$ and MgAl-$PGB_{anhyd,-20}$ refer to samples of MgAl-$GBP_{ethanol}$ and MgAl-PGB_{anhyd} synthesised at 40 and −20 °C respectively.

Exempting the attempted synthesis of nanohybrids at elevated temperatures, the products of which were poorly crystalline and impure, nine different LDH–drug nanohybrid samples were synthesised: MgAl-GBP$_{water,20}$, MgAl-GBP$_{ethanol,20}$, MgAl-GBP$_{ethanol,0}$, MgAl-GBP$_{ethanol,-20}$, MgAl-GBP$_{ethanol,-40}$, MgAl-GBP$_{anhyd,20}$, MgAl-GBP$_{anhyd,-20}$, MgAl-PGB$_{anhyd,20}$ and MgAl-PGB$_{anhyd,-20}$.

2.2.3 Powder X-ray diffraction

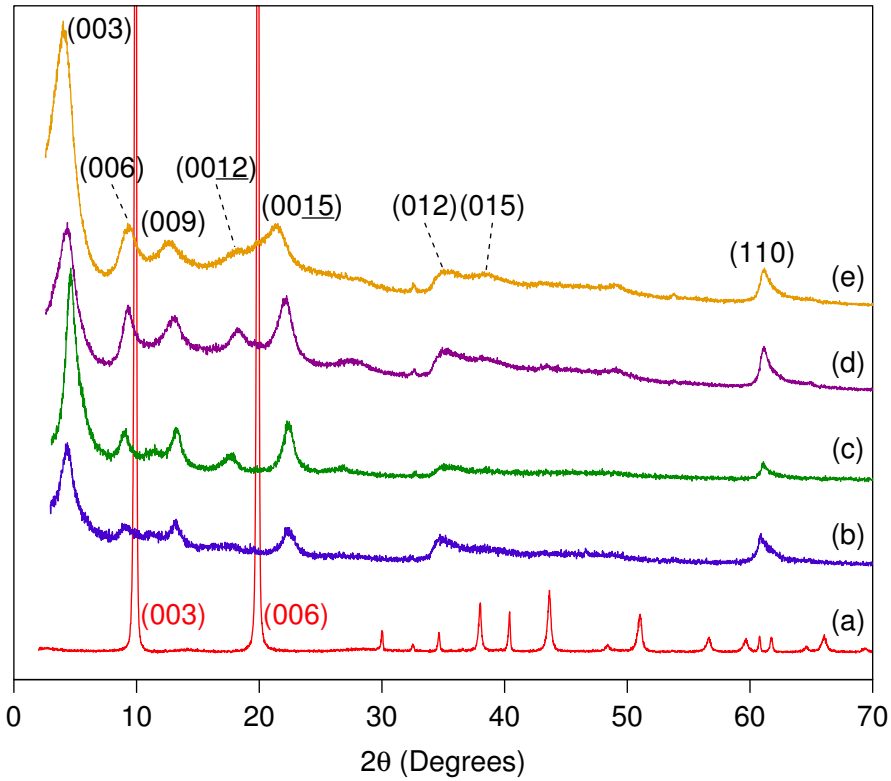


Figure 2.3: The powder XRD patterns of (a) MgAl-NO_3, (b) MgAl-GBP$_{water,20}$, (c) MgAl-GBP$_{ethanol,20}$, (d) MgAl-GBP$_{anhyd,20}$ and (e) MgAl-PGB$_{anhyd,20}$.

Powder XRD patterns of the drug intercalated nanohybrids and the precursor LDH are shown in Figure 2.3. All patterns can be indexed on the basis of a hexagonal lattice with $R\bar{3}m$ rhombohedral symmetry. The basal Bragg reflections, indexed as (003), are found at low values of 2θ in the nanohybrids, (2θ = 4.26 – 4.64°, d_{003} = 19.0 – 20.7 Å for MgAl-GBP; 2θ = 4.05 – 4.35°, d_{003} = 20.3 – 21.8 Å for MgAl-PGB), relative to the precursor LDH (2θ = 9.93°, d_{003} = 8.9 Å for MgAl-NO_3), which is indicative of intercalation of larger guest species into the interlayer region of the

LDH. Although not clear from visual inspection, Bragg reflections are sharper and more intense in the patterns of samples that underwent restacking in ethanol rather than water, and sharper still for those synthesised anhydrously, as evidenced by the differences in FWHM values seen in Table 2.1. Furthermore, small reflections at $2\theta = 9.91°$ and $2\theta = 19.82°$ in MgAl-GBP$_{\text{water,20}}$ and MgAl-GBP$_{\text{ethanol,20}}$ correspond to the (003) and (006) reflections of MgAl-NO_3, indicating that this has also formed during the restacking process of these two nanohybrids.

Cell parameters are given in Table 2.1. The interlayer species of LDHs have very little effect on the a parameter, as this is predominantly determined by the metal hydroxide layers. Restacking in ethanol leads to a small decrease in the length of the a parameter compared to water, whilst anhydrous restacking leads to an additional reduction. The c parameter lies along the stacking direction, and so directly relates to the basal spacing, and the gallery height of the interlayer region, which is dependent on the interlayer species and any cointercalated molecules. Although there is variation in c parameters of the nanohybrids, it does not follow any obvious trend relating to differences in restacking conditions, and can be attributed to differences in the orientation of the nitrate and drug ions, and any cointercalated molecules.

Given that the thickness of metal hydroxide layers is generally reported as 4.8 Å,[35] this gives interlayer region distances of 14.9 to 15.4 Å for MgAl-GBP and of 15.2 to 15.7 Å for MgAl-PGB respectively. The dimensions of GBP and PBG can be approximated from their crystal structures. The maximum length, width and depth of GBP given from this approximation are 8.4, 5.0 and 4.5 Å, and those for PGB are 8.1, 6.2 and 5.2 Å.[36,37] These values, together with the values for the interlayer distances, can be used to propose possible orientations for the drug species within the layers, as illustrated in Figure 2.4. Despite GBP having a greater maximum length than PGB, the greater interlayer distance is produced by PGB, due to its more bulky shape and greater conformational freedom, which prevent it from packing so closely in the interlayer region. The height of the interlayer region in the nanohybrids is sufficiently large for a bilayer of the drug ions to fit between the metal hydroxide sheets, such that the hydrophobic ends of the ions face towards each other, and the charged carboxylate and hydrophilic amine groups face towards the metal hydroxide sheets, as has been found when intercalating other surfactant-like drug ions into

Table 2.1: Cell parameters, and positions and full width at half maximum (FWHM) values of Bragg reflections in powder XRD patterns of the nanohybrids.

Sample	Cell parameters (Å)		Reflection position/FWHM (degrees, 2θ)							
	a	c	(003)		(006)		(009)		(110)	
MgAl-GBP$_{\text{water,20}}$	3.040	59.09	4.52	1.061	9.13	0.979	13.14	0.816	60.89	0.653
MgAl-GBP$_{\text{ethanol,20}}$	3.039	59.36	4.64	0.979	9.11	1.142	12.67	0.916	60.93	0.494
MgAl-GBP$_{\text{ethanol,0}}$	3.036	60.70	4.30	0.816	8.90	0.816	13.07	0.889	60.98	0.580
MgAl-GBP$_{\text{ethanol,-20}}$	3.035	59.91	4.43	0.734	8.96	0.616	13.11	0.734	61.00	0.544
MgAl-GBP$_{\text{ethanol,-40}}$	3.037	60.58	4.26	0.779	9.03	0.706	13.07	0.742	60.97	0.510
MgAl-GBP$_{\text{anhyd,20}}$	3.029	59.50	4.36	0.669	9.31	0.602	13.10	1.071	61.14	0.479
MgAl-GBP$_{\text{anhyd,-20}}$	3.030	59.19	4.42	0.535	9.20	0.468	13.28	0.535	61.13	0.474
MgAl-PGB$_{\text{anhyd,20}}$	3.030	61.72	4.05	0.937	9.36	1.071	12.60	0.971	61.13	0.468
MgAl-PGB$_{\text{anhyd,-20}}$	3.029	60.05	4.35	0.687	9.28	0.602	12.83	0.704	61.16	0.535

LDHs.[38,39]

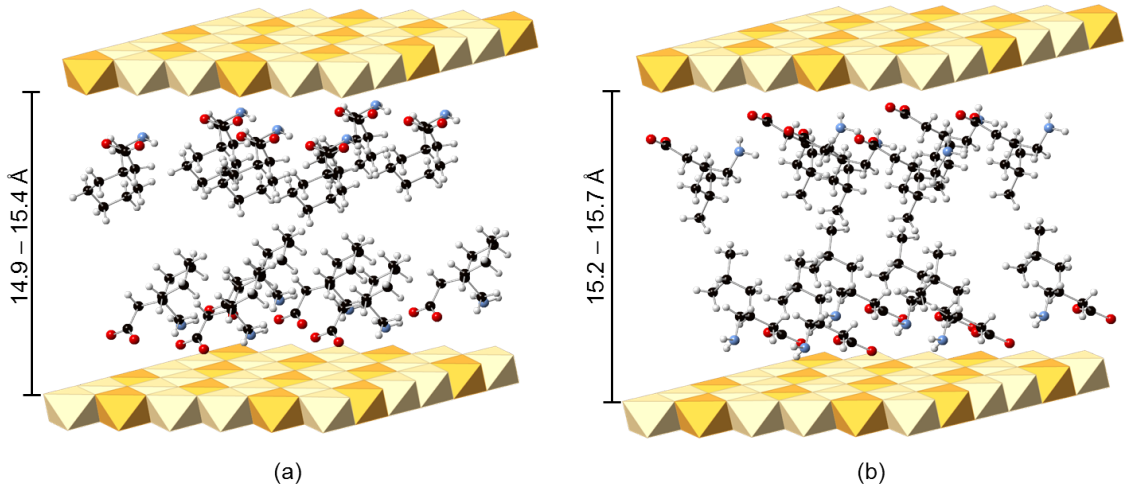


Figure 2.4: The possible orientations of (a) GBP and (b) PGB in the interlayer regions of the nanohybrids.

The full width at half maximum (FWHM) of Bragg reflections in XRD patterns of the nanohybrids can be used as a measure of the the nanohybrids' crystallinity, relative to one another, and are detailed in Table 2.1. The FWHM values of the $(00l)$ reflections indicate the extent of crystallinity in the z direction of individual crystalline regions, which, as this is in the direction in which stacking occurs, can be used as a measure of how well ordered successive layers are stacked together. Clear trends can be seen in the FWHM values of the $(00l)$ reflections, with restacking temperature having the most influence. Reducing restacking temperature consistently results in increased crystallinity of the particles in the z direction, up until $-20\,°C$. Reducing the reactions temperature beyond this produces no further increase in crystallinity.

Differing the restacking solvent has a much less pronounced effect on crystallinity in the z direction, however a small improvement in crystallinity is seen when restacking is performed anhydrously in ethanol, in comparison to restacking in water or nonanhydrous ethanol. The FWHM value for the (110) reflection relates to the extent of crystallinity in the xy plane, so is a measure of the crystallinity of the metal hydroxide sheets in the nanohybrids. The (110) FWHM values remain largely consistent across almost all nanohybrids, ranging from 0.468 to 0.580° 2θ with no obvious trend, with the exception of MgAl-GBP$_{\text{water,20}}$, which shows a marginally higher FHWM of 0.653°

2θ. This indicates that the crystallinity of the individual LDH sheets is unaffected by differences in the restacking procedure, and that the individual sheets still retain a reasonably high degree of crystallinity, despite undergoing the delamination and restacking procedure.

2.2.4 Fourier transform infrared spectroscopy

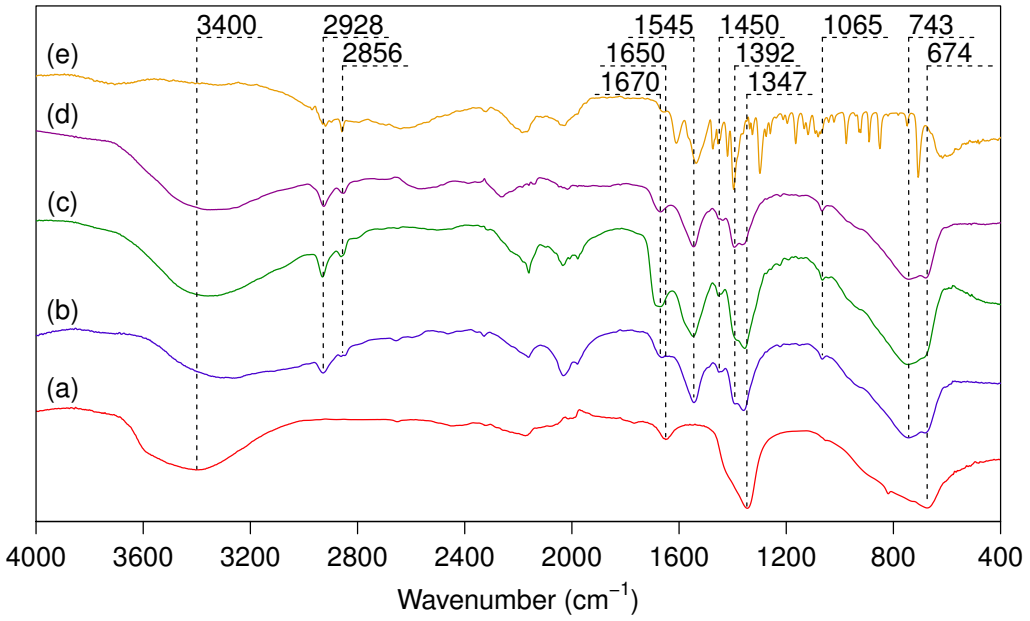


Figure 2.5: FTIR spectra of (a) MgAl-NO_3, (b) MgAl-$GBP_{water,20}$, (c) MgAl-$GBP_{ethanol,20}$, (d) MgAl-$GBP_{anhyd,20}$, (e) pristine GBP.

Examples of the FTIR spectra of the GBP and PGB nanohybrids are shown in Figures 2.5 and 2.6 respectively, alongside spectra of the pristine drugs and the precursor LDH for comparison. Characteristic absorption bands of the drugs can be seen in spectra of the nanohybrids. In the case of GBP, the pristine drug appears as its most stable polymorph, known in the literature as form II.[40] Upon intercalation, the spectra of the MgAl-GBP nanohybrids do not show a close agreement with the spectrum of a specific polymorph of GBP, but all absorptions fall within ranges that correspond to characteristic absorptions in all GBP polymorphs. However, most absorptions seen in the fingerprint region of each polymorph, below 1350 cm^{-1}, are absent.[41,42] Absorptions are seen at 2928 and 2856 cm^{-1} relating to the asymmetric and symmetric NH_2 stretches, at 1670 cm^{-1} relating to the ionised asymmetric

carboxylate stretch, at 1545 cm^{-1} relating to the NH_2 scissoring vibration and at 1450 and 1392 cm^{-1} relating to CH_2 bends.

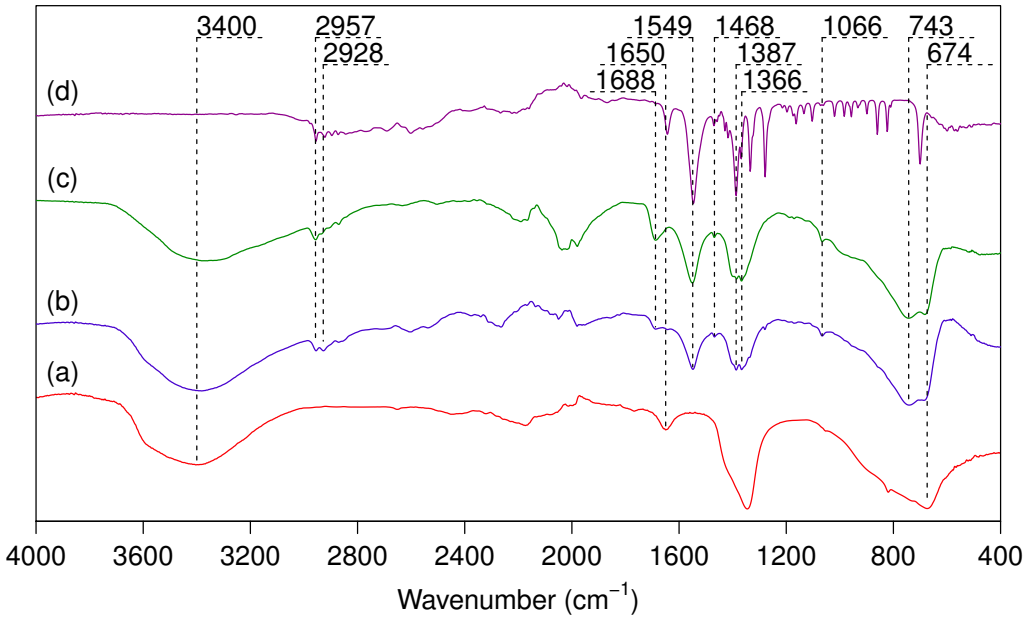


Figure 2.6: FTIR spectra of (a) MgAl-NO_3, (b) MgAl-$PGB_{anhyd,20}$, (c) MgAl-$PGB_{anhyd,-20}$ and (d) pristine PGB.

The different polymorphs of PGB have been less well explored, but a similar difference is observed between the spectrum of the pristine drug, which corresponds to polymorphic form I, and the spectra of the MgAl-PGB nanohybrids, which do not agree exactly with any specific polymorph of PGB, but show good agreement within the ranges of characteristic absorptions across different polymorphs.[43,44] Absorptions at 2957 and 2928 cm^{-1} relate to the asymmetric and symmetric NH_2 stretches, those at 1688 cm^{-1} relate to the ionised asymmetric carboxylate stretch and at 1549 cm^{-1} to the scissoring vibration; absorptions at 1468, 1387 and 1366 cm^{-1} relate to CH_2 bends.[45] No absorptions characteristic of the lactam decomposition products were seen. In particular, any absorption at 1699 cm^{-1} relating to the cyclic C=O stretch is notably absent from all spectra.[46] In addition to the absorption bands from the drug ions, absorptions typical of LDHs are seen, including broad shouldered absorptions between 670 and 900 cm^{-1} relating to the M−OH stretch, and between 3200 and 3500 cm^{-1}, relating to the O−H stretches of the layers (and cointercalated water, in the case of the precursor LDH).

Noticeable line broadening is seen in the spectra of the nanohybrids, which is

attributable to variation in the bound conformations of the drug ions in the interlayer regions. In all nanohybrids, an absorption at 1347 cm^{-1} is seen, which corresponds to NO_3^-, indicating the presence of nitrate ions. However, this absorption is more intense in the spectra of MgAl-$GBP_{water,20}$ and MgAl-$GBP_{ethanol,20}$ than in other nanohybrids, which corroborates with the evidence from XRD data indicating the greater presence of MgAl-NO_3 in these samples. An absorption at 1311 cm^{-1}, corresponding to formamide, was seen in samples that had not been dried under high vacuum for a sufficient length of time, although it was absent from spectra after additional drying. It is also worth noting that the absorption at 1650 cm^{-1}, which is derived from cointercalated water molecules, is not present in the spectra of any MgAl-GBP_{anhyd} or MgAl-PGB_{anhyd} samples, indicating the absence of cointercalated water.

2.2.5 Solid state ^{13}C NMR spectroscopy

Solid state ^{13}C CP/MAS NMR spectra, seen in Figure 2.7 were useful in determining whether the intercalated species were the intended drug ions, their lactam decomposition products or a mixture of both. The spectra of the pristine drug molecules show resonances at 29.2 and 31.8 ppm for the α-amino methylene carbon atoms and 169.4 and 168.8 ppm for the carbonyl carbon atoms of GBP and PGB respectively. Lactamisation causes these resonances to shift significantly and broaden due to the adjacent ^{14}N nucleus, which would result in distinctive resonances in the spectra.[47] However, the nanohybrids present resonances at 34.4 and 161.3 ppm for MgAl-GBP and 33.4 and 163.8 ppm for MgAl-PGB. Whilst there are small changes to chemical shift values, these are attributable to the changes in geometry and ordering adopted by the drug ions in the nanohybrids relative to the pristine drug crystals, as has been seen in other drugs upon intercalation, and in different polymorphs of GBP.[48] All other resonances could be assigned to the cyclohexyl and isobutyl groups of GBP and PGB respectively, indicating that the unaltered drug ions were the intercalated species.

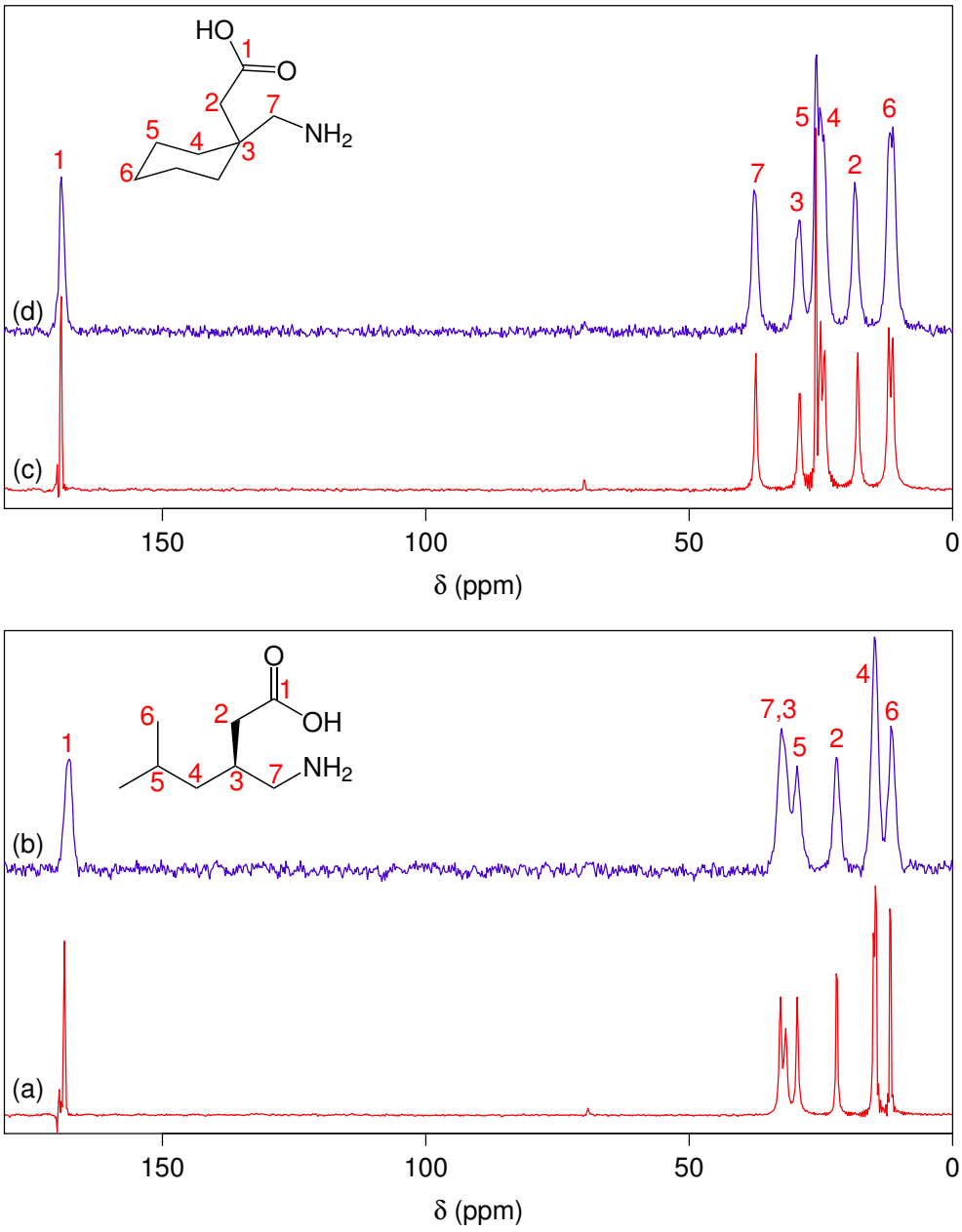


Figure 2.7: The assigned ^{13}C CP/MAS solid state NMR spectra of (a) PGB, (b) MgAl-PGB$_{anhyd,-20}$, (c) GBP and (d) MgAl-GBP$_{anhyd,-20}$.

2.2.6 Deintercalation experiments

The deintercalation experiments investigated by solution phase ^{1}H NMR spectroscopy reveal that, upon deintercalation, most samples of the nanohybrids release only the intended drug species, along with trace amounts of residual solvents, evident from small resonances at 8.44 ppm denoting formamide and 1.17 and 3.65 ppm denoting ethanol. Spectra of the deintercalated drugs are in good agreement with both those of the pristine drug samples and literature values, GBP giving resonances of $\delta = 1.37$ to 1.51 ppm (10H, m), 2.42 ppm (2H, s), 3.00 ppm (2H, s), and PGB giving resonances of $\delta = 0.89$ ppm (6H, t), 1.22 ppm (2H, t), 1.66 ppm (1H, m), 2.11 to 2.35 ppm (2H, m), 2.98 ppm (2H, ddd).[49] The only sample that shows any evidence of drug decomposition is MgAl-GBP$_{\text{water,20}}$, which in addition to resonances attributable to GBP, shows resonances attributable to the lactam at $\delta = 3.06$ ppm (s) and 3.29 ppm (s), in agreement with literature values.[14] The ratio of GBP to decomposition product released was calculated at 11:1 from integration of the NMR spectrum.

2.2.7 Thermogravimetric analysis

TGA shows only very minor weight loss of the nanohybrids when heated up to 185 °C, indicating there was no appreciable cointercalated water or other solvents, such as ethanol or formamide. Between 185 and 410 °C, weight loss of the nanohybrids can be attributed first to the thermal decomposition of the drug ions, as the carboxyl groups are lost as carbon dioxide and followed by the loss the remaining amide and hydrocarbon species between 190 and 270 °C in the case of GBP, and 185 and 250 °C in the case of PGB, and then to the liberation of nitrate ions as NO_x species between 280 and 410 °C. Between 410 and 600 °C, weight loss is also minimal, as the temperature is not sufficient to calcine the remaining LDH layers into oxide species.

2.2.8 Elemental analysis and drug content

Elemental C, H, N analysis was used to calculate the drug content of the samples and, where possible, compared to values derived experimentally from release studies. Full details of the observed and calculated C, H, N percentages are given in Appendix A.1.

Table 2.2: Drug content, metal ion ratios and formulae of the nanohybrids.

Sample	Drug content (W/W %)	Mg:Al ratio	Formula
MgAl-GBP$_{water,20}$	29.2	1.84	$Mg_{1.94}Al_{1.06}(OH)_6(C_9H_{16}NO_2)_{0.533}(NO_3)_{0.523}$
MgAl-GBP$_{ethanol,20}$	33.4	1.89	$Mg_{1.96}Al_{1.04}(OH)_6(C_9H_{16}NO_2)_{0.621}(NO_3)_{0.417}$
MgAl-GBP$_{ethanol,0}$	33.8	1.83	$Mg_{1.94}Al_{1.06}(OH)_6(C_9H_{16}NO_2)_{0.641}(NO_3)_{0.419}$
MgAl-GBP$_{ethanol,-20}$	34.4	1.79	$Mg_{1.93}Al_{1.08}(OH)_6(C_9H_{16}NO_2)_{0.667}(NO_3)_{0.409}$
MgAl-GBP$_{ethanol,-40}$	33.8	1.86	$Mg_{1.95}Al_{1.05}(OH)_6(C_9H_{16}NO_2)_{0.635}(NO_3)_{0.414}$
MgAl-GBP$_{anhyd,20}$	36.6	1.82	$Mg_{1.94}Al_{1.06}(OH)_6(C_9H_{16}NO_2)_{0.714}(NO_3)_{0.417}$
MgAl-GBP$_{anhyd,-20}$	36.8	1.83	$Mg_{1.94}Al_{1.06}(OH)_6(C_9H_{16}NO_2)_{0.717}(NO_3)_{0.343}$
MgAl-PGB$_{anhyd,20}$	34.4	1.86	$Mg_{1.95}Al_{1.05}(OH)_6(C_8H_{16}NO_2)_{0.692}(NO_3)_{0.357}$
MgAl-PGB$_{anhyd,-20}$	34.7	1.80	$Mg_{1.93}Al_{1.07}(OH)_6(C_8H_{16}NO_2)_{0.715}(NO_3)_{0.357}$

EDX analysis was used to establish the Mg : Al ratio in the nanohybrids, as delamination–restacking procedures typically alter this ratio, due to partial dissolution of metal ions during delamination.[50] Together, these data were used to estimate the overall formulae of the nanohybrids, as can be seen in Table 2.2.

2.2.9 Scanning electron microscopy

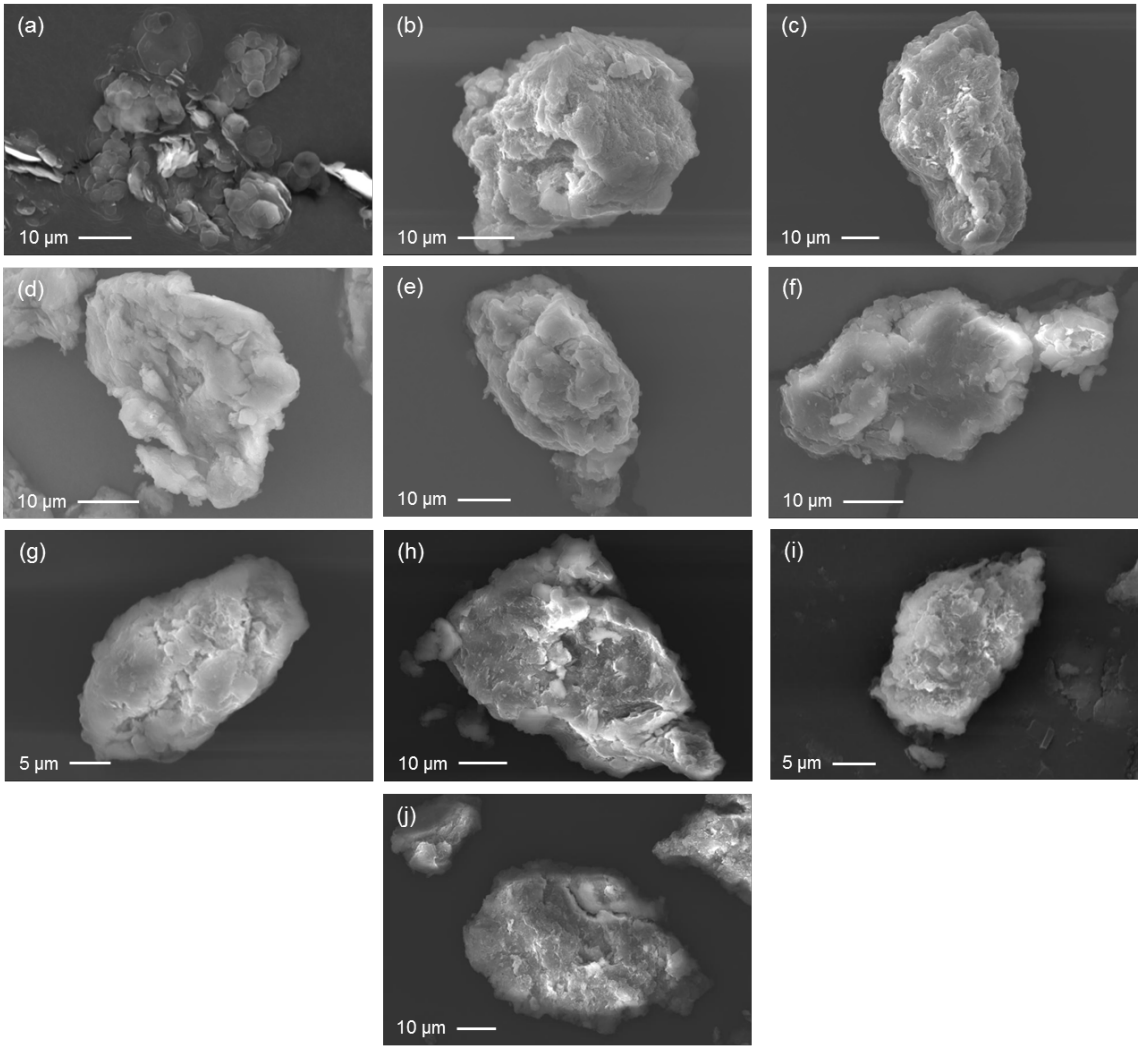


Figure 2.8: SEM images of (a) MgAl-NO_3, (b) MgAl-$GBP_{water,20}$, (c) MgAl-$GBP_{ethanol,20}$, (d) MgAl-$GBP_{ethanol,0}$, (e) MgAl-$GBP_{ethanol,-20}$, (f) MgAl-$GBP_{ethanol,-40}$, (g) MgAl-$GBP_{anhyd,20}$, (h) MgAl-$GBP_{anhyd,-20}$, (i) MgAl-$PGB_{anhyd,20}$ and (j) MgAl-$PGB_{anhyd,-20}$.

SEM images of the nanohybrids, presented in Figure 2.8, show significantly different morphology to the precursor LDH before delamination. The precursor LDH shown

in Figure 2.8(a) exhibits well defined circular-hexagonal platelets with an average diameter of 2 µm, whereas the nanohybrids form larger aggregates composed of rounder, thicker particle shapes with many irregularities caused by the restacking process. All nanohybrids exhibit similar morphologies, independent of the restacking conditions, with average particle diameters of 30 to 40 µm.

2.2.10 Transmission electron microscopy

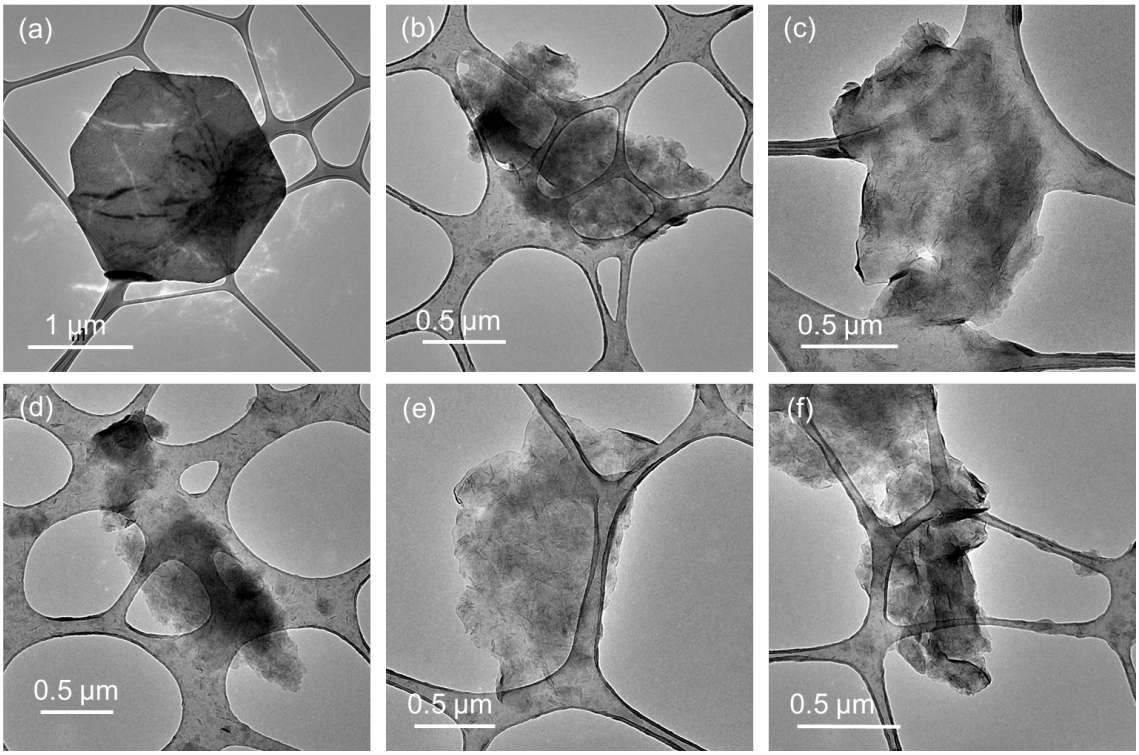


Figure 2.9: TEM images of (a) MgAl-NO_3, (b) MgAl-$GBP_{water,20}$, (c) MgAl-$GBP_{ethanol,20}$, (d) MgAl-$GBP_{anhyd,20}$, (e) MgAl-$GBP_{anhyd,-20}$ and (f) MgAl-$PGB_{anhyd,-20}$.

The morphology of the nanohybrids can be examined further in TEM images, seen in Figure 2.9. Again, the difference between the clearly defined hexagonal precursor particles and the nanohybrids is evident. The TEM images of the nanohybrids still show irregular aggregated particles, but they are much smaller, with average diameters of around 700 nm, as the preparation of the TEM grids facilitates the breakup of the larger aggregates. The images also reveal that the nanohybrids are constituted of much smaller (diameter of 80 – 100 nm), irregularly shaped sheets of

LDH layers, indicating that the large platelets of the precursor are also broken apart into significantly smaller sheets upon delamination.

Some smaller, nonaggregated particles can be seen surrounding the main nanohybrid particles, indicating that the aggregated particles can be readily broken apart into their smaller constituents. The small individual particles, whether they are part of an aggregate particle or separate, resemble flat platelets with both rounded, smooth edges, and straight edges with sharp corners, indicating where they have broken apart from larger sheets during delamination.

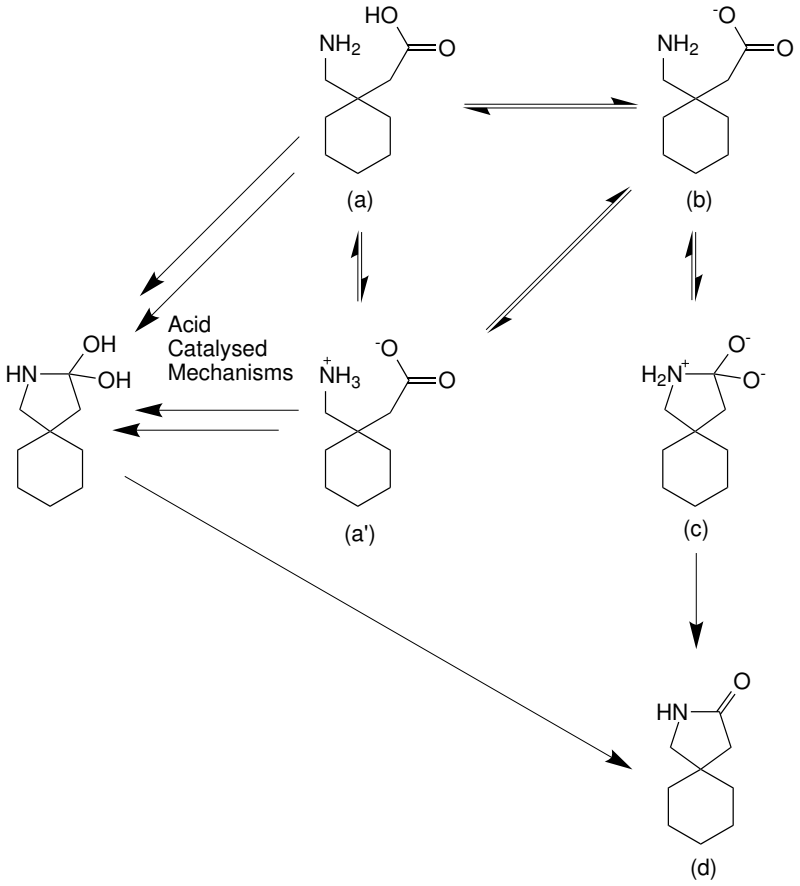
2.3 Effects of restacking conditions

2.3.1 Restacking solvent

It is noted by Wu *et al.* that LDH restacking can be undertaken using either water or ethanol as the restacking solvent.[34] However, where the coassembly method has been used to intercalate new species, only restacking in water has been reported.[27,51] Performing the restacking procedure in both solvents revealed a significant difference in the quality of the resulting samples, with those formed in ethanol showing higher drug loading, greater crystallinity, fewer impurities and more regular morphology than those formed in water. In particular, the absence of reformed MgAl-NO_3 LDH particles in the ethanol restacked samples and absence of lactam decomposition product from these samples upon deintercalation were significant advantages gained from restacking in ethanol compared to water. The reduced solubility of GBP in ethanol compared to water explains the greater drug loading of MgAl-$GBP_{ethanol,20}$ relative to MgAl-$GBP_{water,20}$ (50.5 % as compared to 59.8 % of the theoretical maximum loading), and also the lack of MgAl-NO_3 impurity, as it causes a greater affinity for intercalation of GBP within the LDH layers, rather than remaining in solution, whilst also preferentially causing restacking to occur around the drug ions, rather than the nitrate ions.

The effect of the solvent on the rate of lactamisation of GBP is important, as it is this that leads to the presence of the lactam upon deintercalation of

GBP from MgAl-$GBP_{water,20}$, and its absence upon deintercalation of GBP from MgAl-$GBP_{ethanol,20}$. This is because the rate of lactamisation in water, which is dominated by a base catalysed mechanism at the pH required for the restacking procedure, is sufficiently high to cause partial lactamisation of the GBP, and allow the resulting lactam, or a metastable intermediate, to be cointercalated along with the GBP during restacking, yet this rate is not sufficiently high for lactamasation in ethanol.



Scheme 2.2: The base catalysed mechanism for the decomposition of gabapentin into 2-aza-spiro[4,5]decan-3-one proposed by Zambon *et al.*[14]

An explanation can be provided by examining the base catalysed mechanism of lactamisation of GBP, proposed by Zambon *et al.*[14] and shown in Scheme 2.2. In the basic conditions found during restacking, both the neutral **(a)** and zwitterionic **(a')** forms of GBP are deprotonated to produce the target anion for intercalation, **(b)**. The next step on the decomposition pathway involves nucleophilic attack of the primary amine group on the carbonyl group to produce the polar intermediate,

(c). This intermediate then subsequently breaks down to the final lactam product, **(d)**. The nucleophilic attack and subsequent protonation and abstraction of oxygen progress significantly slower in ethanol than water. This leads to a significant build up of the lactam during the restacking process in water, but not in ethanol, which is reflected in the results from delamination of the two products.

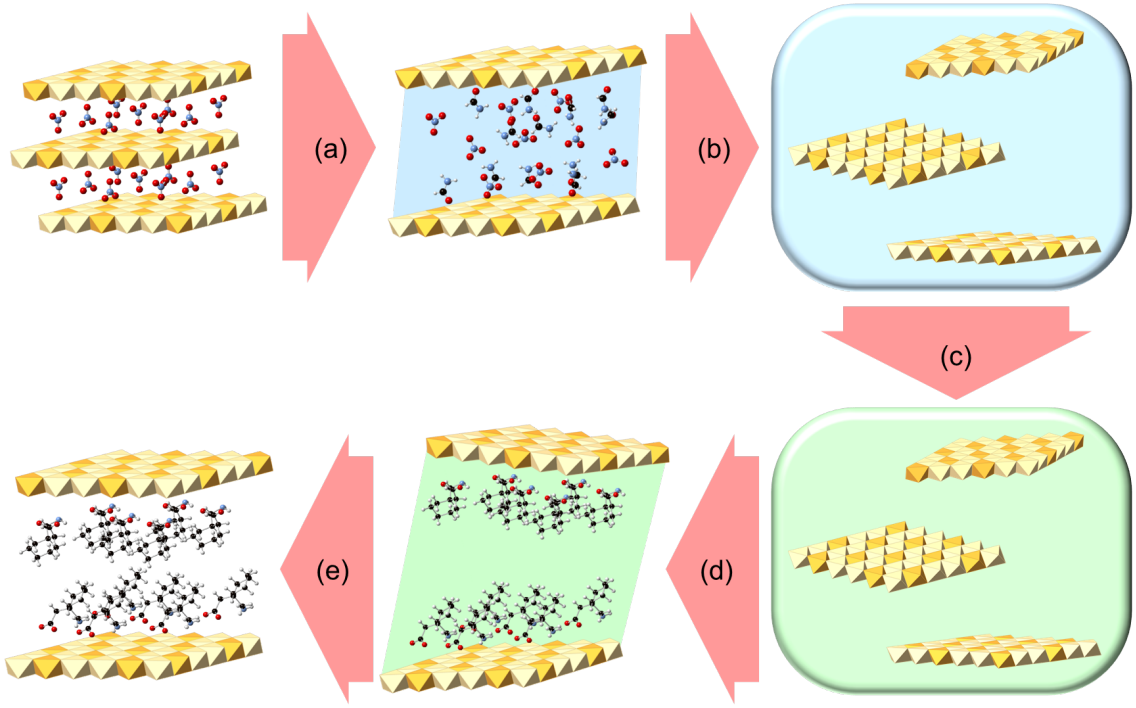
Performing traditional LDH syntheses such as coprecipitation or ion-exchange reactions in nonaqueous solvents or nonaqueous solvent–water mixtures generally produces LDHs that are less crystalline than the analogous products synthesised in water.[52–55] The reasons for doing so are typically to increase the solubility of a poorly water soluble target ion, which would otherwise fail to intercalate, or only partially intercalate with poor loading.[56,57] It is significant then, that in the case of GBP intercalation, the coassembly method of LDH synthesis produces a more crystalline product in ethanol than in water, as indicated by the full width half maximum values of Bragg reflections in the powder XRD patterns of the nanohybrids, as detailed in Table 2.1. The reasons for this unusual difference in crystallinity can be understood by considering the solvent effects present during the restacking procedure, which also allows us to propose a potential mechanism.

2.3.1.1 Restacking mechanism

Prior to restacking, delaminated LDH sheets are well solvated by formamide, due to strong hydrogen bonding and its high polarity ($\varepsilon_r = 111.0$ at 20 °C).[34,58] Upon addition to the restacking solution, the LDH sheets are less well solvated, as the formamide is gradually stripped from the surface of the LDH sheets, due to the negative enthalpy of mixing between it and the restacking solvent. Electrostatic forces between the drug anions and the positively charged sheets lead to a monolayer of the drug ions covering the sheets, further reducing the extent of layers' solvation.

The much lower dielectric constant of the restacking solvent ($\varepsilon_r = 80.4$ for water and $\varepsilon_r = 25.1$ for ethanol at 20 °C)[59] compared to formamide allows attractive forces between the coated LDH sheets to be felt much more strongly, allowing spontaneous restacking to gradually occur as individual sheets aggregate and then contract together in a reversal of the first step of the delamination mechanism reported by Liu

et al.[32] This forces the restacking solvent, along with any residual formamide, out from between the layers, which are now much less hydrophilic at their surfaces, due to the orientation of the bound drug anions. The carboxylate and amine groups of the drug anions face towards the LDH sheets due to electrostatics and hydrogen bonding, leaving the alkyl groups to face outwards, ultimately resulting in the bilayers of drug ions in the interlayer regions observed in powder XRD samples. This proposed mechanism for the restacking process, which results in the formation of nanohybrids, is illustrated in Scheme 2.3.



Scheme 2.3: Schematic of delamination mechanism detailed by Liu *et al.*[32] and the proposed restacking mechanism of LDH sheets into nanohybrids. Delamination of the precursor nitrate LDH occurs in a two step process, upon addition of formamide, (a). Intercalation of formamide molecules causes swelling of the LDH layers, leading to full delamination and solvation of the LDH sheets in the presence of an excess of formamide, (b). Restacking occurs upon addition of the LDH–formamide suspension to the restacking solution, (c). The LDH sheets are much less well solvated in the restacking solution, and electrostatic interactions between the positive sheets and drug anions in the solution lead to monolayers of anions forming on the sheets, (d). Aggregation of the charge neutral, poorly solvated drug covered sheets occurs, expelling solvent molecules from the interlayer region in a reversal of the initial swelling step, (e).

The differences in nanohybrid crystallinity resulting from using water or ethanol as the

restacking solvent can now be explained, based on the above mechanism. Firstly, as ethanol is significantly less polar than water, yet still miscible with formamide, when the delaminated LDH sheets are added to the solvent, they are significantly less well solvated in ethanol than in water. Ethanol forms weaker, and fewer hydrogen bonds with the delaminated sheets than water, although it also displaces the formamide on the surfaces less quickly. GBP is also less well solvated by ethanol than water, as evidenced from its lower solubility.[60] In addition, due to the significantly lower dielectric constant of ethanol, the GBP ions are drawn to the surfaces of the LDH sheets much faster, where they bind with greater energy, due to weaker competing effects from the solvent. Secondly, once the sheets have been bound by drug ions, they aggregate more readily in ethanol, also due to the difference in dielectric constants of the solvents, leading to larger crystalline domains in the nanohybrids. Thirdly, during the aggregation step, when sheets are contracting from a swelled state to their final state, the majority of solvent molecules from between their layers is expelled, whilst some fraction is cointercalated alongside the drug ions. Due to its greater ability to form hydrogen bonds, water is cointercalated to a much greater extent than ethanol. This affects crystallinity directly by leading to greater turbostratic disorder, whilst also providing a more favourable environment for nitrate ions to cointercalate, further contributing to turbostratic disorder, and consequently to the reduced crystallinity seen in MgAl-GBP$_{\text{water}}$ as compared to MgAl-GBP$_{\text{ethanol}}$.

2.3.2 Water presence in restacking

Performing the restacking procedure anhydrously highlights the effect of the presence of water during the restacking procedure. FWHM values in Table 2.1 reveal that samples synthesised anhydrously show still higher crystallinity than those synthesised in ethanol where water was not excluded from the system. In addition, higher drug loading is also seen, as detailed in Table 2.2. When present during the restacking procedure, water preferentially cointercalates within the interlayer region, even when only present in small amounts, causing a much more significant effect than may be expected. As was seen when comparing restacking solvents, cointercalated water facilitates the cointercalation of nitrate ions alongside drug ions. Cointercalation of nitrate ions leads to increased turbostratic disorder, causing the reduced crystallinity

seen in MgAl-GBP$_{ethanol}$ samples relative to analogous MgAl-GBP$_{anhyd}$ samples, and also reduces the weight percentage of drug in the resulting nanohybrids. Due to these effects, anhydrous synthesis presents a significant improvement to the coassembly method, particularly noteworthy when considering that, with the exception of some specific examples, water is an essential reagent in all other LDH synthesis methods: coprecipitation, ion-exchange, hydrothermal, salt–oxide and calcination–rehydration.[53,61,62]

2.3.3 Restacking temperature

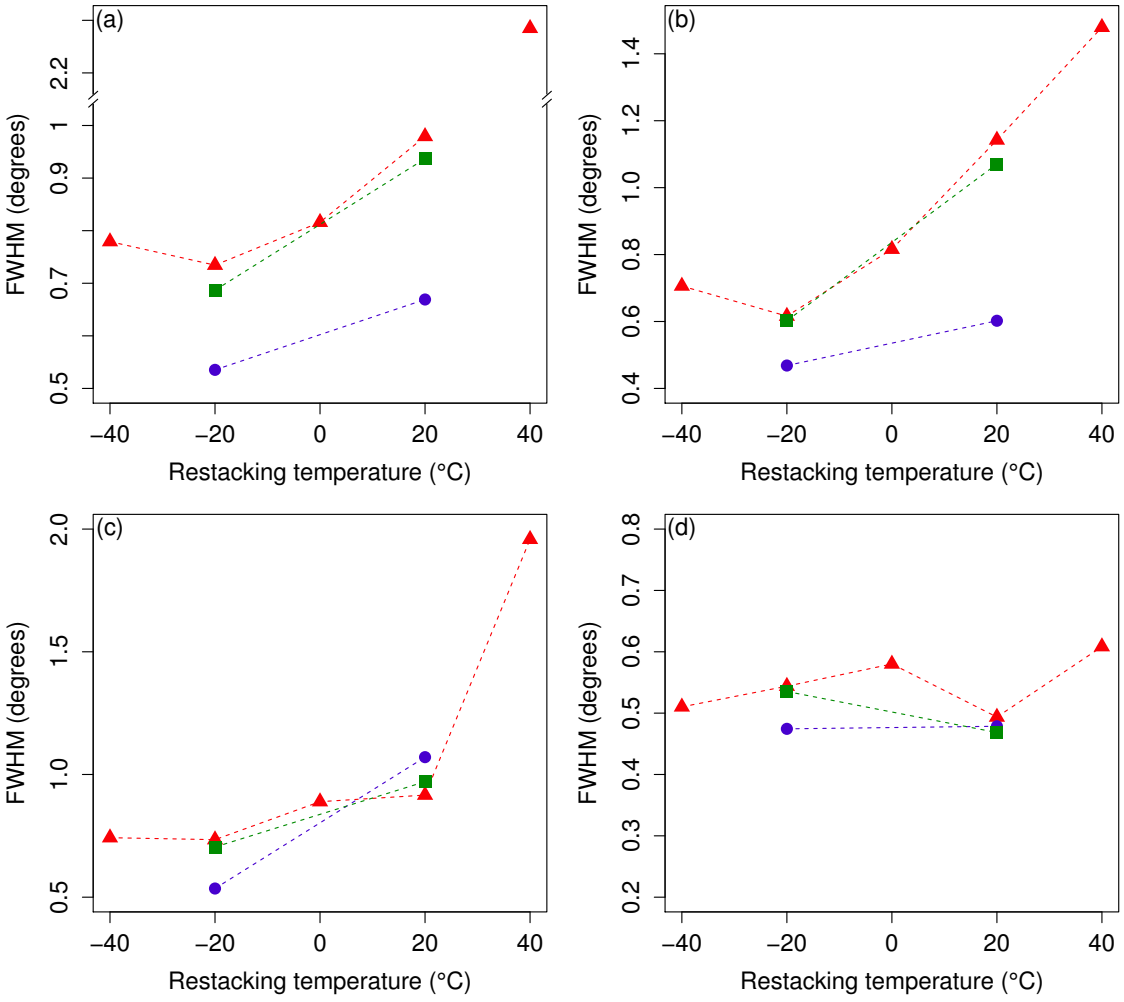


Figure 2.10: FWHM values of the (a) (003), (b) (006), (c) (009) and (d) (110) Bragg reflections in the powder XRD diffraction patterns of MgAl-GBP$_{ethanol}$, ▲, MgAl-GBP$_{anhyd}$, ●, and MgAl-PGB$_{anhyd}$, ■, synthesised at different restacking temperatures.

The effect of temperature on the restacking procedure is also unusual when compared to other synthesis methods of LDHs. Increasing reaction temperature often leads to greater crystallinity in coprecipitation syntheses and higher drug loading in ion-exchange reactions, with some intercalation reactions only proceeding successfully at elevated temperatures.[62–65] Conversely, the quality of samples synthesised through the coassembly method is seen to improve upon reducing reaction temperature during the restacking procedure, with an optimum reaction temperature being reached at −20 °C, positively affecting both crystallinity and drug loading in the resulting samples. The effect of temperature was investigated on three groups of samples, MgAl-GBP$_{\text{ethanol}}$, MgAl-GBP$_{\text{anhyd}}$ and MgAl-PGB$_{\text{anhyd}}$. Attempts to synthesise samples of MgAl-GBP$_{\text{ethanol}}$ at elevated temperatures were unsuccessful. When attempted at 40 °C, restacking yielded only small amounts of nanohybrid, which turned out to be poorly crystalline and with significant MgAl-NO_3 impurity, whilst an attempt at 80 °C yielded a poorly crystalline product that contained no GBP at all, presumably due to decomposition to the lactam during restacking. Using FWHM values as a measure of crystallinity, Figure 2.10 displays the relationship between crystallinity and restacking temperature. Figure 2.11 shows the relationship between drug loading and restacking temperature on the samples studied.

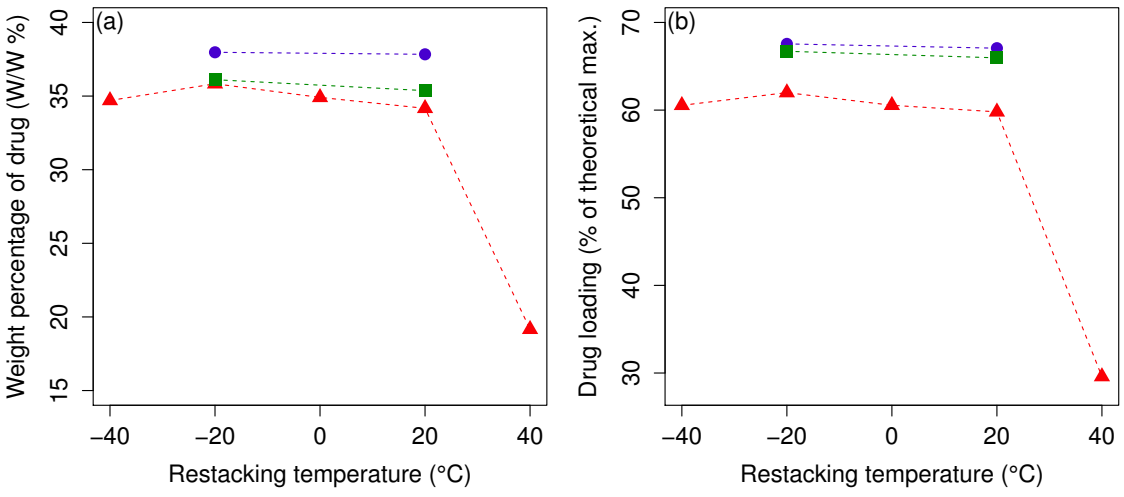


Figure 2.11: The drug loading of MgAl-GBP$_{\text{ethanol}}$, ▲, MgAl-GBP$_{\text{anhyd}}$, ●, and MgAl-PGB$_{\text{anhyd}}$, ■, synthesised at different temperatures, displayed as a function of (a) weight percentage and (b) percentage of the theoretical maximum.

The effect of temperature can be understood with reference to the restacking mecha-

nism proposed previously in Section 2.3.1.1. The dielectric constants of formamide and ethanol increase with falling temperature.[58,59] This has the effect of reducing the strength of the attractive force felt between LDH sheets during the restacking process at lower temperatures, leading to slower restacking, which in turn leads to a lower incidence of defects during restacking and a greater degree of crystallinity in the resulting particles. This is analogous to how slower crystallisation leads to more crystalline particles during a recrystallisation procedure. Secondly, the solubilities of the drug ions decrease with falling temperature. With reduced solubility, there is a greater energetic incentive for the drug anions to bind to the cationic LDH sheets, which results in a greater proportion of drug ions binding to, and subsequently residing between, LDH sheets upon restacking, explaining the increased figures for drug loading.

The improvement in the attributes of the nanohybrids by reducing restacking temperature reaches a maximum at −20 °C, with a further decrease in temperature producing a marginal reduction in the crystallinity and drug loading of the nanohybrids. At temperatures lower than −20 °C, other effects, such as increased viscosity of formamide are expected to exert a greater influence on the restacking procedure, preventing the attributes of the nanohybrids from improving any further.

2.4 Release behaviour

The release behaviour of the highest quality nanohybrid samples was investigated, specifically those with highest drug loading and highest crystallinity according to FWHM values from diffraction patterns. For both drugs, this was the sample synthesised anhydrously at −20 °C. The cumulative release profiles for both samples in each buffer solution at 37 °C are shown in Figure 2.12. In all cases, release profiles typical of LDHs were seen, featuring a rapid initial release controlled primarily by dissolution of drug ions on and close to the surface of the particles, followed by more gradual release controlled by diffusion of drug ions and buffer ions through the interlayer regions of the particles. At all pHs, initial release occurred much faster for the GBP containing nanohybrid, reaching 90 % release within the first 10 to 20 min, whereas release from the PGB containing nanohybrid took 20 to 60 min to reach

90 %.

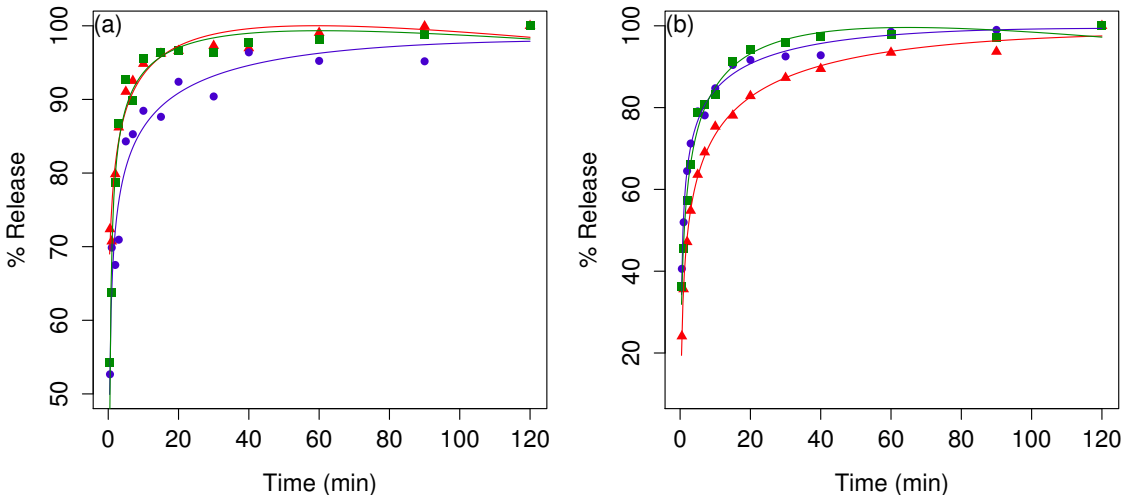


Figure 2.12: *In vitro* release profiles of (a) MgAl-GBP$_{\text{anhyd,-20}}$, and (b) MgAl-PGB$_{\text{anhyd,-20}}$ at 37 °C in pH 2.0 sulphate buffer, ▲, pH 4.0 phosphate buffer, ●, and pH 7.0 phosphate buffer, ■.

The relationship between buffer pH and rate of release is not common to both nanohybrids, with release of GBP occurring the slowest in the pH 4.0 buffer whilst the slowest release of PGB occurred in pH 2.0 buffer. In both cases, however, the fastest release was seen in pH 7.0 buffer. The complexity of this relationship can be attributed to the fact that release rate is dependent both on the solvation of the ion being intercalated, the ion being deintercalated, the relationship between the two during interlayer diffusion, and also, when considering release into acidic solution, the extent to which dissolution of the LDH particles occurs.

2.4.1 Kinetic analysis

Five kinetic models most frequently associated with release from LDHs were fitted to the release data and evaluated using a least squares regression. The models chosen were Avrami–Erofe'ev, Elovich, simple first order, modified Freunlich and parabolic diffusion, as these have all found use is different LDH systems.[66–73] Of these, the Avrami–Erofe'ev model is most commonly used; it is based on a two-step system of proliferation of nucleation sites, followed by growth of these sites. The correlation coefficients, r^2, of each fitting are displayed in Table 2.3. In most cases,

the Avrami–Erofe'ev model was found to be the best fit for the data, with the only exception being release of GBP at pH 7.0, which shows a particularly close fit for the modified Freundlich model. Despite this anomaly, the data for this series also show a close fit to the Avrami-Erofe'ev model, and so as the Avrami-Erofe'ev model fits the data more consistently, it can be taken to be the best model for evaluating the kinetics of drug release from the nanohybrids.

Table 2.3: Evaluation of different kinetic models of release using correlation coefficients, r^2. Highlighted figure indicates closest fit for each release profile.

Sample	Buffer pH	Model correlation coefficient, r^2				
		Avrami–Erofe'ev	Elovich	Simple first order	Modified Freundlich	Parabolic diffusion
MgAl-GBP$_{\text{anhyd,-20}}$	pH 2.0	0.941	0.874	0.360	0.777	0.881
	pH 4.0	0.927	0.900	0.397	0.917	0.829
	pH 7.0	0.919	0.788	0.250	0.972	0.821
MgAl-PGB$_{\text{anhyd,-20}}$	pH 2.0	0.982	0.976	0.403	0.960	0.868
	pH 4.0	0.979	0.937	0.376	0.873	0.848
	pH 7.0	0.971	0.916	0.339	0.944	0.862

As the Avrami–Erofe'ev model is a good fit to all the sets of data, it can be used to extract both the rate constant, k_r, and the reaction exponent, n, as can be seen in Table 2.4. These figures give some insight into the mechanistic behaviour of the drug release. It is notable that the rate constants do not vary greatly across the different pHs, although marginally higher rate constants can be seem for release in the pH 7 buffer. The reaction exponent is more revealing, however, as the this value can be used as a measure for whether the release is diffusion controlled or phase boundary controlled, i.e. dissolution controlled. For release from two dimensional, layered matrices, such as LDHs, if $n < 0.5$, it implies a purely diffusion controlled mechanism, whereas if $0.5 < n < 1$, the release proceeds from specific nucleation sites and their subsequent growth, rather than purely diffusion. In almost all cases, $n < 0.5$, and so it can be gleaned that the mechanism in these cases is diffusion controlled, although in release from MgAl-PGB$_{\text{anhyd,-20}}$ at pH 7 $n > 0.5$, indicating that the release mechanism may also proceed via nucleation sites and subsequent growth.[65,74]

Table 2.4: Values of the rate constants, k_r, and reaction exponents, n, for the release of GBP and PGB in buffers of varying pH, as determined by the Avrami–Erofe'ev model.

Sample	Buffer pH	Rate constant, $k_r \times 10^{-3}$ (s^{-1})	Reaction exponent, n
MgAl-$GBP_{anhyd,-20}$	2.0	0.129	0.326
	4.0	0.127	0.037
	7.0	0.159	0.193
MgAl-$PGB_{anhyd,-20}$	2.0	0.099	0.788
	4.0	0.096	0.292
	7.0	0.128	0.410

2.5 Effect on drug stability

Intercalation of a guest species into an LDH host can confer increased stability onto the guest species, both through electrostatic interactions between the guest and host layers, and through restriction of the guest species in the interlayer region. However, in other instances these same effects, or others, such as the specific local environment on the surface of the LDH layers, can lead to increased reactivity of guest species, a feature utilised by the application of LDHs in catalysis. There is no record in the literature of the effect of LDH layers on the stability of GABA or its derivatives, so it was unknown whether the act of intercalation would stabilise or destabilise the guest ions.[75–77] Previous attempts to stabilise GBP and the similar drug baclofen using cyclodextrin failed due to resulting conformational restriction.[16] The anionic form of GBP has been shown to be the most reactive with respect to decomposition, which must also be taken into consideration.[14] However, it was hoped that the stabilising influence of the electrostatic interactions would outweigh any increase in reactivity caused by conformational restriction within the LDH layers, on conversion into the anionic forms of the drugs.

2.5.1 Stability studies

Aqueous stability studies were performed on MgAl-$GBP_{anhyd,-20}$ and MgAl-$PGB_{anhyd,-20}$ by suspending the samples in deionised water, at both room temperature and 80 °C. For comparison, the pristine drugs were dissolved in deionised water under the same

conditions. The samples were stirred gently during the course of the studies and aliquots were taken a predetermined intervals for analysis for the drug concentration.

The rate of decomposition of both GBP and PGB in aqueous solution fits a pseudo first-order rate equation, with the cyclisation rate constant, k_{obs}, providing a means of direct comparison of different conditions. As decomposition of these species occurs slowly at room temperature, decomposition studies were performed at 80 °C, as well as at room temperature. As with the release studies, the nanohybrids which showed the highest drug loading and crystallinity were chosen for decomposition studies, those synthesised anhydrously at −20 °C. Plots detailing the change in concentration of the drug ions, [drug], over time during the stability studies can be found in Appendix A.2. Values of k_{obs} were obtained by taking the gradient of plots of ln[drug] expressed as a function of time, t, from the start of the decomposition experiment, as shown in the example in Figure 2.13.

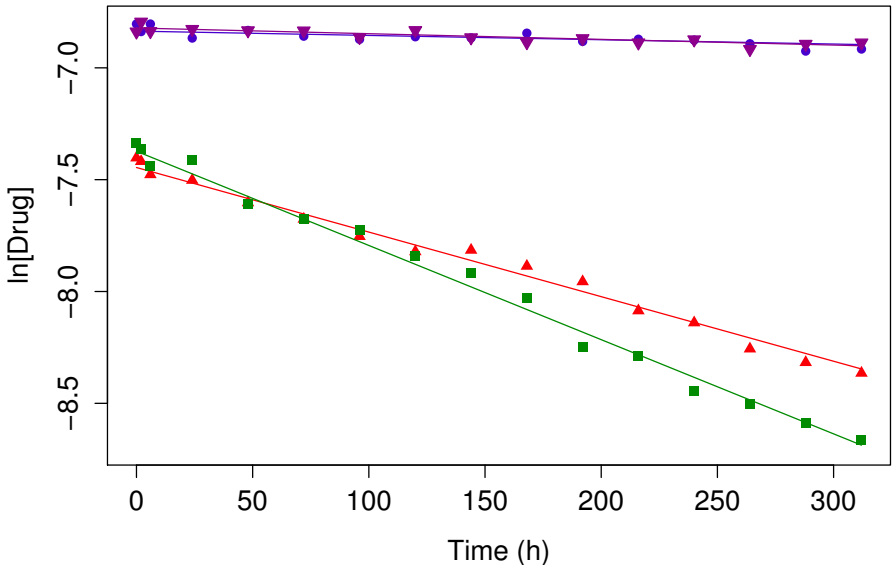


Figure 2.13: The natural logarithm of drug concentration as a function of time during the decomposition studies, from which the cyclisation constant, k_{obs}, can be calculated. These studies were carried out at 80 °C, the samples are pristine GBP, ▲, MgAl-GBP$_{anhyd,-20}$, ●, pristine PGB, ■, and MgAl-PGB$_{anhyd,-20}$ ▼.

The cyclisation rate constants are detailed in Table 2.5 and show that decomposition of both drugs is significantly retarded through intercalation into LDHs, both at ambient and elevated temperatures. At 80 °C, decomposition of the pristine drugs in solution was significant over a two week period, whereas decomposition of the drugs

within the intercalation compounds was only just measurable within experimental error, the cyclisation rate constant being reduced by a factor of 15.0 in the case of GBP, and 16.6 in the case of PGB. Similarly, at 20 °C measurable decomposition of the pristine drugs occurred within a four week period, whereas decomposition of the drugs within the nanohybrids was not sufficiently significant to be measurable.

Table 2.5: Drug cyclisation rate constants for the pristine drugs and nanohybrids. *Decomposition over the course of a four week period was too slow to calculate the cyclisation constant accurately, within experimental error.

Sample	Cyclisation rate constant, $k_{obs} \times 10^8$ (s^{-1})	
	at 20 °C	at 80 °C
Pristine GBP	13.9	80.2
MgAl-$GBP_{anhyd,-20}$	< 1*	5.34
Pristine PGB	17.9	117
MgAl-$PGB_{anhyd,-20}$	< 1*	7.06

2.5.1.1 NMR spectroscopy decomposition studies

The NMR decomposition studies confirmed that, at 80 °C, the sole decomposition products from the nanohybrids were the lactam analogues of the drugs within the respective nanohybrids. At 20 °C, even after four weeks, decomposition was insufficient to be detectable through NMR. All spectra were consistent with those of NMR dissolution experiments, showing resonances relating to the drug ions, with the addition of small resonances at 3.06 ppm (s) and 3.29 ppm (s) corresponding to the lactam analogue of GBP, or at 0.79 ppm (t) corresponding to the lactam analogue of PGB in samples that had been heated at 80 °C. In addition, upon integration of the resonances, the ratios between the drug ions and the lactam analogues were in good agreement with those predicted from the cyclisation rate constants, seen in Table 2.6, once solvent kinetic isotope effects (SKIE) had been taken into account, and assuming NMR experiments were conducted with 40 mg nanohybrid in 1 mL D_2O. The SKIE value calculated by Zambon *et al.* for lactamisation of GBP at pH 7.16 was used for predictions using both drugs (SKIE = $k_H/k_D = 6.9$), owing to the lack of solvent kinetic isotope effect values for the lactamisation of PGB.[14]

Table 2.6: The ratio of drug ions to lactam analogues that remain in the nanohybrids after heating at 80 °C in D_2O for four weeks, derived experimentally from integration of NMR spectra and predicted from cyclisation rate constants.

Sample	Drug : Lactam ratio	
	Experimental (from NMR)	Predicted (from k_{obs})
$MgAl\text{-}GBP_{anhyd,\text{-}20}$	50	52.8
$MgAl\text{-}PGB_{anhyd,\text{-}20}$	46	44.8

2.6 Future work

Experiments to investigate the LDH restacking mechanism *in situ* would be an insightful continuation of this work, but have not been included in this thesis due to time constraints. However, this work is ongoing and *in situ* EDXRD investigations into the LDH restacking mechanism under different experimental conditions are scheduled to take place on the Joint Engineering, Environmental and Processing Beamline I12 (JEEP) at Diamond Light Source in summer 2016.

2.7 Conclusion

Gabapentin and pregabalin were successfully intercalated into a MgAl-NO_3 LDH through a delamination–restacking method, resulting in LDH–drug nanohybrids with maximum drug loading percentages of 37 and 35 % by weight. The parameters of the restacking process were found to have a significant effect on the drug loading, crystallinity and purity of the nanohybrids, with restacking in anhydrous conditions in ethanol at −20 °C found to maximise all three properties in the resulting nanohybrids. To explain the effects of varying restacking parameter, a possible mechanism for the restacking process was proposed. The drug release profiles of the nanohybrids were measures in biomimetic buffers and found to fit the Avrami–Erofe'ev model for release most closely. The stability of the drugs was found to be significantly increased by intercalation into the nanohybrids, with intercalation reducing the cyclisation rate constant of gabapentin by a factor of 15.0, and that of pregabalin by a factor of 16.6. The improved delamination–restacking method resulted in nanohybrids of sufficient quality and stability to be usable in pharmaceutical suspensions and other

wet formulations.

2.8 References

(1) Goa, K.; Sorkin, E. English *Drugs* **1993**, *46*, 409–427.
(2) Benkert, O.; Hippius, H., *Kompendium Der Psychiatrischen Pharmakotherapie*; Springer: 2007.
(3) Attal, N.; Cruccu, G.; Haanpää, M.; Hansson, P.; Jensen, T. S.; Nurmikko, T.; Sampaio, C.; Sindrup, S.; Wiffen, P. *Eur. J. Neurol.* **2006**, *13*, 1153–1169.
(4) Happe, S.; Sauter, C.; Klösch, G.; Saletu, B.; Zeitlhofer, J. *Neuropsychobiology* **2003**, *48*, 82–86.
(5) Sobel, S. V., *Successful Psychopharmacology: Evidence-Based Treatment Solutions for Achieving Remission*; W. W. Norton: 2012.
(6) Zour, E.; Lodhi, S.; Nesbitt, R.; Silbering, S.; Chaturvedi, P. English *Pharm. Res.* **1992**, *9*, 595–600.
(7) Nahata, M. C. *Pediatr. Neurol.* **1999**, *20*, 195–197.
(8) Meyer-Wonnay, H. R.; Schneider, M. D. Pregabalin composition. EP 1543831 A1., 2005.
(9) Aomatsu, A. Stabilized pharmaceutical preparations of gamma-aminobutyric acid derivatives and process for preparing the same. WO 1999059573 A1., 1999.
(10) Gordi, T.; Hou, E.; Kasichayanula, S.; Berner, B. *Clin. Ther.* **2008**, *30*, 909–916.
(11) Wallace, M. S.; Irving, G.; Cowles, V. E. *Clin. Drug Investig.* **2010**, *30*, 765–776.
(12) Kavoussi, R. *Eur. Neuropsychopharmacol.* **2006**, *16*, 128–133.
(13) Sharma, V.; Sharma, S.; Khokra, S. L.; Sahu, R. K.; Jangde, R.; Singh, J. *Der Pharm. Lett.* **2011**, *3*, 326–333.
(14) Zambon, E.; Giovanetti, R.; Cotarca, L.; Pasquato, L. *Tetrahedron* **2008**, *64*, 6739–6743.
(15) Kearney, A.; Mehta, S.; Radebaugh, G. *Int. J. Pharm.* **1992**, *78*, 25–34.
(16) Cutrignelli, A.; Denora, N.; Lopedota, A.; Trapani, A.; Laquintana, V.; Latrofa, A.; Trapani, G.; Liso, G. *Int. J. Pharm.* **2007**, *332*, 98–106.
(17) Potschka, H.; Feuerstein, T. J.; Löscher, W. English *Naunyn. Schmiedebergs. Arch. Pharmacol.* **2000**, *361*, 200–205.
(18) Augart, H.; Gebhardt, U.; Herrmann, W. Hydrolysis of gabapentin or the lactam to form acid addition salt, conversion to pure compound by ion exchanging; antiepileptic agents. US 6054482., 2000.
(19) Choy, J.-H.; Park, T.; Kim, S.-T.; Son, Y.-H. Pharmaceutical composition for the treatment of cancer comprising LMH-RA complex. WO 2006091009 A1., 2006.
(20) Ryu, S.-J.; Jung, H.; Oh, J.-M.; Lee, J.-K.; Choy, J.-H. *J. Phys. Chem. Solids* **2010**, *71*, 685–688.
(21) Wang, Y.; Wu, P.; Hou, Y.; Zhu, N.; Dang, Z. *Ind. Eng. Chem. Res.* **2012**, *51*, 11128–11136.
(22) Thompson, C.; Bravo, C. M. L.; O'Hare, D. Layered double hydroxides. WO 2014053822 A1., 2014.
(23) Chen, C.; Han, C.-H.; Sweeney, M.; Cowles, V. E. *J. Pharm. Sci.* **2013**, *102*, 1155–1164.
(24) Wu, Q.; Sjastad, A. O.; Vistad, O. B.; Knudsen, K. D.; Roots, J.; Pedersen, J. S.; Norby, P. *J. Mater. Chem.* **2007**, *17*, 965–971.
(25) Hansen, E. W.; Norby, P.; Roots, J.; Wu, Q. *J. Phys. Chem. C* **2007**, *111*, 11854–11861.
(26) Vial, S.; Prevot, V.; Leroux, F.; Forano, C. *Microporous Mesoporous Mater.* **2008**, *107*, 190–201.
(27) Huang, G.; Ma, S.; Zhao, X.; Yang, X.; Ooi, K. *Chem. Commun.* **2009**, *1*, 331–333.
(28) Zhang, Y.; Song, M.; Yun, R.; Meng, Q.; Yan, D. *Chinese J. Chem.* **2014**, *32*, 859–864.
(29) Shuang, W.; Xiaowen, W.; Haiping, L.; Renjie, Z.; Wanguo, H. *Chem. J. Chinese Univ. - Chinese* **2014**, *35*, 1982–1987.
(30) Hibino, T.; Jones, W. *J. Mater. Chem.* **2001**, *11*, 1321–1323.
(31) Hibino, T. *Chem. Mater.* **2004**, *16*, 5482–5488.
(32) Liu, Z.; Ma, R.; Osada, M.; Iyi, N.; Ebina, Y.; Takada, K.; Sasaki, T. *J. Am. Chem. Soc.* **2006**, *128*, 4872–4880.

(33) Ma, R.; Liu, Z.; Li, L.; Iyi, N.; Sasaki, T. *J. Mater. Chem.* **2006**, *16*, 3809–3813.
(34) Wu, Q.; Olafsen, A.; Vistad, O. B.; Roots, J.; Norby, P. *J. Mater. Chem.* **2005**, *15*, 4695–4700.
(35) Allmann, R. *Chimica* **1970**, 99–108.
(36) Ibers, J. *Acta Crystallogr. Sect. C* **2001**, *57*, 641–643.
(37) Venu, N.; Vishweshwar, P.; Ram, T.; Surya, D.; Apurba, B. *Acta Crystallogr. Sect. C* **2007**, *63*, 306–308.
(38) Ogawa, M.; Asai, S. *Chem. Mater.* **2000**, *12*, 3253–3255.
(39) Khan, A. I.; Lei, L.; Norquist, A. J.; O'Hare, D. *Chem. Commun.* **2001**, *22*, 2342–2343.
(40) Zong, Z.; Desai, S.; Kaushal, A.; Barich, D.; Huang, H.-S.; Munson, E.; Suryanarayanan, R.; Kirsch, L. English *AAPS PharmSciTech* **2011**, *12*, 924–931.
(41) Hsu, C.-H.; Ke, W.-T.; Lin, S.-Y. *J. Pharm. Pharm. Sci.* **2010**, *13*, 67–77.
(42) Choknud, S.; Saisa-ard, O.; Haller, K. J. *Eng. J.* **2012**, *16*, 29–36.
(43) Khanduri, C.; Jayachandra, S.; Shah, J. Polymorphic form i of pregabalin and processes for its preparation. US 20060270871., 2006.
(44) Devcic, M.; Zegarac, M. New polymorphic forms of pregabalin., 2008.
(45) Harikrishnan, S.; Bhoopathy, T. J. *Chem. Sci. Trans.* **2014**, *3*, 624–633.
(46) Hsu, C.-H.; Lin, S.-Y. *Thermochim. Acta* **2009**, *486*, 5–10.
(47) Dempah, K. E.; Barich, D. H.; Kaushal, A. M.; Zong, Z.; Desai, S. D.; Suryanarayanan, R.; Kirsch, L.; Munson, E. J. *AAPS PharmSciTech* **2013**, *14*, 19–28.
(48) Conterosito, E.; Croce, G.; Palin, L.; Pagano, C.; Perioli, L.; Viterbo, D.; Boccaleri, E.; Paul, G.; Milanesio, M. *Phys. Chem. Chem. Phys.* **2013**, *15*, 13418–13433.
(49) Chimatadar, S. A.; Basavaraj, T.; Thabaj, K. A.; Nandibewoor, S. T. *J. Mol. Catal. A Chem.* **2007**, *267*, 65–71.
(50) Li, L.; Ma, R.; Ebina, Y.; Iyi, N.; Sasaki, T. *Chem. Mater.* **2005**, *17*, 4386–4391.
(51) Wu, X.; Li, H.; Song, S.; Zhang, R.; Hou, W. *Int. J. Pharm.* **2013**, *454*, 453–61.
(52) Malherbe, F.; Forano, C.; Besse, J.-P. *Microporous Mater.* **1997**, *10*, 67–84.
(53) Gardner, E.; Huntoon, K. M.; Pinnavaia, T. J. *Adv. Mater.* **2001**, *13*, 1263–1266.
(54) Chang, Z.; Evans, D. G.; Duan, X.; Vial, C.; Ghanbaja, J.; Prevot, V.; de Roy, M.; Forano, C. *J. Solid State Chem.* **2005**, *178*, 2766–2777.
(55) Gunawan, P.; Xu, R. *J. Mater. Chem.* **2008**, *18*, 2112–2120.
(56) Ayala-Luis, K. B.; Koch, C. B.; Hansen, H. C. B. *Appl. Clay Sci.* **2010**, *48*, 334–341.
(57) Gerds, N.; Katiyar, V.; Koch, C. B.; Risbo, J.; Plackett, D.; Hansen, H. C. B. *Appl. Clay Sci.* **2012**, *65–66*, 143–151.
(58) Dunn, L. A.; Stokes, R. H. *Trans. Faraday Soc.* **1969**, *65*, 2906–2912.
(59) Wyman, J. *J. Am. Chem. Soc.* **1931**, *53*, 3292–3301.
(60) Divi, M. K. P.; Padakandla, G. R.; Rao, M. A. N.; Nowshuddin, S.; Prasad, M. Process for the preparation of gabapentin. US 20110306787., 2011.
(61) Carlino, S. *Solid State Ionics* **1997**, *98*, 73–84.
(62) He, J.; Wei, M.; Li, B.; Kang, Y.; Evans, D. G.; Duan, X., *Preparation of Layered Double Hydroxides*; Structure and Bonding, Vol. 119; Springer-Verlag: 2006, pp 89–119.
(63) Gunawan, P.; Xu, R. *J. Pharm. Sci.* **2008**, *97*, 4367–4378.
(64) Kuehn, T.; Poellmann, H. *Clays Clay Miner.* **2010**, *58*, 596–605.
(65) Markland, C. Novel Apects of Layered Double Hydroxide Chemistry., D.Phil Thesis, University of Oxford, 2011.
(66) Avrami, M. *J. Chem. Phys.* **1939**, *7*, 1103–1112.
(67) Avrami, M. *J. Chem. Phys.* **1940**, *8*, 212–224.
(68) Avrami, M. *J. Chem. Phys.* **1941**, *9*, 177–184.
(69) Hancock, J. D.; Sharp, J. H. *J. Am. Ceram. Soc.* **1972**, *55*, 74–77.
(70) Li, Z. *Langmuir* **1999**, *15*, 6438–6445.
(71) Kodama, T.; Harada, Y.; Ueda, M.; Shimizu, K.; Shuto, K.; Komarneni, S. *Langmuir* **2001**, *17*, 4881–4886.

(72) Yang, J.-H.; Han, Y.-S.; Park, M.; Park, T.; Hwang, S.-J.; Choy, J.-H. *Chem. Mater.* **2007**, *19*, 2679–2685.
(73) Markland, C.; Williams, G. R.; O'Hare, D. *J. Mater. Chem.* **2011**, *21*, 17896–17903.
(74) Williams, G. Cation-Ordered Layered Double Hydroxides: Formation Mechanisms, New Materials, and Intercalation Chemistry., D.Phil, DPhil Thesis, Oxford University, 2005.
(75) Aisawa, S.; Kudo, H.; Hoshi, T.; Takahashi, S.; Hirahara, H.; Umetsu, Y.; Narita, E. *J. Solid State Chem.* **2004**, *177*, 3987–3994.
(76) Phan, T.-A. T. Novel host-guest systems for ultrasound-mediated drug delivery., Ph.D. Thesis, Ann Arbor, 2007, p 180.
(77) Yoshitake, S.; Suzuki, T.; Miyashita, Y.; Aoki, D.; Teramoto, Y.; Nishio, Y. *Carbohydr. Polym.* **2013**, *93*, 331–338.

3. Studies on the stability of catecholamine drugs intercalated into layered double hydroxides

3.1 Introduction

Catecholamines are organic species containing both catechol (1,2-benzenediol) and amine functional groups, and joined by an ethylene bridge, the most simple example being the neurotransmitter dopamine. The catecholamine motif can be found in neurotransmitters (dopamine, norepinephrine, epinephrine), biological intermediates and metabolites (levodopa, α-methylnorepinephrine), and pharmaceutical drugs (carbidopa, methyldopa, entacapone), as seen in Figure 3.1.

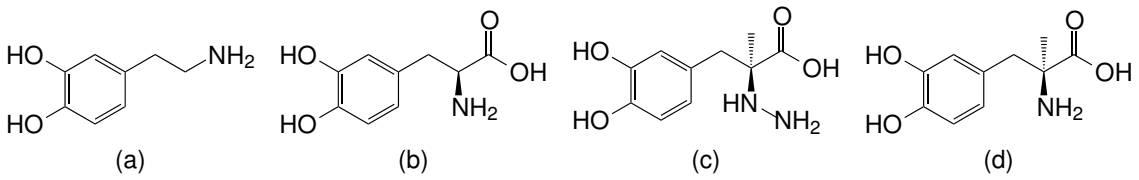
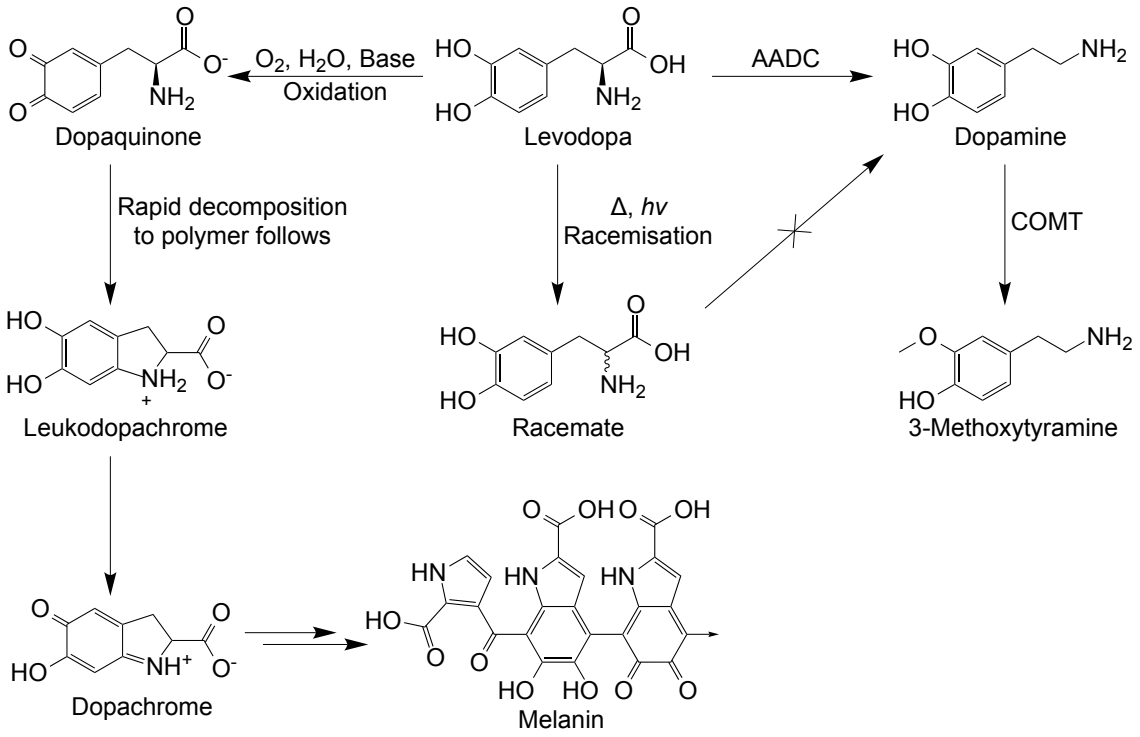


Figure 3.1: The structures of the catecholamine species (a) dopamine, (b) levodopa, (c) carbidopa and (d) methyldopa.

As with catechol itself and other compounds containing the catechol substructure, catecholamines are unstable in atmospheric conditions, degrading via oxidative decomposition first to benzoquinone analogues, and then on to melanin-type species through complex polymerisation reactions described by the Raper–Mason scheme of melanogenesis.[1] *In vivo*, catecholamines can also be metabolised by catechol-O-methyl transferase (COMT) enzymes, or undergo other transformations, such as the decarboxylation of levodopa to dopamine by aromatic L-amino acid decarboxylase

(AADC) enzymes.[2] In addition, chiral species such as levodopa may undergo racemisation to biologically inactive isomers when exposed to heat or ultraviolet radiation.[3] These various decomposition pathways are illustrated in Scheme 3.1.



Scheme 3.1: Major decomposition routes of levodopa *in vivo* and in atmospheric conditions.

3.1.1 Catecholamine drugs

Since its discovery for the treatment of parkinsonism in 1967 by Cotzias *et al.* the catecholamine drug levodopa (L-DOPA) has become and remains the most common and most effective treatment for parkinsonism in the world.[4–7] Despite its widespread use for nearly half a century, the development of varied formulations for the effective delivery of levodopa and other catecholamine drugs remains problematic, due to their high susceptibility to oxidative decomposition in solution.[2,8,9] However, due to their unique ability in the treatment of parkinsonism, there is a significant need to develop solution-based formulations of such drugs, as the dysphagia typically experienced by patients suffering from parkinsonism can make swallowing these drugs in tablet form uncomfortable, dangerous or impossible.[10,11]

In addition, the rapid absorption and metabolism of levodopa has made controlled release formulations of the drug the preferred option for many patients, as significant negative symptoms can recur as soon as the *in vivo* concentration of levodopa falls below the therapeutic window.[12,13] Therefore, developing a solution-based formulation, which also exhibits controlled release properties is desirable. This raises additional challenges, as it has been shown that solution phase preparations of levodopa (prepared immediately prior to ingestion, before significant decomposition can occur) are absorbed and metabolised faster than unmodified solid tablets.[14] Formulations of levodopa have been created in attempts to address issues of dysphagia and levodopa's short acting duration, such as oral disintegrating tablets, implantable controlled release matrices and duodenal infusions, yet all have had other drawbacks, such as the need for frequent redosing or an invasive method of administration, which have prevented them from being widely applicable solutions.[15,16]

Endogenous levodopa is synthesised by the body as a biological precursor to the neurotransmitter dopamine. The pharmacological action of exogenous levodopa results from boosting concentrations of levodopa within the brain, which in turn increases neural dopamine levels, counteracting the effect of reduced numbers of dopamine receptors seen in patients with parkinsonism. This effect cannot be achieved through direct administration of dopamine itself, as its increased hydrophobicity means it is unable to cross the blood-brain barrier.[13]

Carbidopa (C-DOPA) is another catecholamine drug, routinely administered alongside levodopa, which acts as a peripheral AADC inhibitor, as it cannot cross the blood-brain barrier. This prevents peripheral metabolism of levodopa, reducing unwanted side effects caused from synthesis of peripheral dopamine, such as nausea and hypotension, and also increases the concentration and duration of levodopa within the brain, allowing smaller doses of levodopa to be used.[17,18] As with levodopa, carbidopa is unstable with respect to base catalysed oxidation, and has a shorter half-life than levodopa in solution in equivalent conditions. Decomposition of carbidopa can also result in the production of hydrazine, which is highly toxic and carcinogenic, further emphasising the need for formulations to be stable.[14] Carbidopa is also chiral, but is much less susceptible to racemisation than levodopa, due to increased bulk around its chiral centre, leading to a prohibitively high activation

energy of conversion. Consequently, it is only oxidative decomposition which is of concern when considering the stability of carbidopa.

The third catecholamine drug being considered in this chapter is methyldopa (M-DOPA), which acts as a competitive peripheral AADC inhibitor, and is used in the treatment of hypertension, particularly gestational hypertension, and pre-eclampsia, caused by excess amounts of peripheral dopamine, norepinephrine and epinephrine.[19] Its pharmacological action is due both to its inhibition of peripheral AADC, and also to the action of its major metabolite, α-methylnorepinephrine, which acts as an agonist of presynaptic central nervous system α_2-adrenergic receptors, resulting in reduced sympathetic nervous system output and lower blood pressure.[20]

Methyldopa is not used in the same context as carbidopa, as an adjunct to levodopa therapy for parkinsonism. It is, however, used in preference to other antihypertensives when treating pregnant women, due to its higher foetal safety profile, and in treating diabetics and renal failure patients, who require multidrug therapies.[20,21] As with carbidopa, it is susceptible to oxidative decomposition, but not to racemisation. Methyldopa is not as widely used as levodopa and carbidopa, although there may be interest in liquid formulations of methyldopa for those that suffer gestational nausea or difficulty swallowing tablets. From a chemical perspective, it is useful to consider methyldopa alongside carbidopa and levodopa, as it is the structural intermediary analogue between these two drugs, possessing the β-methyl group of carbidopa, yet instead of the hydrazino group, it possesses the amino group of levodopa.

3.1.2 Attempts to stabilise catecholamine drugs

There have been previous attempts to stabilise levodopa and levodopa/carbidopa formulations. Stabilisation of liquid formulations has mainly been achieved through using an acid buffer, such as ascorbic acid or citric acid, alongside other buffers and chelating agents such as EDTA. Such formulations show a reduced the rate of oxidative decomposition, but not to an extent where they could be applicable for anything beyond short-term storage of levodopa/carbidopa.[8,14] Solid formulations, such as encapsulation in enteric coatings or other controlled release matrices, remain sufficiently stable, provided they are kept in dry environments and not exposed to

extremes of heat and light.[22,23]

Intercalation of levodopa into inorganic silica and phyllosilicate matrices has been investigated by Jaber *et al.*, with the aim of creating controlled release formulations of levodopa.[24] The matrices were all found to be unsuitable for levodopa storage and release, the specific chemistry of the different phyllosilicates and silica leading to different reasons for failure in all cases. The mildly acidic nature of the silica prevented the intercalation of levodopa internally, whilst both the smectites investigated, laponite and saponite, catalysed the decomposition of levodopa upon successful intercalation, due to the weakly basic nature of the matrices catalysing oxidation reactions with O_2 species.

The intercalation of levodopa into both magnesium–aluminium and zinc–aluminium layered double hydroxides through ion-exchange methods has been reported, and in the case of the magnesium–aluminium LDH, the effect of intercalation on the stability of levodopa with respect to racemisation has been investigated.[3,25,26] It was found that intercalation increased the stability of levodopa with respect to racemisation at both room temperature and elevated temperatures, when dry. However, the effect of intercalation on the main route of oxidative decomposition was not investigated, nor was the influence of water on the stability of the intercalation product. The two-step ion-exchange synthesis has been the only successful intercalation method reported for levodopa, so synthesis via a one-pot coprecipitation route would be a potentially useful improvement, and provide a valuable comparison between the effects of different synthesis methods on the resultant LDHs and the stability of the intercalated drugs.

As has been found for other drugs, intercalation of catecholamines into layered double hydroxides could potentially provide sufficient stability against their various decomposition routes, including oxidative decomposition and racemisation.[27–29] This could allow liquid formulations of these drugs to be made in the form of suspensions of LDH–drug nanohybrids, also making use of the ability of layered double hydroxides to control the release of the intercalated drugs. These would be the first formulations of such drugs to effectively stabilise them in liquid form whilst also solving the drawback of rapid absorption and metabolism, by allowing the creation of sustained release liquid formulations.

Whilst it is hoped that LDH intercalation will stabilise the catecholamine drugs, De Victoria Rodriguez *et al.* recently demonstrated the activation of a catecholamine-modified LDH for use in catalysis, resulting in oxidation of the catecholamine species.[30] A bisphosphonate-derivatised dopamine analogue, pictured in Figure 3.2, was adsorbed on the surface of zinc–aluminium LDH particles, causing the catechol groups to position themselves away from the LDH particles. The redox activity of the catechol groups was then harnessed to synthesise gold nanoparticles, in the process oxidising the catechol groups to quinones, although polymerisation of the catecholamine was prevented due to the functionalisation of the amine group.

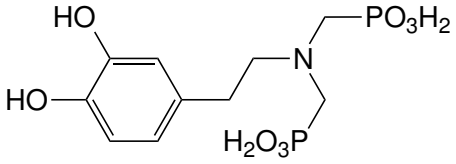


Figure 3.2: The structure of the bisphosphonate-derivatised dopamine analogue used by De Victoria Rodriguez *et al.*[30]

As the catecholamine drugs being investigated are being intercalated between LDH layers, rather than adsorbed on the surface of LDH particles, the aim is that increased stability will be conferred on the drug ions through favourable electrostatic interactions with the layers, rather than reduced stability due to exposure of the reactive catechol moieties. Besides intercalation between the LDH layers, additional methods of stabilising the the drug ions can be incorporated into the LDH–drug nanohybrids. One such method is to incorporate a reducing agent into the LDH sheets, such as a reducing transition metal ion like Fe^{2+} or Co^{2+}, as this preferentially oxidises in place of the catecholamine ion, delaying the onset of oxidative decomposition. As the only sufficiently biocompatible reducing transition metal ion is Fe^{2+}, this is the only option for incorporation into the LDH sheets.

3.1.3 Scope of this Chapter

In this chapter, the intercalation of catecholamine drugs levodopa, carbidopa and methyldopa into layered double hydroxides is reported. Two methods of drug intercalation are attempted, ion-exchange and coprecipitation, and the nanohybrid products compared over a range of metrics to find the most suitable synthesis

method. The drug ions are intercalated into magnesium–aluminium LDHs, a range of Fe^{2+} containing LDHs is synthesised, and intercalation of levodopa is attempted. Drug release profiles from the LDH–drug nanohybrids are recorded and their release kinetics modelled. The stability of the drugs in the nanohybrids is investigated under a range of both dry and wet conditions, with both their stability with respect to oxidative decomposition and with respect to racemisation measured. From this work, the suitability of LDHs for developing liquid dosage forms of catecholamine drugs in the form of suspensions, is then evaluated.

3.2 Synthesis of MgAl-drug LDH nanohybrids

Intercalation reaction outcomes were significantly affected by exposure to oxygen during synthesis. Successful intercalation reactions produced an off-white solid, due to unavoidable slight decomposition of the drug ions in the reaction mixtures. Unsuccessful intercalation attempts, where the flow of nitrogen gas was not sufficiently high to prevent substantial oxidative decomposition, produced brown and blue-black solids. The solid products of ion-exchange synthesis reactions were powdery in nature and did not aggregate on drying; they are denoted herein as MgAl-$LDOPA_{IE}$, MgAl-$MDOPA_{IE}$ and MgAl-$CDOPA_{IE}$ for the L-DOPA, M-DOPA and C-DOPA containing samples respectively. The products from coprecipitation syntheses dried into large, hard aggregates that required separating by grinding in a pestle and mortar before they could be characterised or used for further reactions or analyses; they are denoted herein asMgAl-$LDOPA_{CP}$ and MgAl-$MDOPA_{CP}$ for the L-DOPA and M-DOPA containing samples respectively.

3.2.1 Powder X-ray diffraction

Powder X-ray diffraction patterns of the MgAl-drug nanohybrids synthesised by ion-exchange are shown in Figure 3.3, alongside the MgAl-NO_3 ion-exchange precursor LDH. All patterns can be indexed on the basis of a hexagonal lattice with $R\bar{3}m$ rhombohedral symmetry and are very similar, with only very slight differences seen in the positions of Bragg reflections, relating to minor differences in interlayer distances

between the different nanohybrids. This is unsurprising, as the size and shape of the three drug ions are very similar, with the maximum length of all three falling within a distance of 9.1 Å (±0.05 Å).

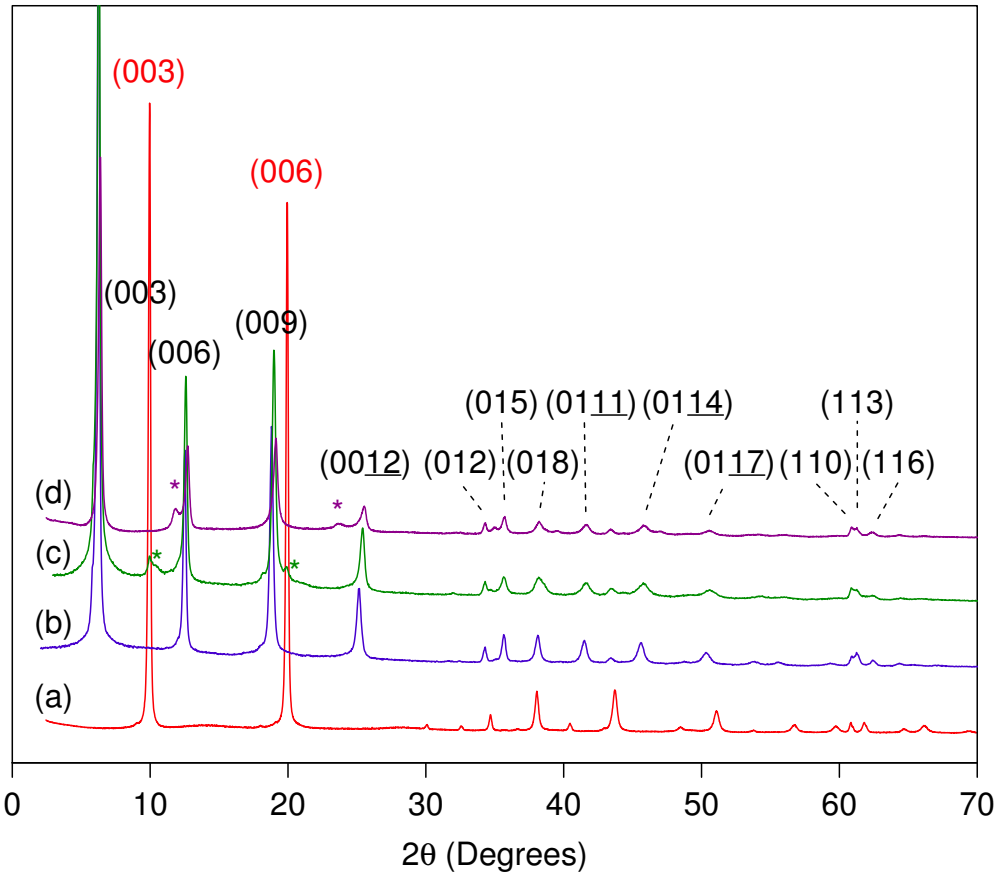


Figure 3.3: The powder XRD patterns of (a) MgAl-NO_3, (b) MgAl-$LDOPA_{IE}$, (c) MgAl-$MDOPA_{IE}$ and (d) MgAl-$CDOPA_{IE}$. * denotes MgAl-NO_3 impurity phase and * denotes MgAl-CO_3 impurity phase.

The basal Bragg reflections of the nanohybrids, indexed as (003), indicate the intercalation of a larger guest species into the LDHs relative to the precursor, as evidenced by their positions at lower values of 2θ. This corresponds to an increase in the c lattice parameters of the nanohybrids, and consequently the interlayer distance, as the thickness of the metal hydroxide layers remains constant at 4.8 Å. The basal reflections of the nanohybrids are found at $2\theta = 6.27°$, $d_{003} = 14.1$ Å in MgAl-$LDOPA_{IE}$, $2\theta = 6.30°$, $d_{003} = 14.0$ Å in MgAl-$MDOPA_{IE}$ and $2\theta = 6.40°$, $d_{003} = 13.8$ Å in MgAl-$CDOPA_{IE}$, giving interlayer distances of 9.3, 9.2 and 9.0 Å respectively.

The diffraction pattern for MgAl-LDOPA$_{IE}$ is in good agreement with those from the literature, showing no sign of impurities, albeit displaying higher crystallinity and a greater number of well-defined Bragg reflections, due to the highly crystalline precursor LDH used in ion-exchange reaction.[3,25] There are small amounts of impurities present in the diffraction patterns of MgAl-MDOPA$_{IE}$ and MgAl-CDOPA$_{IE}$, in the case of MgAl-MDOPA$_{IE}$ as small amount of the precursor nitrate LDH remains, indicated by Bragg reflections falling at $2\theta = 9.9$ and 19.8°, whereas in the MgAl-CDOPA$_{IE}$, the impurity is the carbonate containing LDH with Bragg reflections at $2\theta = 11.9$ and 23.6°.

The maximum length of all three drug ions is approximately the same distance of 9.1 Å, from the carboxylic acid group to the diphenol group. Consequently, a near-vertical orientation of the drug ions as monolayers between the LDH sheets is consistent with both the ion sizes and the interlayer distances observed, as seen in Figure 3.4. This also makes chemical sense as both ends of the drug ions are hydrophilic, and so both electrostatic and hydrogen bonding interactions will be maximised in this orientation, whereas ions that tend to form bilayers are generally surfactant-like.[31,32]

The powder XRD patterns of the nanohybrids synthesised by coprecipitation are shown in Figure 3.5. Whereas all three catecholamine drugs could be successfully intercalated through ion-exchange, the only drug that showed signs of successful intercalation through coprecipitation was L-DOPA. All attempts at synthesising nanohybrids containing M-DOPA through coprecipitation returned poorly crystalline LDHs containing a combination of both nitrate and carbonate ions, which produced a basal Bragg reflection at $2\theta = 11.1°$, $d_{003} = 8.0$ Å. Due to the difficulty of intercalating M-DOPA through coprecipitation, intercalation of C-DOPA was not attempted. The difference in success of the coprecipitation syntheses is likely due to the lower oxidative stability of M-DOPA (and also C-DOPA) relative to L-DOPA, which is caused by the presence of the β-methyl group in these compounds.

The basal Bragg reflection of MgAl-LDOPA$_{CP}$ is seen at $2\theta = 7.9°$, $d_{003} = 11.2$ Å, which is substantially higher than the ion-exchange analogue, and translates to a significantly smaller interlayer distance of 6.4 Å, which suggests a much more angled orientation of the drug ion within the layers, when compared to the ion-exchange

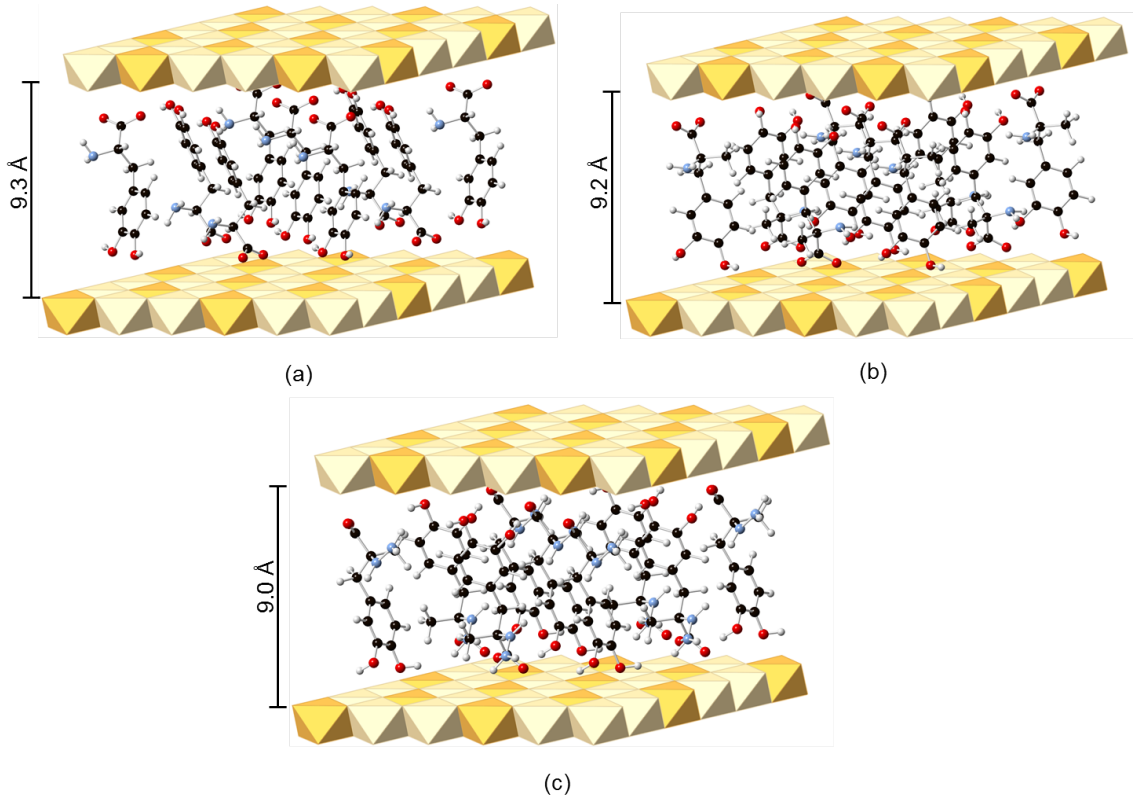


Figure 3.4: The possible orientations of (a) L-DOPA, (b) M-DOPA and (c) C-DOPA in the interlayer regions of the magnesium–aluminium nanohybrids.

synthesised nanohybrids. The smaller interlayer distance could, however, also be caused by either the intercalation of a different ion, such as a decomposition product, or by a poor drug loading percentage, which could lead to the angled orientation of the guest ions, as they would have greater freedom to orientate themselves. The nanohybrids synthesised by ion-exchange show a significantly higher crystallinity than those synthesised by coprecipitation, as evidenced from the increased number and sharpness of the Bragg reflections in the ion-exchange nanohybrid patterns.

Table 3.1: The cell parameters of the magnesium–aluminium catecholamine nanohybrids.

Sample	Cell parameters (Å)	
	a	c
MgAl-LDOPA$_{IE}$	3.039	42.38
MgAl-MDOPA$_{IE}$	3.041	42.11
MgAl-CDOPA$_{IE}$	3.040	41.67
MgAl-LDOPA$_{CP}$	3.045	32.58

The cell parameters calculated from the powder XRD patterns are given in Table 3.1.

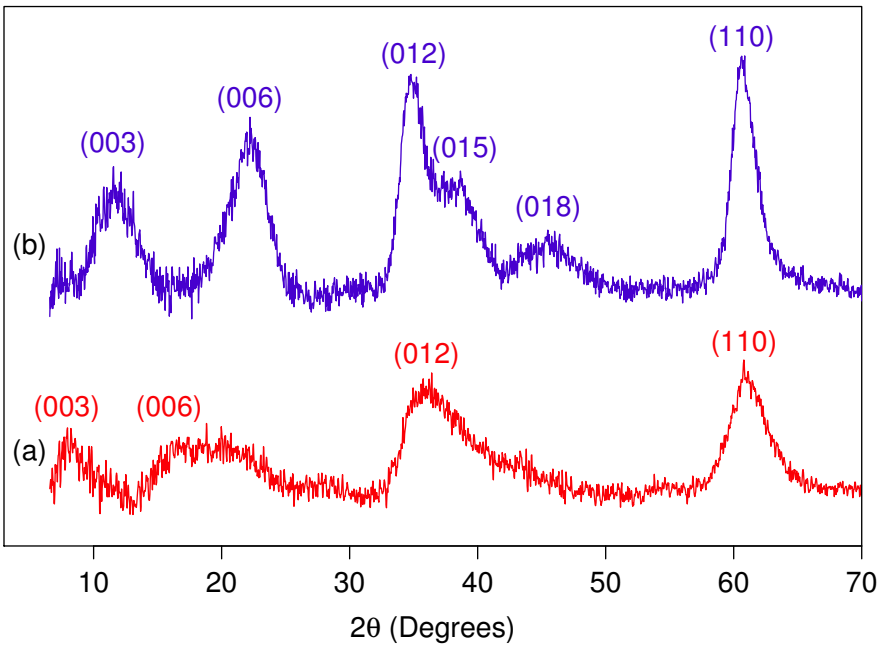


Figure 3.5: The powder XRD patterns of (a) MgAl-LDOPA$_{CP}$ and (b) MgAl-MDOPA$_{CP}$.

Very little difference is seen in the a parameters of the different nanohybrids, which also show little change from the precursor nitrate LDH ($a = 3.042$ Å in MgAl-NO_3). This is as expected, as the a parameter, which lies perpendicular to the stacking direction, is primarily influenced by the species in the metal hydroxide layers, with only a very minor influence being imparted from the interlayer species.

In contrast, the c parameter, which lies along the stacking direction, is directly affected by the interlayer distance, which is in turn influenced by the guest ion. As already discussed, the maximum length of all three drug ions is very similar, and the calculated interlayer distance matches a near-vertical orientation of the drugs within the layers. This explains why the interlayer distance, and by extension the c parameters of all three ion-exchange nanohybrids are so similar, despite there being differences in the the other dimensions of the drug ions. Interestingly, the small differences in the interlayer distances and c parameters of the ion-exchange nanohybrids follows a reverse trend when compared to the the bulkiness of their respective ions, with most bulky C-DOPA leading to the smallest interlayer spacing, least bulky L-DOPA giving the largest interlayer spacing, and M-DOPA evenly placed in the middle on both measures.

Two factors may explain the differences in the interlayer distances observed. First,

differences in the drug loading of the nanohybrids may contribute, as lower drug loading percentages will allow a more angled position of the drug ions, leading to a reduction in gallery height. Second, increased interactions between the drug ions and the metal hydroxide layers will draw the layers closer together. The hydrazino group of C-DOPA allows for possible hydrogen bonding with the layers, and optimum interaction when the drug ion is at a slight off-vertical angle. The β-methyl of both M-DOPA and C-DOPA may also affect the positions of both the carboxylate groups and the amino/hydrazino groups, allowing for greatest interactions only at a slight angling of the drug ions.

3.2.2 Fourier transform infrared spectroscopy

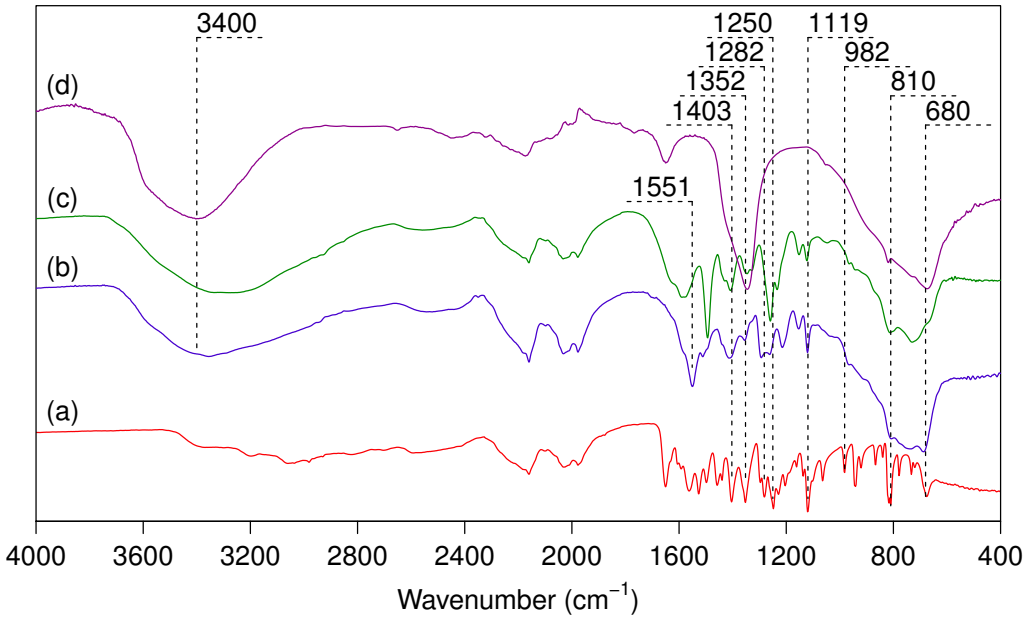


Figure 3.6: FTIR spectra of (a) pristine L-DOPA, (b) MgAl-LDOPA$_{IE}$, (c) MgAl-LDOPA$_{CP}$ and (d) MgAl-NO$_3$.

The FTIR spectra of the magnesium–aluminium nanohybrids can be seen in Figures 3.6, 3.7 and 3.8, alongside the spectra of the pristine drugs and the precursor nitrate LDH. The spectra of the nanohybrids show absorptions relating to both the intercalated drug ion and those characteristic of LDHs, although some absorptions found in the pristine drugs are absent due to the drug ions being constrained between the LDH layers. Additionally, the absorptions relating to drug ions in the

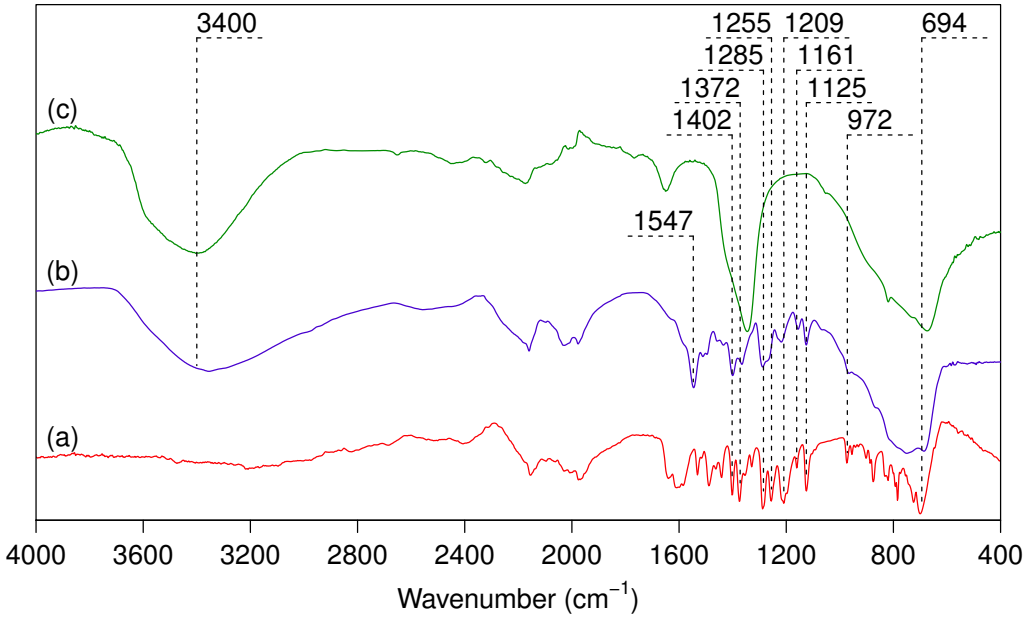


Figure 3.7: FTIR spectra of (a) pristine M-DOPA, (b) MgAl-MDOPA$_{IE}$, (c) MgAl-NO$_3$.

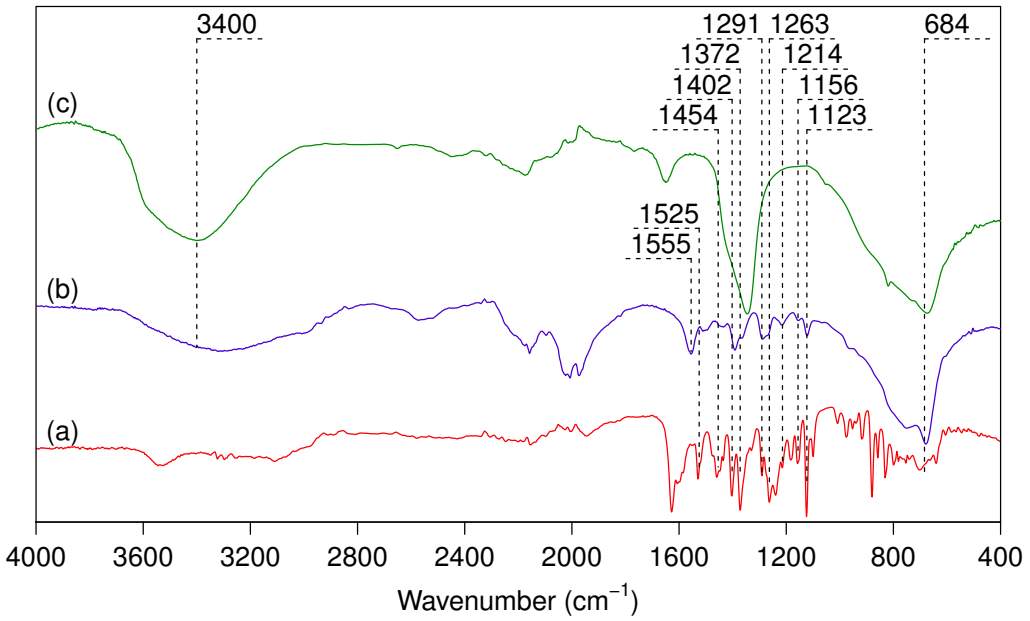


Figure 3.8: FTIR spectra of (a) pristine C-DOPA, (b) MgAl-CDOPA$_{IE}$, (c) MgAl-NO$_3$.

nanohybrids are broadened when compared to those of the pristine drug samples, also due to the drug ions being constrained by the LDH layers, which leads to greater variations in characteristic absorption energies.

In all pristine drug samples absorptions seen between 1650 and 1600 cm^{-1} relate to the carbonyl stretch of the unionised drug, whereas in the corresponding ion-exchange nanohybrids the absorptions at 1551, 1547 or 1555 cm^{-1}, relate to the ionised asymmetric carboxylate stretch. In both the pristine drug ions and the corresponding nanohybrids, the absorptions at 1402 – 1403 cm^{-1} related to the symmetric carbonyl stretches. Absorptions seen at 1282 and 1250 cm^{-1} (L-DOPA), 1285 and 1255 cm^{-1} (M-DOPA), and 1291 and 1263 cm^{-1} (C-DOPA) relate to the to the bending modes of the catechol groups. Absorptions seen at 1352 and 1372 cm^{-1} correspond to ring deformation modes of the drug ions. Absorptions at 1119, 1125 and 1123 cm^{-1} relate to C−N the stretching mode in the respective drugs and corresponding nanohybrids. Additional absorptions are seen at 1161 and 1156 cm^{-1} in the spectra of M-DOPA and C-DOPA and their respective nanohybrids, corresponding to the β-methyl stretch, and a further absorption in C-DOPA and its respective nanohybrid at 1525 cm^{-1} which corresponds to the hydrazino NH−NH_2 bending mode.

All nanohybrid samples and the precursor LDH show a broad absorption around 3400 cm^{-1} relating to the O−H stretching modes of the metal hydroxide layers and cointercalated water. The shape of this broad absorption differs in the nanohybrids when compared to the precursor LDH as there is also a contribution from the phenolic O−H stretch of the catechol groups in the drug ions. The LDH layers also contribute the pronounced, broad absorptions in the nanohybrids seen at 600 – 900 cm^{-1}, which are attributable to the M−OH stretching and bending modes. This intense absorption obscures many of the minor fingerprint absorptions attributable to the drug ions within this region, with the exception of those seen at 810, 680, 694 and 684 cm^{-1}.

The absorptions corresponding to the intercalated guest ion in the spectrum of MgAl-$LDOPA_{CP}$ do not match directly with MgAl-$LDOPA_{IE}$, suggesting that it may be a different species, such as an intermediate in the decomposition pathway, or that it is constrained in a different orientation that has led to the the changes in the

absorption bands seen.

The absorption at 1347 cm^{-1} seen in the precursor LDH corresponds to the interlayer nitrate ions, but is notably absent in all nanohybrids, including MgAl-$MDOPA_{IE}$, which is surprising considering the powder XRD pattern of this nanohybrid indicates the presence of MgAl-NO_3 as a minor impurity. This suggests that either nitrate ions are not present in the samples, or are present in low enough quantities that any small absorption from the nitrate ions is masked by the shoulder of neighbouring absorptions of the drug ions in their FTIR spectra, which is possible on close inspection of the spectrum of MgAl-$MDOPA_{IE}$. Similarly, none of the nanohybrid spectra display noticeable absorptions around 1353 cm^{-1}, which would imply the presence of carbonate ions. As the powder XRD spectrum of MgAl-$CDOPA_{IE}$ indicates the presence of MgAl-CO_3 in the sample, it is likely that the absorption is hidden under the shoulder of the absorption at 1372 cm^{-1} in the nanohybrid sample.

3.2.3 Solid state ^{13}C NMR spectroscopy

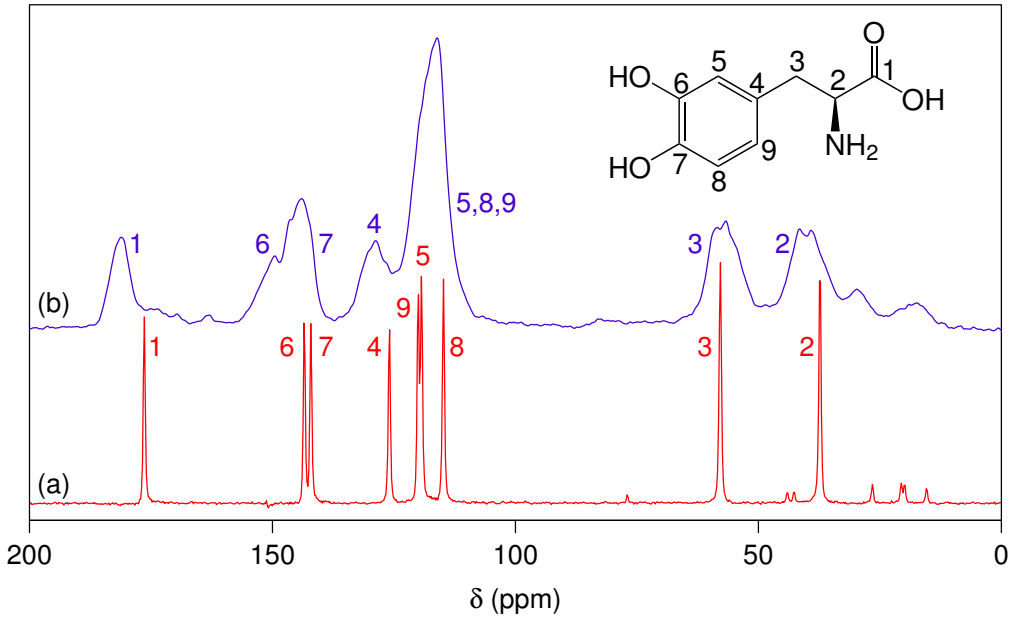


Figure 3.9: Solid state ^{13}C CP/MAS NMR spectra of (a) pristine L-DOPA and (b) MgAl-$LDOPA_{IE}$.

The solid state ^{13}C CP/MAS NMR spectra of the nanohybrids confirm the presence of the drug ions in between the layers. The chemical shifts of resonances in the spectra

of the pristine drugs and the ion-exchange synthesised nanohybrids match closely and agree with literature values.[1,33,34] The assigned spectra of pristine L-DOPA and MgAl-LDOPA$_{IE}$ can be seen in Figure 3.9. The pristine drug shows resonances at δ = 177, 144, 142, 126, 120, 119, 115, 58 and 38 ppm, whilst the nanohybrid shows resonances at δ = 181, 150, 144, 129, 119, 57 and 39 ppm, with the resonances of the three unsubstituted aromatic carbon atoms coalescing into one large peak at 119 ppm. In the case of M-DOPA, the pristine drug gives resonances of δ = 176, 144, 143, 126, 122, 119, 116, 62, 41 and 23 ppm and the nanohybrid gives resonances of δ = 184, 151, 144, 126, 117, 59, 43 and 23 ppm, which can both be assigned in the same manner as L-DOPA, with the additional resonances at 23 ppm corresponding to the β-methyl group, and the resonances of the unsubstituted aromatic carbon atoms again coalescing into a single peak. C-DOPA can be similarly assigned, with spectra showing resonances of the pristine drug at δ = 175, 144, 143, 126, 121, 117, 116, 68, 43 and 19 ppm and of the nanohybrid at δ = 181, 151, 145, 128, 119, 65, 44 and 22 ppm.

The resonances in the spectra of the nanohybrids are substantially broader than those in the spectra of the pristine anions, due to the variations in orientation of the drug ions within the interlayer regions of the nanohybrids, which affects the local environments of the drug ions due to electrostatic interactions with the metal hydroxide sheets, creating variations in the resulting chemical shift values of resonances. In particular, the chemical shift differences between the carbonyl carbons in the pristine drugs and those in the nanohybrids can be attributed to the deprotonation of the drug species, with small changes in the chemical shift values of aromatic carbon atoms attributable to changes in the hydrogen bonding of the catechol groups. Besides the resonances that could be assigned to drug molecules in the spectra of pristine drugs, spinning sidebands were clearly present, see in the regions of 210 – 250 ppm and 10 – 40 ppm. In the spectra of the nanohybrids, broad, low intensity resonances are seen over the same ranges, indicating these resonances are also spinning sidebands; no other resonances were visible in the spectra of the nanohybrids. However, the metal hydroxide layers in the nanohybrids reduce the effective concentration of the drug ions and any other organic species in the samples, reducing the effective sensitivity of the technique, so low amounts of organic species

such as decomposition products are not detectable through this method.

The spectrum of MgAl-LDOPA$_{CP}$, seen in Figure 3.10 does not show close agreement with that of either MgAl-LDOPA$_{IE}$ or pristine L-DOPA, which suggests that, rather than containing intercalated L-DOPA ions, it contains a decomposition product. The spectrum shows resonances at 181, 177, 170, 152, 144, 126, 119, 72 and 51 ppm, which can be assigned to the decomposition product dopachrome, a precursor to melanin.[33]

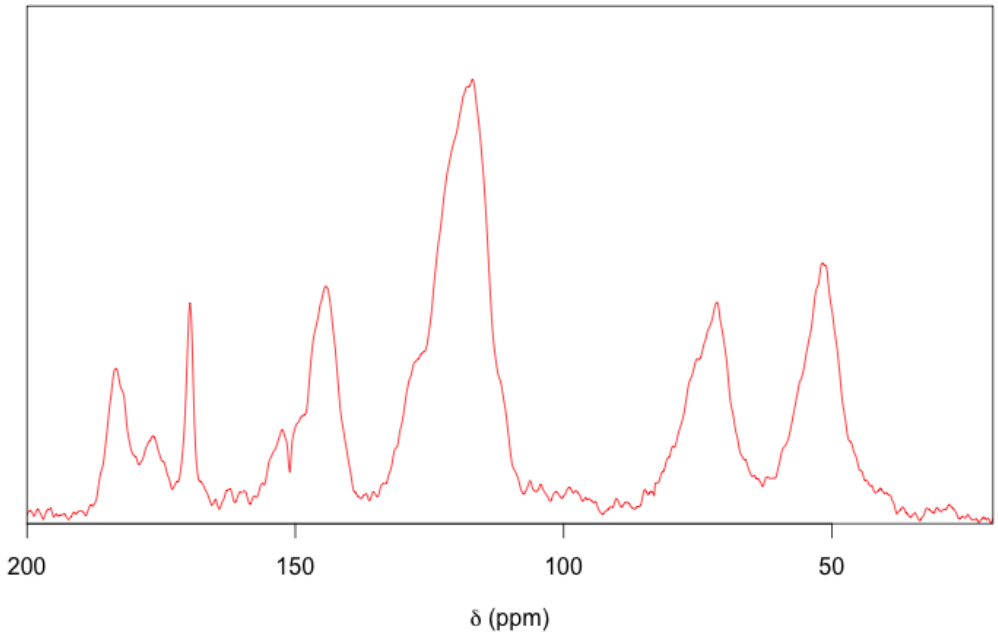


Figure 3.10: Solid state ^{13}C CP/MAS NMR spectrum of MgAl-LDOPA$_{CP}$.

3.2.4 Dissolution experiments

The presence of the drug species was confirmed by dissolving the nanohybrids in a solution of DCl in D_2O followed by ^{1}H NMR spectroscopy of the resulting solution. This also allowed the presence, identity and relative concentration of any decomposition products contained in the nanohybrids to be ascertained prior to conducting release and decomposition studies. As the drug ions are unstable in basic solutions, dissolution in an acid solution was used for NMR investigation, as opposed to the deintercalation experiments involving a solution of Na_2CO_3 in D_2O and reported in Section 2.2.6, as reactions in alkaline conditions would lead to rapid

decomposition of any drug ions present. The greater sensitivity of solution NMR spectroscopy in relation to solid state NMR spectroscopy allows the detection of decomposition products not detectable by the solid state technique.

The spectra from the dissolution experiments were compared to spectra of the pristine drugs in acid solution. Pristine L-DOPA gave resonances at chemical shift values of $\delta = 4.76$ ppm (1H, d, $J = 8.1$ Hz), 4.71 ppm (1H, d, $J = 2.1$ Hz), 4.59 ppm (1H, dd, $J = 8.1$, 2.1 Hz), 2.22 ppm (1H, dd, $J = 7.4$, 5.4 Hz), 1.10 ppm (1H, dd, $J = 14.7$, 5.4 Hz) and 0.98 ppm (1H, dd, $J = 14.7$, 7.4 Hz); pristine M-DOPA gave resonances at $\delta = 4.99$ ppm (1H, d, $J = 2.1$ Hz), 4.88 ppm (1H, d, $J = 8.1$ Hz), 4.79 ppm (1H, dd, $J = 8.1$, 2.1 Hz), 1.30 ppm (1H, d, $J = 14.4$ Hz), 0.94 ppm (1H, d, $J = 14.4$ Hz) and -0.36 ppm (3H, s); pristine C-DOPA gave resonances at $\delta = 5.06$ ppm (1H, d, $J = 8.2$ Hz), 4.97 ppm (1H, s), 4.85 ppm (1H, d, $J = 8.2$ Hz), 1.31 ppm (1H, d, $J = 14.3$ Hz), 1.18 ppm (1H, d, $J = 14.3$ Hz) and -0.25 ppm (3H, s). The solutions resulting from dissolution experiments with all the of the ion-exchange synthesised nanohybrids gave spectra that matched the pristine drugs exactly, with the addition of a large solvent peak due to the dissolved metal hydroxide sheets, indicating that any decomposition of the drug ions during both synthesis and dissolution was too minor to be detected by NMR spectroscopy. It should be noted that comparison of the spectra of the drugs in DCl/D_2O with those in D_2O reveals as substantial upfield shift of all the resonances in the acid solution, of around 1.3 – 1.6 ppm.

The spectrum of the solution obtained from dissolving MgAl-LDOPA$_{CP}$ contains resonances can can be assigned to L-DOPA, but in addition resonances can be seen at 0.30 ppm (s), -0.11 ppm (s) and -0.23 ppm (s), whilst the resonances at 4.76 and 4.71 ppm relating the the aromatic protons of L-DOPA appear uneven and integrate to higher values than expected, indicating that they are partially masking additional resonances. These additional resonances can be attributed to L-DOPA decomposition products such as dopachrome.[35]

3.2.5 Thermogravimetric analysis

The water content of the nanohybrids was deduced through thermogravimetric analysis (TGA), and is displayed in Table 3.2. The TGA plot of MgAl-LDOPA$_{IE}$ is

Table 3.2: Water content, drug content, metal ion ratios and formulae of the nanohybrids.

Sample	Water content (W/W %)	Drug content (W/W %)	Mg : Al ratio	Formula
MgAl-LDOPA$_{\mathrm{IE}}$	11.0	39.6	1.95	$Mg_{1.98}Al_{1.02}(OH)_6(C_9H_{10}NO_4)_{0.78}(NO_3)_{0.23} \cdot 2.4H_2O$
MgAl-MDOPA$_{\mathrm{IE}}$	9.1	37.2	1.96	$Mg_{1.99}Al_{1.01}(OH)_6(C_{10}H_{12}NO_4)_{0.66}(NO_3)_{0.35} \cdot 1.9H_2O$
MgAl-CDOPA$_{\mathrm{IE}}$	9.6	38.4	1.95	$Mg_{1.98}Al_{1.02}(OH)_6(C_{10}H_{13}N_2O_4)_{0.62}(CO_3)_{0.20} \cdot 1.9H_2O$
MgAl-LDOPA$_{\mathrm{CP}}$	11.6	42.5	2.02	$Mg_{2.01}Al_{0.99}(OH)_6(C_9H_{10}NO_4)_{0.87}(NO_3)_{0.12} \cdot 2.6H_2O$

also included in Figure 3.11 as an example. All nanohybrids underwent an initial phase of mass loss as they were heated up to 140 °C, which can be attributed to the loss of cointercalated water. Mass loss next occurred between 240 and 365 °C for MgAl-LDOPA$_{IE}$, between 210 and 310 °C for MgAl-MDOPA$_{IE}$, between 220 and 345 °C in MgAl-CDOPA$_{IE}$, which is consistent with decarboxylation of the drug ions, and can be used to corroborate the calculated drug content from elemental analysis. Between 370 and 440 °C, all the nanohybrids showed mass loss corresponding to the loss of the remaining organic fragments of the drug ions and any other organic guests, this was followed loss of any intercalated inorganic nitrate or carbonate ions, between 460 and 520 °C. The pattern of mass loss from MgAl-LDOPA$_{CP}$ is complicated by the mix of both L-DOPA and dopachrome in the sample, as it shows overlapping mass loss regions between 235 and 350 °C and between 330 and 395 °C, which can be attributable to decarboxylation of L-DOPA and dopachrome respectively. Dopachrome has been shown to exhibit greater stability with respect to decarboxylation when compared to L-DOPA, which is supported difference in decarboxylation temperatures seen.[35] Beyond 520 °C, minimal mass loss was observed in all nanohybrids as the temperature wasn't sufficient to cause calcination of the remaining LDH layers into metal oxides.

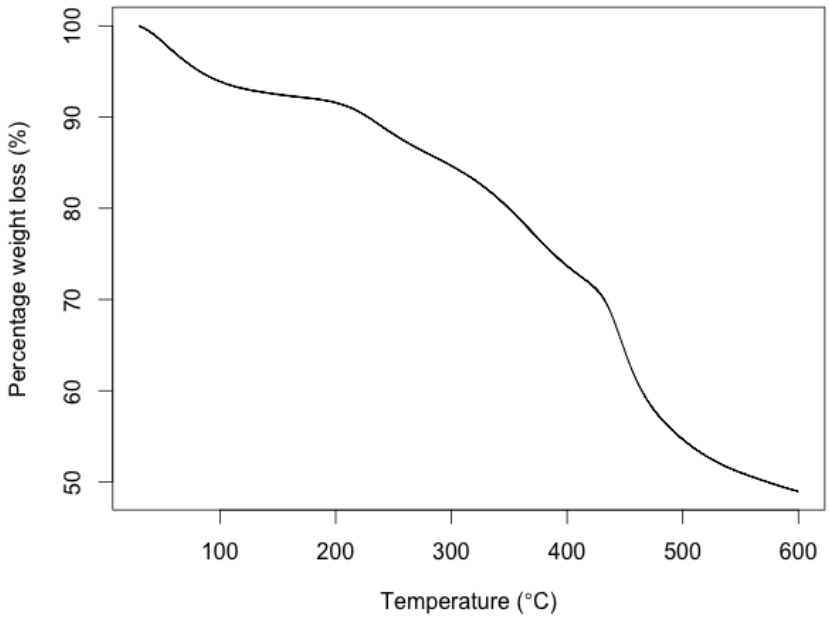


Figure 3.11: TGA plot of MgAl-LDOPA$_{IE}$, showing percentage mass loss as a function of temperature.

3.2.6 Elemental analysis and drug content

The figures of water content calculated from TGA were used in conjunction with C, H, N elemental analysis data to calculate the the drug loading of the the nanohybrids. Full details of the observed and calculated C, H, N data is included in Appendix B.1. The relative values of C and N content in the nanohybrids indicated the the presence of nitrate and carbonate ions in the samples, as already identified by their powder XRD patterns. EDX allowed the ratios of metal ions in the nanohybrids to be calculated, which along with the drug content data allowed the formulae of the nanohybrids to be estimated, as detailed in Table 3.2. The calculated drug content of the coprecipitation sample was higher than that of the ion-exchange samples, however as indicated from FTIR and NMR spectra, this sample contained substantial amounts of the decomposition product dopachrome, which has a sufficiently similar formula to L-DOPA to prevent accurate calculation of the ratio of these two species.

The mass percentage contribution from different fragments of the drug ions in the nanohybrid can be calculated and compared to the corresponding mass losses that the were assigned in the TGA. Table 3.3 details both the calculated mass percentages the ion fragments in the nanohybrids and the experimentally deduced mass percentages using TGA. The similarity between the two sets of values in all the ion-exchange synthesised nanohybrids is confirmation of the low levels of any decomposition products contained in these samples, as the greater the mass proportion of these in the samples, the further the TGA-derived values will diverge from the calculated values. The values for MgAl-LDOPA$_{CP}$ do show substantial differences, however, corroborating with evidence from from its solid state NMR and FTIR spectra that suggest the interlayer ion in this sample is not L-DOPA, but in fact one of its decomposition products.

Having calculated the mass percentage of the drug ions in the nanohybrids, the drug loading percentages as a function of the theoretical maximum drug loading can also be calculated. For each of the ion-exchange samples, the drug loading percentage is high, being 74, 64 and 61 % for the L-DOPA, M-DOPA and C-DOPA samples respectively. As all these drugs are active within dosage ranges of 10 to 100 mg, this indicates that the effective drug concentration in all the ion-exchange nanohybrids is

Table 3.3: The calculated and TGA-derived mass percentages of drug ion fragments in magnesium–aluminium nanohybrids.

Sample	Calculated mass percentage (%)		TGA-derived mass percentage (%)	
	COO	Other organic	COO	Other organic
MgAl-LDOPA$_{IE}$	8.9	30.7	10	32
MgAl-MDOPA$_{IE}$	7.8	29.4	9	31
MgAl-CDOPA$_{IE}$	9.0	37.0	8	35
MgAl-LDOPA$_{CP}$	9.5	33.0	15	37

sufficient for practicable dosages (less than 1 g) of nanohybrids to contain therapeutic amounts of the drug ions.

3.2.7 Scanning electron microscopy

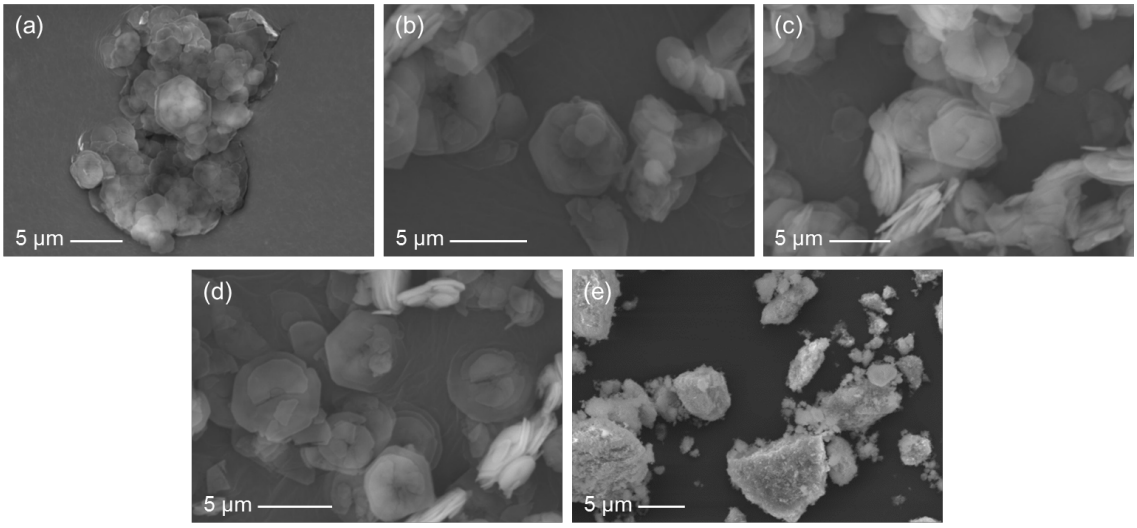


Figure 3.12: SEM images of (a) MgAl-NO_3, (b) MgAl-LDOPA$_{IE}$, (c) MgAl-MDOPA$_{IE}$, (d) MgAl-CDOPA$_{IE}$ and (e) MgAl-LDOPA$_{CP}$.

Scanning electron microscopy images of the nanohybrids, seen in Figure 3.12, show the significant differences in morphology between the coprecipitation and ion-exchange synthesised nanohybrids, as is typical for these synthesis routes, and as their powder X-ray diffraction patterns predicted. All ion-exchange synthesised species exhibit the same morphology of well-defined thin hexagonal platelets, with a high aspect ratio. No difference is seen between samples containing different drug ions. Comparison with the precursor nitrate LDH in Figure 3.12(a) shows very little change in morphology,

with no noticeable pitting, rounding, fracturing or reduction in size of the nanohybrid particles, indicating that the ion-exchange process has not affected the LDH sheets negatively through partial dissolution or mechanical wear. The particles of the coprecipitation sample are much less well-defined, indicating that the individual LDH particles have aggregated together during synthesis, eliciting the irregular 'rock-like' structures seen in Figure 3.12(e). Due to aggregation, the coprecipitation particles do not exhibit a high aspect ratio. Their maximum diameter is also much smaller than the ion-exchange samples.

3.2.8 Discussion

All the nanohybrid samples synthesised by ion-exchange were shown to contain their intended drug ion, and in sufficiently high loading percentages to for their potential use to be practical at therapeutic dosages of the intercalated drugs. In addition, it was observed that dissolution of the nanohybrids returned the drug ions intact and with only very minor decomposition of the drug ions occurring during the synthesis process. In comparison, the only LDH sample synthesised through coprecipitation that shows intercalation of an organic species, MgAl-LDOPA$_{CP}$, appears to contain the decomposition products of L-DOPA, most probably leukodopachrome and dopachrome in their metastable anionic forms, before they are able to undergo further polymerisation reactions to form melanin. The higher pH needed for the coprecipitation synthesis clearly prevents the intercalation of L-DOPA and other catecholamine drugs through a one pot method. Consequently, the most appropriate method for intercalating catecholamine drugs appears to be ion-exchange.

3.3 LDH precursors containing Fe^{2+}

The main route of decomposition for catecholamine drugs is initiated by an oxidation step. The incorporation of a reducing agent, such as a reducing transition metal cation, into a host LDH may help to prevent this first step of the decomposition process. To test this hypothesis, a series of LDHs containing Fe^{2+} in varying amounts was synthesised, iron being the only suitable metal that is also sufficiently biocom-

patible. Besides fougèrite, the naturally occurring mineral with the ideal formula $Fe_4^{2+}Fe_2^{3+}(OH)_{12}CO_3 \cdot 3\,H_2O$ and its closely related species such trébeurdenite, there are a limited number of examples of Fe^{2+} containing LDHs.[36–39] The reducing capacity of Fe^{2+} containing LDHs has been demonstrated for use in catalysis and waste management.[40,41] The inclusion of Fe^{2+} as a ternary component in magnesium–aluminium LDHs through standard coprecipitation methods has been reported, but samples have shown poor crystallinity, and a systematic variation of iron content has never been made.[42,43] The readily oxidisable nature of Fe^{2+} makes the synthesis of of LDHs containing this ion more challenging than most LDH syntheses, and as such there has only been one reported synthesis of a highly-crystalline LDH containing Fe^{2+} through homogeneous coprecipitation.[39]

The homogeneous coprecipitation method of Liu *et al.* was modified to synthesise a range of LDHs containing Fe^{2+}, Mg^{2+} and Al^{3+} ions, and is detailed fully in Section 6.5.3.[39] One iron–aluminium LDH was synthesised, alongside three magnesium–iron–aluminium LDH samples. A M^{2+}:M^{3+} ratio of 2:1 was maintained in the starting materials for three of the four samples. After initial investigations showed Mg^{2+} ions were less well incorporated into the samples than Fe^{2+} ions, a fourth sample with a M^{2+}:M^{3+} reactant ratio of 3:1 was synthesised. Details of their names and the metal ion ratios used in their synthesis are given in Table 3.4.

Table 3.4: Reactant ratios of the Fe^{2+} containing LDHs synthesised.

Sample name	Reactant metal ion ratio		
	Mg	Fe	Al
FeAl-CO_3	0	2	1
$MgFeAl_a$-CO_3	1.8	0.2	1
$MgFeAl_b$-CO_3	1	1	1
$MgFeAl_c$-CO_3	2	1	1

The LDH syntheses and all subsequent reactions were conducted under a gentle flow of N_2 gas to prevent oxidation of the Fe^{2+} ions. All samples were stored in a vacuum desiccator at 1×10^{-2} mbar for the same reason. The homogeneous coprecipitation syntheses results in LDHs containing interlayer carbonate ions. Consequently, decarbonation with HNO_3 in MeOH was necessary to create nitrate LDHs that could undergo subsequent drug ion intercalation. As HNO_3 is an oxidising agent, samples

were also decarbonated using HCl in MeOH to produce the chloride analogues.

All Fe^{2+} containing carbonate, nitrate and chloride LDHs were blue in colour, with those containing greater amounts of iron exhibiting a darker colour, ranging from sky blue of $MgFeAl_b$-CO_3 to battleship blue-grey of FeAl-CO_3, as illustrated in Figure 3.13. Where reactions were unsuccessful due to exposure to oxygen, the solid products were orange-brown in colour, as is typical for Fe^{3+} containing LDHs.

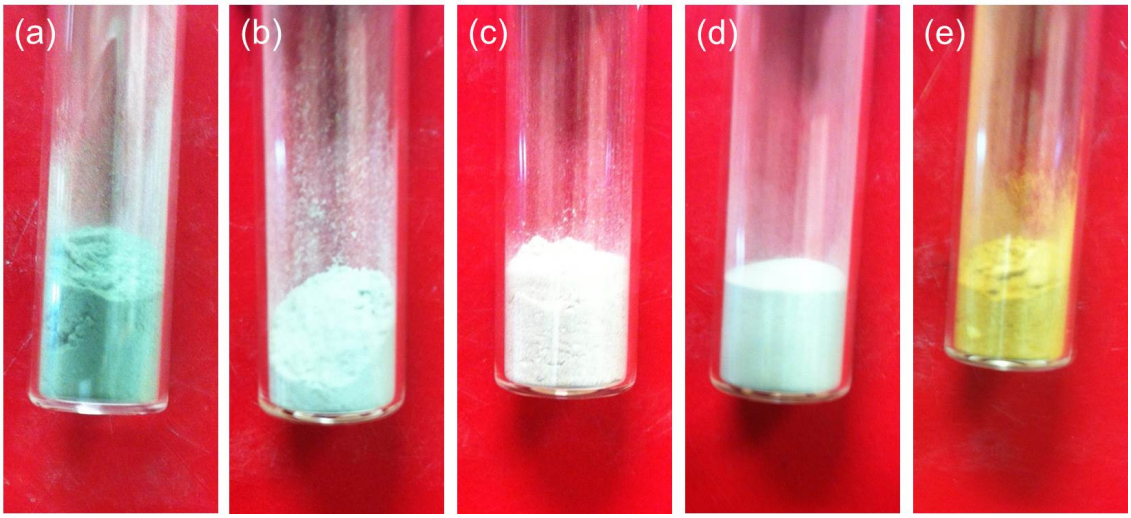


Figure 3.13: Examples of Fe^{2+} containing LDHs, (a) FeAl-CO_3, (b) $MgFeAl_a$-Cl, (c) $MgFeAl_b$-NO_3, (d) $MgFeAl_c$-CO_3 and (e) an oxidised LDH sample from a failed reaction

3.3.1 Powder X-ray diffraction

Figure 3.14 shows the powder XRD patterns of the Fe^{2+} containing carbonate LDHs. As with MgAl-CO_3, patterns could be indexed on a hexagonal lattice with $R\bar{3}m$ rhombohedral symmetry. The pattern and cell parameters of FeAl-CO_3 matched that found in the literature.[39] Besides small differences in the positions of the Bragg reflections, the patterns of FeAl-CO_3 and $MgFeAl_b$-CO_3 are almost identical, and can be indexed with the same labels. The pattern of $MgFeAl_a$-CO_3 shows fewer Bragg reflections, possibly due to lower crystallinity, but can also be assigned the same indexing labels as FeAl-CO_3. It also contains some minor impurity reflections that correspond to brucite, $Mg(OH)_2$. The pattern of $MgFeAl_c$-CO_3 shows differences to the other three patterns, and lies somewhere between that of FeAl-CO_3 and

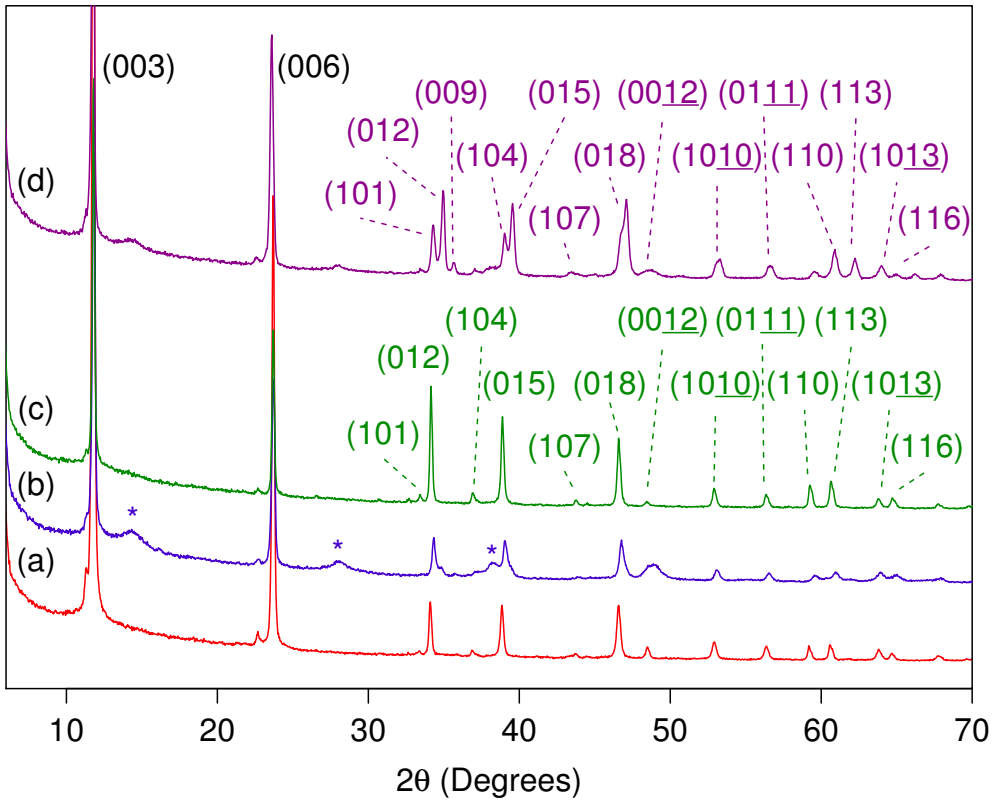


Figure 3.14: The powder XRD patterns of (a) FeAl-CO_3, (b) $MgFeAl_a$-CO_3, (c) $MgFeAl_b$-CO_3 and (d) $MgFeAl_c$-CO_3. * denotes brucite, $Mg(OH)_2$, impurity phase.

$MgAl$-CO_3, presumably due to higher magnesium content. Small Bragg reflections seen to the left of (003) and (006) in the patterns correspond to a minor impurities of the LDH chloride analogues.

The cell parameters calculated from the patterns, given in Table 3.5, reveal the effect of the Mg : Fe ratio on the a parameter, with greater iron content leading to an increase in the a parameter. The c parameter allows the interlayer distance to be calculated, and in all instances it is between 2.69 and 2.72 Å, which is typical of a carbonate LDH, as the strong electrostatic interactions between the carbonate ions and the metal hydroxide layers prevents significant variation in this parameter.

The powder XRD patterns of the Fe^{2+} containing LDHs intercalated with chloride and nitrate ions by successful decarbonation reactions are shown in Figure 3.15. The only LDH that could not be produced through decarbonation was $MgFeAl_a$-NO_3, and all attempts at to obtain this through decarbonation resulted in an oxidised orange-brown

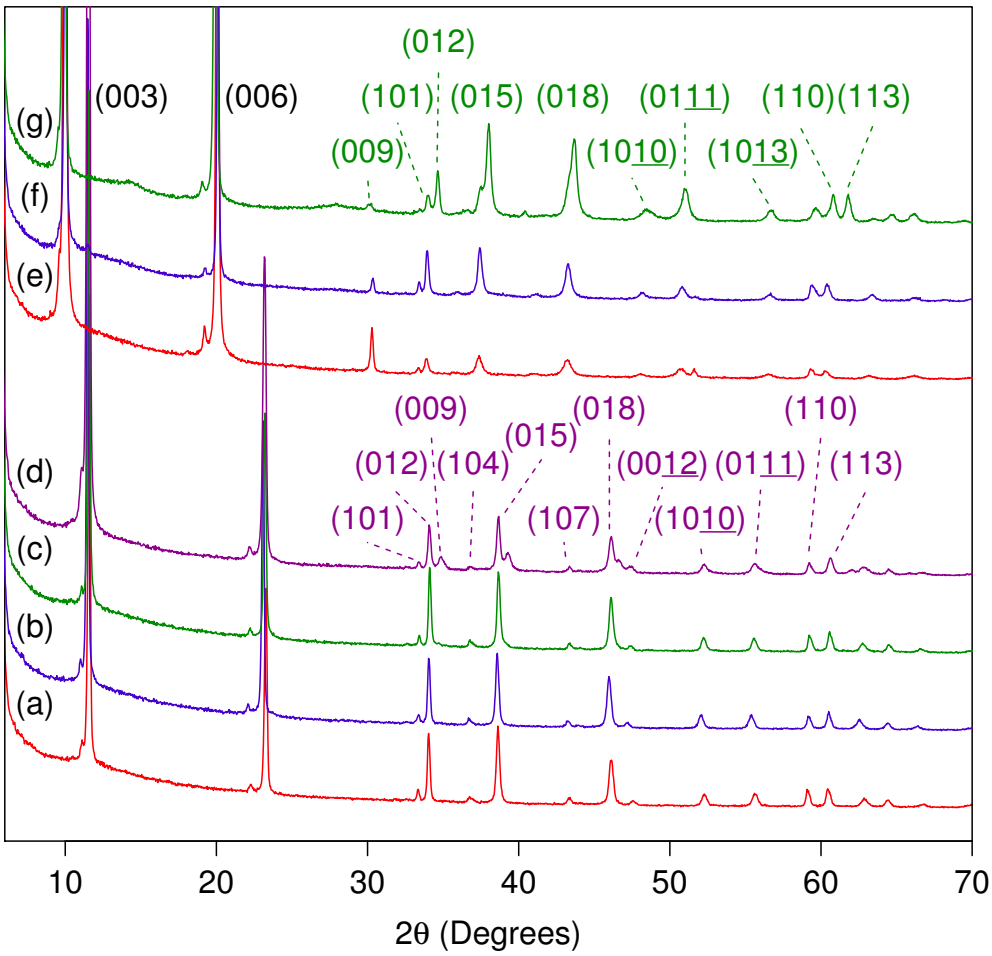


Figure 3.15: The powder XRD patterns of (a) FeAl-Cl, (b) $MgFeAl_a$-Cl, (c) $MgFeAl_b$-Cl, (d) $MgFeAl_c$-Cl, (e) FeAl-NO_3, (f) $MgFeAl_b$-NO_3 and (g) $MgFeAl_c$-NO_3.

LDH-like product containing Fe^{3+} ions. As with the carbonate analogues, all samples exhibited a high degree of crystallinity and could be indexed on a hexagonal lattice with $R\bar{3}m$ rhombohedral symmetry; their lattice parameters and calculated interlayer distances are given in Table 3.5. Minimal changes to the a lattice parameters confirm that the metal hydroxide layers remained largely unchanged by decarbonation. Any changes to the ratios of the metal ions in the layers, due to their dissolution during decarbonation, were low enough to not significantly alter the a parameters in the resulting LDHs. Changes to the c parameters, from which the interlayer distances could be calculated, indicate successful intercalation of the intended guest ions, with all chloride LDHs displaying interlayer distances of 2.8 – 2.9 Å and nitrate LDHs displaying interlayer distances of 4.0 – 4.1 Å, which are consistent with the intercalation of these ions in other LDHs, such as magnesium–aluminium analogues.

Table 3.5: The cell parameters and interlayer distances of the Fe^{2+} containing precursor LDHs, parameters of MgAl analogues have been included for reference.

Sample	Cell parameters (Å)		Interlayer
	a	c	distance (Å)
FeAl-CO_3	3.120	22.52	2.701
$MgFeAl_a$-CO_3	3.103	22.47	2.690
$MgFeAl_b$-CO_3	3.117	22.49	2.697
$MgFeAl_c$-CO_3	3.039	22.55	2.717
MgAl-CO_3	3.042	22.65	2.750
FeAl-NO_3	3.114	26.51	4.037
$MgFeAl_b$-NO_3	3.109	26.48	4.027
$MgFeAl_c$-NO_3	3.044	26.71	4.103
MgAl-NO_3	3.042	26.65	4.083
FeAl-Cl	3.125	22.92	2.840
$MgFeAl_a$-Cl	3.122	23.11	2.903
$MgFeAl_b$-Cl	3.119	22.94	2.847
$MgFeAl_c$-Cl	3.042	22.99	2.863
MgAl-Cl	3.046	23.01	2.870

3.3.2 Fourier transform infrared spectrosopy

FTIR spectra of the LDH samples were typical of inorganic LDHs, displaying broad absorptions around 3400 cm^{-1} and absorptions around 800 cm^{-1}, attributable to the O−H stretching modes of the metal hydroxide layers and cointercalated water, and the various M−OH modes respectively. The intense absorption from the carbonate ions was present in all carbonate LDHs at 1353 cm^{-1}, and absent in all decarbonated samples. The absorption corresponding to the nitrate ions at 1342 cm^{-1} was seen in all nitrate LDHs, while the chloride LDHs displayed no absorptions relating to intercalated ions.

3.3.3 Thermogravimetric and elemental analysis

The amount of cointercalated water in the LDHs was discerned through TGA. C, H, N elemental analysis allowed the amounts of nitrate and carbonate to be calculated in their respective LDHs, alongside the overall hydrogen content in all samples. The

ratio of metal ions was obtained through EDX, as well as chloride for the relevant LDHs. Combining this data allowed the formulae of the LDHs, given in Table 3.6, to be calculated.

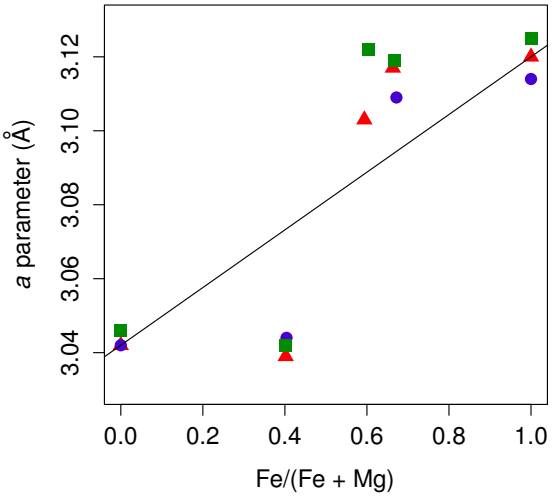


Figure 3.16: Variation of the lattice parameter a as a function of the Fe/(Fe + Mg) ratio in the Fe^{2+} containing LDH samples. The interlayer anions of the LDHs are carbonate, ▲, nitrate, ● and chloride, ■. The values that would be predicted by Vegard's correlation are indicated by the black line.

The EDX data reveals that Mg ions are incorporated into the LDH layers less readily than Fe ions, as in all samples the recorded M^{2+} ion ratio is higher in favour of Fe than in initial reactant ratios. This contrasts with the observations of Liu *et al.* who found that in a series of ternary LDHs synthesised though the homogeneous coprecipitation, where M^{2+} = Co and M'^{2+} = Fe or Zn, the ratio of M^{2+} ions in both the reactants and resulting LDHs changed little. The greater difference in size between Mg^{2+} and Fe^{2+} compared to the ion pairs investigated by Liu and co-workers may explain why Mg is incorporated less readily into the reported LDHs. EDX also confirms that selective dissolution of metal ions during decarbonation is minimal, as the metal ratios in the decarbonated LDHs remain largely unaltered.

Attempts to correlate the observed ratios of M^{2+} ions with the lattice parameter a, indicate that a direct relationship cannot be made, as a plot of a as a function of Fe/(Fe + Mg) reveals in Figure 3.16. The relationship between Fe : Mg ratio and the a parameter does not obey Vegard's correlation, despite that fact that in similar ternary and quaternary systems, a strong correlation between M^{2+} ratios and the a parameter, and also M^{3+} ratios and the a parameter has been observed. However, it

Table 3.6: Water content, metal ion ratios and formulae of the Fe^{2+} containing precursor LDHs.

Sample	Water Content (W/W%)	Mg : Fe : Al ratio	Formula
FeAl-CO_3	9.2	0:1.97:1	$Fe_{1.99}Al_{1.01}(OH)_6(CO_3)_{0.51} \cdot 1.5H_2O$
$MgFeAl_a$-CO_3	9.0	0.78:1.14:1	$Mg_{0.80}Fe_{1.17}Al_{1.03}(OH)_6(CO_3)_{0.51} \cdot 1.3H_2O$
$MgFeAl_b$-CO_3	10.0	0.65:1.28:1	$Mg_{0.67}Fe_{1.31}Al_{1.02}(OH)_6(CO_3)_{0.51} \cdot 1.5H_2O$
$MgFeAl_c$-CO_3	9.1	1.22:0.82:1	$Mg_{1.20}Fe_{0.81}Al_{0.99}(OH)_6(CO_3)_{0.49} \cdot 1.3H_2O$
FeAl-NO_3	5.2	0:1.96:1	$Fe_{1.99}Al_{1.01}(OH)_6(NO_3)_{1.01} \cdot 0.9H_2O$
$MgFeAl_b$-NO_3	6.7	0.63:1.29:1	$Mg_{0.65}Fe_{1.33}Al_{1.03}(OH)_6(NO_3)_{1.03} \cdot 1.1H_2O$
$MgFeAl_c$-NO_3	6.4	1.21:0.82:1	$Mg_{1.20}Fe_{0.81}Al_{0.99}(OH)_6(NO_3)_{0.99} \cdot H_2O$
FeAl-Cl	4.4	0:1.97:1	$Fe_{1.99}Al_{1.01}(OH)_6Cl_{1.01} \cdot 0.7H_2O$
$MgFeAl_a$-Cl	5.6	0.75:1.14:1	$Mg_{0.78}Fe_{1.18}Al_{1.04}(OH)_6Cl_{1.04} \cdot 0.8H_2O$
$MgFeAl_b$-Cl	6.8	0.64:1.28:1	$Mg_{0.66}Fe_{1.31}Al_{1.03}(OH)_6Cl_{1.03} \cdot H_2O$
$MgFeAl_c$-Cl	6.4	1.21:0.81:1	$Mg_{1.20}Fe_{0.80}Al_{0.99}(OH)_6Cl_{0.99} \cdot 0.9H_2O$

has also been observed that LDH systems specifically containing ratios of Mg^{2+} and a ternary M^{2+} ion do not obey Vegard's correlation and it has been speculated that this is due to the smaller size of the Mg^{2+} ions.[44,45] In this instance, the values of the a parameters tend to one of two limits, either 3.04 or 3.10 Å, the a parameters of magnesium–aluminium and iron–aluminium LDHs respectively, depending on whether Mg or Fe is the more abundant ion. In contrast, the c lattice parameter exhibited no change with the ratio of M^{2+} ions, as is consistent with observations from other systems.

3.3.4 Scanning electron microscopy

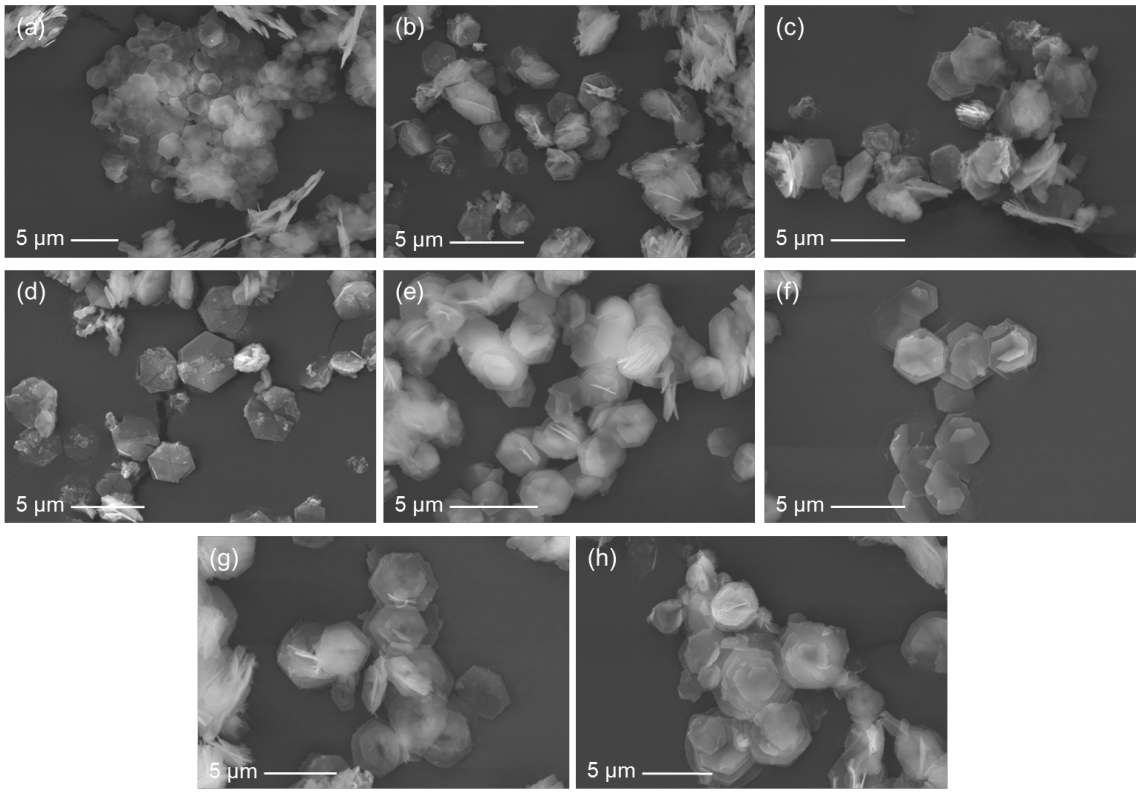


Figure 3.17: SEM images of (a) FeAl-CO_3, (b) $MgFeAl_a$-CO_3, (c) $MgFeAl_b$-CO_3, (d) $MgFeAl_c$-CO_3, (e) FeAl-Cl, (f) $MgFeAl_a$-Cl, (g) $MgFeAl_b$-NO_3 and (h) $MgFeAl_c$-NO_3.

The Fe^{2+} containing LDHs all exhibit well-defined platelet morphologies, as is typical with samples synthesised through homogeneous coprecipitation. The shape of the platelets range from sharp regular hexagons through to rounded hexagon-like shapes, as can be seen from Figure 3.17. The iron-aluminium samples consisted of platelets

that were, on average, shaper and more angular, whereas samples that also contained magnesium exhibited a higher proportion of rounded platelets, whilst also containing more small particles that seem to have formed from the breaking up of the larger platelets. The diameters of the platelets range from 1 to 4 µm, whilst the small 'broken' particles have diameters between 0.1 and 1 µm. The aspect ratio of all platelets is very high, with no platelets exhibiting thicknesses large enough to be accurately measured through SEM. Decarbonation had no major effects on the morphology of the platelets, although more broken platelets were observed in the decarbonated samples, due them being exposed to mechanical wear during the decarbonation procedure. Minor pitting was observed in occasional dercarbonated particles, although most particles observed did not exhibit this phenomenon. Although some aggregation of particles was observed, it was not prevalent in any of the samples, which all displayed lone particles as well as small aggregations of particles.

3.4 Intercalation of L-DOPA into LDHs containing Fe^{2+}

Intercalation of C-DOPA and M-DOPA into an LDH via ion-exchange has been demonstrated with MgAl-NO_3, and was revealed to be largely similar to intercalation of L-DOPA, so to avoid repetition of predictable and unnecessary results, only the intercalation of L-DOPA into the Fe^{2+} containing LDHs was attempted. Seven different precursor LDHs were trialled for intercalation of L-DOPA: FeAl-NO_3, $MgFeAl_b$-NO_3, $MgFeAl_c$-NO_3, FeAl-Cl, $MgFeAl_a$-Cl, $MgFeAl_b$-Cl and $MgFeAl_c$-Cl. All intercalation attempts were conducted under a gentle flow of N_2 gas and protected from light. An extensive range of parameters was trialled for the intercalation reactions, ranging from reaction times of one hour up to two days, reaction pHs ranging from 6.8 through to 11.5, reaction temperatures ranging from 25 to 90 °C and a wide series of drug concentrations and drug : precursor LDH ratios. Despite these attempts, of the seven precursor LDHs, only $MgFeAl_c$-NO_3 successfully underwent ion-exchange reactions to yield the intended nanohybrid product.

The nanohybrid product from the successful ion-exchange reaction, $MgFeAl_c$-LDOPA,

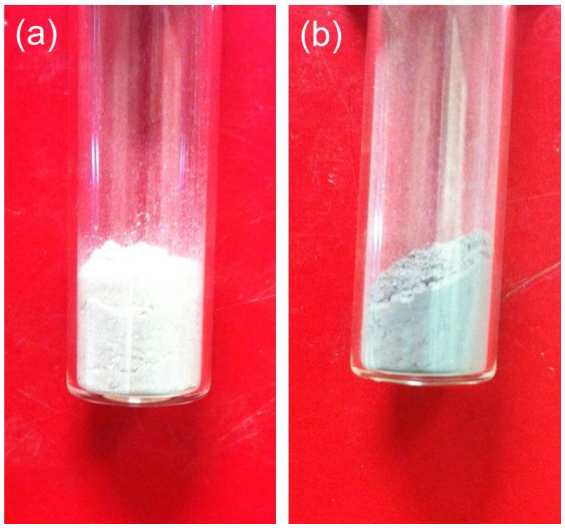


Figure 3.18: The ion-exchange precursor LDH $MgFeAl_c$-NO_3, (a), and the drug intercalated nanohybrid $MgFeAl_c$-LDOPA, (b).

was a bright, pale purple colour, as can be seen in Figure 3.18, alongside the LDH precursor. The products of unsuccessful intercalation reactions were mainly mid to dark brown in colour, although the products of some partially successful intercalation reactions involving $MgFeAl_b$-NO_3, were brown–purple in colour. Despite chloride ions being generally understood as labile and readily exchangeable from interlayer regions of LDHs, none of the chloride LDHs showed any signs of of successful intercalation, although the change of colour in all cases indicates oxidation of the Fe^{2+} ions within the layers to Fe^{3+}. The attempted exchange reactions with the nitrate LDHs reveals a trend that the greater the iron content of the precursor LDH, the less readily it will intercalate L-DOPA, as reactions involving FeAl-NO_3 were completely unsuccessful in all cases, those involving $MgFeAl_b$-NO_3 were partially successful, as already stated, and those involving $MgFeAl_c$-NO_3 were generally successful.

3.4.1 Powder X-ray diffraction

The powder X-ray diffraction pattern of $MgFeAl_c$-LDOPA, seen in Figure 3.19 alongside the pattern of its precursor LDH, indicates successful intercalation of the L-DOPA ion. The diffraction pattern closely resembles that of MgAl-LDOPA, and can be indexed to the same symmetry. The $(00l)$ Bragg reflections fall at very similar values ($d_{003} = 13.9\,\text{Å}$, $2\theta = 6.33°$) to those of the magnesium–aluminium analogues,

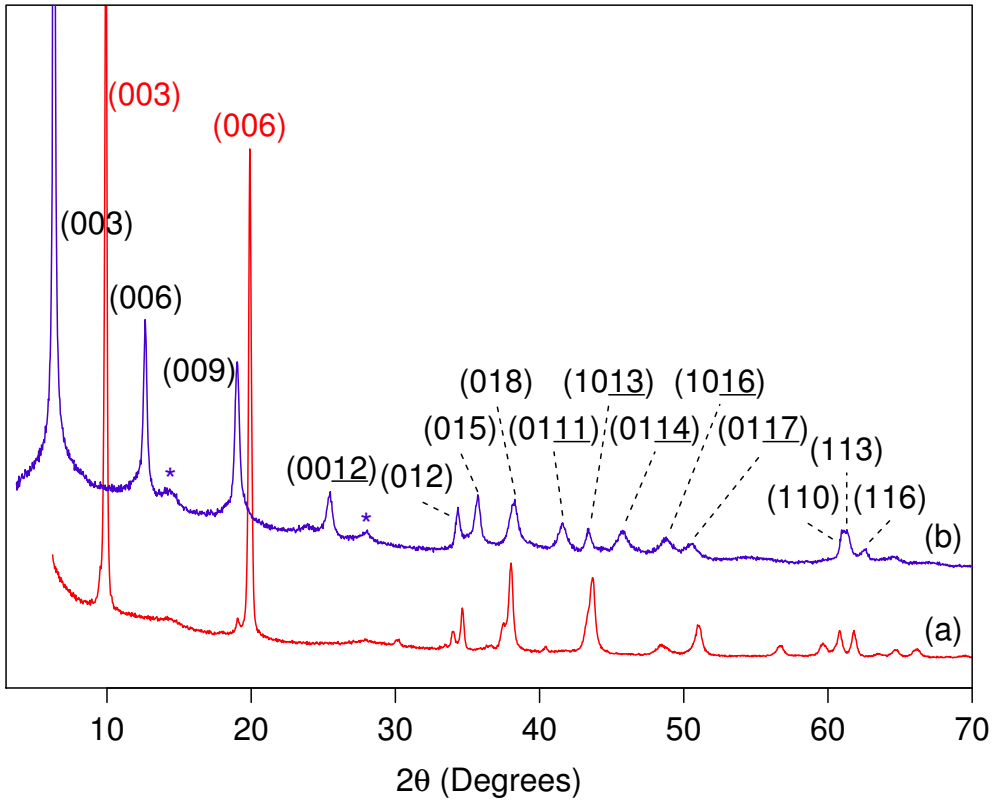


Figure 3.19: The powder XRD patterns of (a) $MgFeAl_c$-NO_3 and (b) $MgFeAl_c$-LDOPA. * denotes brucite, $Mg(OH)_2$, impurity phase.

and calculation of the c lattice parameter gives a value of 41.91 Å. Using this value, an interlayer distance of 9.2 Å can be calculated, which is marginally smaller than the figure calculated for MgAl-LDOPA, 9.3 Å. The a lattice parameter of the nanohybrid is 3.38 Å, showing little change from that of the precursor LDH. Again, this is to be expected, as the a parameter is primarily influences by the metal hydroxide layers. Bragg reflections from the brucite impurity that was present in the precursor LDH can still be seen in the diffraction pattern of the nanohybrid.

3.4.2 Fourier transform infrared spectroscopy

The FTIR spectrum of $MgFeAl_c$-LDOPA, seen in Figure 3.20 bears close resemblance to that of MgAl-$LDOPA_{IE}$, which was depicted in Figure 3.6, showing characteristic absorptions from both the drug ion and from the LDH layers. Shifts and broadening of absorptions relating to the drug ion that were observed in the magnesium–aluminium nanohybrid can also be seen in the iron containing analogue. They can be assigned

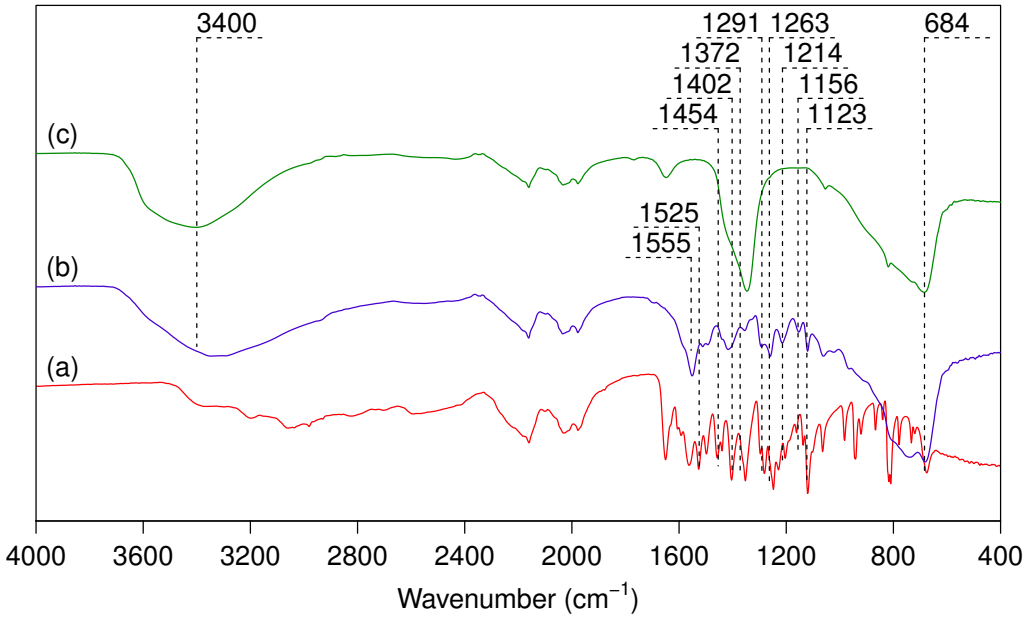


Figure 3.20: FTIR spectra of (a) pristine L-DOPA, (b) $MgFeAl_c$-LDOPA and (c) $MgFeAl_c$-NO_3.

to the same stretching and bending modes detailed in Section 3.2.2, with absorptions at 1551 and 1403 cm^{-1} corresponding to the asymmetric and symmetric carboxylate stretching modes respectively, absorptions at 1282 and 1250 cm^{-1} corresponding to bending modes of the catechol groups, the absorption at 1352 cm^{-1} corresponding to ring deformation modes and the absorption at 1119 cm^{-1} corresponding to the C−N stretching mode. The two broad absorptions of the metal hydroxide layers are clearly present at 3400 and 800 cm^{-1}, corresponding to the O−H stretching modes from the metal hydroxide layers and intercalated water, and to the M−OH stretching modes. The absorption relating to nitrate ions seen in the precursor LDH at 1346 cm^{-1} is absent in the nanohybrid sample, indicating negligible amounts of the precursor ion remain.

3.4.3 Solid state ^{13}C NMR spectroscopy

As with the magnesium–aluminium analogue, the solid state ^{13}C CP/MAS NMR spectrum of $MgFeAl_c$-LDOPA confirmed the presence of L-DOPA ions within the metal hydroxide layers, and showed no evidence that any decomposition products had been intercalated. The spectrum exhibited resonances at δ = 181, 150, 144,

129, 119, 53 and 41 ppm, which were in good agreement with those of pristine L-DOPA, detailed in Section 3.2.3, with the exception that the three resonances from unsubstituted aromatic carbon atoms had coalesced into a single peak, as seen in the spectra of other nanohybrids. As was the case in the spectra of the magnesium–aluminium nanohybrids, broadening of the resonances is seen in the spectrum of $MgFeAl_c$-LDOPA, relative to that of the pristine drug sample, due to variations in drug ion conformation and orientation in the interlayer region, creating a greater variation in the chemical environments experienced by the intercalated drug ions.

The similarity of the spectra of the magnesium–aluminium nanohybrid and the iron containing analogue indicates that there is no major influence on the chemical environments of the drug ions from the presence of Fe^{2+} ions in the metal hydroxide layers, indicating that the iron ions adopt a low spin, diamagnetic electron configuration, as is typical, rather than a high spin, paramagnetic configuration, which would be expected to have a noticeable effect on the chemical environments of the interlayer species.

3.4.4 Dissolution experiments

The ^{1}H NMR spectrum of $MgFeAl_c$-LDOPA dissolved in DCl/D_2O shows resonances at chemical shift values of $\delta = 4.76$ ppm (1H, d, $J = 8.1$ Hz), 4.71 ppm (1H, d, $J = 2.1$ Hz), 4.59 ppm (1H, dd, $J = 8.1$, 2.1 Hz), 2.22 ppm (1H, dd, $J = 7.4$, 5.4 Hz), 1.10 ppm (1H, dd, $J = 14.7$, 5.4 Hz) and 0.98 ppm (1H, dd, $J = 14.7$, 7.4 Hz), confirming that L-DOPA is returned upon dissolution of the nanohybrid. In addition, a large solvent resonance corresponding to water was seen, due to the dissolution of the metal hydroxide layers. No other resonances were seen in the spectrum, suggesting that no measurable decomposition of the drug ions occurred during the ion exchange process. Upon dissolution of the nanohybrid, the resulting solution was bright yellow–green in colour, which gradually turned yellow–orange over the course of 2 – 3 h, which is characteristic of $FeCl_2$ oxidation to $FeCl_3$ *in situ*.

3.4.5 Thermogravimetric and elemental analysis

As with the magnesium–aluminium nanohybrids, thermogravimetric analysis, C, H, N elemental analysis and energy-dispersive X-ray spectroscopy were used in conjunction to arrive at an estimated formula for $MgFeAl_c$-LDOPA. TGA allowed the water content of the nanohybrid to be calculated, with 7.9 % mass loss occurring in the sample between 30 and 130 °C, which is attributable to loss of adsorbed and cointercalated water. The ratio of metal ions was established by EDX as $Mg : Fe : Al = 1.18(\pm 0.005) : 0.79(\pm 0.005) : 1$, which is largely unchanged from the precursor LDH, showing only very minimal leaching of iron and magnesium ions during the ion-exchange procedure. C, H, N elemental analysis data, which is included in full in Appendix B.1, provides a figure for the drug content of 32.8 % by mass. Drawing these figures together, the estimated formula of the nanohybrid can be given as $Mg_{1.19}Fe_{0.80}Al_{1.01}(OH)_6(C_9H_{10}NO_4)_{0.64}(NO_3)_{0.37} \cdot 1.7H_2O$, which indicates a drug loading of 63 % of the theoretical maximum, sufficiently high to facilitate practicable dosages of the nanohybrid.

Further measurements from the TGA data corroborate the estimated formula. Subsequent stages of mass loss to the sample, first of 8.0 % of the total mass between 240 and 340 °C, corresponding to drug decarboxylation, and secondly of 24.0 % of the total mass between 380 and 455 °C, corresponding to loss of the remaining organic species, are in good agreement with those values calculated from the formula given above, the calculated figures being 7.4 and 25.4 % respectively. A final mass loss attributable to the loss of any remaining nitrate ions was seen between 390 and 540 °C.

3.4.6 Scanning electron microscopy

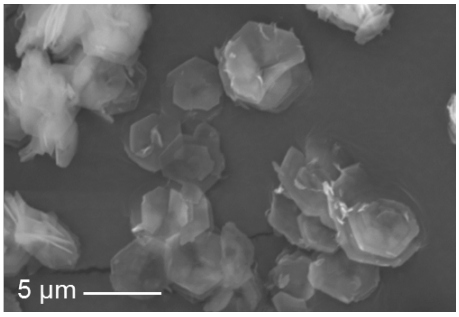


Figure 3.21: An SEM image of $MgFeAl_c$-LDOPA.

The ion-exchange process did not significantly affect the morphology of $MgFeAl_c$-LDOPA, as can be seen from the SEM image of the particles in Figure 3.21. The hexagonal platelet morphology of the precursor LDH, seen in Figure 3.17(h), closely resembles that of the nanohybrid, with few noticeable differences. The SEM images of $MgFeAl_c$-LDOPA show slightly greater numbers of smaller, irregular particles, indicative of some degree of mechanical wear during the ion-exchange process, causing some LDH platelets to fracture into smaller pieces. Consequently, the average size of the nanohybrid particles is marginally smaller than that of the precursor, with a greater range in platelet diameters also seen, mostly falling within 0.5 to 5 µm.

3.5 Nanohybrid release behaviour

The release behaviour of the nanohybrids was investigated in three biomimetic buffer solutions with pH values of 2.0 (stomach acid before eating), 4.0 (stomach acid after eating) and 7.0 (intestinal fluid). The cumulative release profiles of all the samples in each buffer are shown in Figure 3.22. The release profiles are typical of those for LDH particles, consisting of two phases: an initial, rapid release of the majority of the intercalated drug ions, followed by a gradual release of the remaining intercalate. The initial release consists of dissolution of drug ions on and close to the surface of the particles, whilst the progress of the gradual release phase is mediated by diffusion of the drug and buffer ions through the LDH layers. Due to the rapid initial release

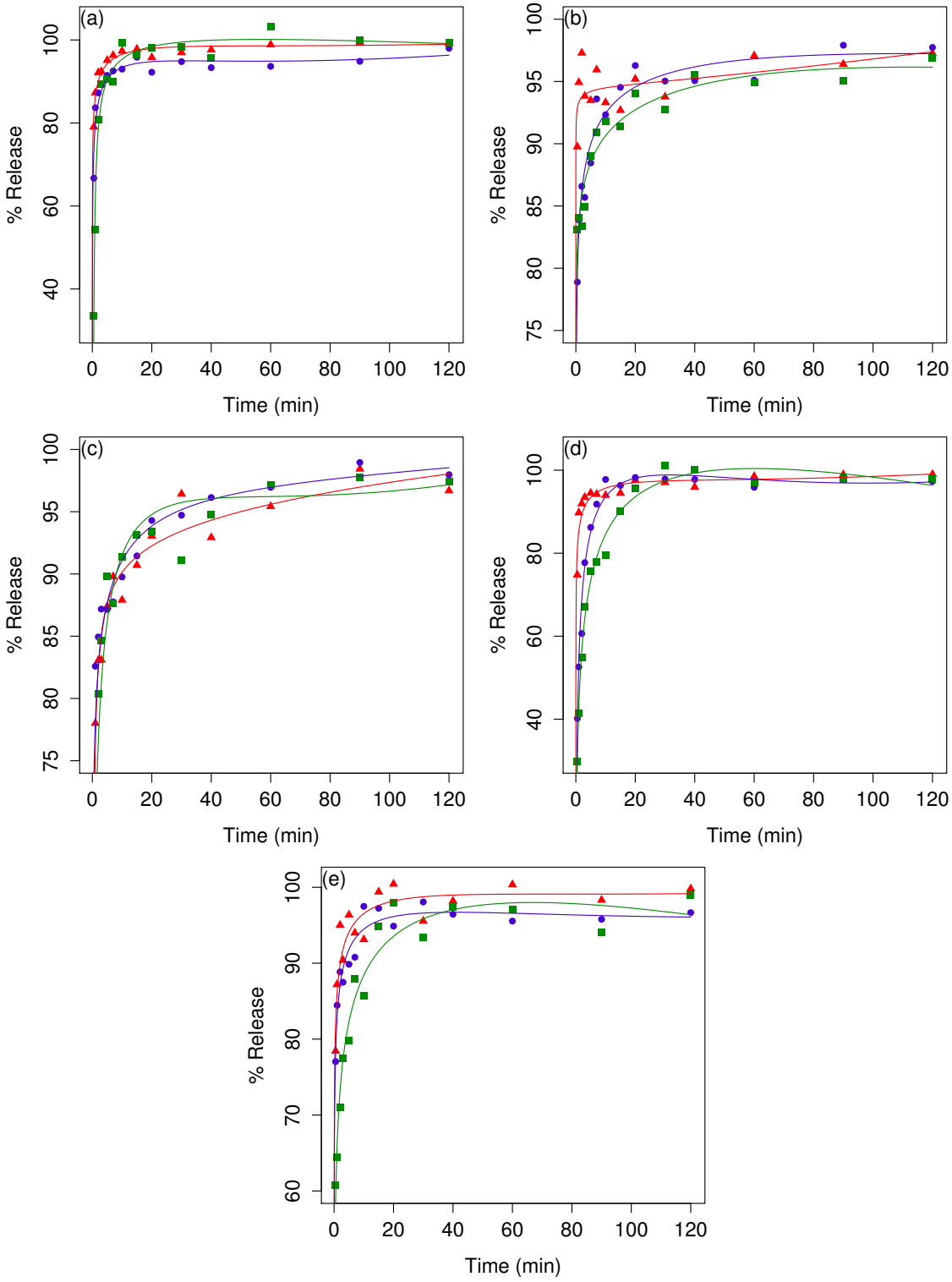


Figure 3.22: *In vitro* release profiles of (a) MgAl-LDOPA$_{IE}$, (b) MgAl-MDOPA$_{IE}$, (c) MgAl-CDOPA$_{IE}$, (d) MgAl-LDOPA$_{CP}$ and (e) MgFeAl$_c$-LDOPA, at 37 °C in pH 2.0 sulphate buffer, ▲, pH 4.0 phosphate buffer, ●, and pH 7.0 phosphate buffer, ■.

phase, all nanohybrids released 90 % of their intercalated drugs within the first 20 min, with release occurring more quickly in more acidic buffer solutions in almost all cases, and 90 % release of intercalated drug ions being reached within 10 min for all samples in the pH 2.0 and 4.0 buffers. This is due to the contribution from dissolution of the LDH layers, in addition to drug ion dissolution and deintercalation, which occurs to a greater extent at a more acidic pH. Interestingly, in both MgAl-LDOPA$_{IE}$ and MgAl-CDOPA$_{IE}$ release occurs at very similar rates at all three pHs, whereas in the other three samples, there is a clear influence from the pH of the buffer solution, with initial rate following the trend pH 2 > pH 4 > pH 7. In the cases of MgAl-MDOPA$_{IE}$ and MgAl-LDOPA$_{CP}$, release at pH 2 happens very rapidly, with near complete release occurring in under a minute.

Although characterisation of MgAl-LDOPA$_{CP}$ revealed that the intercalated species in this sample was not L-DOPA, release of the intercalated guests ion could still be measured, and is included for comparison with the other nanohybrids due to its significantly different morphology, although this does not seem to have impacted significantly on the rate of release, which closely resembles that of the other nanohybrids. MgFeAl$_c$-LDOPA shows the slowest initial release rate at pH 7.0, where deintercalation is a primary mechanism, whereas at lower pH values its release rate is similar to those of the other nanohybrids. No clear trend or major differences can be seen between release rates of the different drug ions, which is unsurprising as they are all similar in both size and chemistry.

3.5.1 Kinetic analysis

As with the release profiles of the nanohybrids in Chapter 2, the release profiles of the catecholamine nanohybrids were assessed for their fit against five models commonly used to describe release from LDHs and other layered compounds. The models, also detailed in Section 2.4.1, are the Avrami–Erofe'ev model, the Elovich model, a simple first order model, the modified Freunlich model and a parabolic diffusion model, and their fit was evaluated using a least squares regression.[46–53] The correlation coefficients, r^2, for the fit of each model are detailed in Table 3.7.

All models except the simple first order model show a reasonably good fit to the data

Table 3.7: Evaluation of different kinetic models of release using correlation coefficients, r^2. Highlighted figure indicates closest fit for each release profile.

Sample	Buffer pH	Model correlation coefficient, r^2				
		Avrami–Erofe'ev	Elovich	Simple first order	Modified Freundlich	Parabolic diffusion
MgAl-LDOPA$_{IE}$	2.0	0.912	0.773	0.287	0.911	0.783
	4.0	0.764	0.664	0.220	0.789	0.754
	7.0	0.809	0.692	0.169	0.769	0.779
MgAl-MDOPA$_{IE}$	2.0	0.274	0.301	0.297	0.257	0.756
	4.0	0.927	0.904	0.441	0.907	0.854
	7.0	0.928	0.922	0.542	0.912	0.911
MgAl-CDOPA$_{IE}$	2.0	0.914	0.847	0.346	0.882	0.790
	4.0	0.941	0.880	0.417	0.889	0.784
	7.0	0.881	0.759	0.240	0.945	0.768
MgAl-LDOPA$_{CP}$	2.0	0.866	0.687	0.266	0.883	0.723
	4.0	0.819	0.778	0.225	0.813	0.841
	7.0	0.952	0.901	0.309	0.946	0.855
MgFeAl$_c$-LDOPA	2.0	0.739	0.705	0.270	0.664	0.769
	4.0	0.736	0.770	0.264	0.678	0.820
	7.0	0.886	0.892	0.377	0.808	0.878

for most cases, with the Avrami–Erofe'ev model exhibiting the closest fit for the majority of release profiles, and consistently showing a good fit to all profiles except that of MgAl-MDOPA$_{IE}$ at pH 2. However, this profile is an anomaly in that release occurs unusually quickly, and so the data in this instance does not provide enough data points within the useful range to allow any of the models to be fitted accurately. Besides the Avrami–Erofe'ev model, the modified Freundlich model shows a good fit in many cases, particularly to those samples that showed slower rates of release at pH 7. Additionally, the parabolic diffusion model exhibits the best fit in instances of release at pH 4 for several samples.

As both the Avrami–Erofe'ev and modified Freundlich models exhibit good fits to the data, these models can be used for for extracting kinetic and mechanistic information about the release of the catecholamine drugs. Both models provide figures for the rate constant, and so will be denoted k_{AE} and k_F, for the Avrami–Erofe'ev and modified Freundlich models, respectively. While the constant, n, given

by the modified Freundlich model is arbitrary and as no physical significance, n for the Avrami–Erofe'ev model denotes the reaction exponent, which may provide mechanistic information. Table 3.8 gives the rate constants and reaction exponents extracted from the data.

Table 3.8: Values of the rate constants, k_{EA} and k_F, and reaction exponents, n, for the release of catecholamine drugs in buffers of varying pH, as determined by the Avrami–Erofe'ev and modified Freundlich models.

Sample	Buffer pH	Reaction exponent, n	Rate constant, $k_{EA} \times 10^{-3}$ (s^{-1})	Rate constant, $k_F \times 10^{-3}$ (s^{-1})
MgAl-LDOPA$_{IE}$	2.0	0.100	2.085	0.131
	4.0	0.151	1.714	0.175
	7.0	0.361	0.990	0.365
MgAl-MDOPA$_{IE}$	2.0	0.120	2.006	0.140
	4.0	0.310	0.928	0.355
	7.0	0.182	0.601	0.646
MgAl-CDOPA$_{IE}$	2.0	0.208	2.062	0.135
	4.0	0.158	1.901	0.144
	7.0	0.181	1.112	0.369
MgAl-LDOPA$_{CP}$	2.0	0.115	1.386	0.267
	4.0	0.092	1.507	0.249
	7.0	0.166	1.216	0.301
MgFeAl$_c$-LDOPA	2.0	0.119	2.710	0.065
	4.0	0.078	1.783	0.177
	7.0	0.062	1.801	0.172

In all cases, the reaction exponent, n, given by the Avrami–Erofe'ev model is < 0.5, which, as discussed in Section 2.4.1, indicates that the release is diffusion controlled, rather than controlled by the proliferation and growth of nucleation sites for release. The two models give differing figures for the reaction constants, with the Avrami–Erofe'ev model indicating a consistently higher rate constant for release, in some cases by over a factor of 10. In is also interesting to note that the release data that gives the highest and lowest rate constants in one model does not give the same highest and lowest rate constants in the other model.

3.6 Decomposition studies

All drug containing nanohybrids were assessed for their ability to stabilise the intercalated drug ions with respect to their main route of decomposition, oxidation, and in the case of L-DOPA, with respect to racemisation, which is the only route of decomposition that has previously been reported as being stabilised through intercalation.[3] For comparison, the speed with which the intercalated guest of MgAl-LDOPA$_{CP}$ decomposed into melanin was also investigated, as well as samples of the pristine drugs. The stability of the nanohybrids was investigated at room temperature, 40 and 80 °C, and also upon exposure to ultraviolet radiation, $\lambda = 254$ nm. The stability of the samples when dry and also when suspended water were investigated, using UV and NMR spectroscopy, and also circular dichroism analysis.

3.6.1 Stability in dry conditions

In all nanohybrid samples gradual discolouration occurred over time, and occurring more rapidly in more extreme conditions. Both the UV and NMR spectra of the various samples reveal a gradual build-up of melanin or pseudomelanin in the samples, alongside an accompanying reduction in the levels of the guest ions, although in all cases the guest ions remained the major species during the course of the stability studies. The samples for UV and circular dichroism analysis were prepared by dissolving the samples in dilute HCl as detailed in Section 6.5.6, whilst ^{1}H NMR spectroscopic analysis was performed in DCl/D_2O with samples prepared in the same manner as those for the dissolution experiments detailed in Section 3.2.4.

The results from UV spectroscopy provided accurate figures for the concentration of the drug ions, and whilst they cannot provide accurate figures for the concentration of decomposition products, due to these being a mixture of different species, as all these species exhibit UV absorption within a similar frequency range, an aggregated concentration of the decomposition products could be approximated as another marker of progress of the decomposition reactions. The UV spectroscopy results for MgAl-LDOPA$_{IE}$ and pristine L-DOPA can be seen in Figure 3.23, whilst results for all the other samples can be found in Appendix B.2. All samples exhibit pseudo

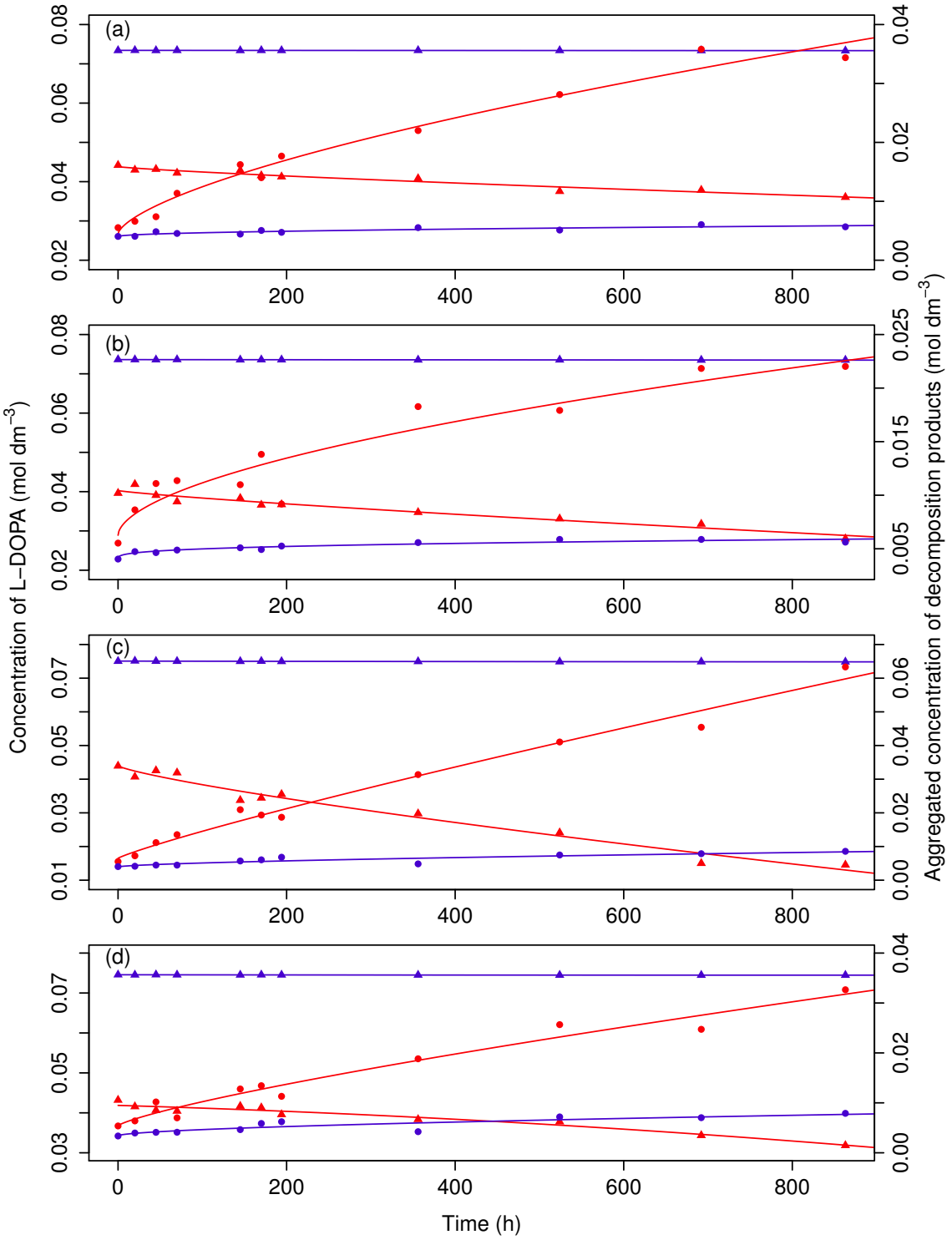


Figure 3.23: The decomposition profiles of MgAl-LDOPA$_{\mathrm{IE}}$ (red) and pristine L-DOPA (blue) in dry conditions at (a) room temperature, (b) 40 °C, (c) 80 °C, and (d) under exposure to ultraviolet radiation. The concentrations of L-DOPA (▲) and the aggregated concentrations of the decomposition products (●) are represented as a function of reaction time, measured through UV spectroscopic analysis.

first order reaction rates with respect to oxidative decomposition, observed from the linear relationship between the natural logarithm of the drug concentration, ln[drug], and the reaction time, t, which can be seen from examples plotted in Figure 3.24. As expected, samples kept at higher temperatures showed more rapid reduction in drug concentration, with those kept at 40 °C reacting faster by factors of 1.53–2.42, and those kept at 80 °C reacting faster by factors of 5.46–7.74, when compared to equivalent samples kept at 20°. Although significant discolouration is observed in the samples exposed to ultraviolet radiation, this was not reflected in their rates of decomposition, which were only marginally greater than that of the control samples, showing only an increase in the reaction rate of between factors of 1.14–1.27. This is likely due to the inability of the ultraviolet radiation to penetrate the solid samples, as its effect is more pronounced on dissolved and suspended samples, as reported in Section 3.6.2.

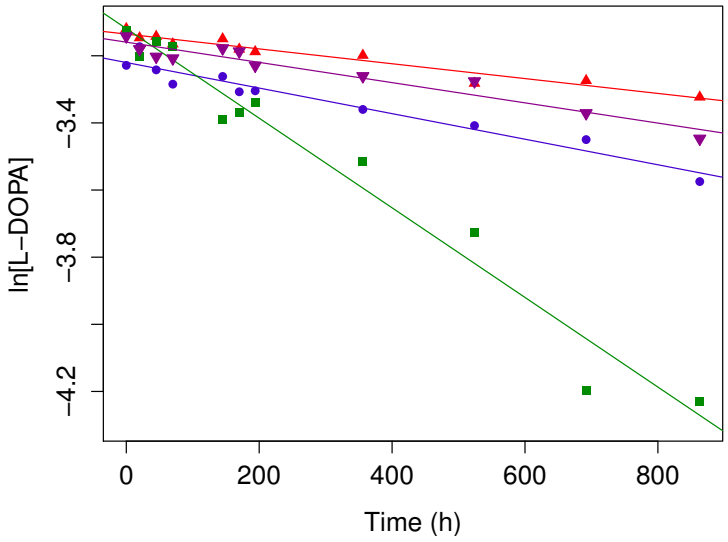


Figure 3.24: The natural logarithm of L-DOPA concentration as a function of time during the decomposition studies in dry conditions at room temperature, ▲, 40 °C, ●, 80 °C, ■, and under exposure to ultraviolet radiation, ▼, with MgAl-LDOPA$_{IE}$, from which the rate constant for oxidative decomposition, k_{obs}, can be calculated.

The effect of LDH intercalation on the stability of the drug ions in the solid state is pronounced, but rather than increasing stability, the rate of oxidative decomposition is invariably increased by intercalation. This can be seen most clearly by comparing the rate constants for decomposition, k_{obs}, of the pristine drugs and their nanohybrid analogues, detailed in Table 3.9. The figures for k_{obs} were obtained by taking the

Table 3.9: The observed rate constants, k_{obs}, for oxidative decomposition of pristine catecholamine drugs and their nanohybrid analogues in dry conditions as a function of temperature and ultraviolet radiation exposure, calculated from UV spectroscopy.

Sample	Decomposition rate constant, $k_{obs} \times 10^{10}$ (s^{-1})			
	20 °C	40 °C	80 °C	20 °C; $h\nu$
Pristine L-DOPA	2.41	5.88	12.6	3.63
Pristine M-DOPA	6.96	13.3	23.0	8.89
Pristine C-DOPA	5.23	11.3	22.6	9.01
MgAl-LDOPA$_{IE}$	659	1010	3800	754
MgAl-MDOPA$_{IE}$	1260	2040	6880	1450
MgAl-CDOPA$_{IE}$	1240	1910	7120	1580
MgAl-LDOPA$_{CP}$	16500	18100	23400	16600
MgFeAl$_c$-LDOPA	982	2380	7610	1130

gradient of linear models of ln[drug] as a function time, t, from the start of the decomposition experiment, such as those displayed in Figure 3.24. In all cases, k_{obs} values for decomposition in the nanohybrid particles are significantly higher those for decomposition of the equivalent pristine drugs, by between two to three orders of magnitude.

The difference in the stabilities of different drugs is reflected in rate constants of both the pristine drugs and the nanohybrids, with decomposition of M-DOPA giving the highest k_{obs} values, and L-DODA giving the lowest values across a given set of conditions. The destabilising effect of intercalation seemed to have a greater effect on M-DOPA and C-DOPA than L-DOPA. The presence of Fe^{2+} in the metal hydroxide layers also has a measurable effect on the stability of intercalated L-DOPA. However, rather than imparting greater stability on the intercalated drug ions, the rate of oxidative decomposition is significantly greater in MgFeAl$_c$-LDOPA than in MgAl-LDOPA$_{IE}$ under all conditions measured. As might be expected, based on the observation that partial decomposition of L-DOPA occurred during synthesis of MgAl-LDOPA$_{CP}$, this nanohybrid showed much more rapid rates of decomposition than any of those synthesised through ion-exchange.

Using the UV spectroscopy results to provide an accurate value for the drug ion concentrations in the samples, the extent of racemisation in the samples could be

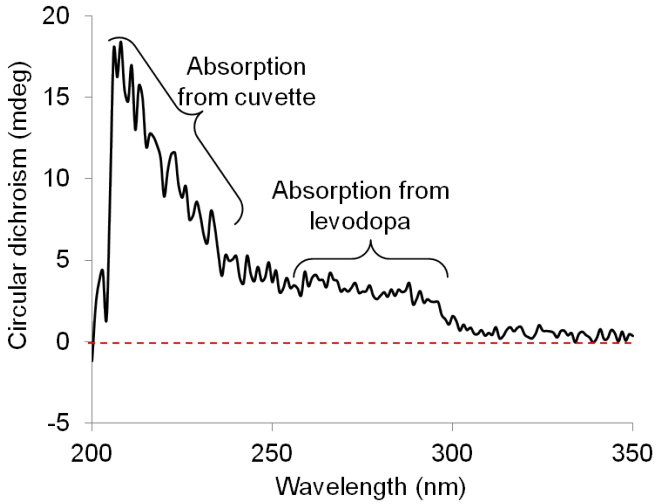


Figure 3.25: An example of a circular dichroism spectrum of a sample of optically pure L-DOPA.

measured using circular dichroism analysis. Circular dichroism measurements allowed much more accurate recording of enantiomeric excess to be taken than would have been possible using a polarimeter, as it provided for recording α_{obs} over a range of wavelengths, allowing any contribution from decomposition products to be identified and corrected for. Across all samples except those of MgAl-LDOPA$_{CP}$, successive circular dichroism spectra, such as the example shown in Figure 3.25, revealed a gradual reduction in α_{obs} over time. Taking into account the gradually decreasing drug concentration in successive samples, the enantiomeric excess of the drug ions in each sample could then be calculated, and revealed that in all cases the enantiomeric excess of the drug ions in each sample remained unchanged over time, and that the reduction in α_{obs} was solely due to a reduction in the concentration of of the drug ions themselves due to oxidative decomposition. Further to this, calculation of the enantiomeric excess showed that no racemisation of the drug ions occurred during the synthesis of any ion-exchange nanohybrids. In contrast, spectra of samples of MgAl-LDOPA$_{CP}$ were not optically active, indicating that the drug ions that were successfully intercalated had been racemised prior to or during intercalation.

Successive NMR spectra of the pristine drugs and the nanohybrids support the findings of the UV spectroscopy. The spectra show resonances corresponding to the drug ions, with chemical shifts and splitting patterns as reported in Section 3.2.4, and to the intermediate decomposition products, with chemical shift values of $\delta = 0.11$,

−0.13 and −0.30 ppm in the L-DOPA containing samples, of δ = 0.71, 0.07, −0.22 and −0.38 ppm in the M-DOPA containing samples, and of δ = 0.67, 0.55, −0.16 and −0.48 ppm in the C-DOPA containing samples. These resonances correspond to the formation of dopachrome and analogous species, which in turn go on to react and polymerise to form melanin and pseudomelanin species, not seen in the NMR spectra themselves as they aggregate into solid particles. Although the relative ratios of the drug ion and decomposition product resonances evolved over time, integration of these resonances could not provide another measure for tracking the progress of the decomposition reactions, as the variations in the observed ratios between the drugs and decompositions products were too great to accurately model the reaction rate. This may be due to the formation of the melanin and pseudomelanin species, which removes the intermediate species from solution.

3.6.2 Stability in wet conditions

The nanohybrids were suspended in water, and solutions of the pristine drug species with similar equivalent drug concentrations were prepared for comparison. Discolouration occurred much more rapidly in the suspensions and solutions than it had in the dry samples, becoming evident within hours. Aliquots of the sample mixtures were extracted at predetermined times, quenched with HCl and diluted to standard concentrations for UV and circular dichroism analysis. An amount of each nanohybrid was suspended in D_2O in an NMR tube for a period of time before addition of DCl and subsequent ^{1}H NMR spectroscopic analysis to confirm that the identities of the decomposition products in solution were the same as those produced by the dry samples.

Results from UV and circular dichroism spectroscopic analysis followed the same general trends as those seen in the results from analysis in the dry conditions, and the plots from which the decomposition rate constants, k_{obs}, were calculated can be found in Appendix B.2. Oxidative decomposition again followed a pseudo first order rate with respect to the drug ions. Both the nanohybrid and pure drug samples show significantly higher rates of oxidative decomposition in wet conditions, with rate constants correspondingly greater by one to two orders of magnitude, reported

Table 3.10: The observed rate constants, k_{obs}, for oxidative decomposition of pristine catecholamine drugs and their nanohybrid analogues in solution or as a suspension in water as a function of temperature and ultraviolet radiation exposure, calculated from UV spectroscopy.

Sample	Decomposition rate constant, $k_{obs} \times 10^9$ (s^{-1})			
	20 °C	40 °C	80 °C	20 °C; $h\nu$
Pristine L-DOPA	3.50	8.42	13.9	8.19
Pristine M-DOPA	4.85	10.0	17.2	10.8
Pristine C-DOPA	4.79	9.03	15.2	13.3
MgAl-$LDOPA_{IE}$	844	2100	4440	2080
MgAl-$MDOPA_{IE}$	1350	2450	4680	2770
MgAl-$CDOPA_{IE}$	1280	2870	6920	3010
MgAl-$LDOPA_{CP}$	9840	10800	11200	10300
$MgFeAl_c$-LDOPA	1410	3440	5050	2860

in Table 3.10.

Decomposition again occurred more rapidly in the nanohybrids than in the pure drug solutions, and increases in temperature had an even greater effect on the rate of decomposition than it had in dry conditions. Exposure to ultraviolet radiation had a much more significant effect on the rates of decomposition in wet conditions, due to the greater ability of the light to penetrate through the solutions and suspensions. The same trend in drug stabilities was observed, with M-DOPA and C-DOPA exhibiting the fastest rates of decomposition and L-DOPA exhibiting the slowest. As in dry conditions, the presence of Fe^{2+} led to more rapid decomposition, and this effect was much more significant in wet conditions, possibly due to partial dissolution of the iron ions allowing them to act as more effective redox catalysts.

Circular dichroism analysis produced the same outcomes in wet condition as in dry conditions. Although there was a gradual reduction in α_{obs} in all samples, this was attributable fully to the reduction in concentrations of the drug ions over time due to oxidative decomposition, and the enantiomeric excess of the drugs in all cases remained constant, with no evidence of racemisation.

The NMR spectra of the partially decomposed nanohybrids exhibited the same resonances as those seen in the spectra of the dry samples after dissolution in DCl/D_2O, corresponding to both the drug ions and the decomposition products.

3.6.3 Discussion

When L-DOPA has been previously intercalated, the only investigation into the stability of the drug that was reported related to its racemisation and its thermal stability, specifically thermally induced decarboxylation.[3] The effect of intercalation on the main route of decomposition, oxidative decomposition, has not been previously addressed. The results of the stability studies indicate that LDH intercalation does not stabilise catecholamine drugs, but in fact the presence of LDH layers seems to destabilise these drugs and accelerate oxidative decomposition. The basic local environment of the LDH layers may be the cause of the increased instability observed. The initial step of the oxidative decomposition process is catalysed by basic conditions, and the presence of the LDH layers creates a basic local environment around the intercalated drug ions, accelerating the initial stage of the decomposition substances. This is analogous to the findings of Jaber *et al.* who found layered inorganic clay materials saponite and laponite catalysed oxidative decomposition of L-DOPA.[24]

The addition of Fe^{2+} ions to the LDH layers, rather than reducing the rate of oxidative decomposition by preferentially oxidising in place of the drug ions, appears to further increase the rate of decomposition. Two factors may explain this effect: firstly, the addition of the iron ions into the layer may increase the basic nature of the local environment, leading to more rapid initiation of the decomposition process. Secondly, after the initial oxidation of some Fe^{2+} to Fe^{3+} ions, the presence of oxidising Fe^{3+} ions may actually act as a catalyst to oxidative decomposition themselves, acting as a redox catalyst between the catecholamine drugs and the O_2 molecules.

Racemisation of the drug ions was prevented by LDH intercalation, as had been previously reported, although as the contribution to drug decomposition from racemisation is negligible compared to that from oxidative decomposition, the utility of this stabilising phenomenon is insignificant. The discovery that the coprecipitation synthesis method, along with causing substantial oxidative decomposition, leads to complete racemisation of L-DOPA gives confirmation that it is not as suitable for the intercalation of catecholamine drugs as the ion-exchange synthesis method.

3.7 Conclusion

Three catecholamine drugs, L-DOPA, M-DOPA and C-DOPA, were intercalated into a magnesium–aluminium LDH using an ion-exchange method. L-DOPA was also intercalated into a magnesium–aluminium LDH using a coprecipitation method. An iron (II)–aluminium LDH and a series of ternary magnesium–iron (II)–aluminium LDHs with varying magnesium to iron ratios were synthesised. The intercalation of L-DOPA into the iron (II) containing LDHs was attempted through an ion-exchange method, and was successfully achieved in one sample. The mass percentage of the drug ions in all the synthesised LDH–drug nanohybrids was greater than 30 %, which is sufficient for therapeutic doses of the drug ions to be delivered by realistic doses of the nanohybrids.

Dissolution experiments of the nanohybrids confirmed that the unaltered drug ions were returned in all ion-exchange samples, whilst decomposition of the drug ions had occurred to some extent in the coprecipitation sample. Drug release profiles of the nanohybrids in biomimetic buffer solutions were recorded, and found to fit the Avrami–Erofe'ev kinetic model of release most closely. Intercalation of the drug ions was found to catalyse the oxidative decomposition of the drug ions into melanin and pseudomelanin. No racemisation of the drug ions was observed over time once intercalated, although the coprecipitation synthesis method was found to racemise L-DOPA. The presence of iron (II) ions in the LDH layers was found to accelerate oxidative decomposition.

It has been established that intercalation into LDHs provides a route for storing catecholamine drugs, although this system leads to accelerated drug decomposition when used in isolation, and so is not suitable for purpose without further modification. However, this system could be combined with another drug delivery technology, such as polymer coating, to prevent decomposition, while still utilising the benefits that LDH intercalation affords. This idea is tested in Chapter 5.

3.8 References

(1) Land, E. J.; Ramsden, C. A.; Riley, P. A. In *Quinones Quinone Enzym. Part A*; Academic Press: 2004; Vol. 378, pp 88–109.
(2) Zhou, Y. Z.; Alany, R. G.; Chuang, V.; Wen, J. *Chromatographia* **2012**, *75*, 597–606.
(3) Wei, M.; Pu, M.; Guo, J.; Han, J.; Li, F.; He, J.; Evans, D. G.; Duan, X. *Chem. Mater.* **2008**, *20*, 5169–5180.
(4) Cotzias, G. C.; Van Woert, M. H.; Schiffer, L. M. *N. Engl. J. Med.* **1967**, *276*, 374–379.
(5) Barbeau, A. *Can. Med. Assoc. J.* **1969**, *101*, 59–68.
(6) Connolly, B. S.; Lang, A. E. *JAMA* **2014**, *311*, 1670–1683.
(7) Fahn, S.; Poewe, W. *Mov. Disord.* **2015**, *30*, 1–3.
(8) Pappert, E. J.; Buhrfiend, C.; Lipton, J. W.; Carvey, P. M.; Stebbins, G. T.; Goetz, C. G. *Mov. Disord.* **1996**, *11*, 24–6.
(9) Pappert, E. J.; Lipton, J. W.; Goetz, C. G.; Ling, Z. D.; Stebbins, G. T.; Carvey, P. M. *Mov. Disord.* **1997**, *12*, 608–610.
(10) Tjaden, K. *Top. Geriatr. Rehabil.* **2008**, *24*, 115–126.
(11) Ertekin, C. *J. Mov. Disord.* **2014**, *7*, 31–56.
(12) Block, G.; Liss, C.; Reines, S.; Irr, J.; Nibbelink, D. English *Eur. Neurol.* **1997**, *37*, 23–27.
(13) Nirenberg, M. J.; Fahn, S. In *Princ. Treat. Park. Dis.* Butterworth-Heinemann: Philadelphia, 2005, pp 3–24.
(14) Almarsson, O.; Meehan, A. J.; Remenar, J.; Zhang, Z. Pharmaceutical compositions and method of using levodopa and carbidopa., 2005.
(15) Ngwuluka, N.; Pillay, V.; Du Toit, L. C.; Ndesendo, V.; Choonara, Y.; Modi, G.; Naidoo, D. *Expert Opin. Drug Deliv.* **2010**, *7*, 203–224.
(16) Antonini, A.; Ray Chaudhuri, K.; Martinez-Martin, P.; Odin, P. English *CNS Drugs* **2010**, *24*, 119–129.
(17) Porter, C. C.; Watson, L. S.; Titus, D. C.; Totaro, J. A.; Byer, S. S. *Biochem. Pharmacol.* **1962**, *11*, 1067–1077.
(18) Pinder, R. M.; Brogden, R. N.; Sawyer, P.; Speight, T. M.; Avery, G. S. English *Drugs* **1976**, *11*, 329–377.
(19) Manyonda, I. T.; Slater, D. M.; Fenske, C.; Hole, D.; Choy, M. Y.; Wilson, C. *BJOG An Int. J. Obstet. Gynaecol.* **1998**, *105*, 641–648.
(20) Sica, D. A. *J. Clin. Hypertens.* **2007**, *9*, 399–405.
(21) Podymow, T.; August, P. *Hypertens.* **2008**, *51*, 960–969.
(22) Gilligan, B.; Wodak, J.; Stark, R.; O'Halloran, M. eng *Med. J. Aust.* **1979**, *2*, 205–207.
(23) Thakur, S.; Chauhan, G. S.; Ahn, J.-H. *Carbohydr. Polym.* **2009**, *76*, 513–520.
(24) Jaber, M.; Bouchoucha, M.; Delmotte, L.; Méthivier, C.; Lambert, J.-F. *J. Phys. Chem. C* **2011**, *115*, 19216–19225.
(25) Duan, X.; Wei, M.; Guo, J.; He, J. Preparation of levodopa chiral intercalated hydrotalcite for the treatment of Parkinson's disease. CN 1850275 A., 2006.
(26) Kura, A. U.; Ali, S. H. H. A.; Hussein, M. Z.; Fakurazi, S.; Arulselvan, P. *Int. J. Nanomedicine* **2013**, *8*, 1103–1110.
(27) Choy, J.-H.; Park, T.; Kim, S.-T.; Son, Y.-H. Pharmaceutical composition for the treatment of cancer comprising LMH-RA complex. WO 2006091009 A1., 2006.
(28) Ryu, S.-J.; Jung, H.; Oh, J.-M.; Lee, J.-K.; Choy, J.-H. *J. Phys. Chem. Solids* **2010**, *71*, 685–688.
(29) Wang, Y.; Wu, P.; Hou, Y.; Zhu, N.; Dang, Z. *Ind. Eng. Chem. Res.* **2012**, *51*, 11128–11136.
(30) de Victoria Rodriguez, M.; Brunet, E.; Nocchetti, M.; Presciutti, F.; Costantino, F. *RSC Adv.* **2014**, *4*, 26912–26917.
(31) Ogawa, M.; Asai, S. *Chem. Mater.* **2000**, *12*, 3253–3255.
(32) Khan, A. I.; Lei, L.; Norquist, A. J.; O'Hare, D. *Chem. Commun.* **2001**, *22*, 2342–2343.

(33) Zhong, J.; Frases, S.; Wang, H.; Casadevall, A.; Stark, R. E. *Biochemistry* **2008**, *47*, 4701–4710.
(34) Chatterjee, S.; Prados-Rosales, R.; Frases, S.; Itin, B.; Casadevall, A.; Stark, R. E. *Biochemistry* **2012**, *51*, 6080–6088.
(35) Katritzky, A. R.; Akhmedov, N. G.; Denisenko, S. N.; Denisko, O. V. *Pigment Cell Res.* **2002**, *15*, 93–97.
(36) Efait, P. R.; Bdelmoula, M. A.; Rolard, F. T.; Énin, J. R. G.; Hrhardt, J. J. E.; Ourrié, G. B. *Am. Mineral.* **2001**, *86*, 731–739.
(37) Ruby, C.; Usman, M.; Naille, S.; Hanna, K.; Carteret, C.; Mullet, M.; François, M.; Abdelmoula, M. *Appl. Clay Sci.* **2010**, *48*, 195–202.
(38) Ma, R.; Liang, J.; Takada, K.; Sasaki, T. *J. Am. Chem. Soc.* **2010**, 613–620.
(39) Liu, Z.; Ma, R.; Ebina, Y.; Iyi, N.; Takada, K.; Sasaki, T. *Langmuir* **2006**, *23*, 861–867.
(40) Chitrakar, R.; Sonoda, A.; Makita, Y.; Hirotsu, T. *Sep. Purif. Technol.* **2011**, *80*, 652–657.
(41) Zhong, Y.; Yang, Q.; Luo, K.; Wu, X.; Li, X.; Liu, Y.; Tang, W.; Zeng, G.; Peng, B. *J. Hazard. Mater.* **2013**, *250–251*, 345–353.
(42) Valente, J. S.; Hernandez-Cortez, J.; Cantu, M. S.; Ferrat, G.; López-Salinas, E. *Catal. Today* **2010**, *150*, 340–345.
(43) Ramos Jiménez, K. N.; Jiménez, Y.; Linares, C. F. *Rev. Lat. Met. Mat.* **2015**, *35*, 315–325.
(44) Tichit, D.; Ribet, S.; Coq, B. *Eur. J. Inorg. Chem.* **2001**, *2001*, 539–546.
(45) Intissar, M.; Segni, R.; Payen, C.; Besse, J.-P.; Leroux, F. *J. Solid State Chem.* **2002**, *167*, 508–516.
(46) Avrami, M. *J. Chem. Phys.* **1939**, *7*, 1103–1112.
(47) Avrami, M. *J. Chem. Phys.* **1940**, *8*, 212–224.
(48) Avrami, M. *J. Chem. Phys.* **1941**, *9*, 177–184.
(49) Hancock, J. D.; Sharp, J. H. *J. Am. Ceram. Soc.* **1972**, *55*, 74–77.
(50) Li, Z. *Langmuir* **1999**, *15*, 6438–6445.
(51) Kodama, T.; Harada, Y.; Ueda, M.; Shimizu, K.; Shuto, K.; Komarneni, S. *Langmuir* **2001**, *17*, 4881–4886.
(52) Yang, J.-H.; Han, Y.-S.; Park, M.; Park, T.; Hwang, S.-J.; Choy, J.-H. *Chem. Mater.* **2007**, *19*, 2679–2685.
(53) Markland, C.; Williams, G. R.; O'Hare, D. *J. Mater. Chem.* **2011**, *21*, 17896–17903.

4. Drug storage and delivery using layered double hydroxide–cyclodextrin nanohybrids

4.1 Introduction

Anionic drugs may be directly intercalated into LDHs; however, the intercalation of neutral and cationic drugs into LDHs requires an additional agent to produce an affinity between the drug species and the interlayer region. One such method that has been used to achieve the intercalation of neutral hydrophobic species is encapsulation within cholate or deoxycholate micelles, which has allowed some poorly soluble neutral species to be intercalated, such as prednisone and camptothecin.[1–3] However, this method has been limited to neutral species, and is dependent on the successful inclusion of target drugs within the hydrophobic interior of the micelles, which is generally undocumented, and does not favour drug species that contain both hydrophobic and hydrophilic sections.

Another potentially wider reaching solution to this problem is through complexation of a desired drug to an anionic cyclodextrin prior to intercalation. Such an approach has been used to intercalate hydrophobic species,[4–6] fragrance molecules,[7] nucleosides,[8] and drugs,[9–11] and there is extensive literature on the complexation affinities between a wide range of chemically varied drug species and cyclodextrins, which could help to identify potential drug targets for such a delivery method.[12,13]

Cyclodextrins (CDs) are a family of cyclic oligosaccharides that are based on α-D-glucopyranoside monomers joined through 1,4-glucoside linkages. They are

produced naturally by enzymatic action on starch, and the most common ring sizes contain 6–8 monomers, prefixed α, β and γ respectively. The chair conformation of the monomers is relatively rigid, with the only conformational freedom of the CD resulting from rotation about the 1,4-glucosidic bond. This causes the CD to adopt the shape of a hollow, truncated cone containing a hydrophobic cavity; the C6 hydroxyl groups of the monomers are located around the narrower end and both C2 and C3 hydroxyl groups located around the wider end, as illustrated in Figure 4.1.[14]

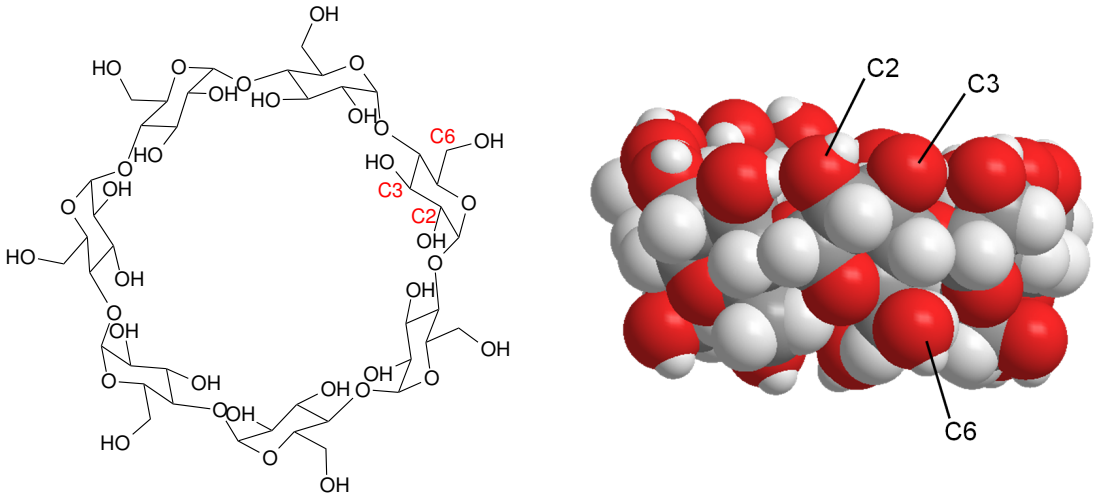


Figure 4.1: The structure and conformation of β-cyclodextrin, showing the positions of the hydroxyl groups where substitution can occur.

Cyclodextrins readily bind both hydrophobic and hydrophilic molecules in their cavities. They are highly biocompatible, and have found use in many applications, notably in drug delivery, where they are primarily used to alter the solubility profile and increase the bioavailability of hydrophobic drugs.[15–17] Cyclodextrins have also found clinical uses themselves, an example being the cyclodextrin sugammadex, which is used to reverse the effects of neuromuscular blocking agents through the formation of inclusion complexes.[18] Different sizes of CDs show strong preferences for different species, and as CDs are chiral, they have found many uses in enantiomeric separation. Cyclodextrins can be easily modified with substituents such as carboxylates and sulfonates to create anionic CDs, and intercalation of these species into LDHs has been known for nearly twenty years.[19]

Use of CDs in conjunction with LDHs has the potential to improve the delivery of a wide variety of drugs, but before this is possible the relationship between drug species, cyclodextrin and host LDH must be fully understood. In particular, the effect of

varying the the degree of substitution, the type of substitution and the location of substitution of anionic groups on CDs has not been investigated systematically, and as such the intercalation of drug species via CD inclusion complexes has been done randomly, rather than with a view to finding the most suitable CD for a given application and drug. Similarly, only a very small number of drug species have been intercalated via cyclodextrin inclusion complexes in the literature, and many classes of drugs which may benefit from such a delivery method have not yet been trialled with it. Both cyclodextrins and LDHs have been used to stabilise drug species,[20,21] and so their use in tandem could potentially provide stability to drugs that cannot be stabilised by either method individually.

4.1.1 Scope of this chapter

In this chapter, a series of substituted cyclodextrins is synthesised and characterised. β-Cyclodextrin is functionalised with both carboxymethyl and sulfobutylether groups, with systematic variation of both the degree and position of substitution. The different cyclodextrins are intercalated into a highly crystalline magnesium–aluminium LDH, the resultant LDH–cyclodextrin nanohybrids are fully characterised and the relationship between the trends in cyclodextrin substitution and LDH intercalation is explored. A selection of model drugs of varying chemistry and pharmacological action are intercalated into the magnesium–aluminium LDH host by first forming inclusion complexes with the substituted cyclodextrins and subsequent intercalation of the inclusion complexes. The drug content of the nanohybrids is determined, and the drug containing nanohybrids are compared to those synthesised without drugs. The orientation of the cyclodextrins and inclusion complexes within the nanohybrid layers is suggested. The drug release profiles of the nanohybrids in biomimetic buffer solutions are recorded and their kinetics modelled. A relationship between the degree of cyclodextrin substitution and release rate is revealed, indicating another useful tool for controlling the release of drugs.

4.2 Functionalisation of β-cyclodextrin

Work was conducted on β-cyclodextrin (β-CD), as it shows the highest binding affinity of the common CDs with most small molecule drug species. β-CD was modified with two different anionic substituents, so that comparison could be made between the two. The first of these modifications was carboxymethylation, whereby CH_2COOH groups were bound through ether linkages to the hydroxyl positions on the cyclodextrins.

Two methods were used for carboxymethylation, non-selective and selective at the C2 hydroxyl groups. The non-selective method reported by Hattori *et al.* was adapted, and was typical of non-selective carboxymethylation of carbohydrates.[22] Chloroacetic acid was added gradually to β-CD, under basic aqueous conditions. By changing the ratio of chloroacetic acid to β-CD, a series of nine partially substituted β-carboxymethyl cyclodextrins (β-CMCDs) was synthesised, labelled [P1] to [P9].

C2 selective carboxymethylation was achieved according to the method reported by Dignam *et al.* involving selective deprotonation of the cyclodextrins with sodium hydride in dry DMF, followed by addition of sodium iodoacetate.[23] The sample was labelled [C2].

Sufobutylation was the second method of modification, whereby $C_4H_8SO_3H$ groups were bound through ether linkages to the cyclodextrin hydroxyl positions to produce β-sulfobutylether cyclodextrin (β-SBECD). Sufobutylation followed the same procedure as non-selective carboxymethylation, replacing the addition of chloroacetic acid with 1,4-butane sultone.[24] One β-SBECD sample was synthesised, labelled β-SBECD.

4.2.1 Nuclear magnetic resonance spectroscopy

The assigned ^{1}H NMR spectrum of a typical β-CMCD sample can be seen in Figure 4.2, showing resonances at $\delta = 5.28$, 5.07, 4.18, 3.95, 3.86, 3.60 and 3.45 ppm. The spectra were consistent with those found in the literature.[23] Each β-CD has twenty one hydroxyl groups where carboxymethylation can possibly occur. Consequently, partial substitution results in a mixture of β-CMCD species, with a variety of substitution patterns. The variation in substitution patterns in the resultant β-CMCD samples

accounts for the relatively large linewidths of the ^{1}H signals in the NMR spectra, as the effect of many permutations of substitution leads to variation in the chemical shift of these resonances, which manifests as the broadening seen. As the carboxymethyl groups are spatially further from the cyclodextrin ring, the resonances corresponding to protons on the carboxymethyl groups do not form a continuous broad peak, but show distinct resonances relating to substitution at different hydroxyl positions. Residual solvent peaks of both methanol and water are seen in all spectra, as both solvents readily adsorb into the cyclodextrin cavity, making their removal difficult.

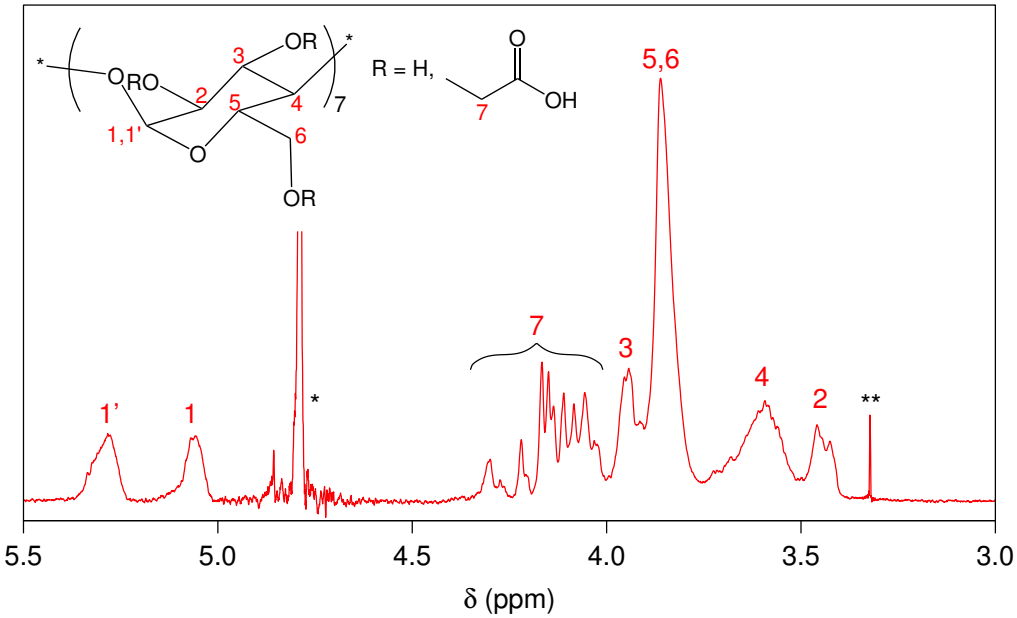


Figure 4.2: Selected region of the ^{1}H NMR spectrum of β-CMCD[P9] in D_2O. * and ** correspond to residual water and methanol respectively.

Integration of the resonances corresponding to the carboxymethyl α protons, labelled in Figure 4.2 as H7 and found between 4.0 and 4.4 ppm, allows the average degree of substitution in each sample to be calculated. The degree of substitution increases across the series of samples from 1.0 to 7.0 carboxymethyl groups per cyclodextrin, β-CMCD[P1] being the least substituted and β-CMCD[P9] being the most. The C2 selectively functionalised sample, β-CMCD[C2], had an average degree of substitution of 3.5 carboxymethyl groups per cyclodextrin.

The average degree of substitution at the C2 positions could be calculated directly from the ^{1}H NMR spectra, as substitution at this position caused a downfield shift in resonance frequency for protons found on adjacent C1 carbon atoms. The ratio

the size of H1 and H1' resonances, seen at 5.07 and 5.28 ppm respectively, indicates the proportion of C1 carbon atoms that lie adjacent to substituted C2 hydroxyls. This provided confirmation that the selectively substituted sample, β-CMCD[C2], had only undergone substitution at the C2 positions as desired, as the degree of substitution at the C2 position was found to equal the overall degree of substitution in this sample.

The $^{13}C\{^{1}H\}$ NMR spectra of the β-CMCD samples provided clear evidence of successful carboxymethylation, corroborating the findings of the ^{1}H spectra, presenting resonances relating to the carbonyl and α-methylene carbon atoms at 177.3 and 60.2 ppm. However, $^{13}C\{^{1}H\}$ NMR spectra in isolation did not provide any further insights into the the substitution pattern of the different samples. The degrees of substitution at C3 and C6 positions were elucidated using 2D ^{13}C–^{1}H heteronuclear multiple-bond correlation (HMBC) spectroscopy, which allowed the complex resonances of the of the carboxymethyl α protons to be assigned. An example of one of the HMBC spectra is given in Figure 4.3. Correlation of the C2, C3 and C6 carbon resonances at 70.2, 79.9 and 80.9 ppm with the various carboxymethyl α proton resonances can be seen, allowing the various peaks to be deconvoluted and assigned. Subsequent integration of these assigned resonances in the ^{1}H NMR spectra allowed the relative degrees of substitution at the difference positions to be quantified. The HMBC spectra assignments were corroborated by comparing the degrees of substitution at the C2 positions calculated using this method and the value calculated directly from inspection of the H1 and H1' resonances in the ^{1}H NMR spectra.

Figure 4.4 gives the full details of the overall average degree of substitution and the distribution across the three hydroxyl positions on the β-CMCD samples. Substitution at the C3 hydroxyl is clearly least favourable, with the average degree of substitution at this position reaching a maximum of 0.5 groups per cyclodextrin in [P8] and [P9], and no substitution observed at this position in [P1], [P2] and [P3]. In comparison, substitution at the C2 hydroxyl position is the most favourable, although the reason for this is not clear, as both the C2 and C3 hydroxyls are located on the wider edge of the cyclodextrin ring and are similarly exposed.

The assigned ^{1}H NMR spectrum of the β-SEBCD sample is shown in Figure 4.5.

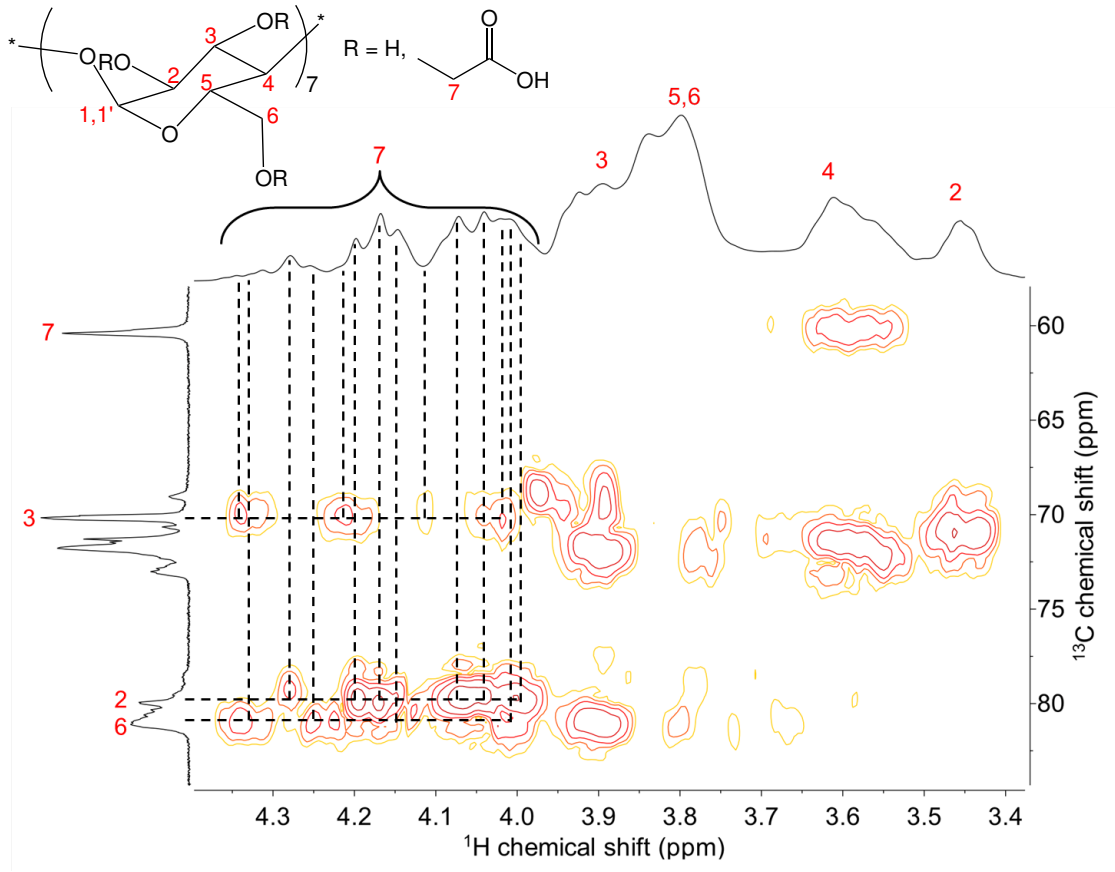


Figure 4.3: The region of the 2D ^{13}C–^{1}H HMBC spectrum of β-CMCD[P9] in D_2O relevant for attributing the positions of carboxymethyl groups.

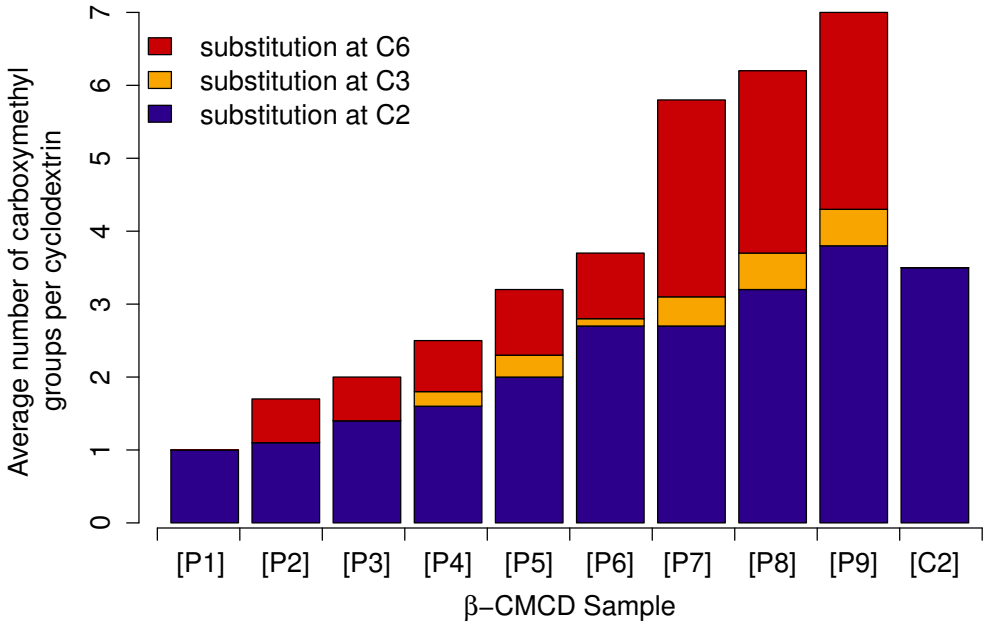


Figure 4.4: The degree of substitution at different positions on the β-CMCD samples.

Resonances were observed at δ = 5.19, 5.08, 3.95, 3.90, 3.78, 3.65, 3.57, 2.95, 1.80 and 1.74 ppm, which is in agreement with the literature.[25,26] As with the β-CMCD samples, the variation in substitution positions resulted in broadened resonances of the protons found on the cyclodextrin structure, while those of the sulfobutyl chain were sharp in comparison. The average degree of substitution in the sample was 9.9 sufobutylether groups per cyclodextrin, calculated from integration of resonances relating to protons on the sulfobutyl chain, with substitution occurring across all hydroxyl positions. As in the case of the β-CMCD samples, the degree of substitution at the C2 hydroxyl positions could be quantified by inspection of the H1 and H1' resonances, as substitution at the C2 position results in downfield shift of the H1 resonance to create the H1' resonance. Compared to the relatively high degree of substitution at the C2 positions in the β-CMCD samples, substitution occurred at only 20 % of C2 hyroxyl positions in the β-SBECD sample, despite the higher overall degree of substitution, which equates to an average degree of substitution of 1.4 groups at the C2 position per cyclodextrin.

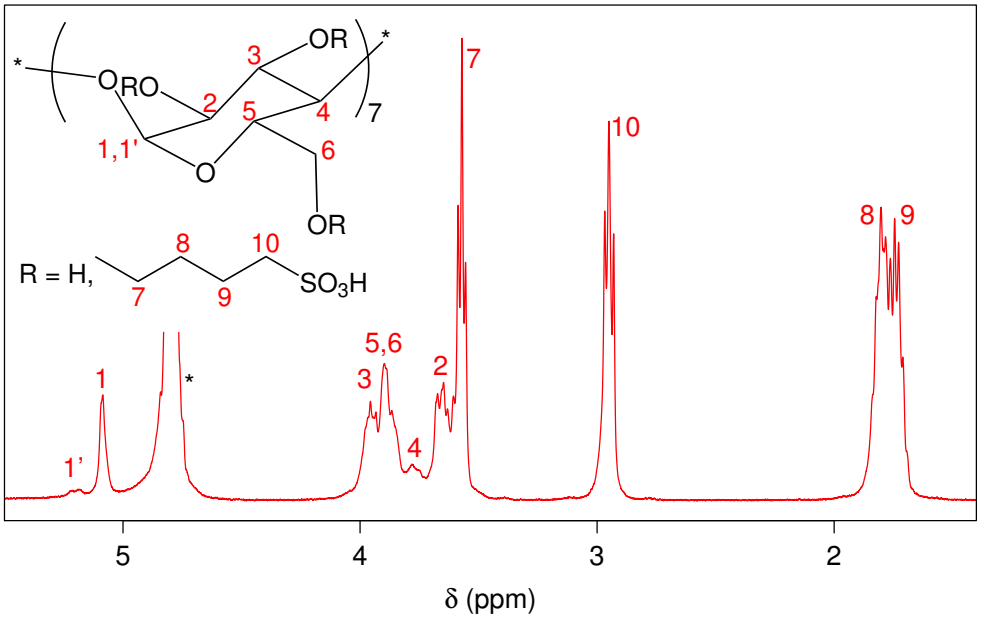


Figure 4.5: Selected region of the ^{1}H NMR spectrum of β-SBECD in D_2O. * corresponds to residual water.

The $^{13}C\{^{1}H\}$ NMR spectrum of the of the β-SBECD sample confirmed successful substitution had occurred, with resonances at 69.9, 50.7, 27.5 and 20.9 ppm corresponding to the carbon atoms on the sulfobutyl chain. The 2D ^{13}C–^{1}H HMBC NMR

spectrum could not be used to discern the degree of substitution at the C3 and C6 hydroxyl positions in the case of β-SBECD, as the resonances of the protons in the sulfobutyl chain did not exhibit any distinction in their chemical shift according to their substitution position, and consequently the resonances could not be deconvoluted to provide quantitative assignments. Consequently, only the degree of substitution across both the C3 and C6 positions combined could be calculated, resulting in a value of 8.5 groups per cyclodextrin.

4.2.2 Fourier transform infrared spectroscopy

FTIR spectra of a range of the β-CMCD samples is displayed in Figure 4.6. The relative intensity of the carbonyl absorption at 1601 cm^{-1}, resulting from the carboxymethyl groups, correlates with the degree of substitution determined from the NMR spectra, corroborating these values. The absorption at 2930 cm^{-1} is due to the stretching vibration of CH_2, both on the carboxymethyl substituents and the cyclodextrin ring. In addition to these absorptions, all spectra show IR bands characteristic of cyclodextrins, most prominently at 1416 and 1324 cm^{-1}, and at 1157, 1085, 1027 and 710 cm^{-1} corresponding to absorptions of C–O, C–O–C of the glucose units and C–O–C of the rings respectively.[19,27] The relative intensity of these absorptions did not change beyond experimental variation. The weak, broad absorption seen around 3300 cm^{-1} can be attributed to the adsorbed water molecules in the cyclodextrin cavities. The spectrum of the selectively substituted sample, β-CMCD[C2], and those of the other β-CMCD samples showed approximately equal IR stretching frequencies.

The FTIR spectrum of the β-SBECD sample can be seen in Figure 4.10 alongside its LDH intercalation compound. The absorptions at 2941 and 2862 cm^{-1} correspond to the stretching vibrations of the CH_2 groups of the alkyl chain of the sulfobutyl groups, whilst the absorption at 1209 cm^{-1} corresponds to the stretching S−O−S vibrations of the sulfonyl groups. The characteristic absorptions of the cyclodextrin rings and glucose units are seen at 1456, 1415, 1174 and 1043 cm^{-1}.[28] The broad water absorption is again observed at 3400 cm^{-1}.

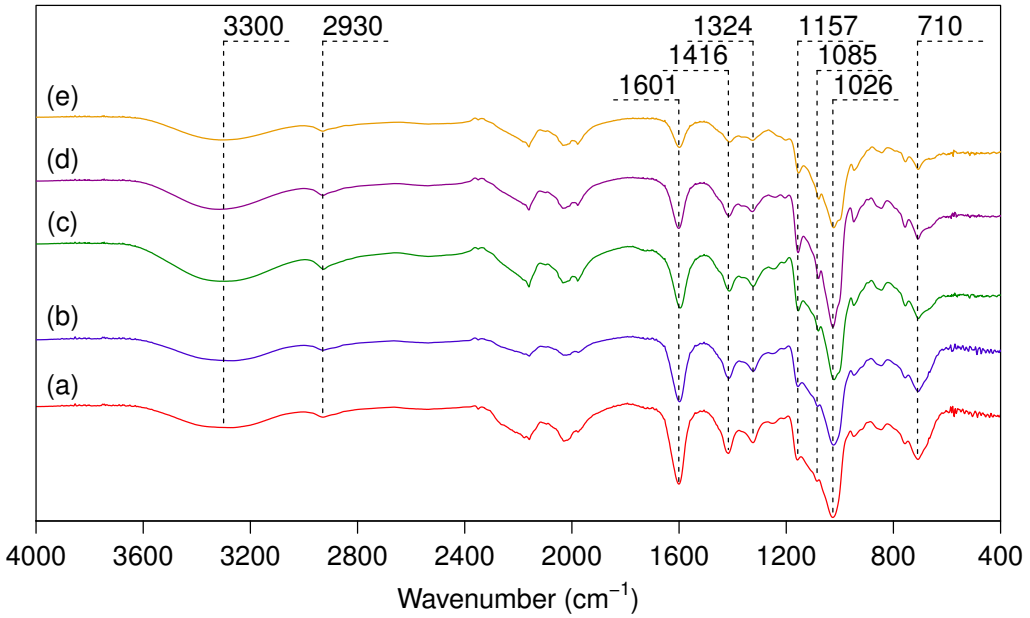


Figure 4.6: The FTIR spectra of (a) β-CMCD[P9], (b) β-CMCD[P7], (c) β-CMCD[P5], (d) β-CMCD[P3] and (e) β-CMCD[P1].

4.2.3 Elemental analysis

Having estimated the degree of substitution from the NMR spectra, C, H, N elemental analysis provided an approximation for the water content of substituted cyclodextrin samples, reported in Table 4.1. The significant amounts of water in the samples that remain after drying under vacuum, is due to its affinity for the empty cavity areas of the cyclodextrins. The variation in water content was random and was not affected by the degree of substitution on the cyclodextrins, ranging between 4 to 7 water molecules per cyclodextrin species.

Table 4.1: The water content of the substituted β-cyclodextrin samples.

Cyclodextrin	β-CMCD										β-SBECD
sample	[P1]	[P2]	[P3]	[P4]	[P5]	[P6]	[P7]	[P8]	[P9]	[C2]	
Water content (%)	7.28	6.81	6.59	7.55	8.03	5.31	6.42	7.78	6.35	7.59	4.70
No. H_2O / β-CD	5.2	5.0	4.9	5.8	6.4	4.2	5.6	7.0	5.8	6.1	6.8

4.3 Intercalation of substituted β-cyclodextrins

The substituted cyclodextrins were intercalated via ion-exchange into highly crystalline MgAl-NO_3 LDH synthesised via the homogeneous coprecipitation–decarbonation method of Iyi *et al.*[29] The ion-exhange process was adapted from the method reported by Mohanambe and Vasudevan, and in all cases resulted in fine white powders that did not stick to themselves or aggregate into large particles.[30] For ease of reading, the β- prefix has henceforth been omitted from the names of the cyclodextrin species in the intercalation compounds.

4.3.1 Powder X-ray diffraction

As can be seen from the literature, intercalation of cyclodextrins into LDHs is accompanied by a significant reduction in crystallinity.[9,31] The highly crystalline precursor LDH was used with the aim of producing sufficiently crystalline LDH–CD nanohybrids so that any distinctions between the structures of the resulting nanohybrids could be observed in their powder XRD patterns, and also to provide well-defined controls for comparison with drug-containing nanohybrids, detailed in Section 4.4.

The diffraction patterns of the nanohybrids (Figure 4.7) all index to a hexagonal lattice with $R\bar{3}m$ rhombohedral symmetry. As predicted, the nanohybrids exhibit significantly reduced crystallinity relative to the precursor LDH. The basal (003) Bragg reflections of the nanohybrids are all seen at values of 2θ below 4.60°, with other $(00l)$ reflections also seen at correspondingly low values of 2θ, which is indicative of intercalation of a large guest species. This translates to unit cell c parameters greater than 57.6 Å and interlayer spacings of greater than 14.4 Å, which is in line with reports from previous intercalation of cyclodextrin species into LDHs.[19]

The MgAl-SBECD samples and the nanohybrids intercalated with β-CMCD samples with low degrees of substitution ([P1]–[P4]) exhibit impurities corresponding to both the nitrate LDH species, whilst the nanohybrids intercalated with more highly substituted β-CMCD species ([P5]–[P9]) appear as pure phases. The nitrate-containing impurity phases seen in the samples were not unreacted precursor LDH, but are

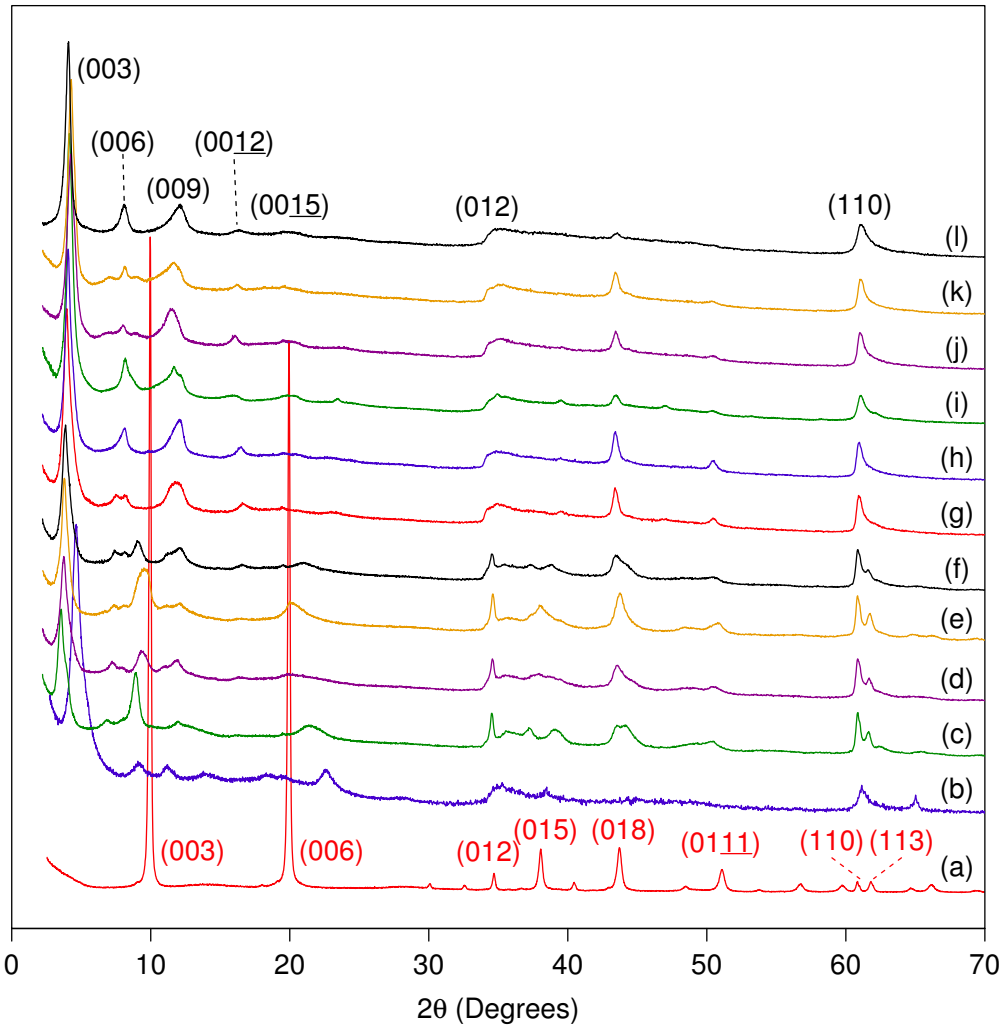


Figure 4.7: The powder XRD patterns of (a) MgAl-NO_3 (b) MgAl-SBECD, (c) MgAl-CMCD[P1], (d) MgAl-CMCD[P2], (e) MgAl-CMCD[P3], (f) MgAl-CMCD[P4], (g) MgAl-CMCD[P5], (h) MgAl-CMCD[P6], (i) MgAl-CMCD[P7], (j) MgAl-CMCD[P8], (k) MgAl-CMCD[P9] and (l) MgAl-CMCD[C2].

new phases, as evidenced from their greatly reduced crystallinity and differences in reflection positions relative to the precursor LDH. The differences in reflection positions are likely due to to the cointercalation of other anionic impurities alongside the nitrate ions.

All nanohybrid diffraction patterns exhibit pronounced Warren-type anisotropy of the (012) Bragg reflection, which is indicative of prevalent stacking disorder in the nanohybrids.[32] The large size of the guest ions and the interlayer distances increase the tendency of both turbostratic disorder and stacking faults to occur, as the greater distance between successive metal hydroxide layers and variation in guest ion orientation reduces the coordination between the metal hydroxide layers, leading to the observed disorder.

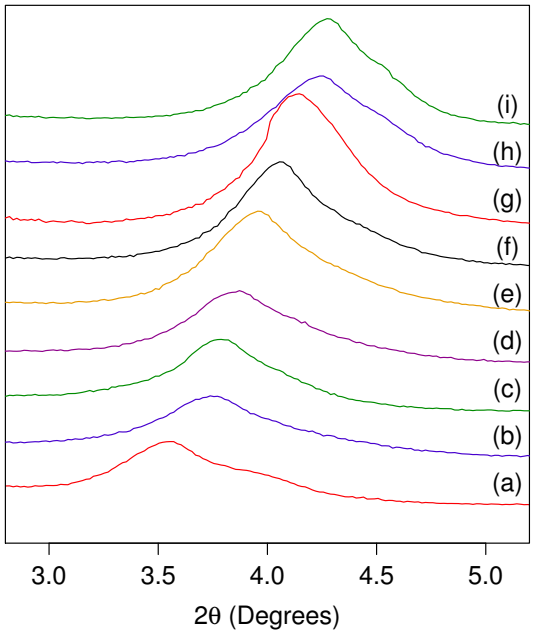


Figure 4.8: Sections of the powder XRD patterns showing the (003) Bragg reflections of (a) MgAl-CMCD[P1], (b) MgAl-CMCD[P2], (c) MgAl-CMCD[P3], (d) MgAl-CMCD[P4], (e) MgAl-CMCD[P5], (f) MgAl-CMCD[P6], (g) MgAl-CMCD[P7], (h) MgAl-CMCD[P8] and (i) MgAl-CMCD[P9].

The β-CMCD intercalated nanohybrid samples all exhibit basal reflections between 3.55 and 4.29° 2θ, and a clear trend, illustrated in Figure 4.8, can be observed between the degree of substitution of the β-CMCD sample and the position of the basal reflection. This pattern is also observed in the positions of the (006) and (009) Bragg reflections, although due to the lower intensity and broader profiles of these

reflections it is less clear. Interestingly, the more highly substituted the β-CMCD sample, the higher the basal reflection is in the XRD pattern of its corresponding nanohybrid. This seems counter-intuitive, as the position of the basal reflection directly relates to the interlayer distance, with a higher basal reflection corresponding to a lower interlayer distance, and so the interlayer distance can be seen to decrease from 20.0 to 15.9 Å as the degree of substitution on the intercalated β-CMCD sample increases.

The more highly substituted a β-CMCD sample is, the larger its size, and so it would be expected that it would also lead to a greater interlayer spacing upon intercalation. However, the reverse trend is observed. This can be understood by considering that the higher degree of substitution also equates to a higher negative charge on the cyclodextrin species. This leads to a greater charge density on more highly substituted β-CMCD species, in turn causing a greater electrostatic attraction between the cyclodextrin species and the LDH layers. The greater electrostatic force may draw the LDH sheets closer together, towards the β-CMCD anions. Also, the greater the charge on the β-CMCD anions, the fewer ions are needed within a given interlayer region to balance the positive charge on the metal hydroxide sheets. This allows more space for the β-CMCD ions to orient themselves within the interlayer region, which may also lead to a reduction in gallery height. The orientation of the cyclodextrin species is discussed further in Section 4.5.

The diffraction pattern of MgAl-CMCD[C2] did not show any significant differences to those of the nanohybrids intercalated with non-selectively substituted β-CMCD samples, and in fact the relationship between the degree of substitution on β-CMCD[C2] and the interlayer distance fitted into the trend seen in the other nanohybrids, as illustrated in Figure 4.9, which shows interlayer distance as a function of the degree of β-CMCD substitution. This may indicate that the position of substitution on cyclodextrins does not greatly influence their intercalation, although as the C2 position was the primary substitution position in the non-selectively substituted β-CMCD samples, the extent to which the samples can be contrasted with β-CMCD[C2] is limited.

Despite the high degree of substitution on the β-SBECD sample, the MgAl-SBECD nanohybrid exhibits impure phases, which is in contrast to the more highly substituted

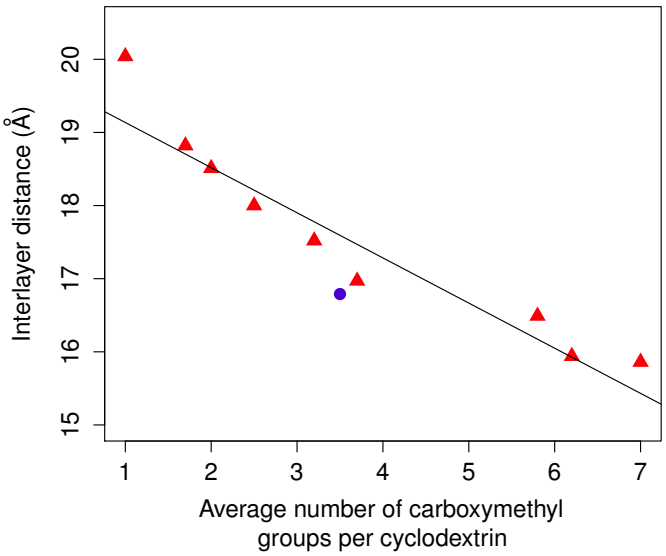


Figure 4.9: The interlayer distance of the β-CMCD intercalated nanohybrids plotted as a function of the degree of carboxymethyl substitution on the non-selectively (▲) and C2 selectively (●) substituted β-cyclodextrins.

β-CMCD intercalated nanohybrids. Additionally, the MgAl-SBECD nanohybrid appears to be less crystalline than the β-CMCD analogues, showing both fewer and broader Bragg reflections in its diffraction pattern. It is notable that despite β-SBECD being a larger species than any of the β-CMCD samples, both due to the higher degree of substitution and the bulkier nature of the sulfobutylether substituents, upon intercalation the resulting nanohybrid does not display a greater interlayer distance. The interlayer distance to substitution ratio does not fit with the trend seen in the β-CMCD samples, presumably due to factors influencing the intercalation of different species. However, the magnitude of the interlayer distance does lends support to the supposition that the charge density is also an important factor alongside size of the guest ion when considering its orientation in the interlayer region.

The lattice parameters of the nanohybrid samples are detailed in Table 4.2. The trend in the c parameters has already been discussed, as it is directly related to the interlayer distance, the c parameter lying in the stacking direction. The a parameter shows virtually no change between all nanohybrid samples as it is dependent on the metal hydroxide layers, which are typically unchanged by ion-exchange reactions.

Table 4.2: The lattice parameters and interlayer distances of the β-cyclodextrin intercalated nanohybrid samples.

Nanohybrid sample	Cell parameters (Å)		Interlayer distance (Å)
	a	c	
MgAl-CMCD[P1]	3.041	74.52	20.04
MgAl-CMCD[P2]	3.042	70.85	18.82
MgAl-CMCD[P3]	3.042	69.92	18.51
MgAl-CMCD[P4]	3.042	68.41	18.00
MgAl-CMCD[P5]	3.039	66.96	17.52
MgAl-CMCD[P6]	3.036	65.31	16.97
MgAl-CMCD[P7]	3.031	63.88	16.49
MgAl-CMCD[P8]	3.035	62.23	15.94
MgAl-CMCD[P9]	3.035	61.99	15.86
MgAl-CMCD[C2]	3.035	64.77	16.79
MgAl-SBECD	3.029	57.08	14.23

4.3.2 Fourier transform infrared spectroscopy

Confirmation that the intended species were intercalated into the nanohybrids was provided by FTIR and solid state NMR spectroscopy. As can be seen from examples in Figures 4.10 and 4.11, the characteristic absorptions of the β-CMCD and β-SBECD species, detailed in Section 4.2.2, are also found in the the spectra of the nanohybrids. As is typical upon intercalation, slight broadening of the cyclodextrin absorptions is apparent in the nanohybrid spectra, along with minor shifts in the maxima of the absorptions, in particular those corresponding to the carbonyl absorption from 1601 to 1584 cm^{-1} in the MgAl-CMCD spectra and the sulfonyl absorption from 1174 to 1164 cm^{-1} in the MgAl-SBECD spectrum, as these modes are influenced most by electrostatic interactions with the metal hydroxide layers.

As might be expected, the same trend in the intensity of the the carbonyl absorptions was observed in the MgAl-CMCD IR spectra as had been seen in the β-CMCD IR spectra. Alongside the absorptions assigned to the β-cyclodextrin species, the nanohybrid IR spectra exhibit broad absorptions at 3400 and 685 cm^{-1} assigned to the O−H stretching modes of the metal hydroxide layers and cointercalated water, and to the M−OH stretching and bending modes. The broad shoulder of the 685 cm^{-1}

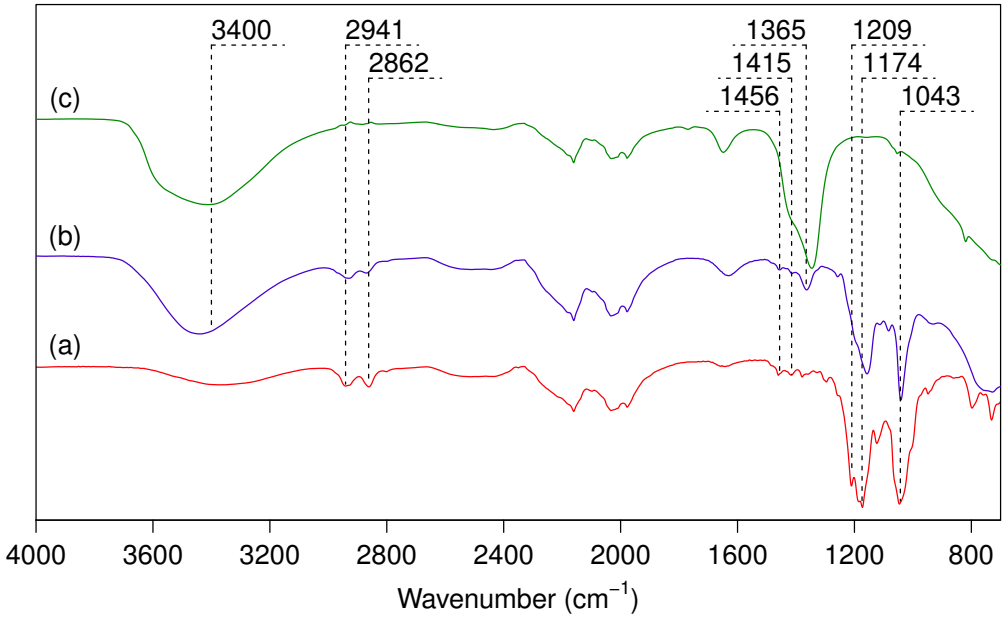


Figure 4.10: The FTIR spectra of (a) β-SBECD, (b) MgAl-SBECD and (c) MgAl-NO_3.

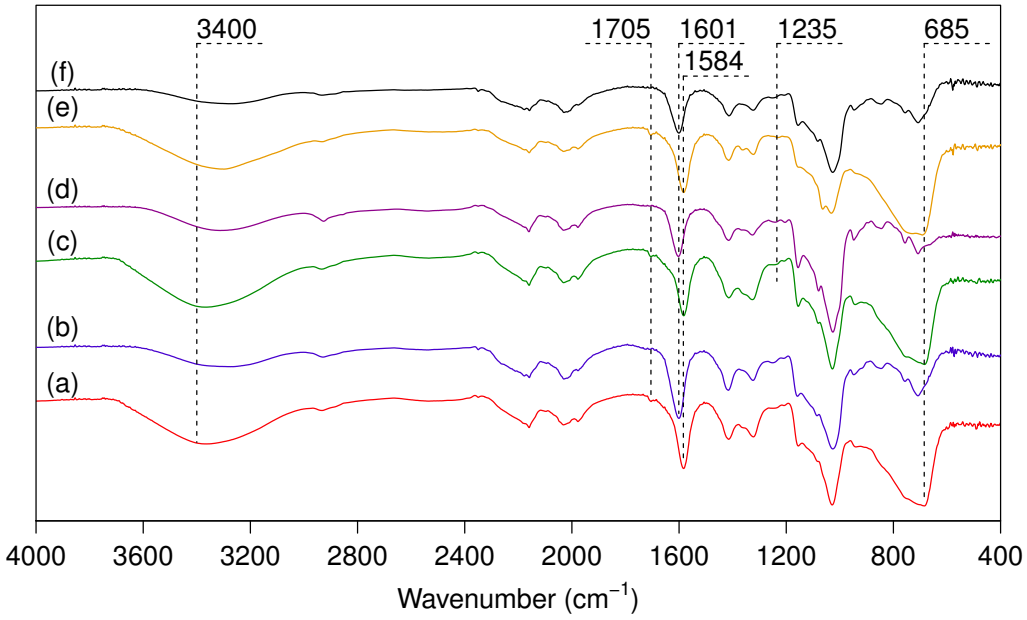


Figure 4.11: The FTIR spectra of (a) MgAl-CMCD[P8], (b) β-CMCD[P8], (c) MgAl-CMCD[P4], (d) β-CMCD[P4], (e) MgAl-CMCD[C2] and (f) β-CMCD[C2].

absorptions mask some of the minor absorptions of the β-cyclodextrin anions. As can be seen in Figure 4.11, the spectrum from MgAl-CMCD[C2] showed now major differences from those of the other MgAl-CMCD nanohybrids. The nanohybrids also all exhibited an additional small absorption at 1705 cm^{-1} not seen in the cyclodextrin spectra, which can be attributed to to the bending mode of the cointercalated water in the nanohybrids.

The spectra of MgAl-CMCD[P1], MgAl-CMCD[P2], MgAl-CMCD[P3] and MgAl-CMCD[P4] exhibit minor absorption peaks at 1235 cm^{-1}, which can be attributed to the nitrate impurities whose presence had been indicated in the powder XRD patterns of these samples.

4.3.3 Solid-state nuclear magnetic resonance spectroscopy

The ^{13}C CP/MAS solid state NMR spectra of the nanohybrids show close agreement with those of their respective β-cyclodextrin species, as can be seen from the examples in Figure 4.12, indicating successful intercalation of the intended anions and no evidence of cointercalation of other organic species. Broadening of the resonances in the NMR spectra of the nanohybrids was observed, relative to the resonances in the NMR spectra of the pure β-cyclodextrin compounds, as is typical with the solid state NMR spectra of LDHs and other inorganic intercalation compounds. This is due to the effect of interactions between the guest ions and the host layers creating variation the chemical environments of the guest ions. The results of the solid state NMR data are consistent with the evidence of the FTIR spectra.

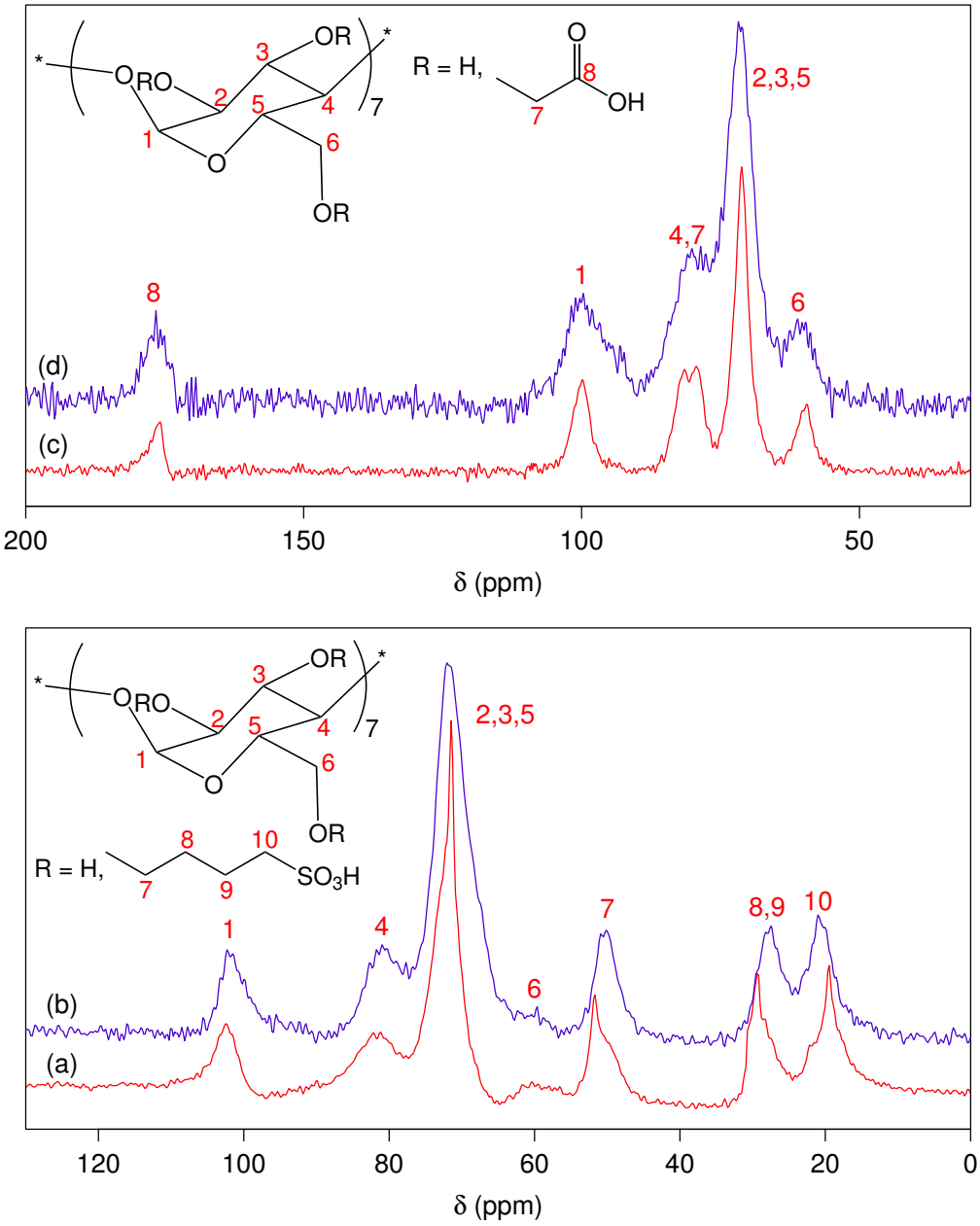


Figure 4.12: The assigned ^{13}C CP/MAS solid state NMR spectra of (a) β-SBECD, (b) MgAl-SBECD, (c) β-CMCD[P9] and (d) MgAl−CMCD[P9].

4.3.4 Formulae calculations

4.3.4.1 Energy dispersive X-Ray spectroscopy

The ratio between the aluminium and magnesium ions in the nanohybrids was confirmed using EDX spectroscopy, although negligible change was observed in the constitution of the metal hydroxide layers of the nanohybrids compared to the precursor LDH, with a ratio of $1.97(\pm 0.005) : 1$ magnesium to aluminium observed across all nanohybrids.

4.3.4.2 Thermogravimetric analysis

The water content of the nanohybrids was calculated through thermogravimetric analysis. As water can reside in both the interlayer region and the cavities of the cyclodextrins themselves, all the nanohybrids were observed as having relatively high water contents when compared to those of other LDH compounds, as can be seen in Table 4.3. Mass loss attributable to water occurred in the nanohybrids up to a temperature of 165 °C, higher than typically observed in LDHs, due to the water contained in the cyclodextrin cavities. Besides this initial mass loss, TGA plots showed a gradual reduction in mass between 310 and 560 °C corresponding to the decomposition of the cyclodextrin species, although more specific attribution to the pattern of mass loss was not possible due to its complexity and the continuous nature of the mass loss.

4.3.4.3 Elemental analysis

C, H, N elemental analysis was used to calculated the extent of intercalation of β-cyclodextrins, and also to quantify the presence of any nitrate ions, as these were the only source of nitrogen. A maximum percentage mass of 50 – 53 % β-CMCD was observed for nanohybrids containing β-CMCD with average degrees of substitution > 3, with a reduction in percentage mass down to 27 % for cyclodextrins with degrees of substitution between 1 and 3, proportional to the degree of substitution. The limiting factor to the intercalation of less substituted species is likely to be their low

Table 4.3: The water content and approximate formulae of the β-cyclodextrin intercalated nanohybrid samples.

Nanohybrid sample	Water content (W/W %)	approximate formula
MgAl-CMCD[P1]	36.4	$Mg_{1.99}Al_{1.01}(OH)_6(C_{44}H_{71}O_{37})_{0.18}(NO_3)_{0.83} \cdot 14.0H_2O$
MgAl-CMCD[P2]	33.5	$Mg_{1.99}Al_{1.01}(OH)_6(C_{44}H_{71}O_{37})_{0.04}(C_{46}H_{72}O_{39})_{0.09}(NO_3)_{0.79} \cdot 10.8H_2O$
MgAl-CMCD[P3]	25.3	$Mg_{1.99}Al_{1.01}(OH)_6(C_{46}H_{72}O_{39})_{0.19}(NO_3)_{0.63} \cdot 8.6H_2O$
MgAl-CMCD[P4]	24.5	$Mg_{1.99}Al_{1.01}(OH)_6(C_{46}H_{72}O_{39})_{0.09}(C_{48}H_{73}O_{41})_{0.09}(NO_3)_{0.56} \cdot 8.0H_2O$
MgAl-CMCD[P5]	19.9	$Mg_{1.99}Al_{1.01}(OH)_6(C_{48}H_{73}O_{41})_{0.20}(C_{50}H_{74}O_{43})_{0.05}(NO_3)_{0.21} \cdot 7.2H_2O$
MgAl-CMCD[P6]	19.6	$Mg_{1.99}Al_{1.01}(OH)_6(C_{48}H_{73}O_{41})_{0.07}(C_{50}H_{74}O_{43})_{0.16}(NO_3)_{0.17} \cdot 6.7H_2O$
MgAl-CMCD[P7]	13.6	$Mg_{1.99}Al_{1.01}(OH)_6(C_{52}H_{75}O_{45})_{0.03}(C_{54}H_{76}O_{47})_{0.14}(NO_3)_{0.02} \cdot 3.7H_2O$
MgAl-CMCD[P8]	11.6	$Mg_{1.99}Al_{1.01}(OH)_6(C_{54}H_{76}O_{47})_{0.13}(C_{56}H_{77}O_{49})_{0.03}(NO_3)_{0.02} \cdot 3.0H_2O$
MgAl-CMCD[P9]	5.6	$Mg_{1.99}Al_{1.01}(OH)_6(C_{56}H_{77}O_{49})_{0.14} \cdot 1.3H_2O$
MgAl-CMCD[C2]	20.7	$Mg_{1.99}Al_{1.01}(OH)_6(C_{48}H_{73}O_{41})_{0.11}(C_{50}H_{74}O_{43})_{0.11}(NO_3)_{0.23} \cdot 7.0H_2O$
MgAl-SBECD	14.8	$Mg_{1.99}Al_{1.01}(OH)_6(C_{78}H_{133}O_{62}S_9)_{0.01}(C_{82}H_{140}O_{65}S_{10})_{0.09} \cdot 4.1H_2O$

charge density, as the ion are too big to adequately balance the charge on the LDH layers on their own, necessitating the cointercalation of nitrate ions. The limiting factor to the intercalation of the more highly substituted ions, however, is simply that, due to their higher charge density, the theoretical maximum loading of these ions needed to balance the charge on the metal hydroxide layers is actually met at the moderate loading percentages seen, and cannot be significantly increased beyond these values. Figure 4.13 illustrates both these trends seen in the loading percentage of β-CMCD. These trends are unexpected, as one might assume that a greater mass percentage of cyclodextrin would be seen in the nanohybrids containing less highly substituted species, as more of the cyclodextrin would be required to balance the charge on the metal hydroxide layers.

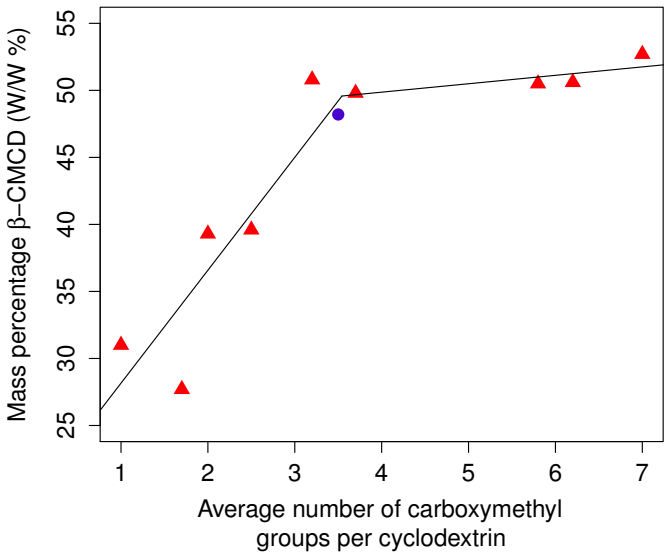


Figure 4.13: The mass percentage of β-CMCD anions in the nanohybrids plotted as a function of the degree of carboxymethyl substitution on the non-selectively (▲) and C2 selectively (●) substituted β-cyclodextrins.

As the β-CMCD samples are a mix of multiples species with differing levels of substitution, any attempt at approximate formulae for the nanohybrid species based simply on elemental analysis data can only be a generalisation, as the exact fractions of the variously substituted species is not known. However, for the purposes of approximating the loading of the β-cyclodextrin species in the nanohybrids, the constitution of the various β-cyclodextrin samples was approximated as a weighted mixture of the of the two β-cyclodextrin with degrees of substitution closest to the average degree of substitution calculated through NMR spectroscopy. As an example,

β-CMCD[P6] has an average degree of substitution of 3.7 carboxymethyl groups per cyclodextrin, so its constitution can be approximated as a mixture of β-CMCD species with 4 and 3 carboxymethyl groups per cyclodextrin respectively, at ratio of 70 : 30. Through this method, the formulae of the nanohybrids can be approximated, as listed in Table 4.3. Apparent discrepancies in charge between intercalated species and the metal hydroxide layers could be rationalised by taking into account the possibility that some of the cyclodextrin species were not fully deprotonated at their carboxymethyl/sulfate groups.

4.3.5 Scanning electron microscopy

The morphology of the highly crystalline precursor LDH has been described and illustrated in Section 3.2.7, where it was observed that intercalation of catecholamine drugs through ion-exchange did not noticeably alter the the particle morphology. In contrast, intercalation of the larger β-cyclodextrin species did not lead to substantial changes in morphology, but did produce observable differences, as depicted in the SEM images in Figure 4.14. Compared to the precursor LDH, MgAl-NO_3, and to the nanohybrids containing catecholamine drugs, shown in Figure 3.12 assuming a morphology of regular hexagonal platelets, with some rounding at the corners of the platelets, the β-cyclodextrin containing nanohybrids form more rounded platelets, many approaching regular circles, and very few sharp corners, although though some hexagon-like shapes can be discerned.

Many of the nanohybrid platelets display irregularities resembling small chips at their edges, and semicircular-shaped platelets are also common, which are likely due to the fracturing of circular platelets into smaller pieces. Both the the chipping and fracturing phenomena are typically caused due to mechanical action on the particles. Another feature of the nanohybrids, that can be seen when viewing platelets from the side, rather than the top, is that some amount of delamination has occurred. Evidence of partial delamination can also be seen from the top vies of some particles, where nanohybrid layers have formed concentric circle patterns. This would help to explain the effects of the mechanical action seen, as partial delamination thins and weakens the platelets, making such actions more feasible.

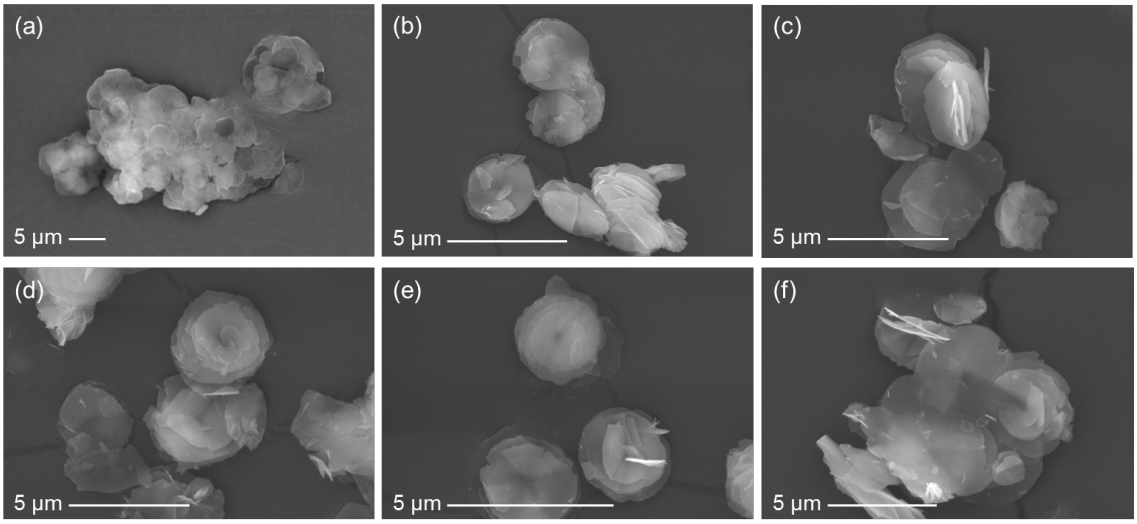


Figure 4.14: SEM images of (a) MgAl-NO_3, (b) MgAl-CMCD[P2], (c) MgAl-CMCD[P4], (d) MgAl-CMCD[P6], (e) MgAl-CMCD[P8] and (f) MgAl-SBECD.

The large size of the guest anions explains why these features are seen in the cyclodextrin containing nanohybrids, whilst they were not seen when intercalating the the smaller catecholamine anions. As was observed in the powder XRD patterns of the nanohybrids, substantial stacking faults are present in the nanohybrids due to the size of the guest ions weakening interlayer interactions, which also leads to the partial delamination that in turn causes the other features seen the in the nanohybrid morphology. The increased temperature used in the ion-exchange process of the cyclodextrins may also contribute to the features seen, as the increased energy will accentuate the effects of mechanical action.

4.4 Intercalation of β-cyclodextrin–drug complexes

Intercalation of cyclodextrin–drug inclusion complexes into the precursor LDH was achieved through ion-exchange, adhering to the same method used to intercalate the cyclodextrins in Section 4.3, with various modifications, dependent of the drug being complexed. The primary modification to the method was in the solvent used, as the complexation of poorly water soluble drugs necessitated that ion-exchange reactions were carried out in mixtures of water with miscible organic solvents, namely

acetone, ethanol and tetrahydrofuran (THF). Additionally, changes to the reaction temperature and duration were made.

These modifications were necessary to encourage the formation of the cyclodextrin–drug inclusion complexes prior to intercalation, so as to prevent the uncomplexed cyclodextrin anions being intercalated preferentially. However, the optimum conditions for the complexation and intercalation reactions are often opposing. For example, complexation is more favourable at reduced temperatures, whereas optimum intercalation conditions are achieved at elevated temperatures.

4.4.1 Model drugs

Four model drugs were chosen for cyclodextrin complexation, covering a wide variation in both structure and function. Three were chosen due to their known high affinity for β-CD, as indicated by their complexation constants, K_c, which were all $> 20\,000\,\mathrm{dm^3 mol^{-1}}$,[12,13] and one was chosen due to its instability, as it was envisaged this effect would be countered by intercalation into the nanohybrids. The drugs selected for their complexation constants were testosterone (TST), a steroid, chlorpromazine (CPZ), a cationic tricyclic antipsychotic, and cinnarizine (CIN), a piperazine containing antihistamine. Cefuroxime axetil (CFA), a cephalosporin antibiotic, was the drug chosen due to its instability.[33] After some initial success with chlorpromazine, three other tricyclic drugs were included for study, namely promethazine (PMZ), an antihistamine, imipramine (IMI) and amitriptyline (AMI), both antidepressants. All drugs being investigated are strongly UV active, as this allows their concentration during release experiments to be measured accurately using UV spectroscopy, even at low concentrations. Their structures are shown in Figure 4.15.

Besides structural and chemical reasons, all drugs chosen are subject to other issues relating to either their formulation, or the formulation of closely related but prohibitively expensive drugs, that may be remedied through LDH intercalation. The instability of CFA has already been mentioned, as this prevents its formulation in stable liquid suspensions. As it is an antibiotic commonly given to children, liquid suspensions are highly desirable, yet it have a very bitter taste and currently

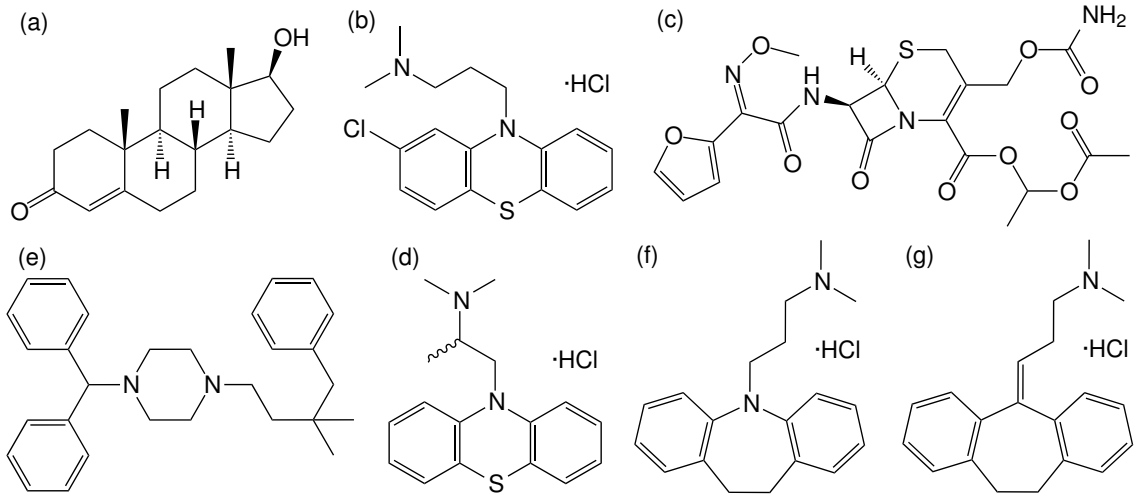


Figure 4.15: The structures of (a) testosterone, (b) chlorpromazine, (c) cefuroxime axetil, (d) cinnarizine, (e) promethazine, (f) imipramine and (g) amitriptyline.

such suspensions have to be prepared at the time of using and cannot be stored, and coated tablets have been unsuccessful due to the propensity of CFA to form gels.[34] CIN is commonly used as a travel sickness aid, yet it has a bitter taste and is conventionally formulated as a tablet, making its use sometimes inappropriate in the exact situation for which it is intended, whereby its use can increase the sickness felt by some patients. It has also been found that co-administration with a cyclodextrin can significantly increase the bioavailability of CIN.[35,36] TST is a typical steroidal drug, which form an extensive family of drugs, many with well established issues relating to their formulation.[37] Investigating their delivery with layered double hydroxides may provide another tool with which to overcome these issues. Tricyclics are another broad family of drugs encompassing many applications, but have been widely noted for their unpleasant taste, which has a lingering affect on patients' sense of taste after administration.[38,39]

Complexation and ion-exchange reactions were conducted with all eleven cyclodextrin species (β-CMCD[P1]–[P9], [C2] and β-SBECD) and the drugs CPZ, TST, CIN and CFA. After preliminary trials, reactions with PMZ, IMI and AMI were conducted with a selection of the cyclodextrin species (β-CMCD[P3], [P6], [P9], [C2] and β-SBECD). The ^{1}H NMR spectra of the nanohybrids, discussed in Section 4.4.4, revealed that CFA was decomposed during the complexation–intercalation process, and so characterisation data of these nanohybrids is not included below.

4.4.2 Powder X-ray diffraction

Powder XRD patterns of the nanohybrids containing cyclodextrin–drug complexes were broadly similar to those of the nanohybrids investigated in Section 4.3, as can be seen from the examples given in Figure 4.16. The nanohybrids could be indexed in the same fashion, to a hexagonal lattice with $R\overline{3}m$ rhombohedral symmetry, and they displayed similar reductions in crystallinity when compared to the precursor LDH. The positions of the (003) basal Bragg reflections at values of 2θ between 3.55 and 4.29° indicate successful intercalation of the cyclodextrin species, although the XRD patterns alone cannot establish whether it is the cyclodextrin–drug complexes that have been intercalated in each case or simply the uncomplexed cyclodextrin ions.

The ion-exchange reactions involving inclusion complexes comprising β-CMCD[P1] and CPZ did not yield any nanohybrid product, with powder X-ray diffraction of the products indicating return of the precursor nitrate LDH on all attempts to intercalate the β-CMCD[P1]{CPZ} complex. Similarly, attempts to intercalate β-CMCD[P2]{CPZ} were largely unsuccessful, with powder X-ray diffraction showing substantial amounts of the precursor LDH being returned and only minor Bragg reflections corresponding to a successful intercalation product. As the average degree of substitution for these nanohybrids is 1.0 and 1.7 respectively, the majority of the anions comprising β-CMCD[P1] are monovalent, as are a substantial amount of those comprising β-CMCD[P2]. As CPZ is cationic, the resulting complex formed with the drug species is neutral, and thus consequently intercalation is unfavourable.

A feature seen in the diffraction patterns of all the nanohybrids intercalated with the cationic tricyclic drugs and β-CMCD species was the presence of MgAl-Cl LDH. As chloride was the counter ion to the drug cations, which were in excess to optimise complexation, a fraction of the anions preferentially formed the chloride LDH. This impurity was not seen in nanohybrids intercalated with β-SBECD complexes, presumably due to its greater affinity for intercalation and higher charge.

Closer inspection of the diffraction patterns of the nanohybrids reveals differences in the positions of the $(00l)$ Bragg reflections between those of complex containing nanohybrids and those of the uncomplexed cyclodextrin containing nanohybrids, as

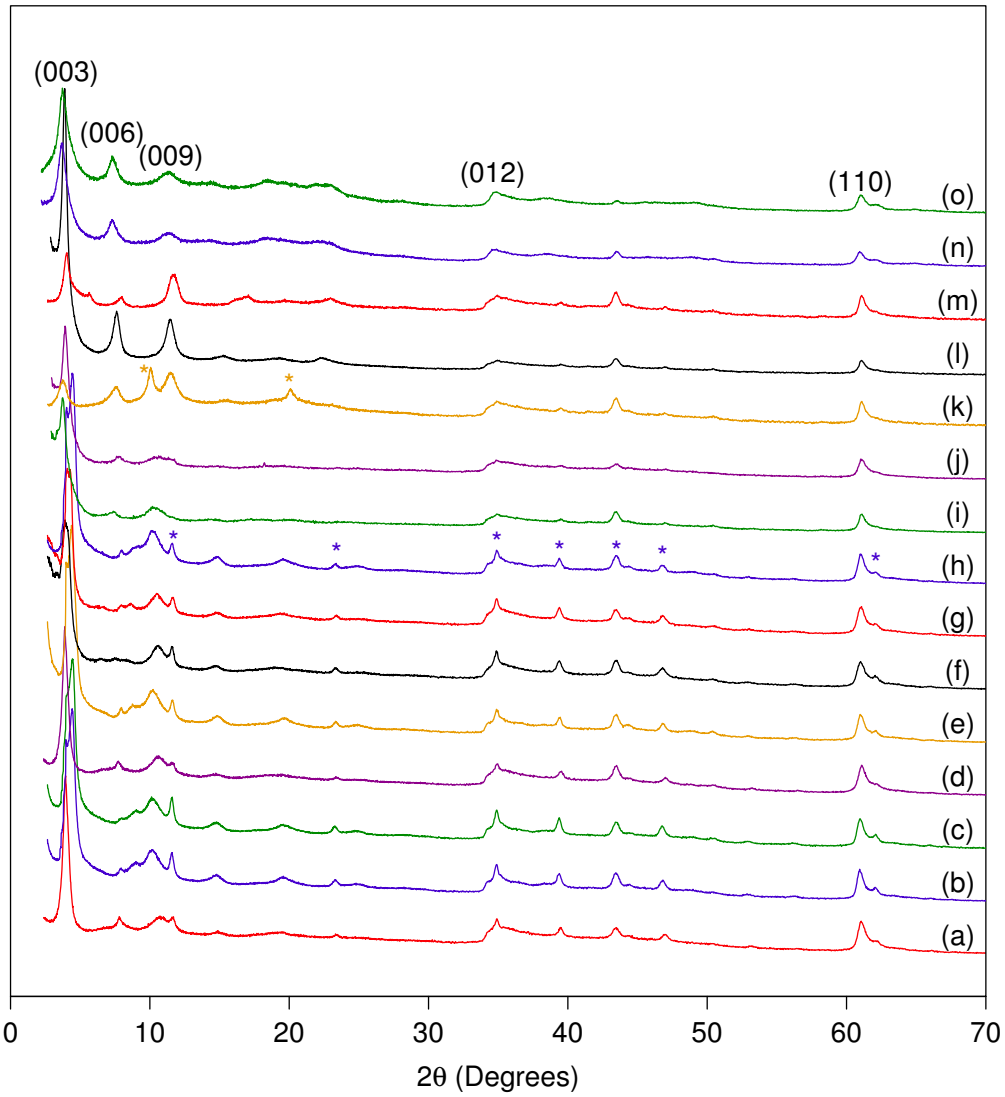


Figure 4.16: The powder XRD patterns of (a) MgAl-CMCD[P4]{CPZ}, (b) MgAl-CMCD[P7]{CPZ}, (c) MgAl-CMCD[C2]{CPZ}, (d) MgAl-CMCD[P3]{PMZ}, (e) MgAl-CMCD[P6]{PMZ}, (f) MgAl-CMCD[C2]{IMI}, (g) MgAl-CMCD[P6]{IMI}, (h) MgAl-CMCD[P9]{AMI}, (i) MgAl-CMCD[P1]{CIN}, (j) MgAl-CMCD[P5]{CIN}, (k) MgAl-CMCD[P2]{TST}, (l) MgAl-CMCD[P4]{TST}, (m) MgAl-CMCD[P8]{TST}, (n) MgAl-SBECD{CIN} and (o) MgAl-SBECD{AMI}, * denotes MgAl-NO_3 and * denotes MgAl-Cl impurity phases.

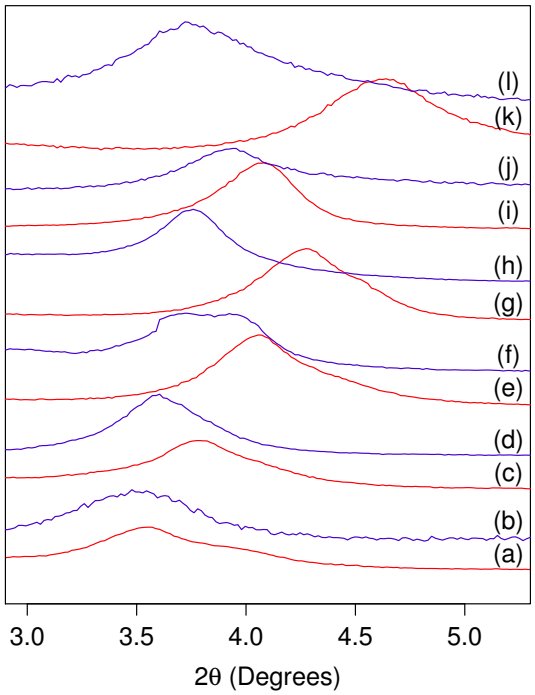


Figure 4.17: Sections of the powder XRD patterns showing the differing positions of the (003) Bragg reflections of (a) MgAl-CMCD[P1], (b) MgAl-CMCD[P1]{TST}, (c) MgAl-CMCD[P3], (d) MgAl-CMCD[P3]{IMI}, (e) MgAl-CMCD[P6], (f) MgAl-CMCD[P6]{CPZ}, (g) MgAl-CMCD[P9], (h) MgAl-CMCD[P9]{PMZ}, (i) MgAl-CMCD[C2], (j) MgAl-CMCD[C2]{CIN}, (k) MgAl-SBECD and (l) MgAl-SBECD{AMI}.

illustrated by examples in Figure 4.17. The positions of the (00l) Bragg reflections in the diffraction patterns of the nanohybrids intercalated with the drug–cyclodextrin complexes are all at lower values of 2θ than those of comparable nanohybrids intercalated the same uncomplexed cyclodextrins. The difference in the positions of the (003) Bragg reflections across all cases is not great, ranging from 0.05 to 1.20° 2θ, but the differences do show correlations that correspond to the complexation of different drugs. Specifically, diffraction patterns of nanohybrids intercalated with TST inclusion complexes show (003) Bragg reflections at 0.9 to 0.55° 2θ lower than drug-free analogues, whilst the same difference between diffraction patterns of nanohybrids intercalated with CIN inclusion complexes and their drug-free analogues ranges from 0.11 to 0.78° 2θ, and for all the cationic tricyclic drugs is 0.18 to 1.20° 2θ.

It has already been established in Section 4.3.1 that the degree of substitution of a cyclodextrin species is directly related to the position of the (00l) reflections seen in the diffraction pattern of its nanohybrid intercalation product, and by extension to the interlayer distance of the nanohybrid. The differences in the positions of the (00l) Bragg reflections indicate that in addition to the degree of cyclodextrin substitution, the positions of the (00l) Bragg reflections (and the interlayer distances) are also influenced by whether the intercalated cyclodextrin is also part of an inclusion complex, and the identity of its inclusion complex guest species. The implications of these trends are discussed further in Section 4.5.

The lattice parameters of the nanohybrids containing β-cyclodextrin–drug complexes are detailed in full in Appendix C.1. The a parameters of the various nanohybrids show little variation, ranging from 3.029 to 3.042 Å, as was the case with the nanohybrids containing uncomplexed cyclodextrins. The values of c parameters reflect the patterns seen in in the positions of the (00l) Bragg reflections, and directly relate to differences interlayer spacing of the nanohybrids, which can be understood through considering changes to the size, shape and orientation of the β-cyclodextrin–drug complexes, discussed in Section 4.5. Warren-type anisotropy is again seen for the (012) Bragg reflections, indicating substantial stacking faults. This can again be explained by the large size of the interlayer anions reducing coordination between adjacent metal hydroxide layers.

4.4.3 Fourier transform infrared spectroscopy

FTIR spectroscopy of the nanohybrids, whilst useful in indicating that the cyclodextrin species had been intercalated, was not ultimately instructive in determining the presence of the drugs in the nanohybrids. The concentrations of the drug species within the nanohybrids were not sufficiently high for major absorptions relating to the drug species to be observed within the nanohybrid spectra to the extent that they could be diagnostic of the presence of the drug species. Additionally, complexation of the drug species within the cyclodextrins has the effect of broadening and reducing the intensity of absorptions relating to these species, making such absorptions harder to identify.

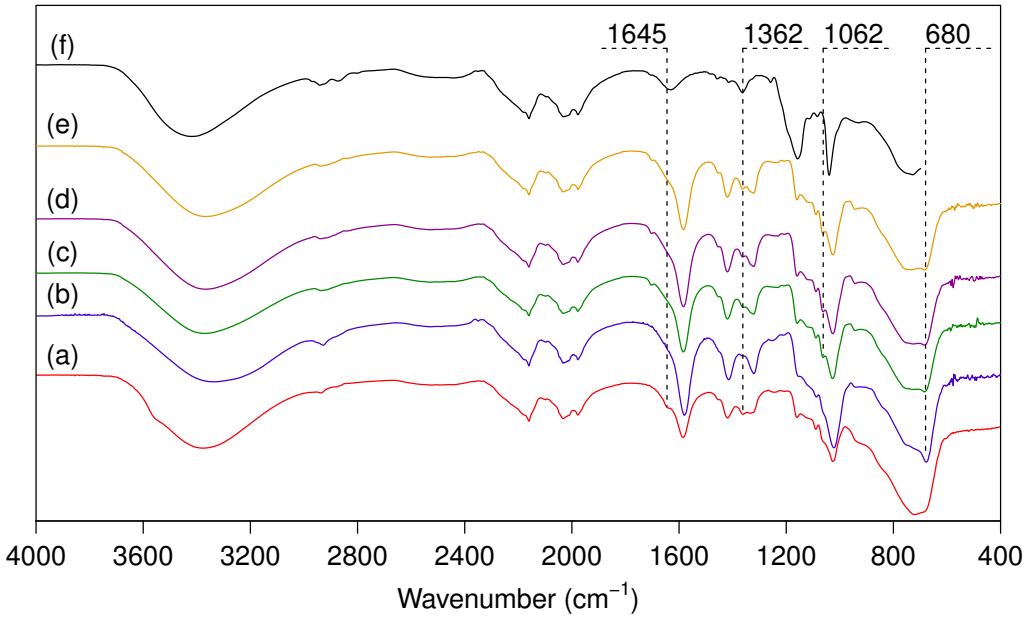


Figure 4.18: The FTIR spectra of (a) MgAl-CMCD[P2]{TST}, (b) MgAl-CMCD[P7]{CIN}, (c) MgAl-CMCD[P3]{CPZ}, (d) MgAl-CMCD[P9]{PMZ}, (e) MgAl-CMCD[P6]{AMI} and (f) MgAl-SBECD{IMI}.

In the spectra of some nanohybrid samples, absorptions attributable to the most intensely absorbing modes of the drug species were just visible, although without the presence of other characteristic absorptions, these individual absorptions were not sufficient to confirm the presence of the desired drug species, rather than an impurity. In the spectra of nanohybrids containing TST, absorptions were seen at 1645 cm^{-1} on the shoulder of the β-CMCD carbonyl absorption, which could be attributed to the carbonyl absorption of TST, in spectra of nanohybrids containing CIN, an absorption is seen at 680 cm^{-1}, whilst in many of the spectra of the nanohybrids containing tricyclic drugs CPZ, PMZ, IMI and AMI, an absorption at 1062 cm^{-1} may be attributable to modes relating to the dimethylammonium groups in these compounds, as can be seen from examples in Figure 4.18.

Also seen in Figure 4.18, IR bands relating to the intercalation of the cyclodextrin species and to the metal hydroxide layers are in good agreement with those of the nanohybrids containing uncomplexed cyclodextrin anions (Figures 4.10 and 4.11). Whilst it is unsurprising that intercalation of the cyclodextrins was successful in aqueous conditions, it is a valuable observation that intercalation is still successful in the mixed water–organic solvent conditions necessary for drug complexation. Addi-

tionally absorptions corresponding to the cyclodextrin species are seen at 1362 cm^{-1} in the spectra of the samples, indicating that complexation of the drug ions may have had a small effect on the positions of the absorptions relating to the β-cyclodextrin ring, whilst the absorptions relating to the substituted groups appear unaffected by drug complexation.

As was the case when intercalating the less substituted β-CMCD anions ([P1]–[P4]) without drugs, the spectra of some of nanohybrids containing inclusion complexes comprising these β-CMCD species show a small absorption at 1235 cm^{-1} relating to cointercalated nitrate ions, which suggests that these nanohybrids are likely to also show low loading percentages of the inclusion complexes. Absorptions relating to any of the organic solvents used in the ion-exchange reactions were not present in any spectra, suggesting that either they were not significantly cointercalated alongside the inclusion complexes, presumably due to preferential cointercalation of water, or that any appreciable amount of residual solvent was removed during drying of the particles.

4.4.4 Nuclear magnetic resonance spectroscopy

Whilst FTIR spectroscopy was not sufficiently sensitive to establish the presence of the drug ions in the nanohybrids, dissolution experiments with the nanohybrids conducted in DCl/D_2O, and subsequent ^1H NMR spectroscopy of the resulting solutions allowed the identification of the drug ions in the nanohybrids. Alongside resonances of the cyclodextrins in the ^1H NMR spectra from dissolution experiments, the resonances of the drug species could be identified and matched to literature values.[33,40–45]

Cefuroxime axetil was the only drug that was not returned intact upon dissolution of the nanohybrids, as it is unstable with respect to hydrolysis.[34] Consequently, further characterisation efforts and release experiments with nanohybrids hoped to contain CFA were not undertaken, as its presence within the nanohybrids could not be established.

4.4.5 Elemental analysis

Due to the complexity of the nanohybrids containing mixtures of partially substituted cyclodextrin anions, drug species, cointercalated nitrate ions and water, simple C, H, N elemental analysis was not sufficiently informative to provide details of drug loading, and so this was calculated through UV spectroscopic analysis. EDX analysis confirmed that the ratio of metal anions within the metal hydroxide layers remained largely unchanged at 1.97 Mg : Al.

Table 4.4: The drug content of the cyclodextrin–drug complex containing nanohybrids.

Nanohybrid	Drug content (W/W %)					
sample	CIN	TST	CPZ	PMZ	IMI	AMI
MgAl-CMCD[P1]	1.9	2.6	-	-	-	-
MgAl-CMCD[P2]	1.9	2.1	-	-	-	-
MgAl-CMCD[P3]	2.1	2.8	3.5	3.8	4.1	3.1
MgAl-CMCD[P4]	2.4	3.6	3.9	-	-	-
MgAl-CMCD[P5]	2.9	3.7	4.9	-	-	-
MgAl-CMCD[P6]	2.7	4.1	4.2	4.9	4.2	4.4
MgAl-CMCD[P7]	3.7	5.0	6.2	-	-	-
MgAl-CMCD[P8]	3.6	5.5	6.9	-	-	-
MgAl-CMCD[P9]	3.4	5.0	6.3	6.2	5.4	6.7
MgAl-CMCD[C2]	3.0	3.9	4.4	4.5	4.6	5.2
MgAl-SBECD	2.6	3.9	5.6	6.3	5.8	6.3

The drug content of the nanohybrids is reported in Table 4.4. The mass percentages of the drugs are all within the range of 2 to 7 %, which although low, is still practical for delivering a therapeutic dose, which is typically 10 to 20 mg for the drugs studied in this chapter, which corresponds to a nanohybrid dose between 143 and 1000 mg. The lowest drug contents were seen in nanohybrid samples containing the β-CMCD species [P1]–[P4], which is likely due to the the reduced loading percentages of these species, as was observed when intercalating the uncomplexed cyclodextrin ions in Section 4.3.4.

The tricyclic drugs presented the highest loading percentages across all samples, whilst CIN presented the lowest. The difference in loading percentages was between the different drugs was greater in the nanohybrids containing more highly substituted

cyclodextrin species, and most prominent in samples containing β-SBECD. The difference in loading percentage seen between the cationic tricyclic drugs and the the neutral drugs, particularly in the samples containing more highly substituted cyclodextrin species, can be explained the by greater affinity the cationic drugs have for the anionic cyclodextrin species, due to the presence of electrostatic attraction in addition to the lypophilic affinity between the drug species and the cyclodextrin cavities.

The drug content observed in the nanohybrid samples, when compared to the approximate content of the cyclodextrin species, reveals that in all cases, the nanohybrids contain a mixture of both cyclodextrin–drug complexes and uncomplexed cyclodextrins, which are cointercalated together. This is corroborated in the ^{1}H NMR spectra from dissolution experiments, where integration of the resonances corresponding to the drug species and the cyclodextrin species indicate there is not a 1 : 1 ratio of cyclodextrin species to drug in any of the samples, by generally an excess of cyclodextrin.

4.4.6 Scanning electron microscopy

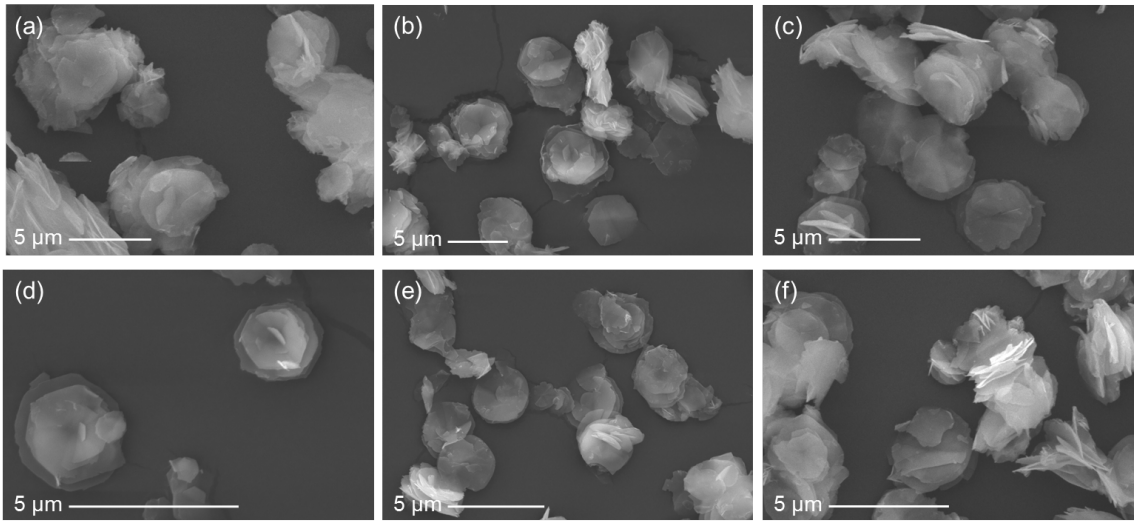


Figure 4.19: SEM images of (a) MgAl-CMCD[P1]{TST}, (b) MgAl-CMCD[P3]{CIN}, (c) MgAl-CMCD[P6]{CPZ}, (d) MgAl-CMCD[P9]{PMZ}, (e) MgAl-CMCD[C2]{AMI} and (f) MgAl-SBECD{IMI}.

Example SEM images of nanohybrids intercalated with inclusion complexes are displayed in Figure 4.19. The morphology of the nanohybrids intercalated with inclusion

complexes was very similar to that of the nanohybrids described in Section 4.3.5. The nanohybrid particles resembled circular platelets, with some approaching rounded hexagonal platelets, and others resembling broken segments of the first two shapes. Many particles exhibited ragged, chipped edges, indicative of mechanical wear to the particles, and partial delamination was prevalent. Neither the presence of the drug moieties nor the organic solvents seemed to have any noticeable impact on the particle morphology.

4.5 Proposed orientation of guest species

Several attempts have been made to speculate the orientation of anionic cyclodextrin species in the interlayer region of LDHs upon intercalation, and one of two orientations are typically suggested, either cyclodextrin rings lying parallel to the LDH sheets, or LDH rings lying perpendicular, as can be seen in Figure 4.20.[9,19,30] Previous speculations were based on relatively few, substantially different examples of LDH–cyclodextrin nanohybrids, whereas the samples described in Sections 4.3 and 4.4 comprise by far the most extensive range of directly comparable LDH–cyclodextrin nanohybrids synthesised to date. Due to the systematic variations in the synthesis of the substituted cyclodextrin species, trends not previously observed in cyclodextrin intercalated LDH nanohybrids have emerged. Based on the incremental differences observed in the interlayer distances, obtained from the powder X-ray diffraction patterns, of both the cyclodextrin–drug containing nanohybrids and the uncomplexed cyclodextrin containing nanohybrids, a more nuanced model of for the orientation of cyclodextrin species the between the metal hydroxide layers can be proposed, taking the varying sizes of the cyclodextrin species and the cyclodextrin–drug inclusion complexed into account.

Figure 4.20 illustrates how the interlayer spacing of a nanohybrid would be expected to differ when intercalated with a typical cyclodextrin–drug inclusion complex as compared to an uncomplexed cyclodextrin anion in both of the previously proposed cyclodextrin orientations, based on the dimensions obtained for cyclodextrin–drug inclusion complexes as compared to uncomplexed cyclodextrins reported in the literature.[46–48] If the cyclodextrin species were to lie parallel to the metal hydroxide

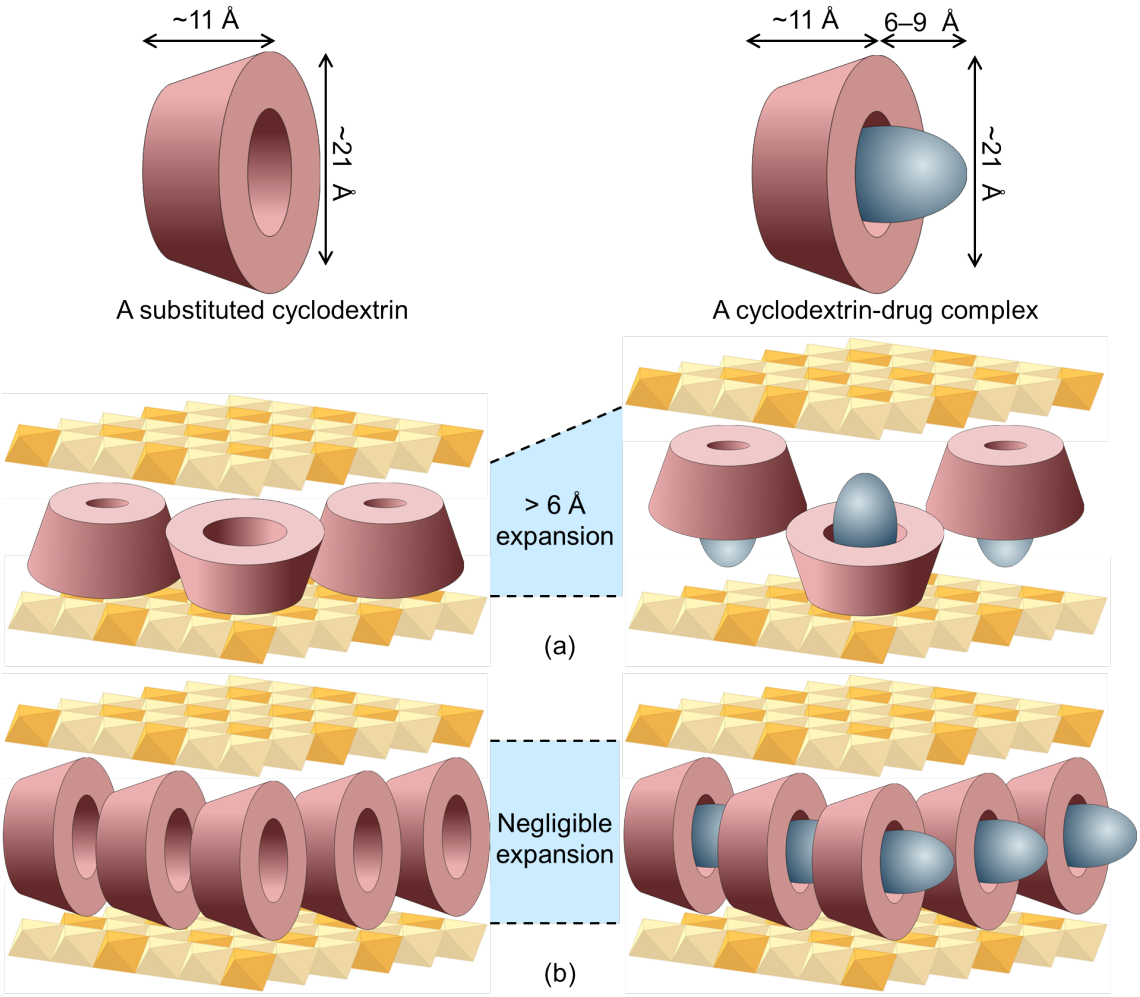


Figure 4.20: A schematic illustrating the previously proposed orientations of cyclodextrin anions within LDH layers within the literature, (a) parallel,[30] and (b) perpendicular,[9] and how such orientations may be expected to influence the interlayer distances of LDHs when the cyclodextrin anions form inclusion complexes with drug species.[46–48]

layers, as in Figure 4.20(a), the difference in interlayer distance upon intercalating a typical cyclodextrin–drug inclusion complex would be approximately 6 to 9 Å greater than upon intercalating an uncomplexed cyclodextrin. If, however, the cyclodextrin species were to lie perpendicular to the metal hydroxide layers upon intercalation, as in Figure 4.20(b), the difference in interlayer distance upon intercalating a cyclodextrin–drug inclusion complex as compared to the uncomplexed cyclodextrin would be negligible. It is evident that neither of these orientations reflect what is observed regarding the differences in interlayer distances in any of the nanohybrids, with the differences in interlayer distances between the complex intercalated nanohybrids and

the uncomplexed cyclodextrin intercalate nanohybrids falling within the range of 0.5 to 4.5 Å.

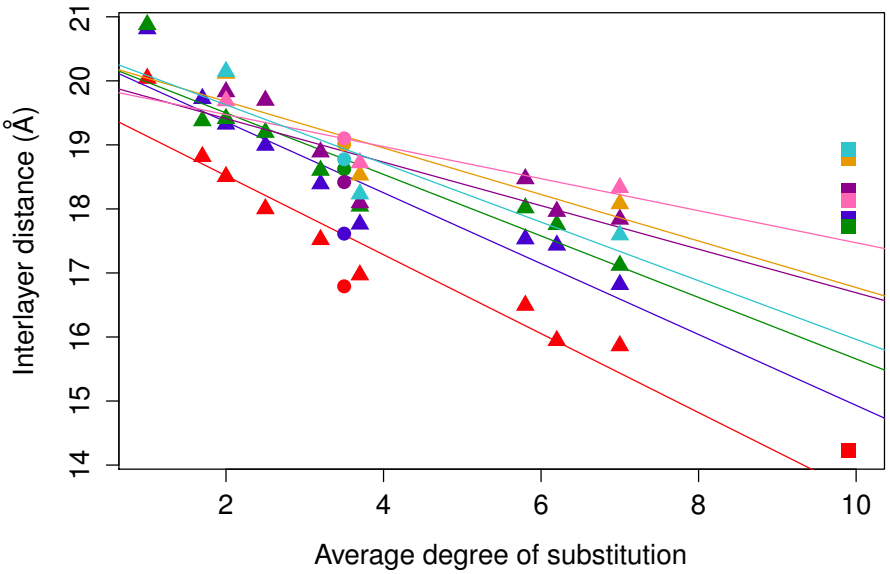


Figure 4.21: The calculated interlayer distances of the cyclodextrin and cyclodextrin–drug complex containing nanohybrids, displayed as a function of the degree of substitution on the cyclodextrin species. Uncomplexed cyclodextrin containing nanohybrids are shown in red, ▲, those containing CIN in blue, ▲, TST in green, ▲, CPZ in purple, ▲, PMZ in orange ▲, IMI in pink, ▲, and AMI in cyan, ▲. The nonselectively substituted β-CMCD containing samples are depicted with a ▲, those containing β-CMCD[C2] with a ●, and those containing β-SBECD with a ■.

Figure 4.21 depicts the interlayer distances of the various nanohybrid species. The differences in interlayer distance between the nanohybrids containing complexed and uncomplexed cyclodextrins can be seen, and the emergence of several trends; these figures are also tabulated in Appendix C.1. It has already been noted that intercalation of the complexed cyclodextrins leads to a larger interlayer distance. What can be also seen is that this increased distance is related to the drug species in the inclusion complexes, indicating that the size of the cyclodextrin–drug complex has a direct influence on the interlayer distance. As the drug species only extend out of one side of the cyclodextrin anions, this also provides information about the orientation of the complexes, as the drug species must be partially angled towards the metal hydroxide layers to have such an effect, as is illustrated in Figure 4.22. Another factor which may contribute to the greater interlayer distances seen in nanohybrids containing cationic tricyclic drugs, is that the positive charge on these drugs will

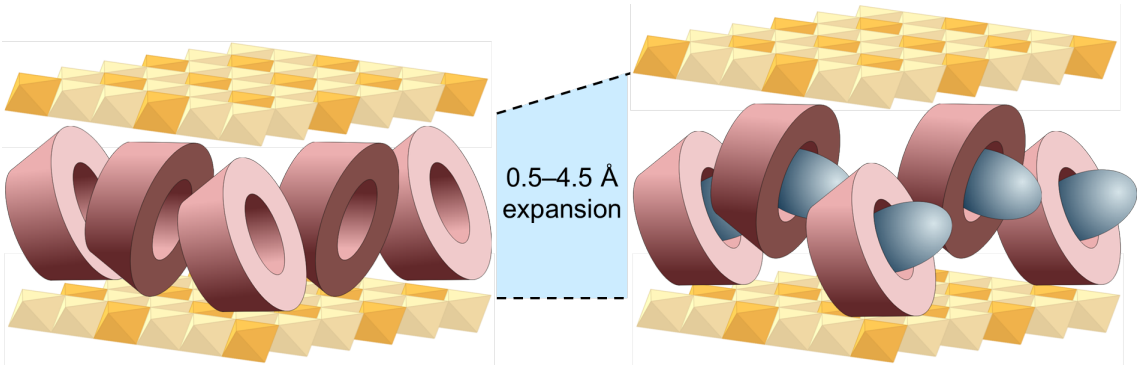


Figure 4.22: A schematic illustrating the proposed angled orientation for cyclodextrin anions and cyclodextrin–drug complexes within an LDH, and how this affects the interlayer distance between the metal hydroxide layers.

reduce the overall negative charge on the cyclodextrin complexes containing these drugs, reducing the electrostatic forces between these species and the metal hydroxide layers and leading to increases in interlayer distance.

Another trend that is noticeable is that the difference in interlayer distance seen between complexed and uncomplexed cyclodextrins is greater when intercalating the more highly substituted β-CMCD species than when intercalating the less highly substituted β-CMCD species. This suggests that the angle of cyclodextrin species within the layers is related to the degree of substitution, with the more highly substituted cyclodextrins angling the drug species more towards the metal hydroxide layers, as is illustrated in Figure 4.23.

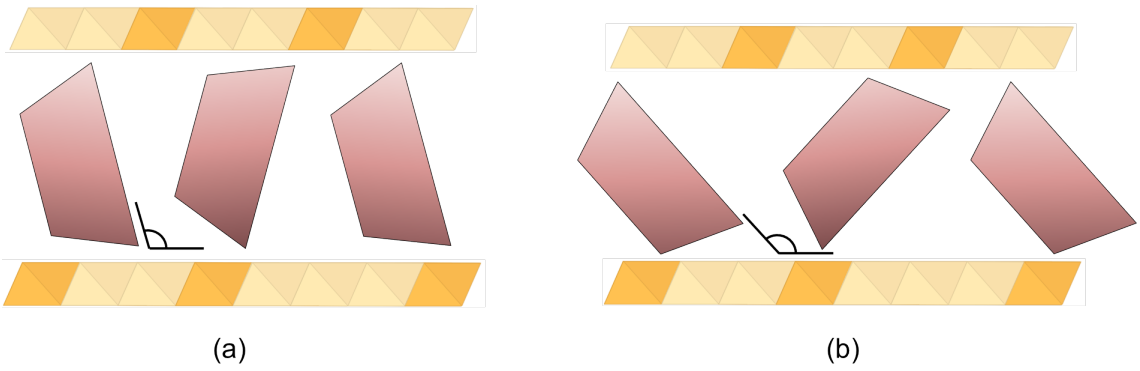


Figure 4.23: A schematic illustrating the proposed angled orientation for cyclodextrin anions within an LDH as viewed along the *xy* plane, showing the difference in orientation and interlayer distance between (a) a partially and (b) a highly substituted cyclodextrin.

The relationship between the angle of the cyclodextrin species within the layers

and their degree of substitution may be rationalised by considering where on the cyclodextrin species the substitution occurs. Greater substitution at the C6 positions, which are on the narrower side of the cyclodextrin ring, may increase the favourability of a more angled orientation, as it allows greater interaction between these groups and the metal hydroxide layers. As substantial substitution at the C6 position only occurs in samples with higher degrees of substitution, a more angled orientation would be expected by these cyclodextrin species. Additionally, the more angled orientation would also lead to a smaller interlayer distance, which alongside the effect of increased electrostatic attraction described in Section 4.3.1, helps to explain the trend seen in the interlayer distances of nanohybrids intercalated with uncomplexed cyclodextrin anions.

Nanohybrid samples containing drug complexes with β-CMCD[C2] are consistent with this hypothesis, but as the degree of substitution of β-CMCD[C2] is not high, it does not provide a substantial contrast to other β-CMCD samples with similar degrees of substitution, in particular β-CMCD[P5] and β-CMCD[P6], which only have low degrees of substitution at the C3 and C6 positions. Consequently, the intercalation of β-CMCD[C2] is not able to provide significant additional information regarding the orientation of cyclodextrin species. Intercalation of a selectively substituted cyclodextrin with a higher degree of substitution would be more informative, as according to he above hypothesis, a greater difference would be seen between the interlayer distances of nanohybrids intercalated with this and the nanohybrids intercalated with non-selectively substituted cyclodextrins (such as β-CMCD[P9]).

The orientation of β-SBECD and its complexes cannot be extrapolated from the trends seen in intercalating the β-CMCD species, due to its larger size, greater charge and degree of substitution, and the greater flexibility the sulfobutyl groups, compared to the carboxymethyl groups. In particular, the interlayer distance of MgAl-SBECD is substantially lower that those of the cyclodextrin species, despite its larger size, suggesting it may lie parallel to the metal hydroxide layers when uncomplexed, as in Figure 4.20(a). However, some common trends are seen, in particular that the interlayer distances of nanohybrids containing β-SBECD–drug complexes are all greater than that containing uncomplexed β-SBECD, yet not so much greater that the interlayer distances seen are coherent with the complexes species lying parallel

to the hydroxide layers, and so it is likely that these species are also angled to some extent, as with the β-CMCD–drug complexes.

4.6 Release studies

Drug release from the nanohybrids was carried out in biomimetic buffers at pH 2.0, 4.0 and 7.0. Release from the nanohybrids at pH 2.0 and 4.0 was only measured on a selection of samples, as it was quickly established that release at these pHs was rapid and dominated by dissolution of the nanohybrid particles. Release at these pHs was measured on fourteen samples: those containing the drugs CIN, TST or CPZ, and those containing the cyclodextrin species β-CMCD[P1], [P5], [P9], [C2] or β-SBECD. Release at pH 7.0 was was measured on all samples, as release rate at this pH was found to be strongly dependent on the cyclodextrin species and the charge on the drug species, due to diffusion being the primary mechanism of release.

Release profiles of the nanohybrids in acid conditions are displayed in Figure 4.24. In all cases, the majority of the drug release occurs very rapidly, with more than 95 % drug release occurring within the first 2 min at pH 2.0 and within 5 min at pH 4.0. Neither the identity of the drug nor the cyclodextrin species appear to influence the rate of drug release at pH 2.0, and any variation in the release rates of the nanohybrids at this pH is apparently random. Due to the speed of the initial release, it is not possible to identify any trends as the majority of the drug release occurs prior to taking the first measurement, 30 s after initiation of the release experiment.

A weak correlation can be seen between the rate of release and the degree of substitution on the cyclodextrin species at pH 4.0, with the initial rapid release phase of nanohybrids containing β-CMCD[P9] and β-SBECD occurring over the course of 3 – 5 min, whilst the initial release phase typically occurs in under 2 – 3 min for the other samples. The speed with which initial release occurs is still too rapid at this pH to be any more informative.

In comparison, significant differences were seen in the release profiles of the nanohybrids at pH 7.0 (Figure 4.25). At this neutral pH, the initial release phase varies widely, with 90 % drug release still being reached in under 3 min by monovalent

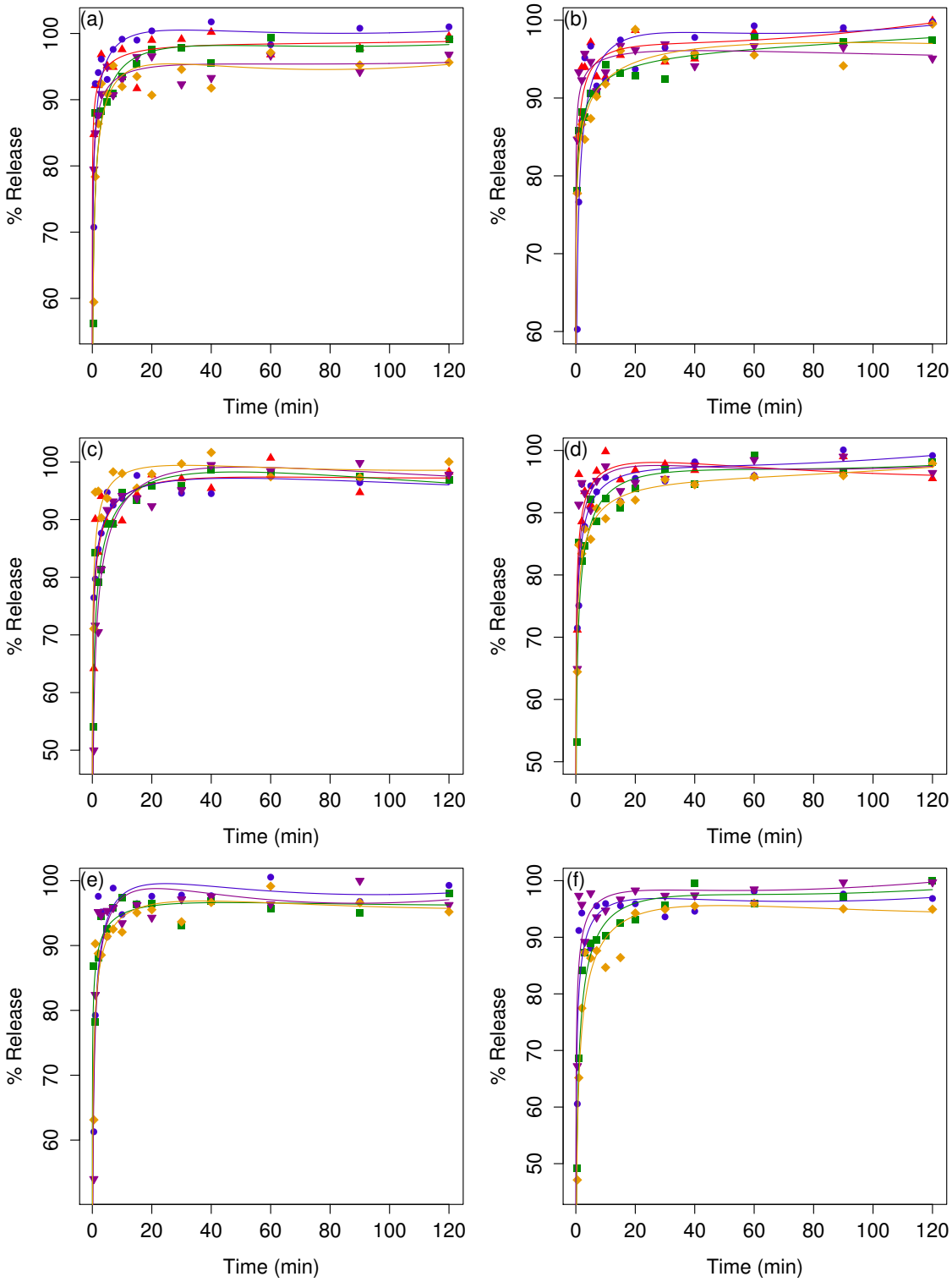


Figure 4.24: *In vitro* release profiles of nanohybrids containing CIN in (a) pH 2.0 sulphate buffer and (b) pH 4.0 phosphate buffer, TST in (c) pH 2.0 sulphate buffer and (d) pH 4.0 phosphate buffer, and CPZ in (e) pH 2.0 sulphate buffer and (f) pH 4.0 phosphate buffer at 37 °C. The cyclodextrin species in the nanohybrids are β-CMCD[P1], ▲, β-CMCD[P5], ●, β-CMCD[P9], ■, β-CMCD[C2], ▼, and β-SBECD◆.

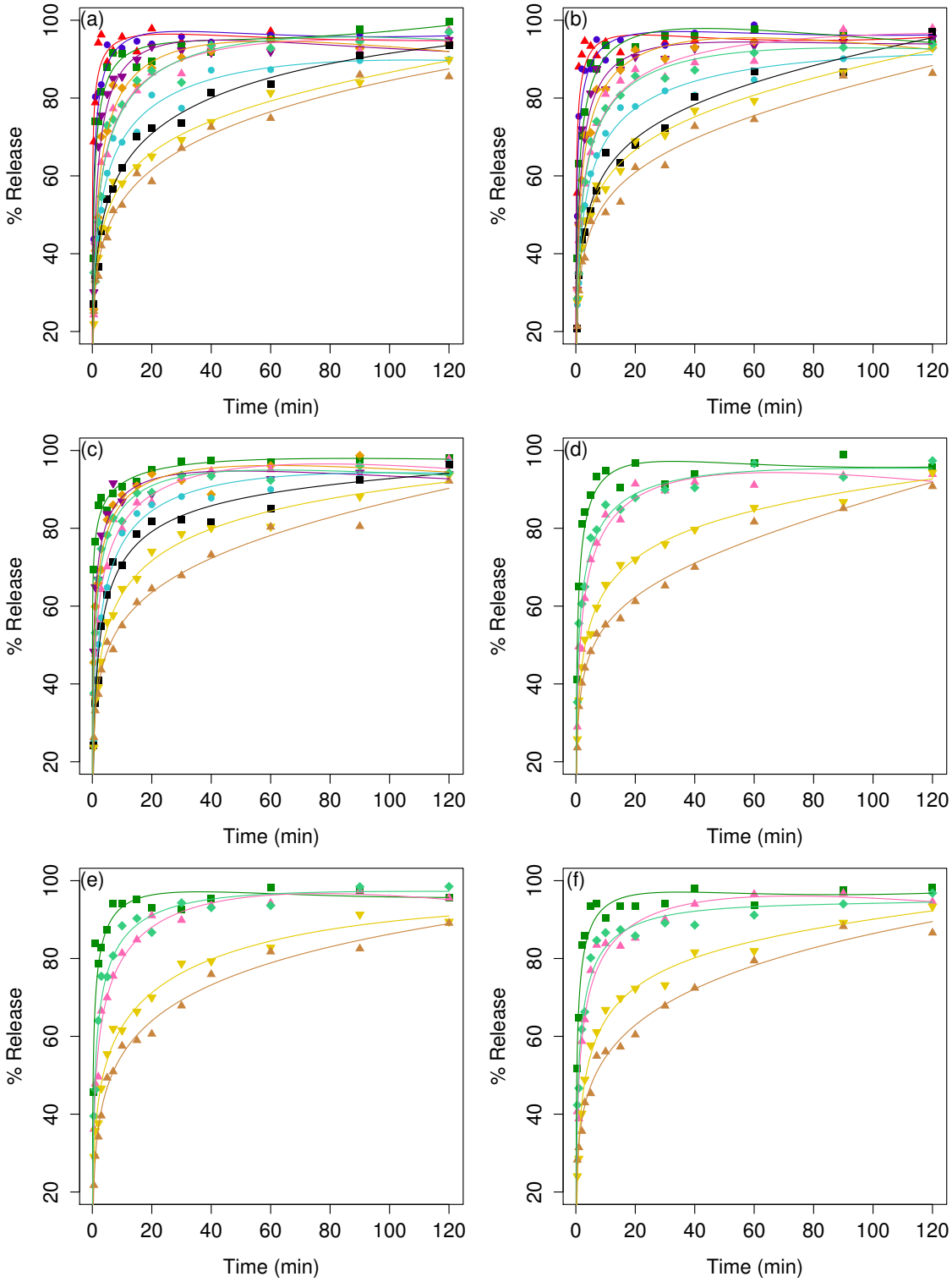


Figure 4.25: *In vitro* release profiles of nanohybrids containing (a) CIN, (b) TST, (c) CPZ, (d) PMZ, (e) IMI, and (f) AMI in pH 7.0 phosphate buffer at 37 °C. The cyclodextrin species in the nanohybrids are β-CMCD[P1], ▲, β-CMCD[P2], ●, β-CMCD[P3], ■, β-CMCD[P4], ▼, and β-CMCD[P5], ◆, β-CMCD[P6], ▲, β-CMCD[P7], ●, β-CMCD[P8], ■, β-CMCD[P9], ▼, and β-CMCD[C2], ◆, and β-SBECD, ▲.

complexes, whereas 90 % drug release is only reached around 100 min in samples containing β-CMCD[P9], and around 120 min in samples containing β-SBECD. There is a clear relationship between the degree of substitution on the cyclodextrin species and the rate of release, whilst the identity of the drug species has little effect. The rate of release of cationic drugs is marginally higher than that of the neutral drugs, but this effect is minor compared to the effect of varying cyclodextrin species. There appears to be no difference in release rates for the drug species of a given charge. TST and CIN both release at approximately the same rate when complexed to a given cyclodextrin. Similarly, the tricyclic drugs also display comparable release rates when complexed to a given cyclodextrin. This indicates that it is the charge on the cyclodextrin species, rather than the drugs with which they are complexed, that is the major factor influencing release rate.

The pattern of release seen in all samples is typical for LDH compounds, with an initial rapid burst followed by a tail of more gradual release. However, within this general pattern there is significant variation that is dependent on the level of substitution on the cyclodextrin species. In samples with low degrees of cyclodextrin substitution (β-CMCD[P1]–[P4]), the rapid release phase constitutes the majority of the release, with at least 90 % of the drug release occurring in this phase. In contrast, the initial burst phase in samples with high degrees of cyclodextrin substitution (β-CMCD[P8], [P9] and β-SBECD) only constitutes around 50 – 60 % of the drug release, and the tailing phase becoming a much more prominent feature in these release profiles. The intermediary samples show a gradual progression in the release profiles from the former to the latter shape as the degree of substitution on the cyclodextrin samples increases.

Both the difference in release rate and in the shape of the release profiles are illustrated in Figure 4.26, which presents the estimated times at which 50 and 90 % drug release is reached in the nanohybrids samples, t_{50} and t_{90}, as functions of their degree of substitution. The figures for t_{50} and t_{90} are also displayed in Table 4.5 for reference. The nanohybrid samples containing β-SBECD have been omitted in the plots to make comparison between β-CMCD containing samples clearer. The relationship between t_{50} and degree of cyclodextrin substitution is almost linear, whereas the relationship between t_{90} and the degree of cyclodextrin substitution reveals higher

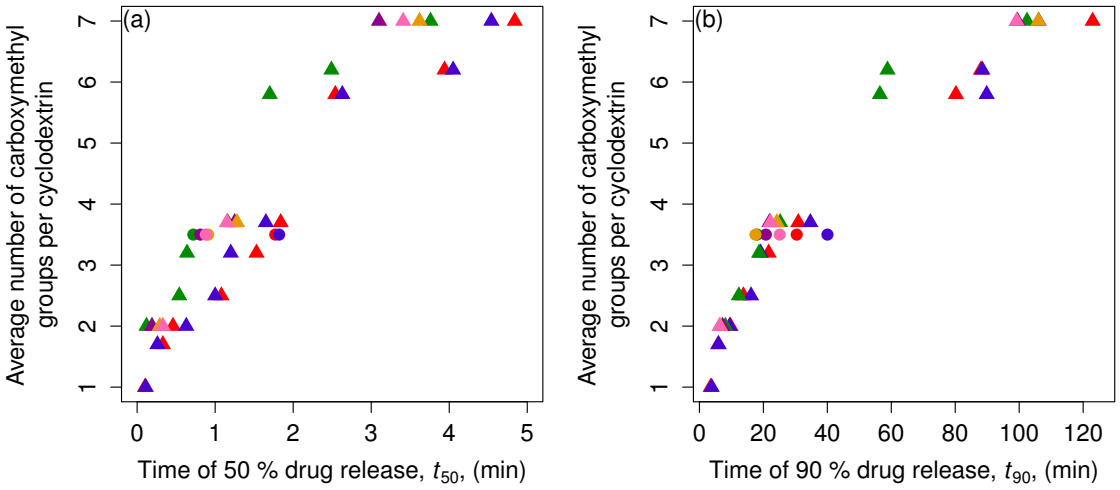


Figure 4.26: The time taken for the nanohybrids to reach (a) t_{50}, 50 % drug release, and (b) t_{90}, 90 % drug release in pH 7 phosphate buffer, compared against the degree of substitution on the β-CMCD species in the samples. Nanohybrids containing CIN are shown in red, ▲, those containing TST in blue, ▲, CPZ in green, ▲, PMZ in purple, ▲, IMI in orange ▲, and AMI in pink, ▲. The nonselectively substituted β-CMCD containing samples are depicted with a ▲and those containing β-CMCD[C2] with a ●.

Table 4.5: The time taken for the nanohybrids to reach t_{50}, 50 % drug release, and t_{90}, 90 % drug release in pH 7 phosphate buffer.

Drug	MgAl-CMCD										MgAl-SBECD
released	[P1]	[P2]	[P3]	[P4]	[P5]	[P6]	[P7]	[P8]	[P9]	[C2]	
						t_{50} (min)					
CIN	0.10	0.33	0.46	1.08	1.53	1.84	2.54	3.94	4.84	1.77	7.26
TST	0.11	0.26	0.63	1.00	1.20	1.65	2.63	4.05	4.54	1.82	7.37
CPZ	-	-	0.12	0.54	0.64	1.16	1.70	2.49	3.76	0.72	6.42
PMZ	-	-	0.19	-	-	1.25	-	-	3.10	0.81	5.96
AMI	-	-	0.33	-	-	1.15	-	-	3.41	0.88	6.53
IMI	-	-	0.29	-	-	1.28	-	-	3.62	0.91	6.51
						t_{90} (min)					
CIN	3.51	5.87	9.71	13.8	21.6	30.9	80.2	88.0	123	30.4	139
TST	3.83	6.00	9.47	16.1	19.1	34.7	89.8	88.5	106	40.0	129
CPZ	-	-	8.10	12.3	18.7	25.2	56.4	58.8	103	18.0	115
PMZ	-	-	7.23	-	-	21.9	-	-	99.5	20.8	148
AMI	-	-	6.33	-	-	22.2	-	-	99.2	25.1	124
IMI	-	-	6.42	-	-	24.2	-	-	106	17.5	129

degrees of substitution to have a greater effect on t_{90}.

The release profiles of nanohybrids containing β-CMCD[C2]–drug complexes were not distinguishable from those of nanohybrids containing non-selectively substituted β-CMCD species, within the error of the release experiments. This lends support to the idea that it is the overall charge on the complexes that is the the governing factor in controlling the rate of release, rather than the shape of the of the complexes. Although, as has already been noted, β-CMCD[C2] is not particularly highly substituted, and so comparisons between this species and the other β-CMCD species can only be limited.

Nanohybrids containing β-SBECD–drug complexes show the lowest rate of release. This is most likely due to the higher charge on this nanohybrid, rather than the difference between sufobutylether and carboxymethyl substituents. However, as there is no direct comparison in the series of β-CMCD species, the extent to which identity of the substituents effects release rate cannot be established.

4.6.1 Kinetic models

The release profiles of the nanohybrids were fitted to the five models for release frequently used to in the context of LDHs, as was the case with the release profiles of nanohybrids in Chapters 2 and 3. The models, also detailed in Section 2.4.1, are the Avrami–Erofe'ev model, the Elovich model, a simple first order model, the modified Freunlich model and a parabolic diffusion model.[49–56] The fit to each model was evaluated using a least squares regression. The correlation coefficients, r^2, for the fit of each model to each release profile are detailed in full in Appendix C.2.

Clear trends can be found in the fit of the different models to the release profiles, which is indicative of different release mechanisms at work for different compounds and in different conditions. The profiles of release in acidic conditions did not find a close match with one particular model, although as release was generally rapid in these conditions, the ability to model the profiles accurately was reduced. The two models that consistently match drug release in acid conditions most closely were the modified Freundlich model for describing rates of desorption from clays and the parabolic diffusion model, which describes radial diffusion in a cylinder,[57–59]

although neither model provides a very close fit, with $0.60 \leq r^2 \leq 0.90$ for the modified Freundlich and $0.68 \leq r^2 \leq 0.89$ for the parabolic diffusion model. The Avrami–Erofe'ev model matches select cases well, but is generally a mediocre fit to the data.

With the exception of the simple first order model, all models display a good fit to the majority of the profiles for release in pH 7.0 buffer. Two obvious rends can be seen, with release from samples containing β-CMCD[P1] to [P5] and [C2] showing a clear preferential fit to the Freundlich model, whilst release from samples containing β-CMCD[P7] to [P9] and β-SBECD present good matches to both the Avrami–Erofe'ev and the Elovich models. Interestingly, release from samples containing β-CMCD[P6] shows roughly equal matches to all three models, suggesting a transition from the mechanism of release found in the the the less highly substituted β-CD samples to the mechanism found in the more highly substituted β-CD samples at around this point.

The modified Freundlich and parabolic diffusion models fit the data most accurately, these models can in principle be used for extracting kinetic and mechanistic data about the release of drugs from the LDH–cyclodextrin models. In particular, the modified Freundlich model can be used to obtain a value for the rate constant for drug release, k_F. The parabolic diffusion model, in contrast, which is based on the rate of radial diffusion in a cylinder, whereby diffusion in perpendicular directions is negligible, in not so useful for extracting mechanistic data, as diffusion in the interlayer space of LDHs occurs in two dimensions, and so the apparent one dimensional diffusion constant and supposed cylinder radius given by this model and not physically meaningful. The high accuracy of this model can be interpreted qualitatively, however, as it implies that diffusion in a single direction between LDH sheets is preferable to a perpendicular direction., This may make physical sense in this instance due to the orientation of the cyclodextrin complexes causing one direction to be more favourable for diffusion than the other, perpendicular direction available to the cyclodextrin complexes. The values of the k_F obtained from the modified Freundlich model are included in Appendix C.3.

The values of k_F, reported in Appendix C.3, firmly support the trends seen visually in the release profiles. The rate constants for release from nanohybrids containing

more highly substituted cyclodextrins are lower than those calculated for release from nanohybrids containing less highly substituted cyclodextrins. This is most apparent for release in pH 7 buffer, whereas in acid buffers there are some anomalies to this general trend. The release rate constants also release a clear different in release rates for a given cyclodextrin when complexed to a neutral drug in comparison to a cationic drug. The rate constants calculated quantitatively support the qualitative trends seen in the release profiles.

4.6.2 Discussion

The release profiles of the nanohybrids in acid media are unremarkable, indicating that when LDH dissolution is the release mechanism, near-complete drug release is rapid, uncontrollable and unaffected by variation of the cyclodextrin species. The release profiles of the nanohybrids in neutral conditions, however, indicate the great potential of release using LDH–cyclodextrin nanohybrids when deintercalation by diffusion is the release mechanism. The release profiles show that a wide variety of drug release rates can be achieved through the intercalation of different cyclodextrin species, and that any release rate within this range can be achieved through selection of a cyclodextrin species with an appropriate degree of substitution. The release profiles have been demonstrated to be independent of the drug species, once the charge of the drug species has been accounted for, and also shown to be consistent and reproducible for a cyclodextrin with a given degree of substitution, which could allow the release profiles of nanohybrids containing cyclodextrin–drug complexes of other drug species to be predicted.

The shape of release profiles of the nanohybrids containing highly substituted cyclodextrins is one that is potentially very useful, as it provides an initial burst of drug release to quickly reach the therapeutic window, followed by the tailing effect which allows the therapeutic effects to be sustained for a significant period of time without exceeding the therapeutic window. This is even without combination with other excipients and coatings, which would allow the drug release to be extended further. The LDH–cyclodextrin nanohybrids demonstrate a reliable way to controllably release both neutral and cationic drugs, but could also potentially be used to

control the release of anionic drugs, which would otherwise deintercalate from LDH species rapidly due to their low charge.

4.7 Conclusion

In this chapter, a series of LDH nanohybrids containing a range of systematically varied, partially substituted β-cyclodextrin samples were synthesised through an ion-exchange method and fully characterised. The nanohybrids showed cyclodextrin loading percentages between 27 and 53 %, which was correlated to the degree of substitution of the β-cyclodextrin species being intercalated.

Using the same range of substituted β-cyclodextrins, six chemically and pharmacologically varied drugs, including both neutral and cationic species, were intercalated into and LDH through prior formation of inclusion complexes with the β-cyclodextrin samples, followed by intercalation of these inclusion complexes, by adapting the ion-exchange method. The resulting LDH–complex nanohybrids were fully characterised, revealing drug loading percentages ranging from 2 to 7 %. The effect on the extent of β-cyclodextrin substitution on the drug loading was explored.

Inspection of the diffraction patterns of the β-cyclodextrin and β-cyclodextrin–drug containing nanohybrids provided information to propose a new hypothesis for the orientation of the anions within the LDH layers. An angled orientation was proposed, that is dependent on the extent to which the β-cyclodextrin species are substituted. This refutes previous models that have been proposed for the orientation of cyclodextrin species within LDH layers.

The drug release profiles of the β-cyclodextrin–drug containing nanohybrids were recorded, and revealed that at neutral pH the extent of substitution of the β-cyclodextrin species was strongly correlated to the rate of drug release, which ranged from 90 % drug release within 5 to over 120 min. The rate of drug release was found to be independent of the drug species being released, indicating that the rate of drug release can be predicted from the extent to which the β-cyclodextrin species is substituted. Additionally, the shape of the release profiles of nanohybrids containing highly substituted β-cyclodextrin species was of interest for its potential in controlled

release, consisting of an initial rapid release phase followed by a gradual tail of drug release.

4.8 References

(1) Li, F.; Jin, L.; Han, J.; Wei, M.; Li, C. *Ind. Eng. Chem. Res.* **2009**, *48*, 5590–5597.
(2) Li, Y.; Li, H.; Wei, M.; Lu, J.; Jin, L. *Chem. Eng. J.* **2009**, *151*, 359–366.
(3) Tyner, K. M.; Schiffman, S. R.; Giannelis, E. P. *J. Control. Release* **2004**, *95*, 501–14.
(4) Medina, A.; Martinez, M.; Gonzalez, J. R.; Diaz, A.; Colon, J. L. In *Abstr. Pap. 232nd ACS Natl. Meet. San Fr. CA, United States*, American Chemical Society: 2006, MEDI–167.
(5) Liu, X. L.; Wei, M.; Wang, Z. L.; Evans, D. G.; Duan, X. *Society* **2008**, 17517–17524.
(6) Xue, X.; Gu, Q.; Pan, G.; Liang, J.; Huang, G.; Sun, G.; Ma, S.; Yang, X. *Inorg. Chem.* **2014**, *53*, 1521–1529.
(7) Ciobanu, A.; Ruellan, S.; Mallard, I.; Landy, D.; Gennequin, C.; Siffert, S.; Fourmentin, S. English *J. Incl. Phenom. Macrocycl. Chem.* **2013**, *75*, 333–339.
(8) Jin, L.; Ni, X.; Liu, X.; Wei, M. *Chem. Eng. Technol.* **2010**, *33*, 82–88.
(9) Nakayama, H.; Kuwano, K.; Tsuhako, M. *J. Phys. Chem. Solids* **2007**, *69*, 1552–1555.
(10) Jin, L.; Liu, Q.; Sun, Z. Z.-Y.; Ni, X.-Y. X.; Wei, M. *Ind. Eng. Chem. Res.* **2010**, *49*, 11176–11181.
(11) Li, S.; Shen, Y.; Liu, D.; Fan, L.; Wu, K.; Xiao, M. *Funct. Mater. Lett.* **2013**, *6*, 1350030–1350033.
(12) Loftsson, T.; Hreinsdóttir, D.; Másson, M. *Int. J. Pharm.* **2005**, *302*, 18–28.
(13) Merzlikine, A.; Abramov, Y. a.; Kowsz, S. J.; Thomas, V. H.; Mano, T. *Int. J. Pharm.* **2011**, *418*, 207–16.
(14) Schneider, H.-J.; Hacket, F.; Rüdiger, V.; Ikeda, H. *Chem. Rev.* **1998**, *98*, 1755–1786.
(15) Davis, M. E.; Brewster, M. E. *Nat. Rev. Drug Discov.* **2004**, *3*, 1023–1035.
(16) Challa, R.; Ahuja, A.; Ali, J.; Khar, R. K. *AAPS PharmSciTech* **2005**, *6*, 329–357.
(17) Tiwari, G.; Tiwari, R.; Rai, A. K. *J. Pharm. Bioallied Sci.* **2010**, *2*, 72–79.
(18) Hogg, R. M. G.; Mirakhur, R. K. *Expert Rev. Neurother.* **2009**, *9*, 599–608.
(19) Zhao, H.; F. Vance, G. *J. Chem. Soc. Dalt. Trans.* **1997**, 1961–1966.
(20) Semenova, E.; Cooper, A.; Wilson, C.; Converse, C. English *J. Incl. Phenom. Macrocycl. Chem.* **2002**, *44*, 155–158.
(21) Ryu, S.-J.; Jung, H.; Oh, J.-M.; Lee, J.-K.; Choy, J.-H. *J. Phys. Chem. Solids* **2010**, *71*, 685–688.
(22) Hattori, M.; Okada, Y.; Takahashi, K. *J. Agric. Food Chem.* **2000**, *48*, 3789–3794.
(23) Dignam, C. F.; Randall, L. a.; Blacken, R. D.; Cunningham, P. R.; Lester, S.-K. G.; Brown, M. J.; French, S. C.; Aniagyei, S. E.; Wenzel, T. J. *Tetrahedron: Asymmetry* **2006**, *17*, 1199–1208.
(24) Ivanyi, R.; Jicsinszky, L.; Hirschberg Gabriella, S.; Vadasz, Z.; Szente, L. Manufacture of sulfobutylated cyclodextrins of pharmaceutical additive quality. HU 2009000229 A2., 2010.
(25) Luna, E. A.; Vander Velde, D. G.; Tait, R. J.; Thompson, D. O.; Rajewski, R. A.; Stella, V. J. *Carbohydr. Res.* **1997**, *299*, 111–118.
(26) Tongiani, S.; Velde, D. V.; Ozeki, T.; Stella, V. J. *J. Pharm. Sci.* **2005**, *94*, 2380–2392.
(27) Wei, M.; Wang, J.; He, J.; Evans, D. G.; Duan, X. *Microporous Mesoporous Mater.* **2005**, *78*, 53–61.
(28) Jain, A. S.; Date, A. A.; Pissurlenkar, R. R. S.; Coutinho, E. C.; Nagarsenker, M. S. *AAPS PharmSciTech* **2011**, *12*, 1163–1175.
(29) Iyi, N.; Yamada, H.; Sasaki, T. *Appl. Clay Sci.* **2011**, *54*, 137–132.
(30) Mohanambe, L.; Vasudevan, S. *J. Chem. Sci.* **2006**, *118*, 105–115.
(31) Liu, X.; Meng, L. English *Korean J. Chem. Eng.* **2013**, *30*, 918–924.
(32) Wang, C. J. Controlled Synthesis and Properties of Layered Double Hydroxides., D.Phil Thesis, University of Oxford, 2012.
(33) Stoeckel, K.; Hofheinz, W.; Laneury, J. P.; Duchene, P.; Shedlofsky, S.; Blouin, R. A. *Antimicrob. Agents Chemother.* **1998**, *42*, 2602–2606.

(34) Du, Y.; Zhai, Y.; Zhang, J.; Wu, C.; Luo, C.; Sun, J.; He, Z. *Asian J. Pharm. Sci.* **2013**, *8*, 287–294.
(35) Basu, B.; Bagadiya, A.; Makwana, S.; Vipul, V.; Batt, D.; Dharamsi, A. *J. Adv. Pharm. Technol. Res.* **2011**, *2*, 266–273.
(36) Raghuvanshi, S.; Pathak, K. *J. Drug Deliv.* **2014**, *2014*, 479246.
(37) Ericson-Neilsen, W.; Kaye, A. D. *Ochsner J.* **2014**, *14*, 203–207.
(38) Schiffman, S. S.; Zervakis, J.; Suggs, M. S.; Shaio, E.; Sattely–Miller, E. A. *Physiol. Behav.* **1999**, *66*, 183–191.
(39) Schiffman, S. S.; Zervakis, J.; Suggs, M. S.; Budd, K. C.; Iuga, L. *Pharmacol. Biochem. Behav.* **2000**, *65*, 599–609.
(40) Warren, R. J.; Eisdorfer, I. B.; Thompson, W. E.; Zarembo, J. E. *J. Pharm. Sci.* **1966**, *55*, 144–150.
(41) Florence, A. T.; Parfitt, R. T. *J. Phys. Chem.* **1971**, *75*, 3554–3560.
(42) Miura, T.; Takagi, H.; Adachi, K.; Kimura, M. *Chem. Pharm. Bull.* **1982**, *30*, 3154–3159.
(43) Buddrus, J.; Herzog, H. *Anal. Chem.* **1983**, *55*, 1611–1614.
(44) Tokumura, T.; Ueda, H.; Tsushima, Y.; Kasai, M.; Kayano, M.; Amada, I.; Nagai, T.; Machida, Y.; Nagai, T. *Chem. Pharm. Bull.* **1984**, *32*, 4179–4184.
(45) Tabeta, R.; Mahajan, S.; Maeda, M.; Saito, H. *Chem. Pharm. Bull.* **1985**, *33*, 1793–1807.
(46) Armstrong, D. W.; Ward, T. J.; Armstrong, R. D.; Beesley, T. E. *Sci.* **1986**, *232*, 1132–1135.
(47) Jadhav, G. S.; Vavia, P. R. *Int. J. Pharm.* **2008**, *352*, 5–16.
(48) Szejtli, J. *Chem. Rev.* **1998**, *98*, 1743–1754.
(49) Avrami, M. *J. Chem. Phys.* **1939**, *7*, 1103–1112.
(50) Avrami, M. *J. Chem. Phys.* **1940**, *8*, 212–224.
(51) Avrami, M. *J. Chem. Phys.* **1941**, *9*, 177–184.
(52) Hancock, J. D.; Sharp, J. H. *J. Am. Ceram. Soc.* **1972**, *55*, 74–77.
(53) Li, Z. *Langmuir* **1999**, *15*, 6438–6445.
(54) Kodama, T.; Harada, Y.; Ueda, M.; Shimizu, K.; Shuto, K.; Komarneni, S. *Langmuir* **2001**, *17*, 4881–4886.
(55) Yang, J.-H.; Han, Y.-S.; Park, M.; Park, T.; Hwang, S.-J.; Choy, J.-H. *Chem. Mater.* **2007**, *19*, 2679–2685.
(56) Markland, C.; Williams, G. R.; O'Hare, D. *J. Mater. Chem.* **2011**, *21*, 17896–17903.
(57) Freundlich, H. *Zeitschrift fur Phys. Chemie* **1907**, *57*, 385–470.
(58) Kuo, S.; Lotse, E. G. *Soil Sci.* **1973**, *116*, 400–406.
(59) Crank, J., *The Mathematics of Diffusion*; Oxford science publications; Clarendon Press: 1979.

5. An investigation of enteric polymer–layered double hydroxide composites for drug delivery

5.1 Introduction

The ability of LDHs to act as stable solid hosts for intercalated guest ions has led to much interest in their use as additives in polymer composites, as this provides a facile route for manufacturing polymer materials containing functional compounds.[1–4] This principle has been applied to the development of materials with diverse functions, for example polymer composites which exhibit antimicrobial properties for medical and food packaging applications,[5–8] flame retardant polymer composites with superior smoke suppression abilities due to intercalated borate ions,[9,10] and biocompatible polymer composites for use in drug delivery.[8,11]

The partnering of LDHs and polymers for use in drug delivery is one of the most active areas of research regarding pharmaceutical applications of LDHs, as it allows the beneficial properties of LDHs to be augmented by those of polymers, which are themselves widely used and studied for pharmaceutical applications.[12–14] In particular, encapsulation within a polymer matrix may be used to confer on LDHs increased resilience to given conditions, such as acidic environments, whilst in return LDH particles act as a reservoir for drugs that may be difficult to encapsulate in polymers directly, due to chemical incompatibilities with their stability or solubility, or drug leaching issues.[15–18] Enteric polymers, designed to dissolve or release drugs at a specific point in the GI tract, have been coupled with drug intercalated LDHs with the aim of passing LDH particles through the stomach without dissolving, so that

drug release may occur in the lower half of the GI tract.[19–24] Composites have been designed with drug release profiles that cannot be achieved by either polymer or LDH materials independently.[25,26] For parenteral delivery of LDH particles, biopolymer coating may improve cell uptake.[27,28] New dosage forms have been reported utilising composites, such at the development of medicated scaffolds and suture threads with a poly(ε-caprolactone)–LDH composite containing tranexamic acid.[29] Additionally, composites containing calcium LDHs have been investigated for use as calcium supplements.[30]

The functionality of LDH–drug nanohybrids synthesised in Chapters 2 and 3 could be significantly enhanced through their inclusion in polymer composites. In Chapter 2, intercalation of gabapentin (GBP) and pregabalin (PGB) into an MgAl-NO_3 LDH substantially improved the aqueous stability of both drugs with respect to lactamisation. However, alongside stability issues, the major shortcoming of both drugs is their rapid excretion, and additionally for GBP, limited bioavailability, which necessitates frequent, large dosages of these drugs to maintain their therapeutic effects.[31,32] Additionally, as both drugs are unstable in acid environments, their oral bioavailability may be improved if they are protected during their passage through the stomach.[33]

The drug release profiles of the nanohybrids MgAl-$GBP_{anhyd,-20}$ and MgAl-$PGB_{anhyd,-20}$ reported in Section 2.4 show moderately fast release at all pH conditions tested, and are not suitable for controlled release in isolation, but encapsulation within polymer matrices may lead to practicable release profiles, provided this is not detrimental to the stability of the drugs. Additionally, a suitable enteric coating may prevent their release in strongly acidic environments. Improved bioavailability and controlled release formulations of both drugs have been reported, most commonly in the form of gastroretentive tablets. The inclusion of the LDH nanohybrids in polymer composites would hopefully produce a dosage form that is stable when suspended in water, and could be formulated as a suspension.[34–39]

Chapter 3 details the synthesis of nanohybrids containing catecholamine drugs, although in stability studies conducted with these nanohybrids, detailed in Section 3.6, it was found that rather than improving that stability of the drug ions, intercalation accelerated the oxidative decomposition of these species, as has been reported in other

interactions between inorganic clay materials and catecholamines.[40] This renders the nanohybrids unsuitable for drug delivery purposes in their unmodified form, but the ability of the nanohybrids to act as solid storage for the drug ions means they could form practicable delivery systems within polymer composites, provided polymer encapsulation prevents or slows the oxidative decomposition process. If the polymer acts as an effective barrier to decrease exposure of the intercalated drug ions to atmospheric oxygen and water, oxidative decomposition may be prevented. In addition, the drug release profiles of polymer composites should be more gradual, and hence practicable for controlled release dosage forms, than those of the nanohybrids reported in Section 3.5.

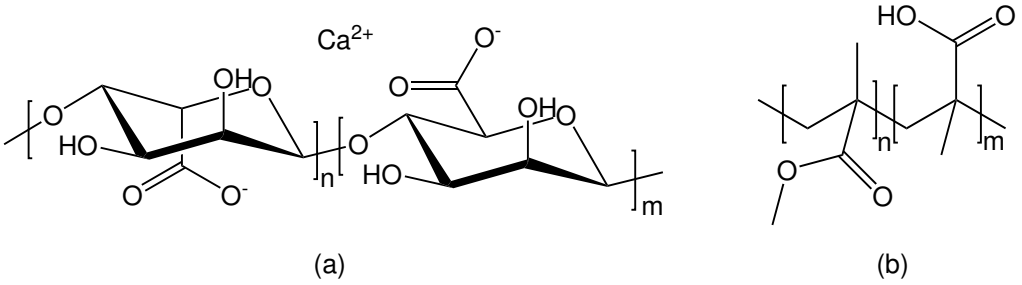


Figure 5.1: The structures of (a) calcium alginate and (b) poly(methyl methacrylate-co-methacrylic acid).

Two of the enteric polymers most commonly used in conjunction with LDHs are calcium linked alginate and poly(methyl methacrylate-co-methacrylic acid), specifically Eudragit®, their structures are given in Figure 5.1.[19–21] Despite enteric coatings having been used alongside LDH particles in several instances, direct comparisons of different enteric coatings when coupled with LDH particles have been limited. As the choice of coating may also impact on the stability of the drug ions in the composites, a comparison of different enteric coatings is also relevant to this investigation. Several formulations of Eudragit® are produced, with varying ratios of methyl methacrylate and methacrylic acid monomers and other substituents tailored to dissolve at different pH values. Of these, the two formulations most appropriate for the delivery of the drugs under investigation are L 100 and S 100, which dissolve at pH 6.0 and 7.0, have ratios of methyl methacrylate to methacrylic acid monomers of 1 : 1 and 2 : 1, and are aimed at inducing drug release in the small intestine and colon respectively.[41]

5.1.1 Scope of this Chapter

In this chapter, polymer–LDH composites are synthesised using four different LDH–drug nanohybrids that were described in Chapters 2 and 3, containing the drugs GBP, PGB and L-DOPA, and three different enteric polymers, Eudragit® L 100, S 100 and calcium alginate, referred to herein as Eud-L, Eud-S and Alg respectively. The drug content of the composites is ascertained, the drug release profiles from the composites are recorded and their release kinetics modelled. The composites containing GBP and PGB are assessed for any reduction in their ability to stabilise the intercalated drug ions, relative to the nanohybrids prior to encapsulation within polymer matrices. The effect of polymer encapsulation on the stability of L-DOPA ions within the relevant nanohybrids is investigated under a range of temperatures and exposure to ultraviolet radiation, in both wet and dry conditions. Based on these studies, the suitability of the different polymer composites for drug delivery is assessed.

5.2 Synthesis of polymer–nanohybrid composites

Two of the LDH–drug nanohybrids described in Chapter 2 were chosen as models, MgAl-$GBP_{anhyd,-20}$ and MgAl-$PGB_{anhyd,-20}$, as they had both the highest drug content and crystallinity, and had also exhibited excellent drug stabilising capabilities. For simplicity, they shall be referred to as MgAl-GBP and MgAl-PGB respectively for the remainder of this chapter. Each nanohybrid was encapsulated within composites with both Eud-L and Eud-S. Alg composites were not synthesised with these nanohybrids. For comparison, pristine GBP was also encapsulated in each of the two polymer matrices.

Two of the LDH–drug nanohybrids described in Chapter 3 were chosen as model nanohybrids, MgAl-$LDOPA_{IE}$ and $MgFeAl_c$-LDOPA. For simplicity, they shall be referred to as MgAl-LDOPA and MgFeAl-LDOPA respectively for the remainder of this chapter. The iron containing nanohybrid was investigated to determine whether the presence of Fe^{2+} ions would still accelerate the rate of drug decomposition when encapsulated within a polymer. Composites were synthesised with each nanohybrid

and all three polymers, Eud-L, Eud-S and Alg. For comparison, pristine L-DOPA was also encapsulated in each of the three polymer matrices. The composites are denoted ⟨polymer⟩{⟨nanohybrid or drug⟩}, *e.g.* Eud-L{MgAl-LDOPA}.

5.2.1 Eudragit®–nanohybrid composites

The synthesis method found to be most effective for creating Eud–nanohybrid composites was the solvent extraction–evaporation method used by Del Arco *et al.* to create microspheres.[21] The method was also adapted to synthesise the Eud–drug composites. Briefly, the nanohybrid or drug sample was suspended in a solution of the chosen Eud polymer dissolved in a dichloromethane–ethanol mixture. This suspension was then added dropwise to a solution of polyvinyl alcohol in water under vigorous stirring and heating at 40 °C. Once filtered and dried, the composites consisted of voluminous fluffy white powders, except for composites containing MgFeAl-LDOPA, which were pale purple.

5.2.2 Alginate–nanohybrid beads

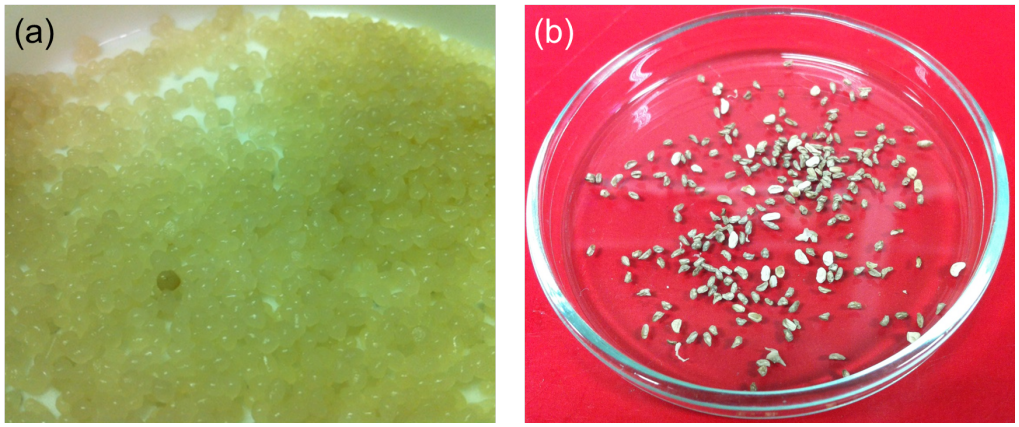


Figure 5.2: The Alg{MgAl-LDOPA} beads (a) before and (b) after drying.

Alg–nanohybrid and Alg–drug beads were synthesised following the method reported by Zhang *et al.* whereby the nanohybrid sample was suspended (the pristine drug was dissolved) in an aqueous solution of sodium alginate, which was subsequently added dropwise to an aqueous solution of calcium chloride.[42] This produced regular spheres of 3 mm diameter which were either opaque pale cream, opaque purple or translucent

white, depending on whether they contained MgAl-LDOPA, MgFeAl-LDOPA or pristine L-DOPA. The sphere diameter decreased to 1 mm upon drying under vacuum, as seen in Figure 5.2. If the turgid beads were exposed to atmospheric oxygen prior to drying, rapid discolouration occurred.

5.2.3 Powder X-ray diffraction

Powder XRD of both the Eud and Alg composites resulted in largely amorphous diffraction patterns, such as the examples depicted in Figure 5.3. In addition to the amorphous baseline caused by the polymer coatings, low intensity Bragg reflections can be seen in the XRD patterns of the polymer–nanohybrid composites, which correspond to the principle Bragg reflections in the XRD patterns of the nanohybrids (Figures 2.3 and 3.3). The (110) Bragg reflections of the nanohybrids are present in all nanohybrid composite XRD patterns. The (006) Bragg reflections can just be seen in the XRD patterns of the nanohybrid composites containing L-DOPA, whilst the (003) Bragg reflections can just be discerned in the XRD patterns of all nanohybrid composites, although it is partially obscured by the amorphous baseline.

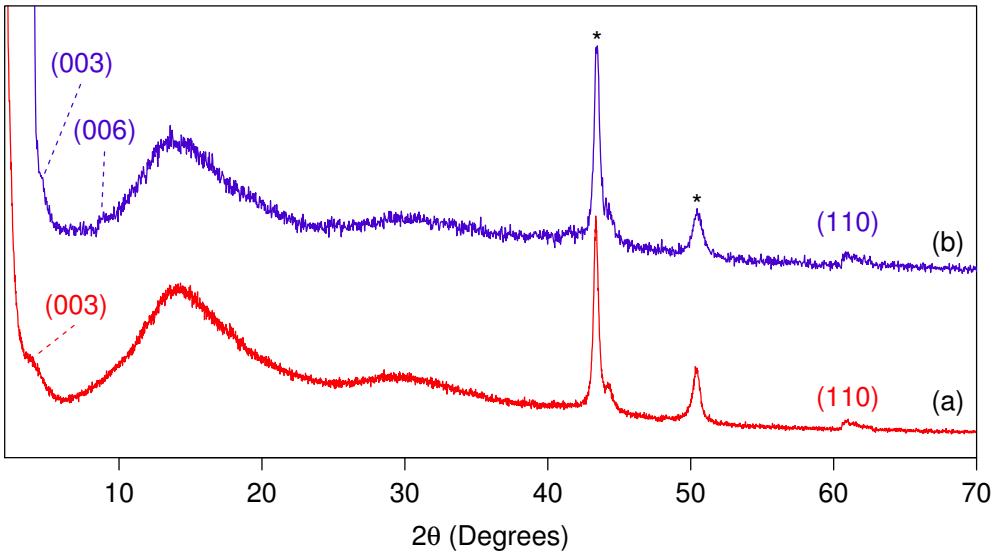


Figure 5.3: The powder XRD patterns of (a) Eud-L{MgAl-GBP} and (b) Eud-S{MgAl-LDOPA}. * denotes Bragg reflections corresponding to the stainless steel sample stage.[43]

Encapsulation of the nanohybrids reduces the effective concentration of the nanohybrid particles, relative to the uncoated nanohybrids, which explains the greatly

reduced intensity of the the Bragg reflections. Additionally, the encapsulation process, which involves suspension and dispersion of the nanohybrids with sonication, may lead to partial delamination or breakup of the nanohybrid particles. This would contribute to a further reduction in the intensities of the Bragg reflections, and may explain why other Bragg reflections of the nanohybrids are not observed in the XRD patterns of the composites. The XRD patterns of the polymer–drug composites do not present any Bragg reflections corresponding to the drug particles, and so their presence in the composites could not be established through this technique.

5.2.4 Fourier transform infrared spectroscopy

Examples of FTIR spectra of the Eud composites are presented in Figures 5.5 and 5.4, alongside spectra of the pristine Eud-L and Eud-S powders and the nanohybrids. All composites present the characteristic absorptions of poly(methyl methacrylate) and poly(methacrylic acid) also seen in the pristine Eud samples.[19] Absorptions at 1726 and 1706 cm^{-1} correspond to the C=O vibrations of the ester and carboxylic acid moieties, and show differing relative intensities in Eud-L in comparison to Eud-S samples. Additionally, absorptions at 1260, 1192 and 1155 cm^{-1} correspond to further vibrations of the ester groups. Small absorptions corresponding to the intercalated drugs are present in the spectra of the polymer–nanohybrid composites, with those containing GBP and PGB presenting an absorption at 1545 and 1549 cm^{-1} attributable to the NH_2 scissoring vibrations of the respective drug ions, and those containing L-DOPA presenting absorptions at 1551 cm^{-1}, which corresponds to the ionised asymmetric carboxylate stretch of the L-DOPA ions; other expected IR bands from the drug ions are obscured by those of the polymers. In contrast, no absorptions relating to the drugs were observed in the spectra of the Eud–drug composites, indicating that little of the drug species have been retained in the polymers. FTIR spectra of Eud composites not presented in Figures 5.5 and 5.4 are included in Appendix D.1.

The FTIR spectra of the Alg composites are presented in Figure 5.6, alongside spectra of sodium alginate (NaAlg) and the L-DOPA nanohybrids. Absorptions corresponding to alginate can be seen in the composites at 3400, 1595, 1416 and

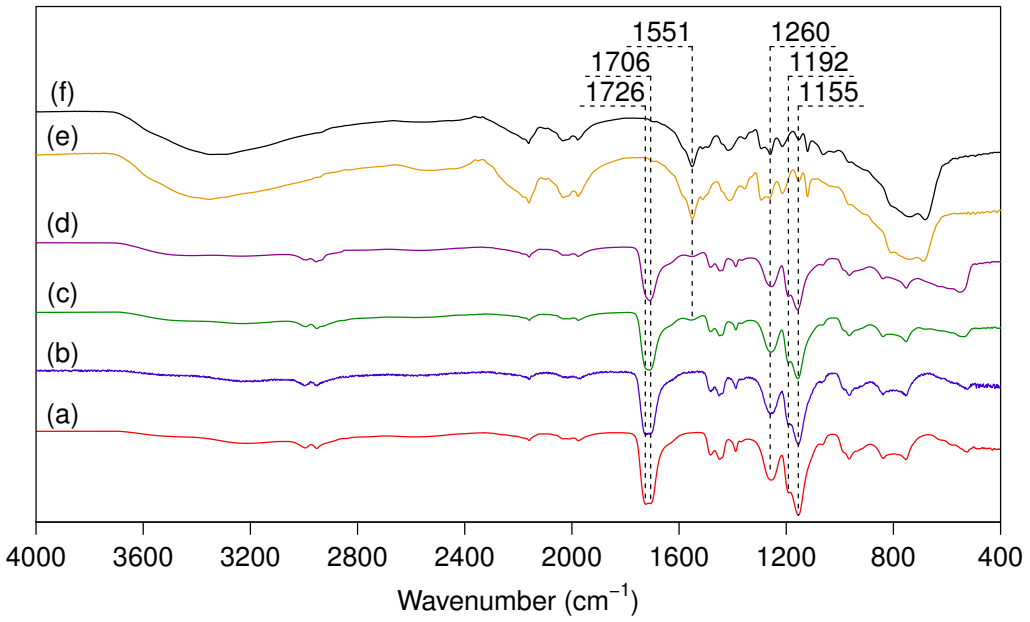


Figure 5.4: The FTIR spectra of (a) Eud-L, (b) Eud-L{L-DOPA}, (c) Eud-L{MgAl-LDOPA}, (d) Eud-L{MgFeAl-LDOPA}, (e) MgAl-LDOPA and (f) MgFeAl-LDOPA.

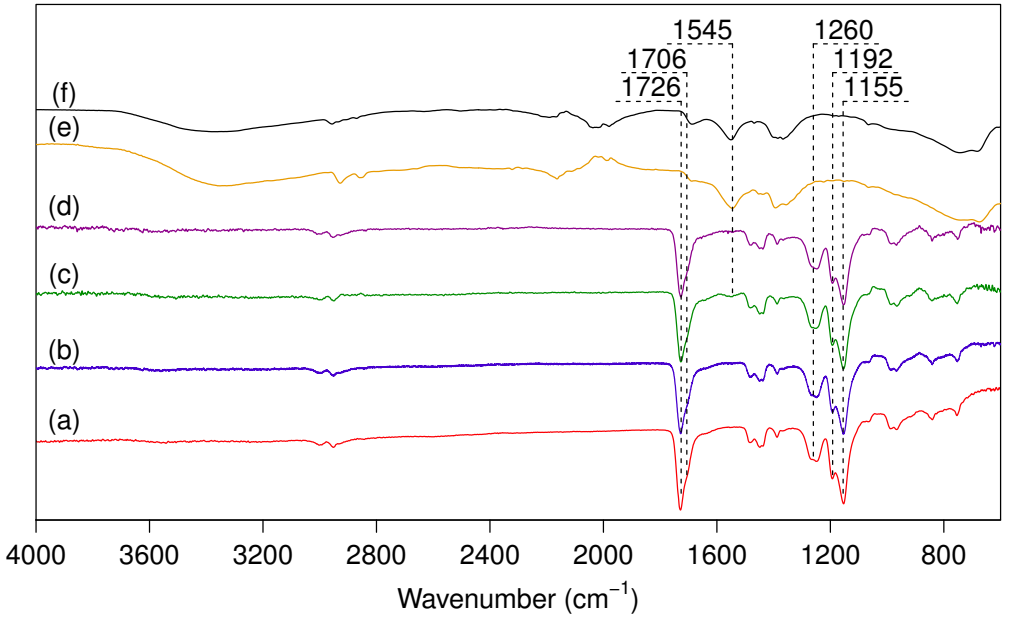


Figure 5.5: The FTIR spectra of (a) Eud-S, (b) Eud-S{GBP}, (c) Eud-S{MgAl-GBP}, (d) Eud-S{MgAl-PGB}, (e) MgAl-GBP and (f) MgAl-PGB.

1032 cm^{-1}, which are attributable to hydroxyl stretching modes, asymmetric and symmetric carboxylate stretching modes, and polysaccharide ether stretching modes respectively. There is a small shift in the carboxylate absorptions from those seen in NaAlg at 1607 and 1404 cm^{-1}, which is due to cross-linking from the Ca^{2+} ions. Absorptions relating to L-DOPA are not seen in the spectra of any of the composites, but this may be due to them being obscured by absorptions of the polymer, particularly the absorptions relating to the asymmetric and symmetric carboxylate stretches of the drug ions at 1551 and 1403 cm^{-1}.[20,44]

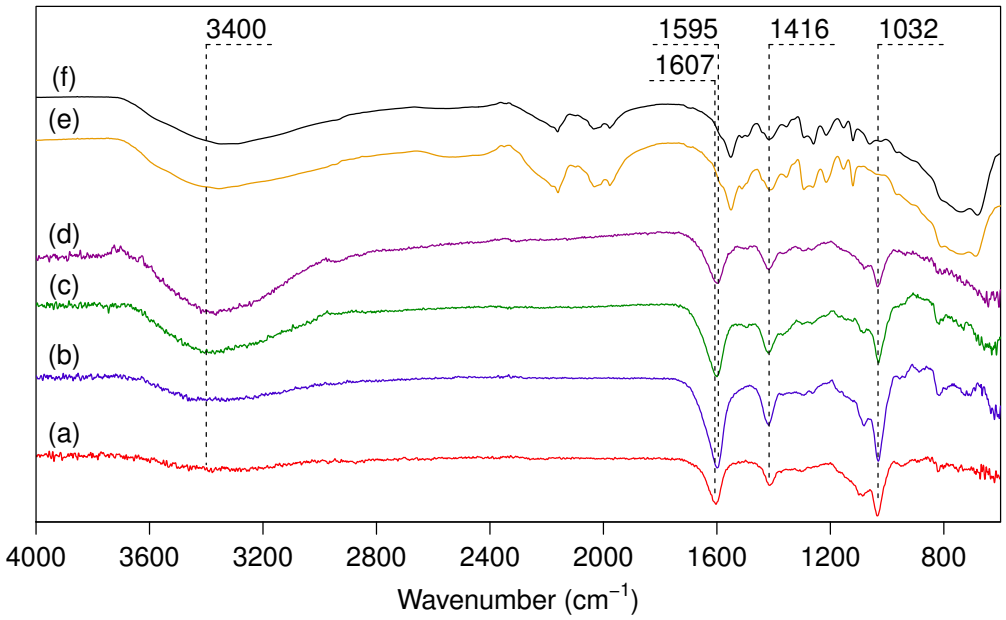


Figure 5.6: The FTIR spectra of (a) NaAlg, (b) Alg{L-DOPA}, (c) Alg{MgAl-LDOPA}, (d) Alg{MgFeAl-LDOPA}, (e) MgAl-LDOPA and (f) MgFeAl-LDOPA.

5.2.5 Drug content

Drug content was determined by suspending the composites in 1.0 M pH 7 phosphate buffer solution at 50 °C to induce total release of the drug ions. The suspensions were then filtered and analysed through either fluorescence or UV spectroscopy, depending on the drug. The experimentally determined drug content of the composites is displayed in Table 5.1, alongside the theoretical maximum drug content that would be expected based on total encapsulation of the nanohybrids and drug particles and no drug leaching during synthesis and the encapsulation efficiency (EE), which is

Table 5.1: The experimentally derived drug content of the polymer–nanohybrid and polymer–drug composites, alongside the theoretical maximum drug content, assuming total encapsulation and no leaching, and the encapsulation efficiency.

Sample	Drug content (W/W %)		Encapsulation
	Experimental	Theoretical	efficiency (%)
Eud-L{MgAl-GBP}	3.03	3.35	90.4
Eud-L{MgAl-PGB}	2.98	3.15	94.6
Eud-S{MgAl-GBP}	3.01	3.35	89.9
Eud-S{MgAl-PGB}	3.02	3.15	95.9
Alg{MgAl-LDOPA}	12.5	13.3	94.0
Alg{MgFeAl-LDOPA}	10.3	11.0	93.6
Eud-L{MgAl-LDOPA}	3.40	3.60	94.4
Eud-L{MgFeAl-LDOPA}	2.90	2.98	97.3
Eud-S{MgAl-LDOPA}	3.49	3.60	96.9
Eud-S{MgFeAl-LDOPA}	2.89	2.98	97.0
Eud-L{GBP}	0.45	9.09	4.95
Eud-S{GBP}	0.66	9.09	7.26
Alg{L-DOPA}	1.40	33.7	4.15
Eud-L{L-DOPA}	0.51	9.09	5.61
Eud-S{L-DOPA}	0.30	9.09	3.30

defined in Equation 5.1.[21]

$$\mathrm{EE}(\%) = \frac{\text{experimental drug content}}{\text{theoretical drug content}} \times 100 \qquad \textbf{Equation 5.1}$$

The benefit of LDHs being able to act as solid storage for soluble drug ions during processing of dosage forms is evident from examining the drug content of the composites synthesised with the pristine drugs. Despite higher theoretical maximum loading amounts, all the polymer–drug composites contain very little of their encapsulated drug species, with the Alg composite containing 1.4 % L-DOPA by weight, and all Eud composites containing < 1 % of their respective drug ions, which corresponds to EE figures of between 3 and 7 %.

In comparison, all polymer–nanohybrid composites exhibit good EE figures between of 90 and 97 %. In addition to drug leaching during the encapsulation processes, the slightly reduced experimental drug content observed may be due to dissolution of LDH particles not fully coated by the polymers during synthesis, when the samples

were washed with dilute acid. Any remaining adsorbed water in the samples after drying under vacuum also contributes to the discrepancy between the experimental and theoretical drug contents.

Due to the poor drug content of the polymer–drug composites, further microscopy, release and stability studies were not conducted on these samples. It should be noted, however, that the reason for the poor drug content of these samples lies in the synthesis method used for polymer encapsulation, which is designed for encapsulation of insoluble nanoparticles and not soluble drug crystals, and was adapted to maintain consistency between samples and allow close comparison. More appropriate methods of encapsulating soluble drug particles are commonly employed, such as electrospin and electrospray coating and lyophilisation.[45–47] Comparison of the polymer–nanohybrid composites with polymer–drug composites synthesised through these processed would be a useful continuation of this work.

5.2.6 Energy dispersive X-ray spectroscopy

EDX analysis was performed on all Eud composites to determine the presence and ratio of metals ion in the samples. The observed percentages of metal ions in the samples were low in comparison to those observed for the corresponding nanohybrids, which is expected as the presence of the polymer in the composites reduces the effective concentration of the metal ions by a factor of approximately ten. Additionally, as EDX is a surface technique, the polymer coating on the samples may reduce the signal from the metal ions further, although the coatings should be sufficiently thin to allow penetration of the electron beam to the encapsulated nanohybrid particles.

The low observed concentrations of the metal ions resulted in reduced accuracy in the calculation of their ratios. The values obtained are listed in Table 5.2, and despite the increased error, they show close agreement with the ratios found in the corresponding nanohybrids.

Table 5.2: The ratios of the metal ions observed in the nanohybrids and Eud composites, calculated from EDX analysis data.

Sample	Mg : Al ratio (or Mg : Fe : Al ratio where relevant)		
	Nanohybrid (±0.005)	Eud-L composite (±0.05)	Eud-S composite (±0.05)
MgAl-GBP	1.83	1.9	1.8
MgAl-PGB	1.80	1.8	1.8
MgAl-LDOPA	1.95	1.9	2.0
MgFeAl-LDOPA	1.18 : 0.79 : 1	1.2 : 0.8 : 1	1.2 : 0.8 : 1

5.2.7 Scanning electron microscopy

SEM images of the Eud composites, shown in Figures 5.7 and 5.8, help to confirm whether the polymer coatings have completely covered the nanohybrid particles and reveal the successful formation of 'microspheres'.[48] The composites all form similarly sized particles of around 4 to 6 µm in diameter with good size uniformity, although closer inspection of the particles reveals important differences in the morphology of the composites containing the GABAergic drugs and those containing L-DOPA that will become relevant when considering the results of the release studies in Section 5.3.

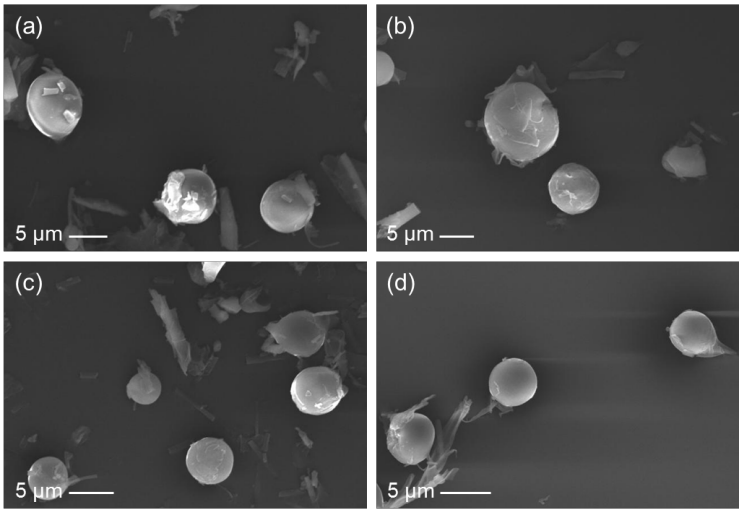


Figure 5.7: SEM images of the composites (a) Eud-L{MgAl-GBP}, (b) Eud-L{MgAl-PGB}, (c) Eud-S{MgAl-GBP}, and (d) Eud-S{MgAl-PGB}.

The composites containing MgAl-GBP and MgAl-PGB nanohybrids all form regular, microspheres with smooth surfaces, and very few instances of irregularly-shaped

particles (Figure 5.7). Comparing the size and shape of the microspheres to those of the nanohybrid particles (Figure 2.8), which resemble large, irregularly-shaped aggregates with typical diameters of 30 to 40 µm, it is evident that during the microencapsulation process the nanohybrid aggregates have been broken apart into smaller particles. It is postulated that this occurred during sonication of the suspended nanohybrid particles in organic Eud solution to ensure an even dispersion of the particles. The resulting smaller particles have clearly provided suitably sized fillers for the microspheres to form around, and from inspection of the surface of the microspheres there is no evidence that any of the nanohybrid particles are exposed.

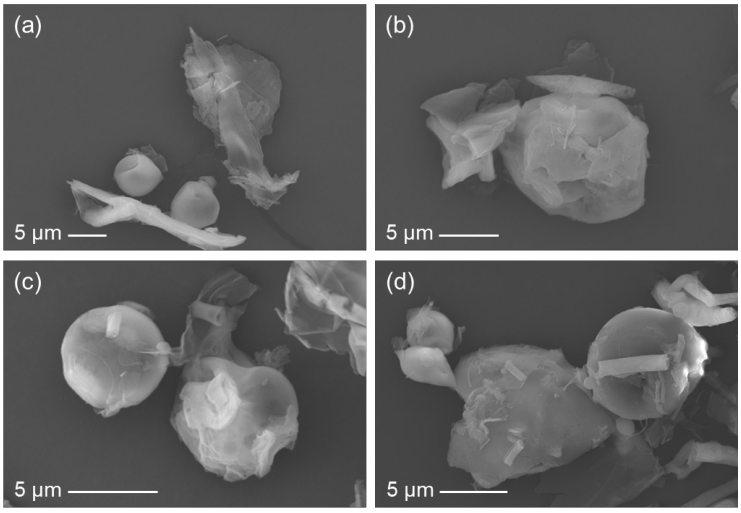


Figure 5.8: SEM images of the composites (a) Eud-L{MgAl-LDOPA}, (b) Eud-L{MgFeAl-LDOPA}, (c) Eud-S{MgAl-LDOPA}, and (d) Eud-S{MgFeAl-LDOPA}.

The Eud composite particles containing MgAl-LDOPA and MgFeAl-LDOPA nanohybrids are of a similar or marginally increased maximum diameter to the nanohybrid particles, pictured in Figures 3.12 and 3.21. They do not form either regular hexagonal platelets, or uniform microspheres, but a mix of particles including irregular shapes with rounded edges, in some cases approximating the hexagonal shapes of the encapsulated nanohybrid particles, and regular microspheres (Figure 5.8). What is notable, when comparing the composites containing L-DOPA to the composites containing GBP and PGB and those reported in the literature,[21,22] is the prevalence of both irregularly-shaped particles, and small irregularities on the surfaces of otherwise regularly-shaped microspheres in the samples of composites containing L-DOPA. This is presumably due to the larger size of the nanohybrid platelets and

their extreme aspect ratio, which discourages the formation of regular microspheres. Whilst the sonication process succeeded in disintegrating the aggregated particles of the MgAl-GBP and MgAl-PGB into smaller sizes more suitable for microencapsulation, the MgAl-LDOPA and MgFeAl-LDOPA nanohybrids consist of individual well-defined platelets, and consequently sonication is unlikely to cause their breakup into smaller particles. As microspheres were unable to form around the larger platelets, this may affect the rate of drug release, as the polymer coating around the nanohybrids may be thinner or disrupted in parts, especially near the edges of the nanohybrid platelets where drug release occurs.

5.3 Release studies

Release studies on the composites were conducted in biomimetic buffers at pH 2.0, 4.0 and 7.0. When suspended in the pH 2 buffer, no visible swelling of the particles took place in either the Eud or Alg samples. At pH 4.0 some visible swelling and partial disintegration occurred in the Alg particles, whilst both Eud samples remained intact, although gradual increases in the viscosity of the buffer containing Eud-L samples suggests some dissolution of these particles. At pH 7.0, swelling of the Alg particles occurred within minutes shortly followed by complete disintegration of the bead structures, whilst the viscosity of all buffers containing Eud samples increased rapidly as the polymers swelled and dissolved.

5.3.1 Release of GBP and PGB

The drug release profiles of the composites containing GBP and PGB are shown in Figure 5.9. When suspended in pH 2.0 buffers, after a small initial burst of drug release which amounted to 2 to 4 % of the total drug content across all samples, the release from the nanohybrids was minimal, with final percentages of drug release after 4 h standing between 3.5 to 7.5 %. Greater leaching occured from samples comprising Eud-L as the coating, and MgAl-GBP nanohybrids as the filler.

Release profiles of the composites in pH 4.0 buffer are largely similar to those observed at pH 2.0, albeit with a greater extent of subsequent drug leaching. Initial drug

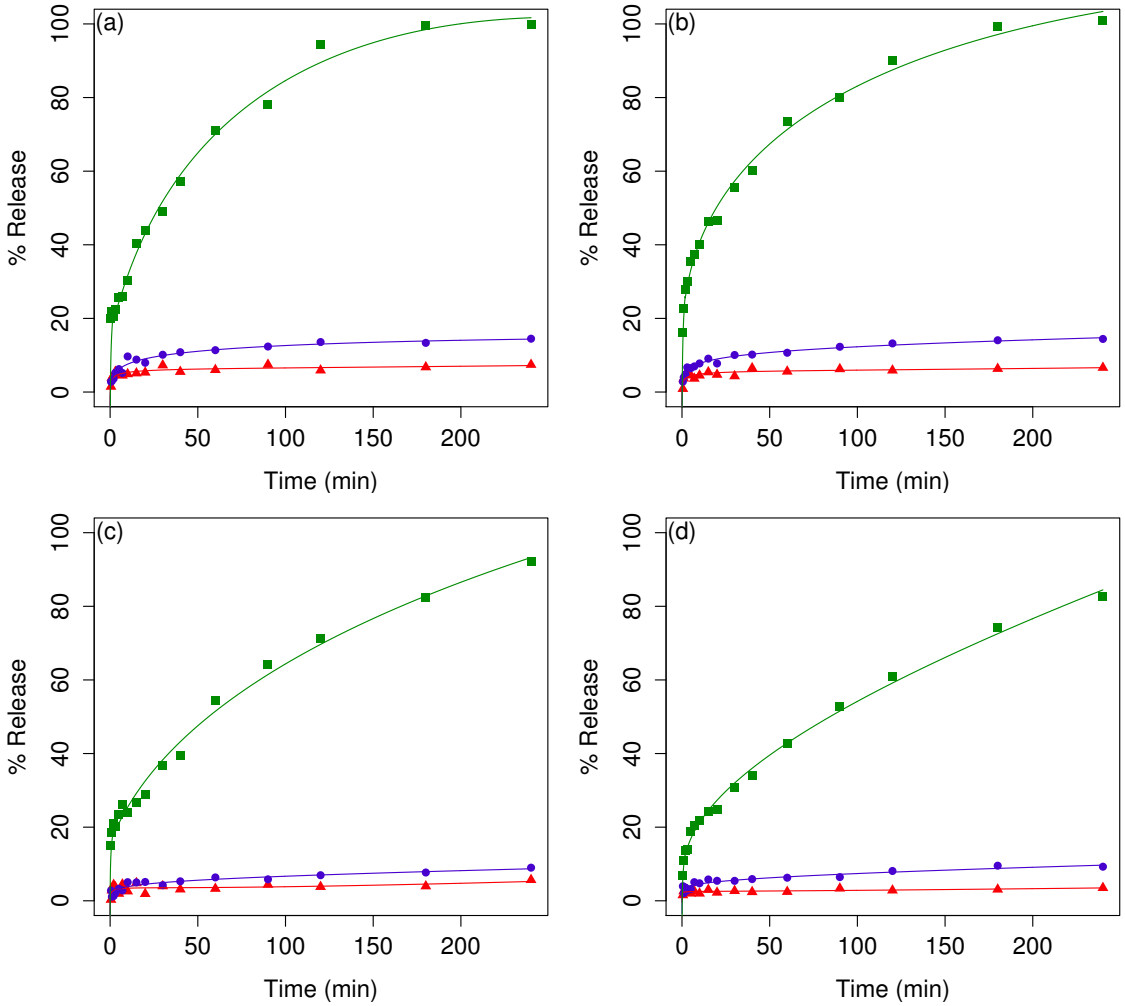


Figure 5.9: *In vitro* drug release profiles of (a) Eud-L{MgAl-GBP}, (b) Eud-L{MgAl-PGB}, (c) Eud-S{MgAl-GBP}, and (d) Eud-S{MgAl-PGB}, at 37 °C in pH 2.0 sulphate buffer, ▲, pH 4.0 phosphate buffer, ●, and pH 7.0 phosphate buffer, ■.

release percentages are again observed at 2 to 4 %, followed by leaching that is dependent on the polymer: both Eud-L samples exhibit 14 to 15 % drug release after 4 h, and Eud-S samples exhibit 8.5 to 9.5 % drug release after 4 h.

At pH 7.0, the drug release profiles of the composites show an initial burst release of 10 to 30 % of the total drug content, significantly higher than the initial bursts observed at the lower pH conditions, although much lower that the initial burst release typically seen in uncoated nanohybrids, which is generally between 70 to 95 %. Following the initial burst, drug release is gradual and constant, with Eud-L composites reaching near-complete drug release within 2 to 3 h whilst the Eud-S

composites reached 90 % release in 3.5 to 4 h. Whilst the shape of both Eud-L and Eud-S profiles during the gradual release stage (from around 10 min after initiation) resemble tapered curves, those of Eud-L show greater curvature, whereas the Eud-S profiles are much closer to linear relationship. The estimated t_{50} and t_{90} figures (time taken to reach 50 and 90 % drug release) for the four composites at pH 7 are detailed in Table 5.3.

Table 5.3: The time taken for the composites containing GBP and PGB to reach t_{50}, 50 % drug release, and t_{90}, 90 % drug release in pH 7 phosphate buffer.

Sample	t_{50} (min)	t_{90} (min)
Eud-L{MgAl-GBP}	27.7	122
Eud-L{MgAl-PGB}	19.5	133
Eud-S{MgAl-GBP}	56.1	220
Eud-S{MgAl-PGB}	84.3	270

5.3.2 Release of L-DOPA

The release profiles of the L-DOPA containing composites are presented in Figure 5.10. Most remarkably, near complete release occurs in all composites and in all pH conditions, despite consisting of polymers used for enteric coatings, which are designed to prevent release at low pH conditions. Additionally, release occurs most rapidly at lower pH conditions. This is in stark contrast to the release profiles of the composites containing GBP and PGB, which exhibited typical release profiles for enteric polymer composites.[21] The L-DOPA release profiles show a strong pH dependence, with all composites exhibiting the slowest rate of release in the pH 7 buffer solution. The pH dependence of the release profiles is more marked in the Eud than in the Alg composites, with all composites exhibiting more rapid release at pH 2, and yet slower release at pH 7. The average difference in t_{90} between release at pH 2 and pH 7 highlights the differing pH dependence of the composites: for the Alg composites this difference is 54 min, whereas this difference is 106 and 136 min for composites of Eud-L and Eud-S respectively. These values are listed in Table 5.4.

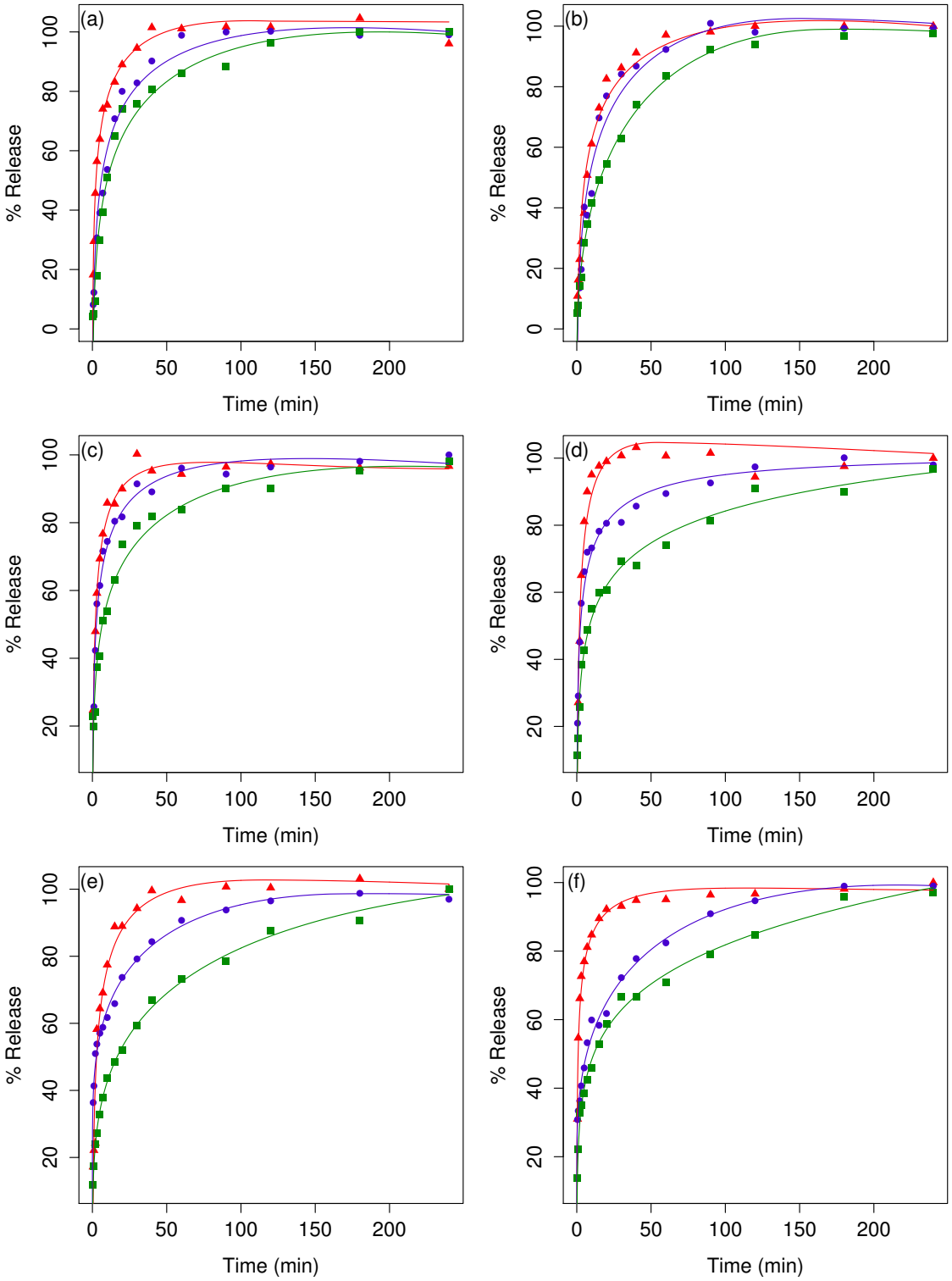


Figure 5.10: *In vitro* drug release profiles of (a) Alg{MgAl-LDOPA}, (b) Alg{MgFeAl-LDOPA}, (c) Eud-L{MgAl-LDOPA}, (d) Eud-L{MgFeAl-LDOPA}, (e) Eud-S{MgAl-LDOPA} and (f) Eud-S{MgFeAl-LDOPA}, at 37 °C in pH 2.0 sulphate buffer, ▲, pH 4.0 phosphate buffer, ●, and pH 7.0 phosphate buffer, ■.

Table 5.4: The time taken for the composites containing L-DOPA to reach t_{90}, 90 % drug release in buffers at pH 2, 4 and 7, and the difference between t_{90} at pH 7.0 and at t_{90} at pH 2.0, Δt_{90}.

Sample	t_{90} (min)			Δt_{90} (min)
	pH 2.0	pH 4.0	pH 7.0	pH 7.0 − pH 2.0
Alg{MgAl-LDOPA}	21.8	45.9	72.6	50.8
Alg{MgFeAl-LDOPA}	43.2	52.8	101	57.8
Eud-L{MgAl-LDOPA}	20.5	34.5	87.0	66.5
Eud-L{MgFeAl-LDOPA}	10.6	48.8	157	146
Eud-S{MgAl-LDOPA}	23.3	72.6	154	131
Eud-S{MgFeAl-LDOPA}	17.3	99.8	158	141

5.3.3 Release kinetics

The release profiles were fitted to the five kinetic release models that have been used throughout this thesis, detailed in Section 2.4.1, and the goodness of fit evaluated using a least squares regression. Values of the correlation constants of the fit to the five models are included in Appendix D.2. Considering the composites as three different systems, namely, Eud composites containing GBP or PGB, Alg composites, and Eud composites containing L-DOPA, the release profiles of each system fit most closely to three different models.

Release from the Eud composites containing GBP and PGB is very clearly modelled most closely by the parabolic diffusion model, which consistently shows high correlation to the data, although the Avrami–Erofe'ev and Elovich models do show a close fit in some instances, notably most closely for release in pH 4 and pH 7 buffers. This model is primarily designed to model 1D radial diffusion.[49,50] In the context of release from LDHs, which is two dimensional, and Eud matrices generally, which is three dimensional, the parameters given by the parabolic diffusion model do not have a physical significance, but the agreement of the data with this model indicates that release is may be occurring in one dimension via cylindrical channels. Similarly, the Elovich model does not provide any physically useful parameters, but the Avrami–Erofe'ev model can be used to extract both the reaction exponent, n, and the rate constant, k, for release in buffers at pH 4 and pH 7, as displayed in Table D.2. In all cases, $n < 0.5$, which indicates that the release mechanism is

a diffusion controlled process, rather than controlled by nucleation sites and and subsequent growth. It can also be seen that the rate constants for release in pH 7 buffer are over an order of magnitude greater then for release in pH 4 buffer, which quantifies the difference seen in the release profiles. The reaction constants, even at pH 7, are also substantially smaller than those reported for release form the uncomplexed nanohybrids, detailed in Table 2.4.

Release data from the Alg composites show good fitting to several models, including the Avrami–Erofe'ev and modified Freundlich, although it is the Elovich model that matches most closely in the majority of cases, which has been applied to sorption processes in many contexts.[51] While the Elovich model does not provide physically interpretable parameters, both the Avrami–Erofe'ev and modified Freundlich models do, and the figures calculated from the models for the reaction exponent, n, and the rate constants given by each model, k_{AE} and k_F, are detailed in Table D.3.

The release from Eud composites containing L-DOPA is also well matched to several models, although in this case it is the modified Freundlich that provides the closest fit in most cases ad most consistently. This model was developed to describe solution phase adsorption processes, and subsequently adapted by Kuo and Lotse to model desorption rates from clay materials.[52,53] It is also notable from the fitting data that the Avrami–Erofe'ev model, which most closely fits the release profiles of the nanohybrids being encapsulated in this chapter, is not the most suitable match for the release data of the composites, although as noted it is still a close match in most cases, and so can still be used for extracting mechanistic and kinetic parameters, also detailed in Table D.3.

For the release of L-DOPA from all the composites, $n < 0.5$, indicating the release mechanisms with both polymers are diffusion controlled. There is, however, a distinct difference seen in the rate constants predicted by the different models, depending on the polymer used. For release from the alginate composites, the Freundlich model calculates a much higher rate constant, k_F, than that calculated by the Avrami–Erofe'ev model, k_{AE}, whereas for the Eudragit complexes, the reverse is true, indicating the differences between the two models.

5.3.4 Discussion

The difference between the release profiles of the composites containing GBP and GBP and those containing L-DOPA is dramatic, and points to substantive differences in the formation of the different composites. Considering only the composites made with Eud polymers, all composites were synthesised in the same manner and no difference was observed during their characterisation, other than the differing particle morphologies discussed in Section 5.2.7. The shape of the nanohybrid platelets has clearly influenced the formation of the microspheres during synthesis of the composites, which in turn has a marked impact on the drug release profiles and the ability of the enteric polymers to protect the nanohybrid particles in acidic environments.

The size and extreme aspect ratio of the nanohybrid particles containing L-DOPA has evidently disrupted the formation of microspheres around them, leading to vulnerable surface areas where the buffer solutions may come into contact with the nanohybrids, allowing dissolution or diffusion to occur. The effect of such vulnerable areas is much more significant in acid solutions, as dissolution of the nanohybrids will proliferate much more readily from small weaknesses than diffusion, which is restricted by the accessibility of the edges of the nanohybrid platelets.

The formation of alginate composites seems to also have been disrupted by the shape of the L-DOPA nanohybrids, as protection of the particles in acid conditions has also been ineffective in these samples. The relative similarity in the release rates for the Alg composites at different pH values, when compared to the analogous Eud composites, along with their more delayed initial release suggests instead a release pattern whereby there is an initial phase during which the buffer rehydrates the composite beads, after which the nanohybrid particles are exposed to the buffer and release occurs relatively rapidly. This explains why there is less of a pH dependence observed for these composites.

No systematic differences were observed in the release profiles from composites containing MgAl-LDOPA and those containing MgFeAl-LDOPA, or between those containing MgAl-GBP and those containing MgAl-PGB. Any differences may be attributed to experimental variation rather than a concerted trend. The difference

between the two Eud formulations in the release rates of composites was apparent, with release from Eud-S composites consistently slower than from Eud-L composites, and Eud-S preventing leaching more effectively in acidic conditions in samples containing GBP and PGB.

The results from the release studies serve to illustrate the importance of different nanohybrid morphologies and sizes when being used to make composite materials. The samples containing the GABAergic drugs all exhibited sustained release profiles in neutral solutions, and demonstrated the protective ability of enteric polymer encapsulation in acidic conditions. A central aim of encapsulating these nanohybrids was to improve their capacity for sustained release, and it has been demonstrated that this is possible with either of the Eud polymers. Sustained release of these composites takes place over a number of hours in both cases, which is a desirable timescale for such dosage forms.

Release from the composites containing L-DOPA, whilst presenting slowed release rates in all cases relative to the uncoated nanohybrid particles, was less promising. The size and shape of the nanohybrid particles seems to have hindered the formation of an effective barrier of enteric polymer between the nanohybrid particles and the release solutions, and rapid release of the majority of the encapsulated drug ions is seen across all pH ranges tested, although release in neutral conditions does does some degree of sustained release. The failure of either polymer to effectively provide protection in acidic conditions has prevented comparisons of the relative efficacy of either polymer in this case. This work does highlight the need for a greater understanding of the relationship between nanohybrid particle size and morphology, and suitability for polymer encapsulation. Further work investigating this relationship would be useful in the development of effective composite dosage forms involving LDH nanohybrids.

5.4 Stability studies

5.4.1 GBP and PGB stability

The stabilising effect of intercalation within LDH layers on GBP and PGB with respect to lactamisation has been observed in Section 2.5. To establish whether a detailed investigation into the drug stabilising effects of the composites containing GBP and PGB was necessary, or whether the same stabilising effect seen in the nanohybrid was also conferred on the composites, an initial study was conducted, whereby each composite was suspended in dilute HCl (0.01 m M, pH 5.0) in sealed containers for a two week period, at both room temperature and 80 °C. Acid was used instead of pure water to prevent dissolution of the polymers. After two weeks, the samples were analysed for any reduction in the concentration of GBP and PGB contents that would indicate lactamisation. None of the four samples showed any change in the concentration of drug contents at either temperature, indicating that lactamisation had not occurred to any measurable extent within the time period. This indicates an improved stabilising ability of the composites in comparison to the nanohybrids, as both nanohybrids had exhibited measurable drug decomposition over a two week period at 80 °C, although not at room temperature. Consequently no further stability studies were pursued with these composites.

5.4.2 L-DOPA stability

Decomposition studies were performed on the L-DOPA containing composites in both dry and wet conditions, at 20 and 80 °C, and under exposure to ultraviolet radiation ($\lambda = 254\,\text{nm}$). With the exception of additional filtering needed to prepare the composite samples for analysis and the use of dilute HCl (0.01 m M, pH 5.0) instead of water for the wet conditions, experiments were analogous to those performed on the nanohybrids in Section 3.6; analyses were not conducted at 40 °C as the analogous experiments conducted in Chapter 3 had provided no substantial insight.

Preliminary investigations into the potential racemisation of drug ions in the uncoated nanohybrids over time had confirmed that no discernible racemisation of the drug

ions occurred under any of the conditions tested. Consequently, rather than analyse every sample for evidence of racemisation, selected aliquots were analysed at two week intervals. As had been found for the uncoated nanohybrid samples, no discernible racemisation to L-DOPA had occurred in any samples. Dissolution experiments coupled with ^{1}H NMR spectroscopy analysis were not feasible with the composites, as the presence of the polymers prevented clean spectra from being obtained.

The varying concentrations of L-DOPA and the aggregated decomposition products in the composites were tracked over time using UV spectroscopy. As the release experiments detailed in Section 5.3 had revealed that complete deintercalation of the drug ions could be effected rapidly using acid media, samples in both wet and dry conditions were prepared for analysis by addition to solutions of HCl, which also quenched the decomposition process, followed by filtering and adjusting to a standard concentration for UV spectroscopy.

Table 5.5: The observed rate constants, k_{obs}, for oxidative decomposition of L-DOPA in polymer–nanohybrid composites under a range of dry and wet conditions, calculated from UV spectroscopy. The observed rate constants for the pristine drug are also included for reference. *Decomposition over the course of a six week period was too slow to calculate the cyclisation constant accurately, within experimental error.

Sample	Decomposition rate constant, $k_{obs}\times10^{10}$ (s^{-1})					
	Dry conditions			*Wet conditions*		
	20 °C	80 °C	20 °C; $h\nu$	20 °C	80 °C	20 °C; $h\nu$
Alg{MgAl-LDOPA}	323	1020	308	8000	44900	18600
Alg{MgFeAl-LDOPA}	544	2760	484	13500	51100	27900
Eud-L{MgAl-LDOPA}	< 1*	< 1*	< 1*	7.92	77.7	9.97
Eud-L{MgFeAl-LDOPA}	< 1*	< 1*	< 1*	6.66	81.4	7.25
Eud-S{MgAl-LDOPA}	< 1*	< 1*	< 1*	6.68	54.3	9.38
Eud-S{MgFeAl-LDOPA}	< 1*	< 1*	< 1*	5.37	62.7	7.99
Pristine L-DOPA	2.41	12.6	3.63	35.0	139	81.9

The polymer composites had very different influences on decomposition of the drug ions, as can be seen from the observed rate constants, k_{obs}, detailed in Table 5.5. Decomposition was again found to follow a pseudo first order reaction rate, and the observed rate constants were calculated from linear models of the natural logarithm of L-DOPA concentration (ln[L-DOPA]) as a function of time, t. These plots can

be found in Appendix D.4 alongside plots detailing the change in concentrations of L-DOPA and aggregated decomposition products over time.

Both the Alg composites displayed rates of oxidative decomposition across all wet conditions that were largely similar to those seen in their respective uncoated nanohybrids, indicating that encapsulation of the particles in calcium alginate matrices had little effect on reducing the rate of drug decomposition when wet. This suggests that solvated oxygen molecules were able to permeate through the alginate polymer matrices freely in wet conditions to gain access to the nanohybrids, whereby the basic local environment created by the metal hydroxide layers led to accelerated drug decomposition. In dry conditions, the alginate composites appear to offer some protections to the drug ions, as the rate of drug decomposition observed in these samples is slower that than observed in analogous conditions with the uncoated nanohybrids by around a factor of two to three. However, when compared to pristine L-DOPA in dry conditions, drug decomposition in the Alg composites is still much more rapid.

The Eud composites exhibit substantially slower rates of drug decomposition that indicate Eud encapsulation has a major stabilising effect on the drug ions within the nanohybrids across all wet and dry conditions, despite the observed failure of the samples to form regular microspheres. Reduction in the concentration of L-DOPA in the composites over time is minimal in wet conditions, even at elevated temperatures and when exposed to ultraviolet radiation. The rates of oxidative decomposition are lower than those of pristine L-DOPA, and are in fact sufficiently low in dry conditions that accurate measurement of any decomposition over a period of six weeks was not possible within experimental error. Although measurable, decomposition in wet conditions was suppressed significantly and required an extension of the decomposition study time to four weeks to calculate a figure. Samples containing Fe^{2+} ions showed marginally faster rates of decomposition. No noticeable systematic difference in drug stability was observed between composites containing Eud-L and Eud-S.

The success of Eudragit® encapsulation at slowing the oxidative decomposition of L-DOPA in the nanohybrids indicates that the Eudragit® layers are impermeable to oxygen, although in wet conditions small amounts of oxygen can presumably gain

access to the nanohybrids gradually, explaining the small amounts of decomposition found after multiple weeks of exposure to water. This may be improved upon by using smaller nanohybrid particles that could be encapsulated more effectively. There may also be an effect from the methacrylic acid groups of the polymer reducing the pH of the environment surrounding the drug ions, counteracting the effect of the LDH layers and reducing the possibility of base catalysis of the decomposition reaction.

Encapsulation of the nanohybrids within Eudragit® polymers stabilises the drug ions considerably, the only combination of factors to have successfully done so. As the addition of Fe^{2+} ions to the LDH layers had a negative effect on drug stability, the most effective two composites at stabilising L-DOPA were Eud-L{MgAl-LDOPA} and Eud-S{MgAl-LDOPA}. The stability of these composites in aqueous suspension is encouraging, as it suggests that composites consisting of Eudragit® and magnesium–aluminium LDHs could be used to deliver L-DOPA and other catecholamine drugs in stable liquid suspensions in a range of controlled release formulations not previously possible with these drugs.

5.5 Conclusion

Polymer–nanohybrid composites were synthesised with the aim of improving both the stability of the intercalated drugs and the release profiles of the encapsulated nanohybrids. Two nanohybrids containing GBP and PGB were encapsulated in Eudragit® L 100, S 100, resulting in regular microspheres with drug contents of 3 %. These microspheres exhibited resistance to drug release in acid media and consistent sustained drug release profiles in neutral media, which fitted closely to the parabolic diffusion model. Total drug release in neutral conditions was reached in 3 to 5 h and was dependent on the polymer coating used. The stability of the drugs in the nanohybrids was not compromised by encapsulation, and was improved at elevated temperatures.

The two ion-exchange synthesised nanohybrids containing L-DOPA were encapsulated in three different organic polymer matrices, Eudragit® L 100, S 100 and calcium

alginate, to create composites with drug contents of 3 to 4 % (Eudragit) and 10 to 13 % (alginate). The composites synthesised with Eudragit® formed irregularly shaped particles, dues to the size and shape of the nanohybrid platelets. The release profiles of the composites were recorded, and revealed that the polymer coatings did not prevent dissolution of the nanohybrid particles in acid conditions, although in neutral conditions the rate of drug release was significantly reduced, with the alginate composites reaching complete drug release within 2 h, and Eudragit composites reaching complete release within 3 to 4 h. Decomposition studies revealed that encapsulation in calcium alginate did not prevent oxidative decomposition, but encapsulation in either of the Eudragit® polymers had a substantial stabilising effect on the drug ions. This indicates that stable suspensions of Eudragit®–nanohybrid composites containing unstable drugs can be created, which could be developed into a diverse range of controlled release formulations.

5.6 References

(1) Fischer, H. *Mater. Sci. Eng. C* **2003**, *23*, 763–772.
(2) Evans, D. G.; Duan, X. *Chem. Commun.* **2006**, 485–496.
(3) Costa, F. R.; Saphiannikova, M.; Wagenknecht, U.; Heinrich, G. In *Wax Cryst. Control. Nanocomposites· Stimuli-Responsive Polym.* Springer: 2008, pp 101–168.
(4) Basu, D.; Das, A.; Stöckelhuber, K. W.; Wagenknecht, U.; Heinrich, G. *Prog. Polym. Sci.* **2014**, *39*, 594–626.
(5) Sorrentino, A.; Gorrasi, G.; Vittoria, V. *Trends Food Sci. Technol.* **2007**, *18*, 84–95.
(6) Costantino, U.; Bugatti, V.; Gorrasi, G.; Montanari, F.; Nocchetti, M.; Tammaro, L.; Vittoria, V. *ACS Appl. Mater. Interfaces* **2009**, *1*, 668–677.
(7) Bugatti, V.; Gorrasi, G.; Montanari, F.; Nocchetti, M.; Tammaro, L.; Vittoria, V. *Appl. Clay Sci.* **2011**, *52*, 34–40.
(8) Costantino, U.; Nocchetti, M.; Tammaro, L.; Vittoria, V. *Recent Pat. Nanotechnol.* **2012**, *6*, 218–230.
(9) Wang, Q.; Undrell, J. P.; Gao, Y.; Cai, G.; Buffet, J.-C.; Wilkie, C. A.; O'Hare, D. *Macromolecules* **2013**, *46*, 6145–6150.
(10) Gao, Y.; Wu, J.; Wang, Q.; Wilkie, C. A.; O'Hare, D. *J. Mater. Chem. A* **2014**, *2*, 10996–11016.
(11) Ha, J. U.; Xanthos, M. In *ANTEC 2010, Conf. Proc.* Society of Plastics Engineers: 2010, pp 1193–1197.
(12) Schmaljohann, D. *Adv. Drug Deliv. Rev.* **2006**, *58*, 1655–1670.
(13) Mora-Huertas, C. E.; Fessi, H.; Elaissari, A. *Int. J. Pharm.* **2010**, *385*, 113–142.
(14) Arafat, M. *Int. J. Pharm. Pharm. Sci.* **2015**, *7*, 16–21.
(15) Pucciariello, R.; Tammaro, L.; Villani, V.; Vittoria, V. *J. Polym. Sci. Part B Polym. Phys.* **2007**, *45*, 945–954.
(16) Tammaro, L.; Russo, G.; Vittoria, V. *J. Nanomater.* **2009**, 1–8.
(17) Choi, G.; Lee, J.-H.; Oh, Y.-J.; Choy, Y. B.; Park, M. C.; Chang, H. C.; Choy, J.-H. *Int. J. Pharm.* **2010**, *402*, 117–122.
(18) Barkhordari, S.; Yadollahi, M.; Namazi, H. *J. Polym. Res.* **2014**, *21*, 1–9.
(19) Li, B.; He, J.; Evans, D. G.; Duan, X. *Int. J. Pharm.* **2004**, *287*, 89–95.
(20) Alcântara, A. C. S.; Aranda, P.; Darder, M.; Ruiz-Hitzky, E.; Alcantara, A. C. S.; Aranda, P.; Darder, M.; Ruiz-Hitzky, E. *J. Mater. Chem.* **2010**, *20*, 9495–9504.
(21) Del Arco, M.; Fernandez, A.; Martin, C.; Rives, V. *J. Solid State Chem.* **2010**, *183*, 3002–3009.
(22) Pan, D.; Zhang, H.; Zhang, T.; Duan, X. *Chem. Eng. Sci.* **2010**, *65*, 3762–3771.
(23) Mahkam, M.; Davatgar, M.; Rezvani, Z.; Nejati, K. *Int. J. Polym. Mater. Polym. Biomater.* **2013**, *62*, 57–60.
(24) Rezvani, Z.; Shahbaei, M. *Polym. Compos.* **2014**, *36*, 1819–1825.
(25) Xu, Z. P.; Gu, Z.; Cheng, X.; Rasoul, F.; Whittaker, A. K.; Lu, G. Q. M. *J. Nanoparticle Res.* **2011**, *13*, 1253–1264.
(26) Kim, M. H.; Park, D.-H.; Yang, J.-H.; Choy, Y. B.; Choy, J.-H. *Int. J. Pharm.* **2013**, *444*, 120–127.
(27) Depan, D.; Singh, R. P. *J. Appl. Polym. Sci.* **2010**, *115*, 3636–3644.
(28) Yan, M.; Zhang, Z.; Cui, S.; Lei, M.; Zeng, K.; Liao, Y.; Chu, W.; Deng, Y.; Zhao, C. *Int. J. Nanomedicine* **2014**, *9*, 4867–4878.
(29) Tammaro, L.; Costantino, U.; Nocchetti, M.; Vittoria, V. *Appl. Clay Sci.* **2009**, *43*, 350–356.
(30) Kim, T.-H.; Lee, J.-A.; Choi, S.-J.; Oh, J.-M. *Int. J. Mol. Sci.* **2014**, *15*, 22563–22579.
(31) McLean, M. J. *Neurology* **1994**, *44*, 17–22.
(32) Randinitis, E. J.; Posvar, E. L.; Alvey, C. W.; Sedman, A. J.; Cook, J. A.; Bockbrader, H. N. *J. Clin. Pharmacol.* **2003**, *43*, 277–283.
(33) Zambon, E.; Giovanetti, R.; Cotarca, L.; Pasquato, L. *Tetrahedron* **2008**, *64*, 6739–6743.

(34) Chawla, M.; Raghuvanshi, R. S.; Rampal, A. Stable sustained-release oral dosage forms of gabapentin and process for their preparation. WO 2005077332 A2., 2005.
(35) Gordi, T.; Hou, E.; Kasichayanula, S.; Berner, B. *Clin. Ther.* **2008**, *30*, 909–916.
(36) Chen, C.; Han, C.-H.; Sweeney, M.; Cowles, V. E. *J. Pharm. Sci.* **2013**, *102*, 1155–1164.
(37) Wilson, B.; Lavanya, Y.; Priyadarshini, S. R. B.; Ramasamy, M.; Jenita, J. L. *Int. J. Pharm.* **2014**, *473*, 73–79.
(38) Sharma, V.; Sharma, S.; Khokra, S. L.; Sahu, R. K.; Jangde, R.; Singh, J. *Der Pharm. Lett.* **2011**, *3*, 326–333.
(39) Aydogan, E.; Comoglu, T.; Pehlivanoglu, B.; Dogan, M.; Comoglu, S.; Dogan, A.; Basci, N. *Drug Dev. Ind. Pharm.* **2014**, 1–10.
(40) Jaber, M.; Bouchoucha, M.; Delmotte, L.; Méthivier, C.; Lambert, J.-F. *J. Phys. Chem. C* **2011**, *115*, 19216–19225.
(41) Thakral, S.; Thakral, N. K.; Majumdar, D. K. *Expert Opin. Drug Deliv.* **2013**, *10*, 131–149.
(42) Zhang, J.-P.; Wang, Q.; Xie, X.-L.; Li, X.; Wang, A.-Q. *J. Biomed. Mater. Res. Part B Appl. Biomater.* **2010**, *92*, 205–214.
(43) Lee, S. Y.; Huang, E.-W.; Woo, W.; Yoon, C.; Chae, H.; Yoon, S.-G. *Metals (Basel).* **2015**, *5*, 2109–2118.
(44) Pongjanyakul, T.; Puttipipatkhachorn, S. *Int. J. Pharm.* **2007**, *331*, 61–71.
(45) Yu, D.-G.; Williams, G. R.; Wang, X.; Liu, X.-K.; Li, H.-L.; Bligh, S. W. A. *RSC Adv.* **2013**, *3*, 4652–4658.
(46) Illangakoon, U. E.; Yu, D.-G.; Ahmad, B. S.; Chatterton, N. P.; Williams, G. R. *Int. J. Pharm.* **2015**, *495*, 895–902.
(47) Ngwuluka, N. C.; Choonara, Y. E.; Kumar, P.; du Toit, L. C.; Khan, R. A.; Pillay, V. *J. Biomed. Mater. Res. Part A* **2015**, *103*, 1085–1094.
(48) Lorenzo-Lamosa, M. L.; Remuñán-López, C.; Vila-Jato, J. L.; Alonso, M. J. *J. Control. Release* **1998**, *52*, 109–118.
(49) Crank, J., *The Mathematics of Diffusion*; Oxford science publications; Clarendon Press: 1979.
(50) Aharoni, C.; Levinson, S.; Ravina, I.; Sparks, D. L. English *Soil Sci. Soc. Am. J.* **1991**, *55*, 1307–1312.
(51) Allen, E. R.; Hossner, L. R.; Ming, D. W.; Henninger, D. L. *Soil Sci. Soc. Am. J.* **1995**, *59*, 248–255.
(52) Freundlich, H. *Zeitschrift fur Phys. Chemie* **1907**, *57*, 385–470.
(53) Kuo, S.; Lotse, E. G. *Soil Sci.* **1973**, *116*, 400–406.

6. Experimental details

6.1 Analytical techniques

6.1.1 Powder X-ray diffraction

Powder X-ray diffraction (XRD) data were collected on a PAN-Analytical X'Pert Pro diffractometer in reflection mode at 40 kV and 40 mA using Cu Kα radiation ($\alpha_1 = 1.540\,57$ Å, $\alpha_2 = 1.544\,33$ Å, weighted average $= 1.541\,78$ Å). Scans were recorded from $2^\circ \leq 2\theta \leq 75^\circ$ with varying scan speeds and a slit size of 1 mm. Samples were mounted on stainless steel sample holders.

6.1.2 Fourier transform infrared spectroscopy

Fourier Transform Infrared (FTIR) spectra were recorded on a Biorad FTS 6000 FTIR Spectrometer equipped with a high performance DuraSamp1IR II diamond accessory by SensIR Technologies for measuring attenuated total reflection (ATR). Spectra were recorded in the range 400 – 4000 cm^{-1} with 40 scans at 4 cm^{-1} resolution. Absorptions in the range 1667 – 2500 cm^{-1} are from the DuraSamp1IR II diamond surface.

6.1.3 Solid state NMR spectroscopy

^{13}C cross-polarisation magic angle spinning (CP/MAS) Solid State NMR spectra were recorded by Dr Nicholas Rees on a Varian/Chemagnetics Infinity Spectrometer at 50.32 MHz using 7.5 mm zirconia rotors containing *ca.* 300 mg of sample. A double

resonance MAS probe and a MAS rate of 10 kHz were used. A cross-polarisation sequence with a variable X-amplitude spin-lock pulse[1] and phase-modulated proton decoupling were applied. Typically, 13000 transients were acquired using a contact time of 1 ms, an acquisition time of 41 ms (1024 data points zero-filled to 16 K) and a recycle delay of 30 s. All spectra were referenced to adamantane (the upfield methine resonance was taken to be at $\delta = 29.5$ ppm on a scale where $\delta(\mathrm{TMS}) = 0$) as a secondary reference.[2]

6.1.4 Solution phase NMR spectroscopy

Solution phase NMR spectroscopy was used to confirm the release of the unaltered drug species upon deintercalation or dissolution and check for the presence of impurities and decomposition products. For deintercalation reactions, samples were dispersed in 0.1 M Na_2CO_3 in D_2O in NMR tubes by sonication. After 15 min sonication the suspensions were allowed to settle. For dissolution experiments, samples were dissolved in DCl/D_2O (20 % W/W) in NMR tubes. ^{1}H NMR spectra were recorded on the resulting solutions using a Bruker Ascend™ 400 MHz NMR spectrometer and referenced via the residual protio-solvent peak.

6.1.5 Scanning electron microscopy and energy dispersive X-ray spectroscopy

Scanning Electron Microscopy (SEM) analysis was performed using a JSM-6610LV low vacuum scanning electron microscope with an accelerating voltage of 20 kV in secondary electron imaging mode. Samples were adhered to the SEM stage using carbon tape and coated with a 2 nm coating of Pt to reduce charging and improve the image quality. Energy-dispersive X-ray spectroscopy (EDX) data were collected using an Oxford Instruments X-Max^N silicon drift detector.

6.1.6 Transmission electron microscopy

Transmission Electron Microscopy (TEM) analysis was performed on a JEOL 2100 microscope with an accelerating voltage of 200 kV. Samples were dispersed in ethanol with brief sonication, then dropped onto Formvar® film-coated copper grids and left to dry.

6.1.7 Elemental analysis

Elemental C, H, N analysis was performed by a quantitative oxidative combustion technique by Dr Stephen Boyer at the School of Human Sciences, London Metropolitan University.

6.1.8 Thermogravimetric analysis

Thermogravimetric analysis (TGA) measurements were used to determine the cointercalated water content of the nanohybrids, collected using a Perkin-Elmer TGA7 Thermogravimetric Analyser. Samples (10 mg) were heated in platinum pan from 20 to 800 °C at a heating rate of 5 °C min^{-1} under a flowing stream of nitrogen.

6.1.9 Fluorescence spectroscopy

Fluorescence spectra were recorded on an LS 55 Perkin-Elmer Luminescence Spectrometer in emission mode ($\lambda_{\mathrm{excitation}} = 385\,\mathrm{nm}$, scan speed = $300\,\mathrm{nm\,min}^{-1}$, scan range = $410 - 650\,\mathrm{nm}$, excitation slit = 510 nm, emission slit = 5 nm). The emission of fluorescence samples was measured in a quartz fluorimeter cuvette.

6.1.10 Circular dichroism

Circular dichroism spectra were recorded on an Applied Photophysics Chirascan qCD/fluorimeter with scanning emission monochromator and CD photomultiplier

attachments (scan range = 200 − 350 nm). Samples were measured in a quartz cuvette with a path length of 1 mm.

6.1.11 Ultraviolet spectroscopy

Ultraviolet (UV) absorption spectra were recorded on a PG Instruments T60U UV/VIS/NIR spectrometer using wavelength scan mode on medium speed (scan range = 200 − 400 nm). Samples were measured in a 10 mm quartz cuvette.

6.2 General experimental procedures

6.2.1 Synthesis of highly crystalline MgAl-NO_3 LDH

Following the method described by Iyi *et al.*[3,4] with modifications, highly crystalline MgAl-CO_3 LDH was synthesised though homogeneous coprecipitation, followed by decarbonation to obtain MgAl-NO_3 LDH. A solution containing one equivalent of $Mg(NO_3)_2 \cdot 6\,H_2O$, (80.0 mmol) two equivalents of $Al(NO_3)_3 \cdot 9\,H_2O$ (40.0 mmol) and hexamethylenetetramine (114 mmol) in 350 mL degassed, deionised water was placed in PTFE-lined autoclaves. These were sealed and treated hydrothermally at 140 °C for 24 h. After air cooling, the contents were filtered and washed thoroughly with degassed, deionised water followed by methanol, and dried under vacuum. Under flowing N_2 gas, 8.4 g of the resultant white solid was suspended in a solution of $NaNO_3$ (10.6 mmol) in 270 mL degassed methanol. To this suspension, 27 mL of 2 M HNO_3 was added dropwise, and the reaction mixture stirred for 12 h at room temperature under a gentle flow of N_2 gas. The suspension was then filtered and washed thoroughly with methanol, before being dried under vacuum at 2×10^{-2} m bar to obtain a white powder. This LDH was used for all delamination and ion-exchange reactions using a magnesium–aluminium LDH precursor reported in Chapters 2, 3 and 4. The indexed powder XRD patterns of both MgAl-CO_3 and MgAl-NO_3 are presented in Figure 6.1.

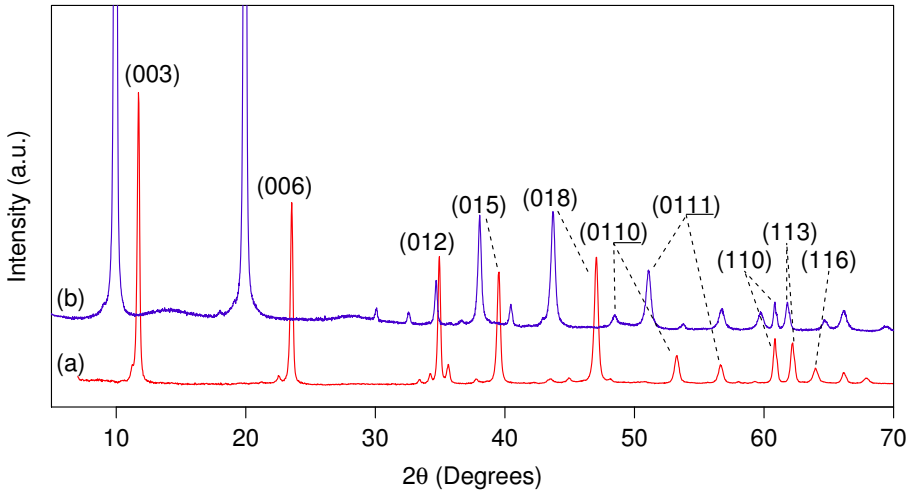


Figure 6.1: The indexed powder XRD patterns of (a) MgAl-CO_3 and (b) MgAl-NO_3.

6.2.2 Preparation of HCl-glycine and phosphate buffers

The 0.1 M pH 2 HCl-glycine buffer was prepared by dissolution of 50.0 mmol glycine and 4.13 mL concentrated HCl (37 % W/W) in degassed MilliQ water to make a solution with a total volume of 500 mL. The 0.1 M pH 4 phosphate buffer was prepared by dissolution of 50.0 mmol KH_2PO_4 in degassed MilliQ water and made up to a total volume of 500 mL. The 0.1 M pH 7 phosphate buffer was prepared by dissolution of 50.0 mmol KH_2PO_4 and 25.0 mmol KOH in degassed MilliQ water and dilution to a total volume of 500 mL. The buffer solutions were used for release studies in Chapters 3, 4 and 5 without alteration. For release studies in Chapter 2, the buffers were diluted at a ratio of 1 : 9 with MilliQ water to make 0.01 M buffer solutions. The 1 M pH 7 phosphate buffer used for determination of drug content of composites in Chapter 5 was prepared by dissolution of 500 mmol KH_2PO_4 and 250 mmol KOH in degassed MilliQ water and dilution to a total volume of 500 mL.

6.2.3 Determination of drug concentration from ultraviolet spectroscopy

The concentrations of drug species in aliquots from release and stability studies in Chapters 3, 4 and 5 were determined directly through ultraviolet spectroscopy without the need to further prepare the samples. Concentrations were calculated

through comparison to calibration curves obtained by measuring the absorption intensity of solutions of known drug concentrations.

6.2.4 Determination of aggregated concentrations of catecholamine decomposition products from ultraviolet spectroscopy

The aggregated concentrations of catecholamine decomposition products in aliquots from stability studies in Chapters 3 and 5 were determined alongside the concentrations of drug species through ultraviolet spectroscopy, by reference to calibration curves. Calibration curves for the aggregated concentrations were obtained in the following manner. Using MilliQ water, 5.00 m M solutions containing each of the catecholamine drugs were prepared in 100 mL volumetric flasks. These solutions were heated at 80 °C for in excess of 2 weeks in air, until full oxidative decomposition of the dissolved drugs had occurred. The volume of each of the solutions was returned to 100 mL using MilliQ water at room temperature and the decomposition products fully redissolved wherever precipitation had occurred, to produce solutions of the decomposition products with equivalent concentrations of 5.00 m M of their respective drugs. Series of solutions of known equivalent concentrations were then made through successive dilutions of the 5.00 m M equivalent solutions with MilliQ water, and their UV absorption intensities were measured, from which calibration curves could be constructed.

6.2.5 Fluorospectroscopic determination of drug concentration

The concentrations of gabapentin and pregabalin in the aliquots from release and stability studies in Chapters 2 and 5 were determined according to the following method.[5] A 1 mL sample was taken from each aliquot and added to 3 mL deionised water. To this was added 5 mL borate buffer (pH 9.0, 0.1 M) and 1 mL acetone solution of fluorescamine (0.72 m M) to make fluorescence samples. Fresh solutions of fluorescamine in acetone were prepared, stored at −5 °C and could be used for up

to 7 d before needing to remade.

The drug concentrations of the fluorescence samples were followed by measuring the emission in the range 454.5 – 579.5 nm in steps of 0.5 nm. Concentrations were calculated using calibration curves obtained by measuring the emission intensity of solutions of known drug concentrations. The solutions of known drug concentration were treated with borate buffer and fluorescamine solution in the same method as the aliquots.

6.3 Materials

Gabapentin (GBP) (> 98.0 % purity) and carbidopa (C-DOPA) (> 98.0 % purity) were purchased from Tokyo Chemical Industry UK, pregabalin (PGB) (> 98.0 % purity) was purchased from Manchester Organics, all were used as received. Eudragit® L 100 and S 100 were supplied by Evonik Industries. Cefuroxime axetil (CFA) was supplied by Nectar Lifesciences. All other reagents used were purchased from Sigma–Aldrich and used as received.

6.4 Experimental procedures from Chapter 2

6.4.1 Delamination of MgAl-NO_3 LDH

Delamination of the MgAl-NO_3 LDH was performed as detailed by Wu *et al.*[6] A sample of LDH (2.0 g) was dispersed in 100 mL of formamide with magnetic stirring and subsequently sonicated until it became transparent (12 – 24 h). The resulting 20 g L^{-1} dispersion of LDH nanosheets in formamide was kept sealed under a nitrogen atmosphere until use to prevent absorption of water. The dispersion remained stable indefinitely, becoming gel-like when left undisturbed and returning to a viscous fluid upon brief agitation.

6.4.2 Synthesis of MgAl-drug nanohybrids

The LDH–drug nanohybrids were synthesised by the following restacking procedure. Investigations into different variables all followed this same general procedure and are detailed subsequently. The pristine drug (1.5 mmol) was dissolved in 20 mL degassed, deionised water or ethanol and an equimolar amount of base (either 1 M NaOH in H_2O or 1 M NaOEt in EtOH) was added under magnetic stirring. To this solution, and whilst maintaining a stirring speed of 500 rpm, 5 mL of the 20 g L^{-1} LDH dispersion in formamide was added dropwise at 1.17 mL min^{-1} using a syringe pump. After the addition had finished, stirring was halted and the pearlescent reaction mixture was left to stand for 2 h. In all cases, the addition and standing time were conducted under a nitrogen atmosphere.

After 2 h of standing time had passed, the reaction mixture was centrifuged at 9000 rpm for 5 min. The resulting solid was resuspended in either water or ethanol and centrifuged. Centrifuge-washing cycles were repeated thrice. The white solid was then dried under vacuum for a minimum of 24 h. To remove final traces of formamide, the solid product was ground to a powder and dried for a further 12 h under high vacuum at 2×10^{-2} m bar.

6.4.3 Comparison of restacking solvent

MgAl-GBP nanohybrids were synthesised using either water or ethanol as the restacking solvent. In both cases, 1 M NaOH in H_2O was used as the base, however, the same solvent that was used for restacking was also used for the centrifuge-washings.

6.4.4 Investigation of water presence in restacking

To provide further comparison, samples of the LDH–drug nanohybrids were synthesised in a rigorously anhydrous environment. Reactions were carried out under a nitrogen atmosphere using standard Schlenk-line apparatus on a dual-vacuum-inlet gas manifold. During the delamination procedure, prior to the addition of formamide, the LDH sample was dried under high vacuum for 6 h. Anhydrous formamide,

Hydranal®, was used as the delamination solvent and stored under molecular sieves. Anhydrous ethanol, stored on molecular sieves, was used as the restacking solvent and the base used was 1 M NaOEt in EtOH, which was prepared *in situ* from anhydrous ethanol and sodium metal. Prior to dissolution in ethanol, GBP and PGB samples were dried for 30 min under at 2×10^{-2} m bar.

6.4.5 Investigation of restacking temperature

In all cases, the restacking procedure was initially performed at room temperature. Synthesis in water and ethanol was attempted at elevated temperature of 40 and 80 °C. In hydrous ethanolic conditions, the restacking procedure was performed at reduced temperatures of 0, −20 and −40 °C, accessed using an ice/water bath and ethylene glycol/ethanol/dry ice baths with ethylene glycol:ethanol ratios of 90 : 10 and 60 : 40 by volume respectively. In anhydrous ethanolic conditions, the restacking procedure was performed at a reduced temperature of −20 °C. In all cases, the desired temperature was maintained from the start of the addition of the LDH dispersion, through to the end of the standing time, after which the reaction mixtures were allowed to return to room temperature for centrifugation, washing and drying.

6.4.6 Release studies

Release of GBP and PGB from the nanohybrids *in vitro* was measured at 37 °C in sulphate (pH 2.0, 0.01 M) and phosphate (pH 4.0, 0.01 M and pH 7.0, 0.01 M) buffer solutions. For each sample measured, 50 mg nanohybrid was suspended in 200 mL buffer solution, which was kept at a constant 37 °C and under magnetic stirring at a rate of 200 rpm. At predetermined time intervals, (typically at 0.5, 1, 2, 3, 5, 7, 10, 15, 20, 30, 40, 60, 90 and 120 min) aliquots of 3 mL were removed from the suspensions and immediately passed through 0.45 µm syringe filters. The drug concentration of each filtered aliquot was then obtained through a fluorospectroscopic method.

6.4.7 Aqueous stability studies

The aqueous stability of the drug ions in the nanohybrids in deionised water was measured at both room temperature and 80 °C. For each sample measured, 50 mg nanohybrid was suspended in 100 mL water. To act as controls, solutions of 10 mg of each pristine drug dissolved in 100 mL water were also prepared. The suspensions and control solutions were then kept at either room temperature or 80 °C whilst being stirred gently. At predetermined time intervals (typically at 2, 6, and then every 24 h for two weeks, then optionally every 48 to 72 h for a further two weeks), aliquots of 2 mL were removed from the suspensions and control solutions, added to 2 mL of 0.2 M Na_2CO_3 solution and stirred for 30 min. The aliquots of suspensions were then passed through 0.45 µm syringe filters. The concentration of drug in each aliquot was then obtained through a fluorospectroscopic method.

To confirm the identities of the decomposition products, samples of nanohybrids were suspended in D_2O in NMR tubes at either room temperature or 80 °C and left for a sufficient period of time for measurable amounts of decomposition products to have formed, typically four weeks, or two weeks for heated samples. Solutions of Na_2CO_3 in D_2O were then added to the suspensions, which were subsequently sonicated and their ^1H NMR spectra recorded.

6.5 Experimental procedures from Chapter 3

6.5.1 General synthesis methods

To ensure minimal decomposition of the drug ions, all reactions involving drug species were covered to prevent exposure to light. All glassware was purged thoroughly with N_2 gas prior to use. Except where explicitly stated otherwise, all reactions were carried out in degassed MilliQ water under flowing N_2 gas. All solids containing drug species or Fe^{II} ions were stored in a vacuum desiccator at 1×10^{-2} m bar prior to characterisation or further reaction.

6.5.2 Synthesis of MgAl-drug nanohybrids

6.5.2.1 Ion-exchange

The method reported by Wei *et al.* was adapted to intercalate the catecholamine drugs.[7] In a 100 mL round bottomed flask, 2.0 mmol of the pristine drug was dissolved in 50 mL water. Using freshly prepared, degassed 1 M NaOH, the pH of the solution was raised, to 9.3 in the cases of L-DOPA and M-DOPA, and 9.7 in the case of C-DOPA. Whilst stirring at 20 °C, 1 mmol of MgAl-NO_3 LDH was added to the solution, and the resulting suspension was stirred for 48 h under a gentle flow of N_2 gas. Minimising the amount of time spent exposed to air, the reaction mixture was transferred to centrifuge tubes and centrifuged at 6000 rpm for 4 min. The supernatant was discarded and the solid was resuspended in water. Centrifuge-washing cycles were repeated twice in water and once in acetone. The off-white solid was then dried under vacuum at 1×10^{-2} m bar for a minimum of 24 h.

6.5.2.2 Coprecipitation

A solution containing L-DOPA (8.4 mmol), $Mg(NO_3)_2 \cdot 6\,H_2O$, (8.4 mmol) and $Al(NO_3)_3 \cdot 9\,H_2O$ (4.2 mmol) in 100 mL water was prepared in a 250 mL round bottomed flask. To this solution, a solution of freshly prepared, degassed 1 M NaOH was added dropwise, under vigorous stirring until the pH of the resulting mixture reached 9.5. The reaction mixture was subsequently stirred at 20 °C for 48 h under a gentle flow of N_2 gas, before centrifuging at 9000 rpm for 5 min.The supernatant was discarded and the solid was resuspended in water. Centrifuge-washing cycles were repeated twice in water and once in acetone. The off-white solid was then dried under vacuum at 1×10^{-2} m bar for a minimum of 24 h and ground into a powder using a pestle and mortar.

6.5.3 Synthesis of Fe^{II} containing precursor LDHs

The homogeneous coprecipitation method described by Liu *et al.*[8] to synthesise highly crystalline CoAl-CO_3 and FeAl-CO_3 LDH particles was adapted to synthesise

FeAl-CO_3 and MgFeAl-CO_3. A solution of mixed metal chlorides (quantities detailed in Table 6.1) and urea (175 mmol) in 500 mL water was heated under reflux for 48 h. The reaction mixture was allowed to cool and the solid product allowed to settle. The bulk of the supernatant was decanted and discarded, and the remaining reaction mixture was centrifuged at 6000 rpm for 5 min. The remaining supernatant was discarded and the solid product was resuspended in degassed water. Centrifuge-washing cycles were repeated twice in water and once in acetone. The pale blue solid was dried under vacuum at 1×10^{-2} m bar.

Table 6.1: The quantities of metal chlorides used to synthesise Fe^{2+} containing LDHs.

Sample	Reactant quantity (mmol)		
	$MgCl_2 \cdot 4\,H_2O$	$FeCl_2 \cdot 6\,H_2O$	$AlCl_3 \cdot 6\,H_2O$
FeAl-CO_3	0	50.0	25.0
$MgFeAl_a$-CO_3	45.0	5.00	25.0
$MgFeAl_b$-CO_3	25.0	25.0	25.0
$MgFeAl_c$-CO_3	50.0	25.0	25.0

The method of decarbonation of the carbonate LDHs to form the nitrate and chloride LDHs was adapted from the salt–acid and acid–alcohol methods reported by Liu *et al.* and Iyi *et al.*[4,8] The carbonate LDH was suspended in a 0.1 M solution of either $NaNO_3$ or NaCl in degassed methanol at an approximate equivalent concentration of 3.5 g LDH per 150 mL solution. To this suspension, a 1.0 M solution of either HNO_3 or HCl was added dropwise at a ratio of 5 mL acid per gramme of LDH. The reaction mixture was stirred for 3 h and then allowed to settle. The bulk of the supernatant was decanted and discarded, and the remaining reaction mixture was centrifuged at 6000 rpm for 5 min. The remaining supernatant was discarded and the solid product was resuspended in degassed methanol. Centrifuge-washing cycles were repeated twice. The mid or pale blue solid was dried under vacuum at 1×10^{-2} m bar.

6.5.4 Synthesis of Fe^{II} containing LDH–drug nanohybrids

The ion-exchange method used to intercalate catecholamine drugs into MgAl-NO_3 detailed in Section 6.5.2.1 was adapted to attempt to intercalate L-DOPA into the Fe^{II} containing nitrate and chloride LDHs. Intercalation was attempted at reaction

pH values of 8.0, 9.0, 10.0 and 11.0 and experiments were repeated with double the quantity of L-DOPA (4.0 mmol) in the reaction mixture. The only successful intercalation attempt was conducted on $MgFeAl_c$-NO_3 with a reaction pH of 10.0 and doubled quantity of L-DOPA. All other details were unchanged from the method reported in Section 6.5.2.1. The solid product was pale purple.

6.5.5 Release studies

Release of catecholamine drugs from the nanohybrids *in vitro* was measured at 37 °C in sulphate (pH 2.0, 0.1 M) and phosphate (pH 4.0, 0.1 M and pH 7.0, 0.1 M) buffer solutions. For each sample measured, 100 mg nanohybrid was suspended in 150 mL buffer solution, which was kept at a constant 37 °C and under magnetic stirring at a rate of 200 rpm. At predetermined time intervals, (typically at 0.5, 1, 2, 3, 5, 7, 10, 15, 20, 30, 40, 60, 90 and 120 min) aliquots of 3 mL were removed from the suspensions and immediately passed through 0.45 µm syringe filters. The drug concentration of each filtered aliquot was then obtained through UV spectroscopic analysis as rapidly as possible, before any significant decomposition of the drug ions occurred.

6.5.6 Dry stability studies

The stability of the drug ions in the nanohybrids in dry conditions in air was measured at room temperature, 40 and 80 °C, and under exposure to ultraviolet light (λ = 254 nm). For comparison, the stability of samples of the pristine drugs was also investigated under the same conditions. Samples were spread thinly onto glass Petri dishes and shielded from other sources of light whilst exposed to the stated conditions. At predetermined times, (every 24 h for the first week, then once per week for the following six weeks) a 10 mg portion of each sample was removed, dissolved in 2.0 mL concentrated HCl (37 % W/W) and diluted to a total volume of 50 mL with water. Samples were then analysed by ultraviolet and circular dichroism spectroscopy to obtain the concentration of drug ions and decomposition products, and the extent of drug racemisation. Additionally, small portions of the nanohybrid and pristine drug

samples were removed at the same predetermined times and dissolved in DCl/D_2O (20 % W/W) for ^1H NMR spectroscopic analysis.

6.5.7 Aqueous stability studies

The aqueous stability of the drug ions in the nanohybrids was investigated under the same set of conditions as those of the dry stability studies. For each of the samples, 50 mg nanohybrid was suspended in 200 mL water. To act as controls, solutions of 20 mg of each pristine drug dissolved in 200 mL water were also prepared. The suspensions and control solutions were then kept at their experimental conditions whilst being stirred gently and shielded from other sources of light. At predetermined time intervals, (after 1, 3, 6, 10, and then every 24 h for up to two weeks) aliquots of 9 mL were removed from the suspensions and control solutions and added to 1 mL concentrated HCl solution. All aliquots were then analysed by UV spectroscopy to obtain the concentration of drug ions and decomposition products, and selected samples were analysed by circular dichroism spectroscopy to confirm that drug racemisation had not taken place.

To confirm the identities of the decomposition products, samples of nanohybrids were suspended in D_2O in NMR tubes at 80 °C and left for a sufficient period of time for measurable amounts of decomposition products to have formed, typically two weeks. Solutions of DCl/D_2O were then added to the suspensions, which were subsequently analysed by ^1H NMR spectroscopy.

6.6 Experimental procedures from Chapter 4

6.6.1 β-Cyclodextrin substitution

6.6.1.1 Non-selective carboxymethylation

The non-selective carboxymethylation method reported by Hattori *et al.* was used, with modifications.[9] In a round bottomed flask, 44 mmol NaOH was dissolved in 10 mL deionised water, followed by 1.43 mmol β-cylodextrin. Under gentle stirring,

2 mmol chloroacetic acid was added to the reaction mixture and stirred for 5 min. β-CMCD samples with varying levels of substitution were synthesised by repeating the addition of 2 mmol chloroacetic acid followed by stirring up to ten times, creating ten different reaction mixtures, containing between 2 and 20 mmol chloroacetic acid, in multiples of 2 mmol. The resulting solutions were sealed and heated at 80 °C for 16 h whilst stirring. The solutions were subsequently cooled in an ice bath and adjusted to between pH 5.0 and 6.0 with concentrated HCl. MeOH (50 mL) was added to the solutions gradually to precipitate out the β-CMCD samples. No precipitate was obtained from the solution that contained only 2 mmol chloroacetic acid, hence only nine non-selectively substituted β-CMCD samples were synthesised. The reaction mixtures were filtered to obtain the white granular solids, which were washed thrice with MeOH. The β-CMCD samples were redissolved in a minimum volume of deionised water and reprecipitated out of solution by the addition of 50 mL MeOH, filtered and again washed thrice with MeOH. The sample was dried at 1 m bar for a minimum of 24 h.

6.6.1.2 C2 selective carboxymethylation

C2 selective carboxymethylation was enacted under a nitrogen atmosphere using standard Schlenk-line apparatus on a dual-vacuum-inlet gas manifold, following the method reported by Dignam *et al.*[10] β-cyclodextrin (2.2 mmol) was dried in a Schlenk by heating to 120 °C at a pressure of 1×10^{-2} m bar for 16 h. To the β-cyclodextrin was added 100 mL dry DMF under vigorous stirring, until the β-cyclodextrin was fully dissolved. NaH (3.2 mmol) was placed in an ampoule and the β-cyclodextrin solution added dropwise whilst stirring. Care was taken to ensure the NaH was fully suspended in the DMF. The reaction mixture was stirred for 24 h at room temperature under flowing N_2 gas, due to the evolution of H_2 gas. Sodium iodoacetate (17 mmol) was added to the reaction mixture, which was then stirred for a further 24 h. The solvent was removed using a rotary evaporator and the excess NaH was reacted with 80 : 20 toluene/isopropanol solution. The resulting suspension was filtered and white residue was washed with acetone. The β-CMCD sample was dissolved in a minimum volume of deionised water and the pH of the solution was adjusted to 7 using HCl. The β-CMCD was reprecipitated out of solution by the

addition of 50 mL MeOH, filtered and washed thrice with MeOH. The sample was dried at 1 m bar for a minimum of 24 h.

6.6.1.3 Sulfobutylation

Sulfobutylation was performed according to the method reported by Ivanyi *et al*.[11] A solution of 861 mmol NaOH and 12.3 mmol β-cyclodextrin in 45 mL deionised water was prepared. To this solution, 348 mmol of 1,4-butane sultone was added portionwise whilst stirring. The resulting solution was heated at 50 °C for 16 h, whilst stirring. After the requisite time had elapsed, 75 mL deionised water was added to the the solution, and the pH adjusted to 5.5 using 1 M HCl. The reaction mixture was then added to 1.5 L EtOH under vigorous stirring, causing a white solid to precipitate out of solution. The reaction mixture was filtered and the solid product retained and washed thrice with MeOH. The β-SBECD sample was redissolved in a minimum volume of deionised water and reprecipitated out of solution by the addition of 50 mL MeOH, filtered and again washed thrice with MeOH. The dissolution-precipitation procedure was repeated twice, and the sample was dried at 1 m bar for a minimum of 24 h.

6.6.2 Intercalation of substituted β-cyclodextrins

Intercalation of the β-CMCD and β-SBECD species into MgAl-NO_3 was conducted through an ion-exchange method adapted from the procedure reported by Mohanambe and Vasudevan.[12] In a 50 mL round bottomed flask, a predetermined amount of a substituted β-cyclodextrin sample was dissolved in 30 mL degassed, deionised water, depending on its degree of substitution. Table 6.2 details the amount of substituted β-cyclodextrin sample used in each case. Using freshly prepared, degassed 0.1 M NaOH, the pH of the solution was raised to 7.0. Whilst stirring at 70 °C, 1.25 mmol of MgAl-NO_3 LDH was added to the solution, and the resulting suspension was sealed under N_2 gas and stirred for 24 h. The reaction mixture was transferred to centrifuge tubes and centrifuged at 6000 rpm for 4 min. The supernatant was discarded and the solid was resuspended in water. Centrifuge-washing cycles were repeated twice in water and once in acetone. The white solid was then dried under

vacuum at 1 m bar for a minimum of 24 h.

Table 6.2: The amounts of substituted β-cyclodextrin samples used in the ion-exchange experiments.

Cyclodextrin	β-CMCD										β-SBECD
sample	[P1]	[P2]	[P3]	[P4]	[P5]	[P6]	[P7]	[P8]	[P9]	[C2]	
Amount used (mmol)	21.0	12.4	10.5	8.40	6.60	5.70	3.60	3.40	3.00	6.00	2.10

6.6.3 Intercalation of β-cyclodextrin–drug complexes

Intercalation of the β-cyclodextrin–drug complexes into MgAl-NO_3 followed a two step process, first involving the formation of the β-cyclodextrin–drug complexs, followed by intercalation through ion-exchange. The solvents and solvent mixtures used for the complexation reactions varied depending on the drug species being complexed and the concentration of the drug species being used. Complexation of all the cationic tricyclic drugs, CPZ, PMZ, AMI and IMI was conducted in deionised water. Complexation of TST to β-CMCD[P1]–[P4] was conducted in a 50 : 50 water/ethanol mixture, and to β-CMCD[P5]–[P9], [C2] and β-SBECD was conducted in a 60 : 40 water/ethanol mixture. Complexation of CIN to β-CMCD[P1]–[P3] conducted in a 25 : 75 water/THF mixture, to β-CMCD[P4]–[P6] and [C2] conducted in a 40 : 60 water/THF mixture, and to β-CMCD[P7]–[P9] and β-SBECD conducted in a 50 : 50 water/THF mixture. Complexation of CFA was conducted in a 55 : 45 water/acetone mixture. In all cases, the solvent or solvent mixtures were degassed with N_2 prior to use.

In a 50 mL round bottomed flask, a predetermined amount of a substituted β-cyclodextrin sample and three molar equivalents of the desired drug species were dissolved in 30 mL of the stipulated solvent or solvent mixture. Table 6.2 details the amount of substituted β-cyclodextrin sample used in each case. Using freshly prepared, degassed 0.1 M NaOH, the pH of the solution was raised to 7.0. The solution was sealed under N_2 gas and stirred at room temperature for 24 h. The temperature of the solution was then raised to 70 °C, 1.25 mmol of MgAl-NO_3 LDH was added to the solution, and the resulting suspension was sealed under N_2 gas and stirred for a further 24 h. The reaction mixture was transferred to centrifuge

tubes and centrifuged at 6000 rpm for 4 min. The supernatant was discarded and the solid was resuspended in the same solvent or solvent mixture that the reaction was conducted in. Centrifuge-washing cycles were repeated once in water and once in acetone. The white solid was then dried under vacuum at 1 m bar for a minimum of 24 h.

6.6.4 Calculation of drug content of nanohybrids

The drug content of the nanohybrids was calculated by dissolving 40 mg of each sample in 20 mL 1.0 M HCl and obtaining drug concentration of the resultant solution through UV spectroscopic analysis. This procedure was performed in triplicate for each sample and the final value for the drug content given is the mean of the three values obtained for each sample.

6.6.5 Release studies

Release of the drug species from the nanohybrids *in vitro* was measured at 37 °C in sulphate (pH 2.0, 0.1 M) and phosphate (pH 4.0, 0.1 M and pH 7.0, 0.1 M) buffer solutions. For each nanohybrid, 200 mg of sample was suspended in 50 mL buffer solution, which was kept at a constant 37 °C and under magnetic stirring at a rate of 200 rpm. At predetermined time intervals, (typically at 0.5, 1, 2, 3, 5, 7, 10, 15, 20, 30, 40, 60, 90, 120, 180 and 240 min) aliquots of 2 mL were removed from the suspensions and immediately passed through 0.45 µm syringe filters. The drug concentration of each filtered aliquot was then obtained through UV spectroscopic analysis.

6.7 Experimental procedures from Chapter 5

6.7.1 General synthesis methods

All glassware was purged thoroughly with N_2 gas prior to use. Except where explicitly stated otherwise, all reactions were carried out under flowing N_2 gas. All

solids containing drug species or Fe^{II} ions were stored in a vacuum desiccator at 1×10^{-2} m bar prior to characterisation or further reaction. To ensure minimal decomposition of L-DOPA, all synthesis of composites involving LDH nanohybrids intercalated with this drug were covered to prevent exposure to light.

6.7.2 Eudragit® composites

The method used to synthesise Eudragit®–LDH composites using LDH–drug nanohybrid samples from Chapters 2 and 3 and Eudragit®–drug composites was adapted from the solvent extraction–evaporation method reported by del Arco *et al.*[13] Under a nitrogen atmosphere, 1.0 g of either Eudragit® L 100 or S 100 was dissolved in a solution of 10 mL degassed ethanol and 5 mL DCM. Under vigorous stirring, 0.1 g of the LDH–drug nanohybrid (MgAl-GBP_{anhyd}, MgAl-PGB_{anhyd}, MgAl-$LDOPA_{IE}$ or $MgFeAl_c$-LDOPA) or the pristine drug (GBP or L-DOPA) was added to this solution, and the resulting suspension was sealed under N_2 gas and sonicated for 10 min. A solution of 10 g polyvinyl alcohol in 200 mL degassed MilliQ water was prepared by heating to 90 °C until fully dissolved and allowed to return to room temperature. The organic LDH suspension was added dropwise using a syringe pump at a rate of 45 mL h^{-1} to the aqueous solution whilst stirring at 500 rpm, under a gentle flow of nitrogen and whilst heating at 40 °C. The reaction mixture was stirred under the same conditions for a further 3 h, before filtering under vacuum and washing with dilute HCl (pH = 5) and distilled water. The resulting fluffy powders were dried under vacuum for 24 h and those containing L-DOPA were stored in a vacuum desiccator at 1×10^{-2} m bar.

6.7.3 Synthesis of alginate composites

Alginate–LDH composite beads were synthesised according to the method detailed by Zhang *et al.*[14] The nanohybrid (MgAl-$LDOPA_{IE}$ or $MgFeAl_c$-LDOPA, 0.4 g) or pristine drug (L-DOPA) being encapsulated was first suspended in 14 mL water and sonicated for 30 min to ensure a thorough dispersion. Sodium alginate (0.8 g) was dissolved in 50 mL water and subsequently stirred for 30 min. The LDH suspension and alginate solution were added together and stirred at 40 °C for 1 h. Calcium

chloride (1.0 g) was dissolved in 100 mL water. Using a syringe pump, the alginate–LDH suspension was added dropwise at a rate of 45 mL h^{-1} to the calcium chloride solution under gentle stirring. Upon completion of the addition, the reaction mixture was stirred at room temperature for a further 1 h. The reaction mixture was subsequently filtered using a Büchner funnel and the turgid beads washed with water thrice and acetone once. The beads were then dried in a vacuum desiccator at 1×10^{-2} m bar.

6.7.4 Determination of composite drug content

The drug contents of the polymer–nanohybrid and polymer–drug composites were determined by suspending 50 mg of each sample 40 mL of 1.0 M pH 7 phosphate buffer solution at 50 °C and stirring vigorously for 1 h under flowing N_2 gas. Aliquots of 3 mL were then removed from the suspensions and immediately passed through 0.45 µm syringe filters. For samples containing L-DOPA, the drug concentration of each filtered aliquot was then obtained through UV spectroscopic analysis as rapidly as possible, before any significant decomposition of the drug ions occurred. For samples containing GBP, the drug concentration of each filtered aliquot was then obtained through a fluorospectroscopic method. This procedure was performed in triplicate for each sample and the final value for the drug content given is the mean of the three values obtained for each sample.

6.7.5 Release studies

Drug release from the polymer–nanohybrid composites *in vitro* was measured at 37 °C in sulphate (pH 2.0, 0.1 M) and phosphate (pH 4.0, 0.1 M and pH 7.0, 0.1 M) buffer solutions. For each sample measured, 150 mg (alginate composites) or 300 mg (Eudragit® composites) of sample was suspended in 100 mL buffer solution, which was kept at a constant 37 °C and under magnetic stirring at a rate of 200 rpm. At predetermined time intervals, (typically at 0.5, 1, 2, 3, 5, 7, 10, 15, 20, 30, 40, 60, 90, 120, 180 and 240 min) aliquots of 3 mL were removed from the suspensions and immediately passed through 0.45 µm syringe filters. For release studies on nanohybrids containing L-DOPA, the drug concentration of each filtered aliquot

was then obtained through UV spectroscopic analysis as rapidly as possible, before any significant decomposition of the drug ions occurred. For release studies on nanohybrids containing GBP or PGB, the drug concentration of each filtered aliquot was then obtained through a fluorospectroscopic method.

6.7.6 GBP and PGB composite stability studies

The stability of GBP and PGB in the polymer–nanohybrid composites suspended in water was measured at room temperature and 80 °C. For each of the samples, a 50 mg portion was suspended in 40 mL dilute HCl solution (0.01 m M, pH 5.0), which was subsequently sealed and stirred for two weeks at the designated temperature. After initial suspension of the composite, and again at the end of the two week period, aliquots of 2 mL were removed from the suspensions and control solutions, added to 2 mL of 0.2 M Na_2CO_3 solution and stirred for 1 h. The aliquots of suspensions were then passed through 0.45 µm syringe filters. The concentration of drug in each aliquot was then obtained through a fluorospectroscopic method.

6.7.7 L-DOPA composite dry stability studies

The stability of L-DOPA in the polymer–nanohybrid composites in dry conditions in air was measured at room temperature, 80 °C, and under exposure to ultraviolet light ($\lambda = 254$ nm). Samples were spread thinly onto glass Petri dishes and shielded from other sources of light whilst exposed to the stated conditions. At predetermined times, (every 24 h for the first week, then once per week for the following six weeks) a 20 mg (alginate composites) or 40 mg (Eudragit® composites) portion of each sample was removed, dispersed in 2.0 mL concentrated HCl (37 % W/W) and diluted to a total volume of 50 mL with water. Samples were then agitated for 30 min and passed through 0.45 µm syringe filters before being analysed by UV spectroscopy to obtain the concentration of drug ions and decomposition products.

6.7.8 L-DOPA composite aqueous stability studies

The aqueous stability of L-DOPA in the polymer–nanohybrid composites in water was investigated under the same set of conditions as those of the dry stability studies. For each of the samples, a 150 mg (alginate composites) or 300 mg (Eudragit® composites) portion was suspended in 200 mL dilute HCl solution (0.01 m M, pH 5.0). The suspensions were then kept at their experimental conditions whilst being stirred gently and shielded from other sources of light. At predetermined time intervals, (after 1, 3, 6, 10, and then every 24 h for two weeks, followed by every 48 to 72 h for a further two weeks) aliquots of 9 mL were removed from the suspensions and added to 1 mL concentrated HCl solution. The aliquots were agitated for 30 min and then passed through 0.45 µm syringe filters. All aliquots were then analysed by ultraviolet spectroscopy to obtain the concentration of drug ions and decomposition products, and selected samples were analysed by circular dichroism spectroscopy to confirm that drug racemisation had not taken place.

6.8 References

(1) Peersen, O. B.; Wu, X. L.; Kustanovich, I.; Smith, S. O. *J. Magn. Reson. Ser. A* **1993**, *104*, 334–339.
(2) Earl, W. L.; Vanderhart, D. L. *J. Magn. Reson.* **1982**, *48*, 35–54.
(3) Iyi, N.; Matsumoto, T.; Kaneko, Y.; Kitamura, K. *Chem. Lett.* **2004**, *33*, 1122–1123.
(4) Iyi, N.; Yamada, H.; Sasaki, T. *Appl. Clay Sci.* **2011**, *54*, 137–132.
(5) Belal, F.; Abdine, H.; Al-Majed, A.; Khalil, N. Y. *J. Pharm. Biomed. Anal.* **2002**, *27*, 253–260.
(6) Wu, Q.; Olafsen, A.; Vistad, O. B.; Roots, J.; Norby, P. *J. Mater. Chem.* **2005**, *15*, 4695–4700.
(7) Wei, M.; Pu, M.; Guo, J.; Han, J.; Li, F.; He, J.; Evans, D. G.; Duan, X. *Chem. Mater.* **2008**, *20*, 5169–5180.
(8) Liu, Z.; Ma, R.; Ebina, Y.; Iyi, N.; Takada, K.; Sasaki, T. *Langmuir* **2006**, *23*, 861–867.
(9) Hattori, M.; Okada, Y.; Takahashi, K. *J. Agric. Food Chem.* **2000**, *48*, 3789–3794.
(10) Dignam, C. F.; Randall, L. a.; Blacken, R. D.; Cunningham, P. R.; Lester, S.-K. G.; Brown, M. J.; French, S. C.; Aniagyei, S. E.; Wenzel, T. J. *Tetrahedron: Asymmetry* **2006**, *17*, 1199–1208.
(11) Ivanyi, R.; Jicsinszky, L.; Hirschberg Gabriella, S.; Vadasz, Z.; Szente, L. Manufacture of sulfobutylated cyclodextrins of pharmaceutical additive quality. HU 2009000229 A2., 2010.
(12) Mohanambe, L.; Vasudevan, S. *J. Chem. Sci.* **2006**, *118*, 105–115.
(13) Del Arco, M.; Fernandez, A.; Martin, C.; Rives, V. *J. Solid State Chem.* **2010**, *183*, 3002–3009.
(14) Zhang, J.-P.; Wang, Q.; Xie, X.-L.; Li, X.; Wang, A.-Q. *J. Biomed. Mater. Res. Part B Appl. Biomater.* **2010**, *92*, 205–214.

7. Summary

In this thesis, the synthesis of layered double hydroxides (LDHs) for use as drug delivery systems was investigated, and the potential of these compounds to provide solutions to typical pharmaceutical problems was explored.

Chapter 1 introduced the background information on pharmaceutics and drug delivery, and the structure, synthesis and general applications of LDHs were described, as well as a systematic review of the biomedical and pharmaceutical applications of LDHs.

In **Chapter 2**, the GABAergic drugs gabapentin and pregabalin were intercalated into an LDH using the coassembly method. The optimum conditions for the restacking process were investigated, and an improved method of anhydrous restacking in ethanol at reduced temperatures was described, and a possible restacking mechanism suggested. The stabilising effect of LDH intercalation on the drug ions was measured, the release rates of the drugs from the compounds was recorded, and their kinetics modelled, from which mechanistic data was extracted.

In **Chapter 3**, the potential for LDHs to stabilise and deliver catecholamine drugs levodopa, carbidopa and methyldopa was explored. The ability of a range of LDHs, synthesised through different methods and with varied metal ratios, to intercalate and stabilise these drugs against racemisation and oxidative decomposition across a variety of conditions was investigated. It was found that LDH intercalation in isolation does not confer greater stability on catecholamine drugs. HTe drug release profiles were recorded and the kinetics modelled, from which mechanistic data could be extracted.

In **Chapter 4**, the potential for LDHs to deliver neutral hydrophobic and cationic drugs through the intercalation of cyclodextrin–drug inclusion complexes was investigated. A range of partially substituted anionic cyclodextrins were synthesised and intercalated into an LDH, both carboxymethyl cyclodextrins and sulfobutylether cyclodextrins. Cyclodextrin–drug inclusion complexes were intercalated, their interlayer orientation was suggested and drug release profiles measured. Kinetic analysis of the drug release profiles yielded mechanistic data. It was found that the release rates

from LDH–cyclodextrin–drug composites were dependent on the level of substitution of the cyclodextrin species and the overall charge on the cyclodextrin–drug complex, and was not noticeably effected by the identity of the drug being released.

Chapter 5 explored the potential of polymer–LDH composites for drug delivery. A selection of drug intercalated LDHs from Chapters 2 and 3 were encapsulated in several enteric polymers typically used for drug delivery. The release profiles and stabilising effects of the composites were measured. It was found that the shape of the LDH particles greatly affected how well LDH particles could be encapsulated, with large platelets with a high aspect ratio failing to be encapsulated as effectively as more rounded particles, which greatly influenced the drug release profiles of the resulting composites. Despite this, it was found that composites consisting on Eudragit polymers that contained levodopa were found to stabilise the drug in both wet and dry conditions.

Chapter 6 detailed the experimental procedures and analytical instruments used throughout this thesis. The **Appendices** contain supplementary characterisation and analytical data that are referred to in the main text.

Appendices

A Supporting data for Chapter 2

A.1 Gabapentin and pregabalin elemental analysis data

Table A.1: Observed and calculated C, H, and N percentages in the gabapentin and pregabalin nanohybrid samples, obtained from elemental analysis.

Sample	C percentage (%)		H percentage (%)		N percentage (%)	
	Obs	Cal	Obs	Cal	Obs	Cal
MgAl-$GBP_{water,20}$	19.4	19.2	4.88	4.88	4.88	4.93
MgAl-$GBP_{ethanol,20}$	21.6	21.7	5.17	5.20	4.67	4.71
MgAl-$GBP_{ethanol,0}$	22.3	22.2	5.17	5.25	4.67	4.76
MgAl-$GBP_{ethanol,-20}$	22.5	22.8	5.36	5.31	4.70	4.76
MgAl-$GBP_{ethanol,-40}$	22.2	22.1	5.28	5.24	4.75	4.73
MgAl-$GBP_{anhyd,20}$	23.6	23.8	5.48	5.41	4.98	4.88
MgAl-$GBP_{anhyd,-20}$	24.1	24.2	5.47	5.50	4.60	4.63
MgAl-$PGB_{anhyd,20}$	21.7	21.5	5.54	5.57	4.82	4.76
MgAl-$PGB_{anhyd,-20}$	22.2	22.0	5.63	5.63	4.87	4.81

A.2 Gabapentin and pregabalin nanohybrid decomposition plots

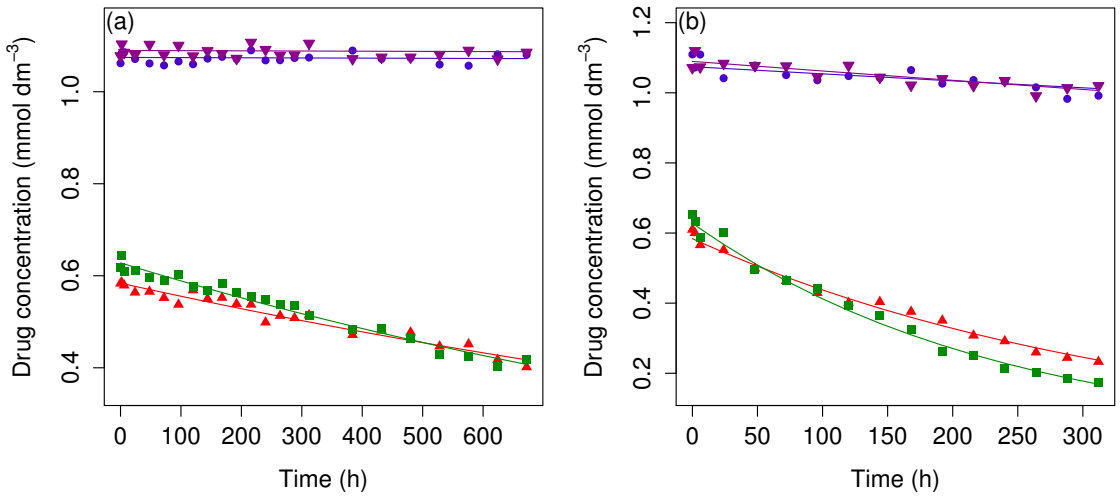


Figure A.1: The concentration of GBP and PGB as a function of time during decomposition studies carried out at (a) room temperature and (b) 80 °C. The samples are pristine GBP, ▲, MgAl-GBP$_{\text{anhyd,-20}}$, ●, pristine PGB, ■, and MgAl-PGB$_{\text{anhyd,-20}}$ ▼.

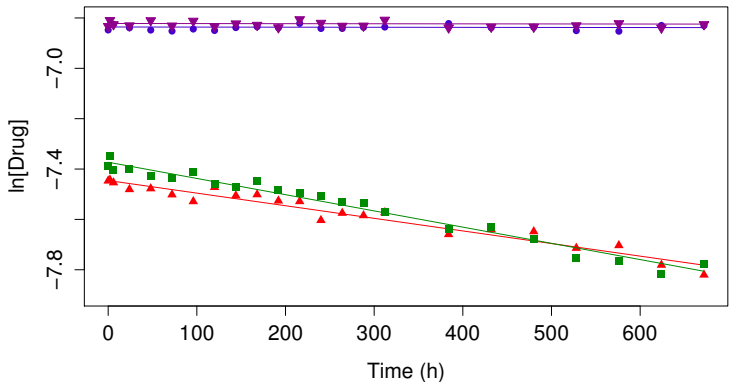


Figure A.2: The natural logarithm of drug concentration as a function of time during the decomposition studies, from which the cyclisation constant, k_{obs}, can be calculated. These studies were carried out at room temperature, the samples are pristine GBP, ▲, MgAl-GBP$_{\text{anhyd,-20}}$, ●, pristine PGB, ■, and MgAl-PGB$_{\text{anhyd,-20}}$ ▼.

B Supporting data for Chapter 3

B.1 Catecholamine nanohybrid elemental analysis data

Table B.1: Observed and calculated C, H, and N percentages in the catecholamine nanohybrid samples, obtained from elemental analysis.

Sample	C percentage (%)		H percentage (%)		N percentage (%)	
	Obs	Cal	Obs	Cal	Obs	Cal
MgAl-LDOPA$_{IE}$	21.7	21.8	4.89	4.84	3.58	3.65
MgAl-MDOPA$_{IE}$	21.4	21.3	4.87	4.81	3.83	3.81
MgAl-CDOPA$_{IE}$	21.3	21.2	4.99	4.96	4.86	4.79
MgAl-LDOPA$_{CP}$	23.4	23.4	4.94	4.99	3.43	3.45
MgFeAl$_c$-LDOPA	18.0	18.1	4.18	4.17	3.70	3.71

B.2 Catecholamine decomposition plots

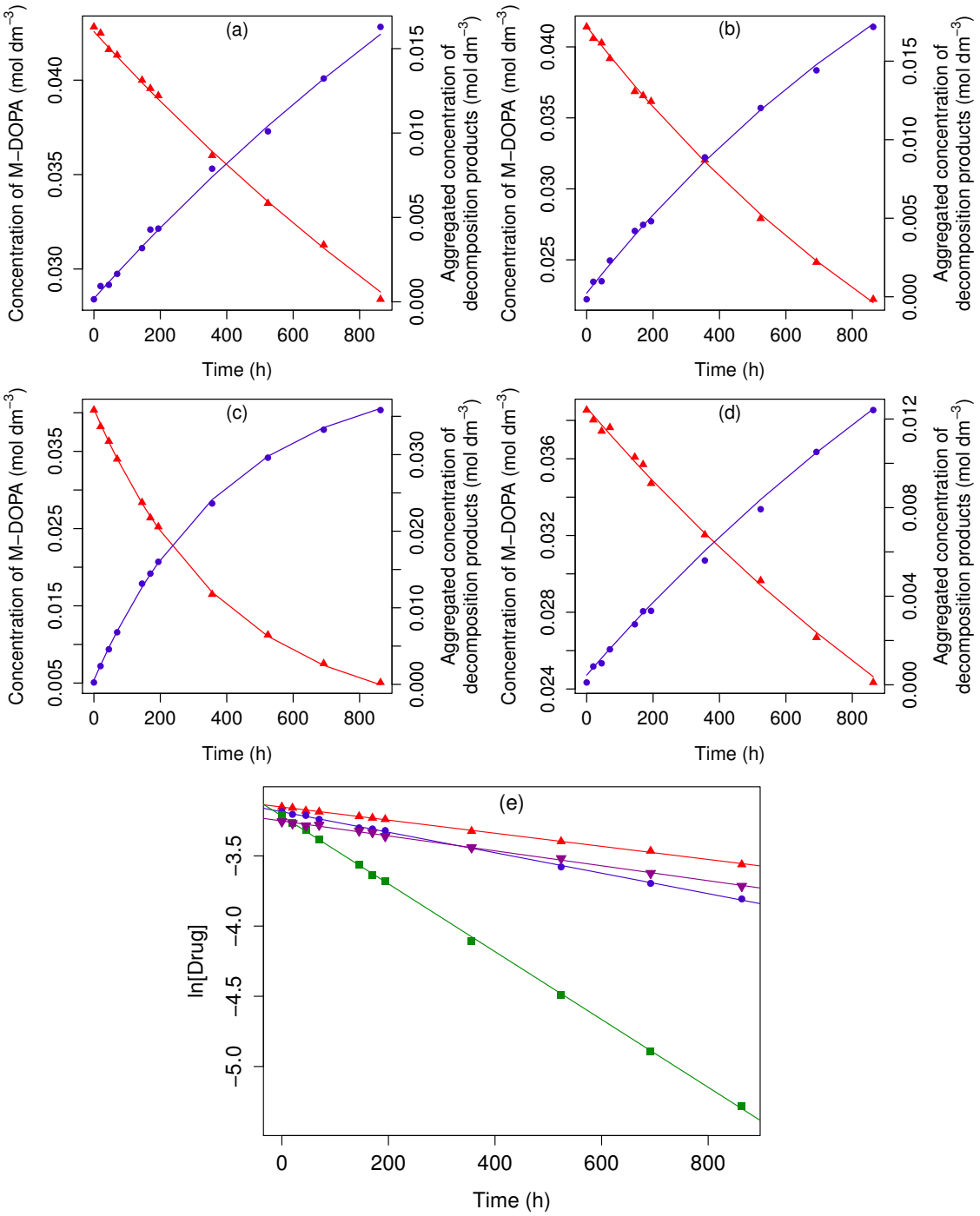


Figure B.1: The decomposition profiles of MgAl-MDOPA$_{IE}$ in dry conditions at (a) room temperature, (b) 40 °C, (c) 80 °C, and (d) under exposure to ultraviolet radiation, detailing the concentrations of M-DOPA (▲) and the aggregated concentrations of the decomposition products (●). Also (e) ln[M-DOPA] plotted as a function of time for the four experiments: room temperature (▲), 40 °C (●), 80 °C (■) and UV radiation (▼).

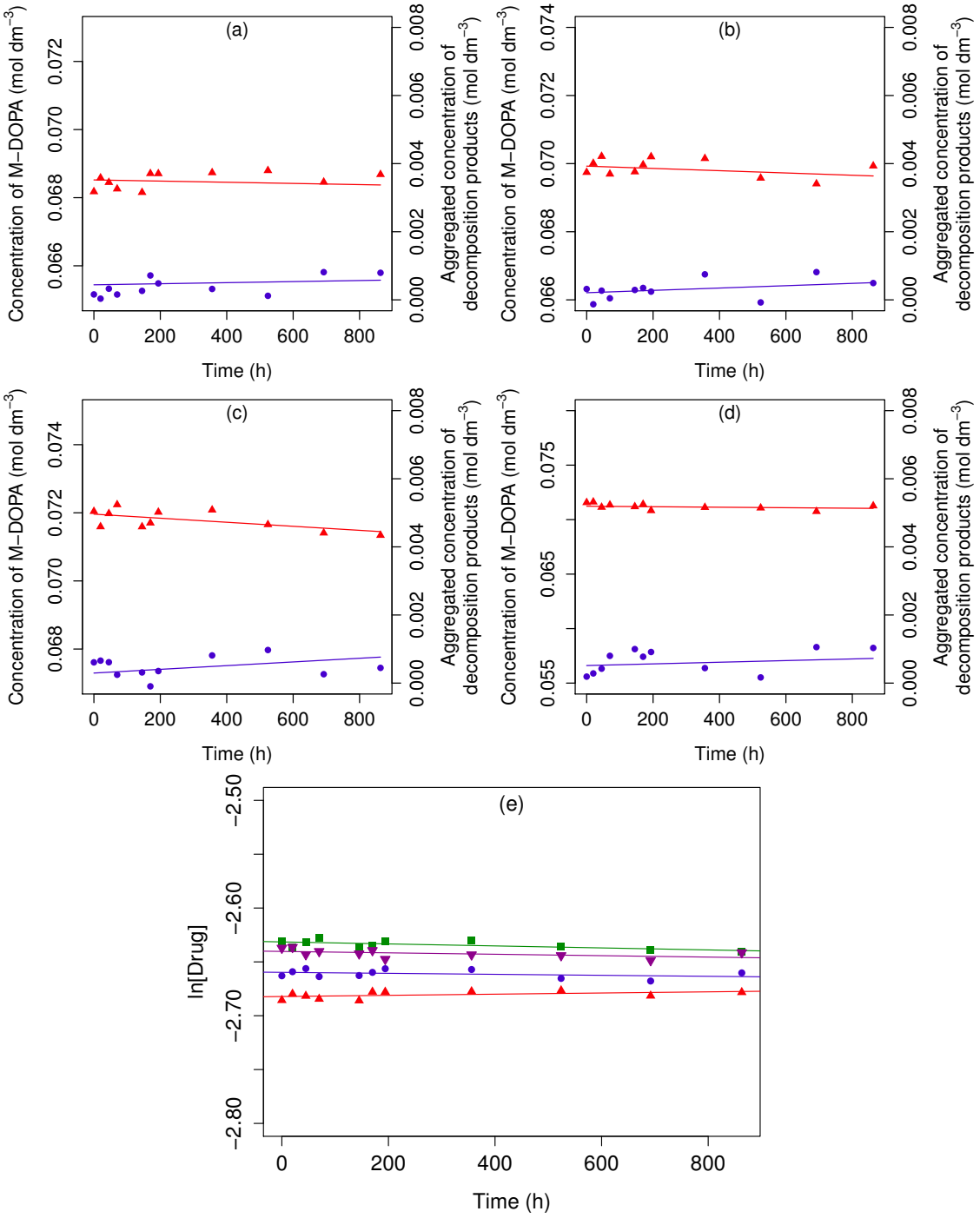


Figure B.2: The decomposition profiles of M-DOPA in dry conditions at (a) room temperature, (b) 40 °C, (c) 80 °C, and (d) under exposure to ultraviolet radiation, detailing the concentrations of M-DOPA (▲) and the aggregated concentrations of the decomposition products (●). Also (e) ln[M-DOPA] plotted as a function of time for the four experiments: room temperature (▲), 40 °C (●), 80 °C (■) and UV radiation (▼).

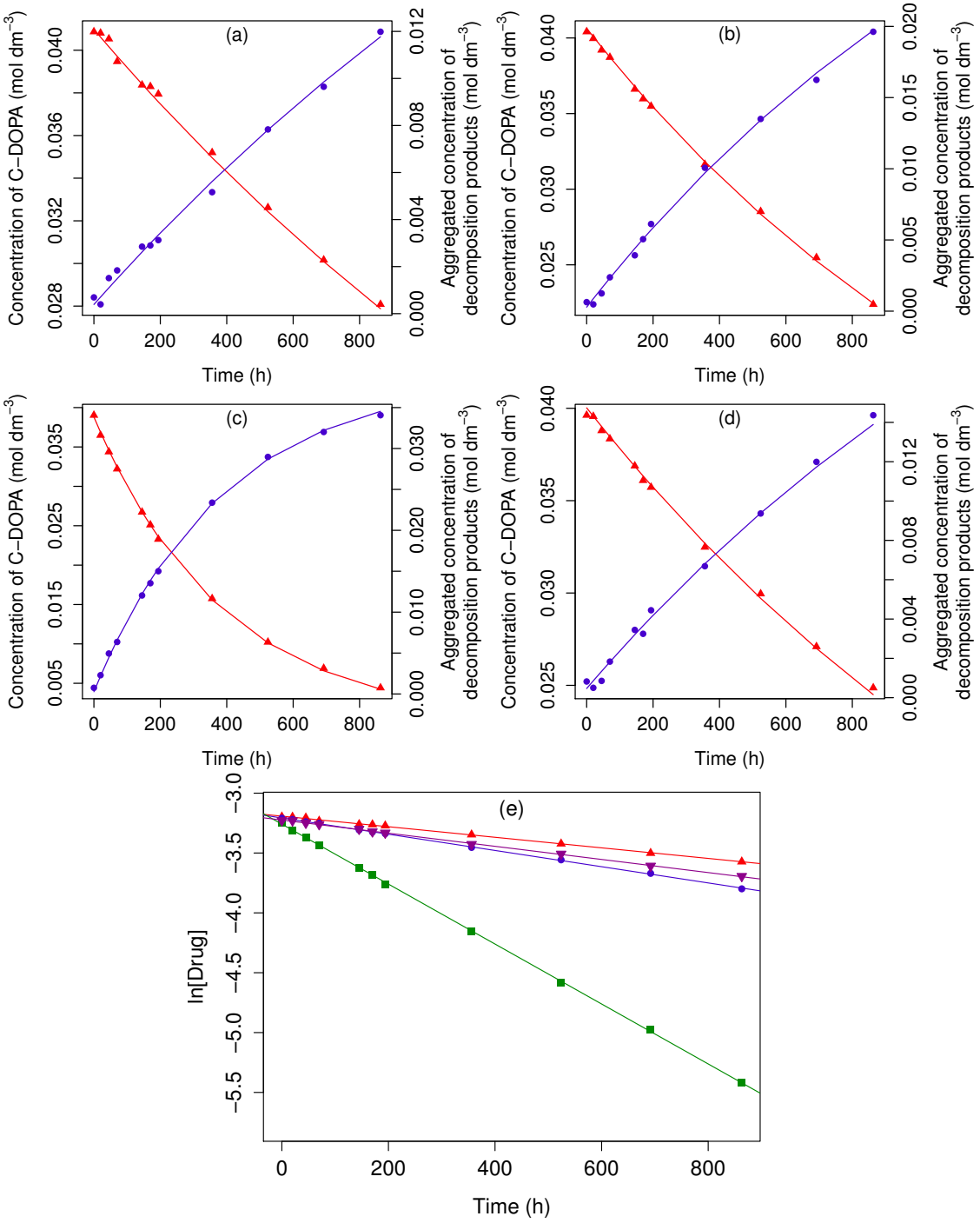


Figure B.3: The decomposition profiles of MgAl-CDOPA$_{\mathrm{IE}}$ in dry conditions at (a) room temperature, (b) 40 °C, (c) 80 °C, and (d) under exposure to ultraviolet radiation, detailing the concentrations of C-DOPA (▲) and the aggregated concentrations of the decomposition products (●). Also (e) ln[C-DOPA] plotted as a function of time for the four experiments: room temperature (▲), 40 °C (●), 80 °C (■) and UV radiation (▼).

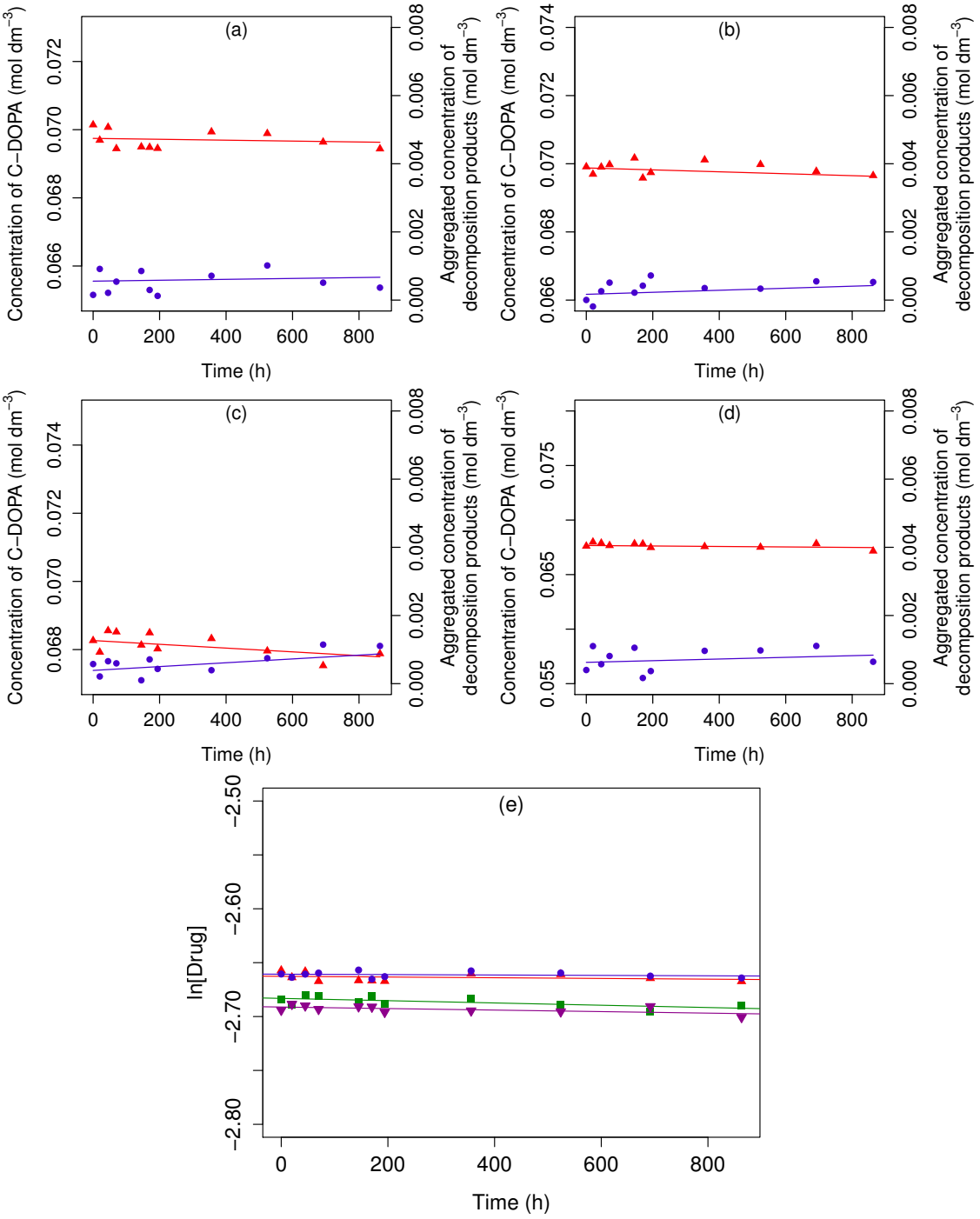


Figure B.4: The decomposition profiles of C-DOPA in dry conditions at (a) room temperature, (b) 40 °C, (c) 80 °C, and (d) under exposure to ultraviolet radiation, detailing the concentrations of C-DOPA (▲) and the aggregated concentrations of the decomposition products (●). Also (e) ln[C-DOPA] plotted as a function of time for the four experiments: room temperature (▲), 40 °C (●), 80 °C (■) and UV radiation (▼).

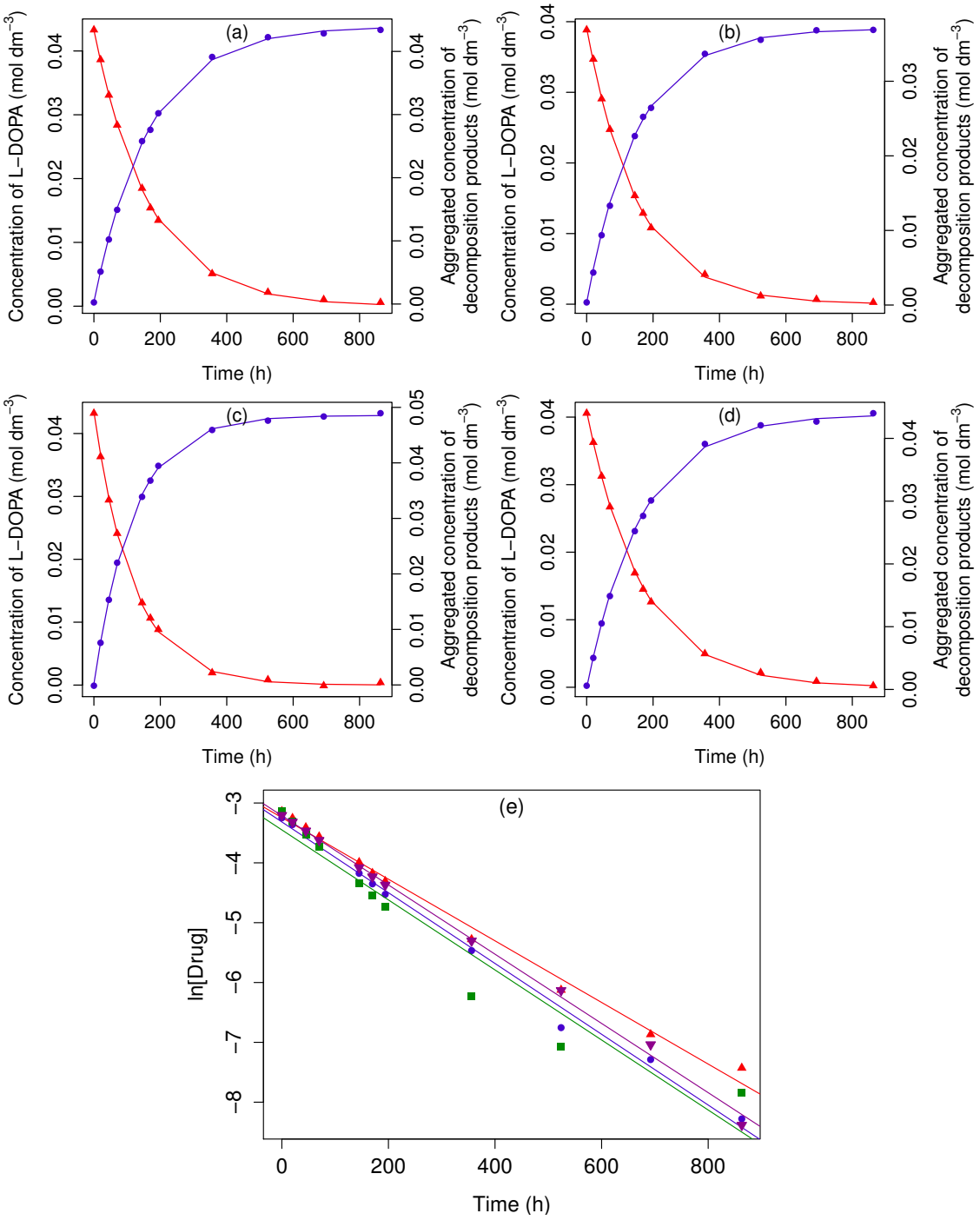


Figure B.5: The decomposition profiles of MgAl-LDOPA$_{CP}$ in dry conditions at (a) room temperature, (b) 40 °C, (c) 80 °C, and (d) under exposure to ultraviolet radiation, detailing the concentrations of L-DOPA (▲) and the aggregated concentrations of the decomposition products (●). Also (e) ln[L-DOPA] plotted as a function of time for the four experiments: room temperature (▲), 40 °C (●), 80 °C (■) and UV radiation (▼).

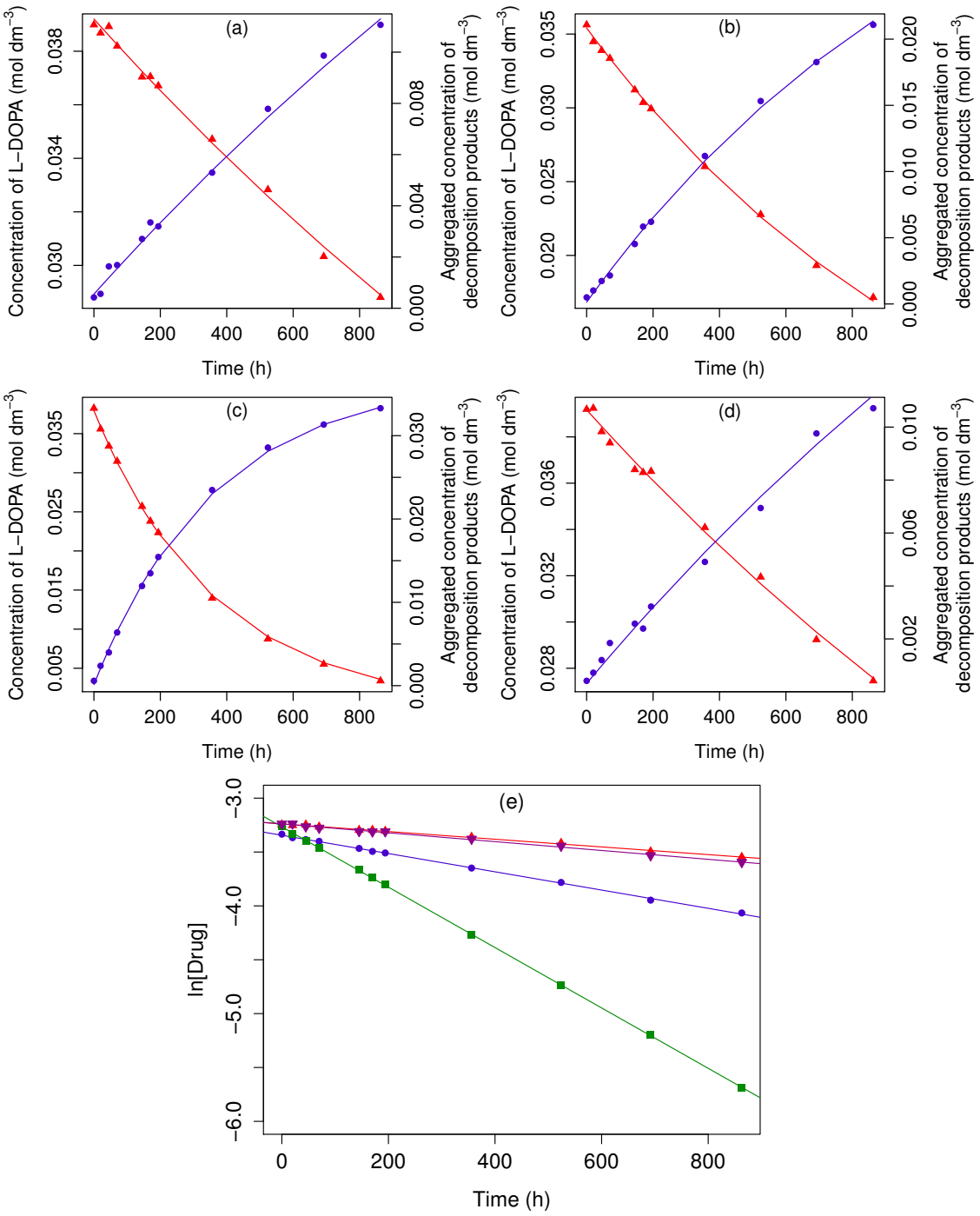


Figure B.6: The decomposition profiles of MgFeAl$_c$-LDOPA in dry conditions at (a) room temperature, (b) 40 °C, (c) 80 °C, and (d) under exposure to ultraviolet radiation, detailing the concentrations of L-DOPA (▲) and the aggregated concentrations of the decomposition products (●). Also (e) ln[L-DOPA] plotted as a function of time for the four experiments: room temperature (▲), 40 °C (●), 80 °C (■) and UV radiation (▼).

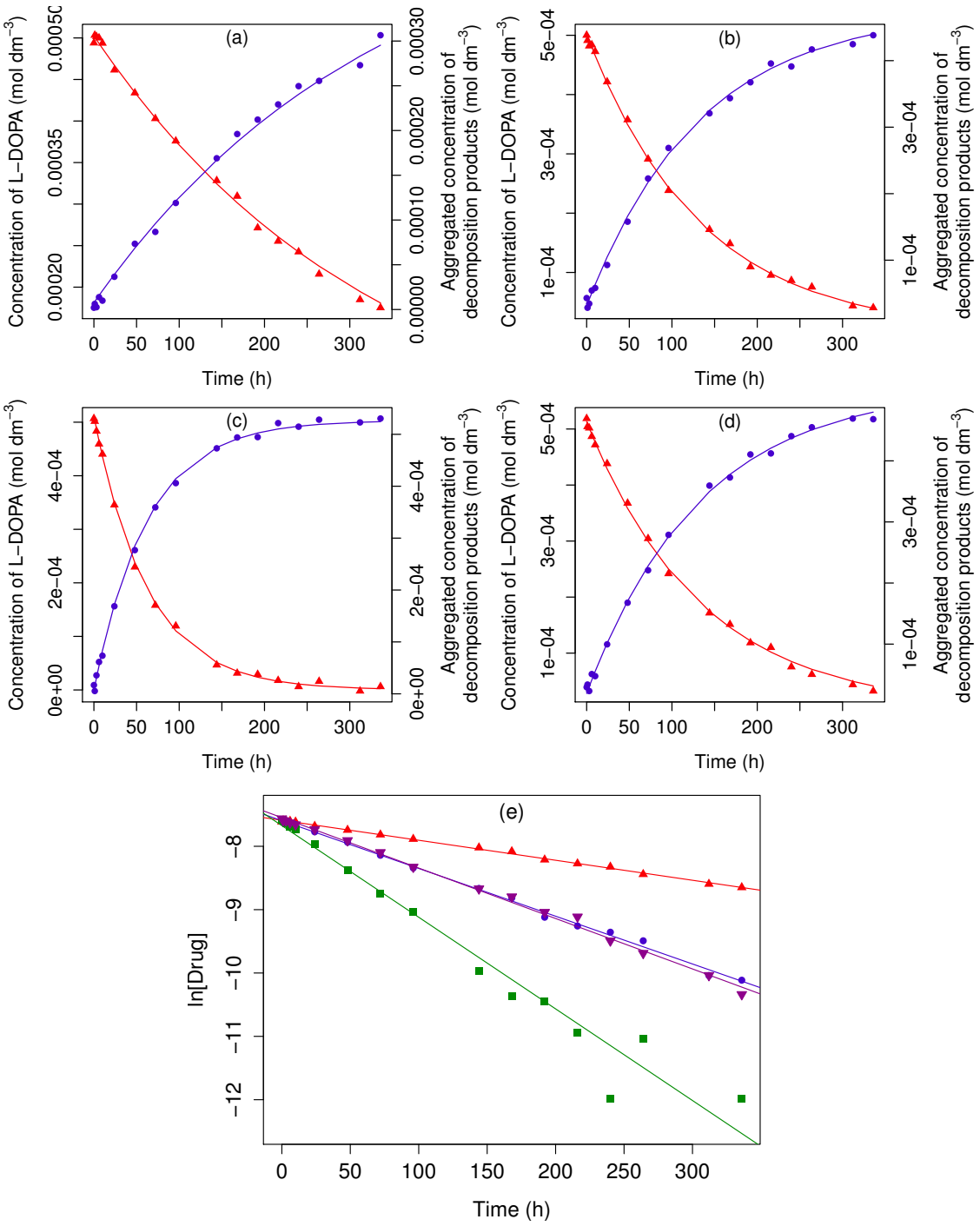


Figure B.7: The decomposition profiles of MgAl-LDOPA$_{IE}$ in aqueous suspension at (a) room temperature, (b) 40 °C, (c) 80 °C, and (d) under exposure to ultraviolet radiation, detailing the concentrations of L-DOPA (▲) and the aggregated concentrations of the decomposition products (●). Also (e) ln[L-DOPA] plotted as a function of time for the four experiments: room temperature (▲), 40 °C (●), 80 °C (■) and UV radiation (▼).

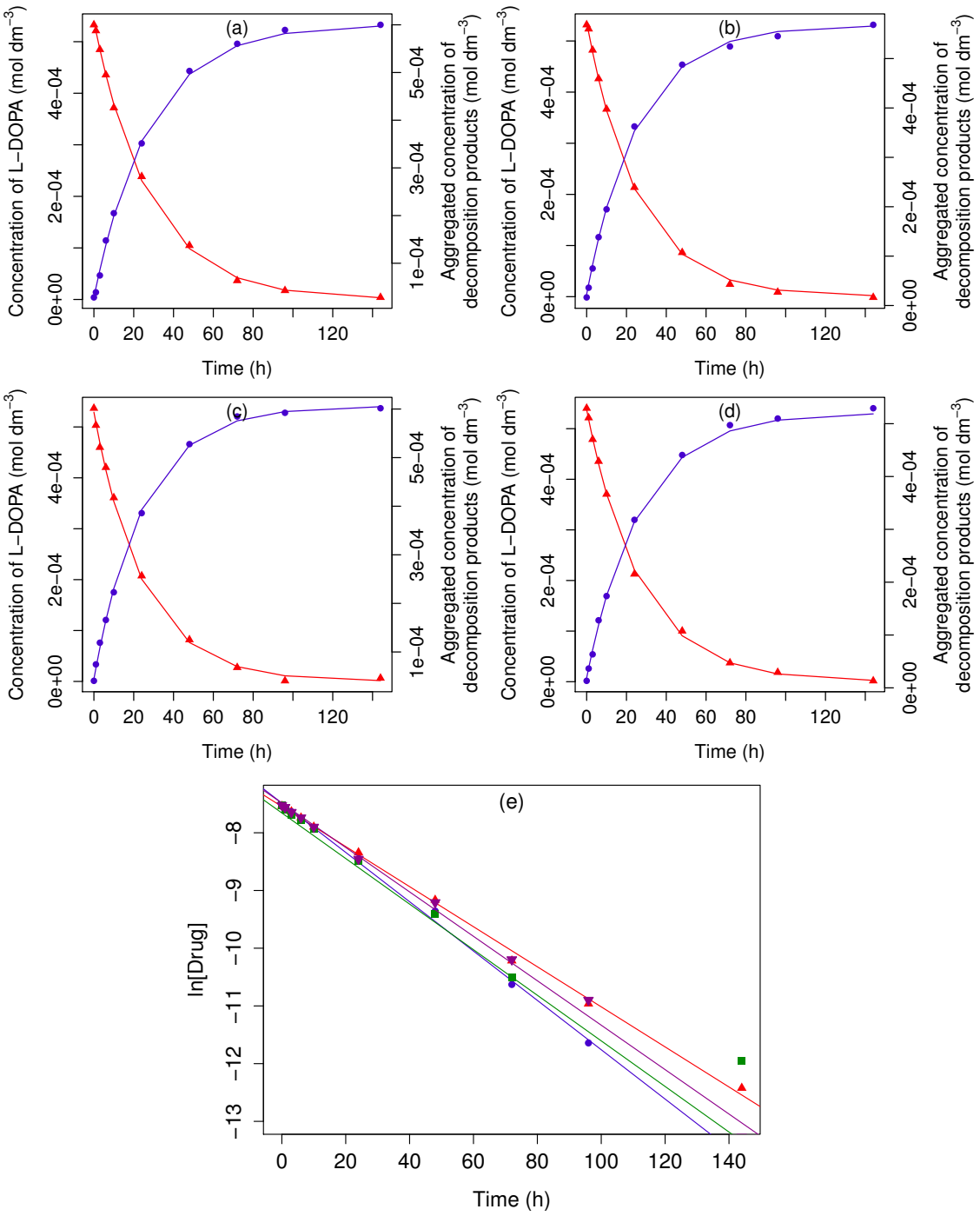


Figure B.8: The decomposition profiles of MgAl-LDOPA$_{CP}$ in aqueous suspension at (a) room temperature, (b) 40 °C, (c) 80 °C, and (d) under exposure to ultraviolet radiation, detailing the concentrations of L-DOPA (▲) and the aggregated concentrations of the decomposition products (●). Also (e) ln[L-DOPA] plotted as a function of time for the four experiments: room temperature (▲), 40 °C (●), 80 °C (■) and UV radiation (▼).

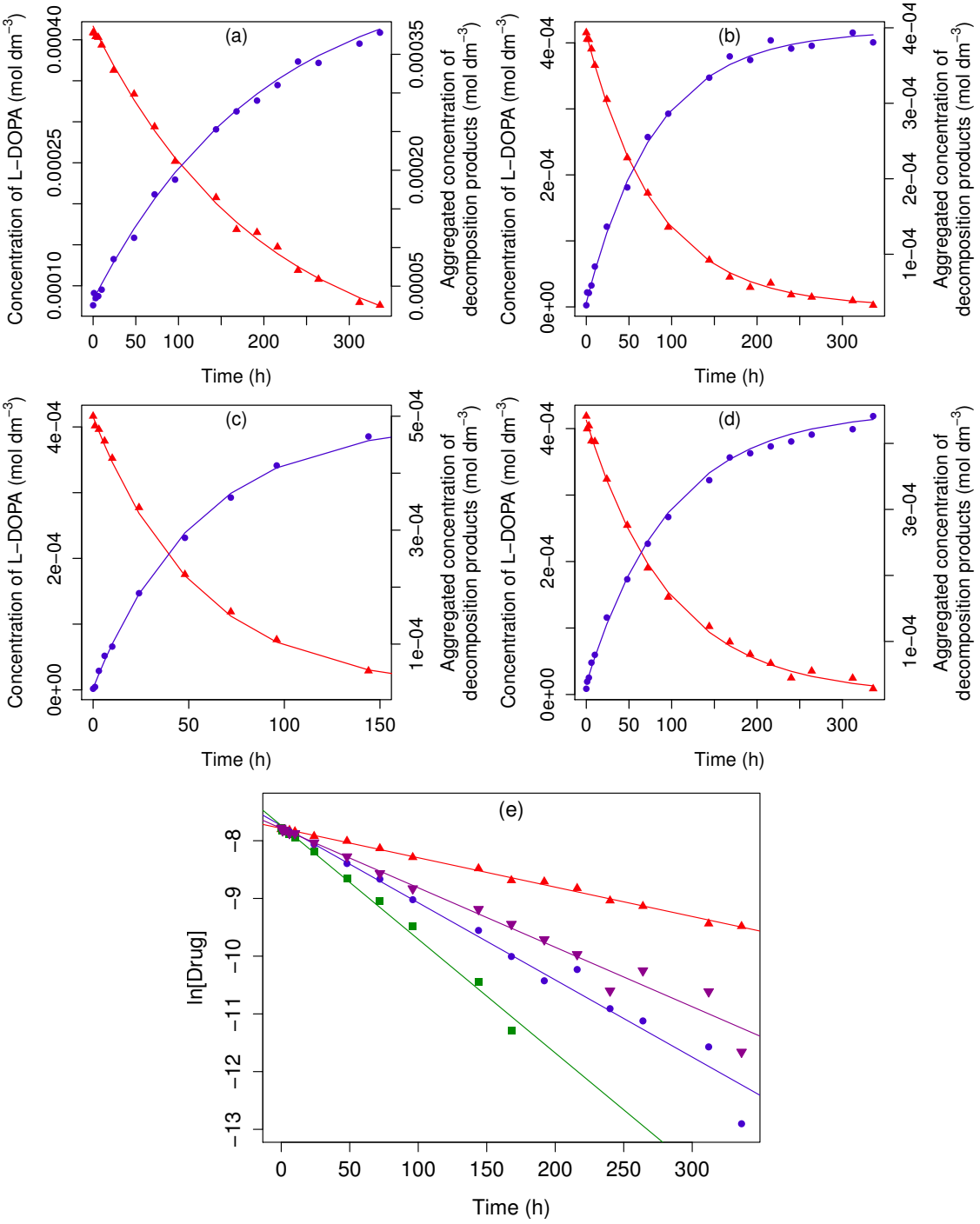


Figure B.9: The decomposition profiles of MgFeAl$_c$-LDOPA in aqueous suspension at (a) room temperature, (b) 40 °C, (c) 80 °C, and (d) under exposure to ultraviolet radiation, detailing the concentrations of L-DOPA (▲) and the aggregated concentrations of the decomposition products (●). Also (e) ln[L-DOPA] plotted as a function of time for the four experiments: room temperature (▲), 40 °C (●), 80 °C (■) and UV radiation (▼).

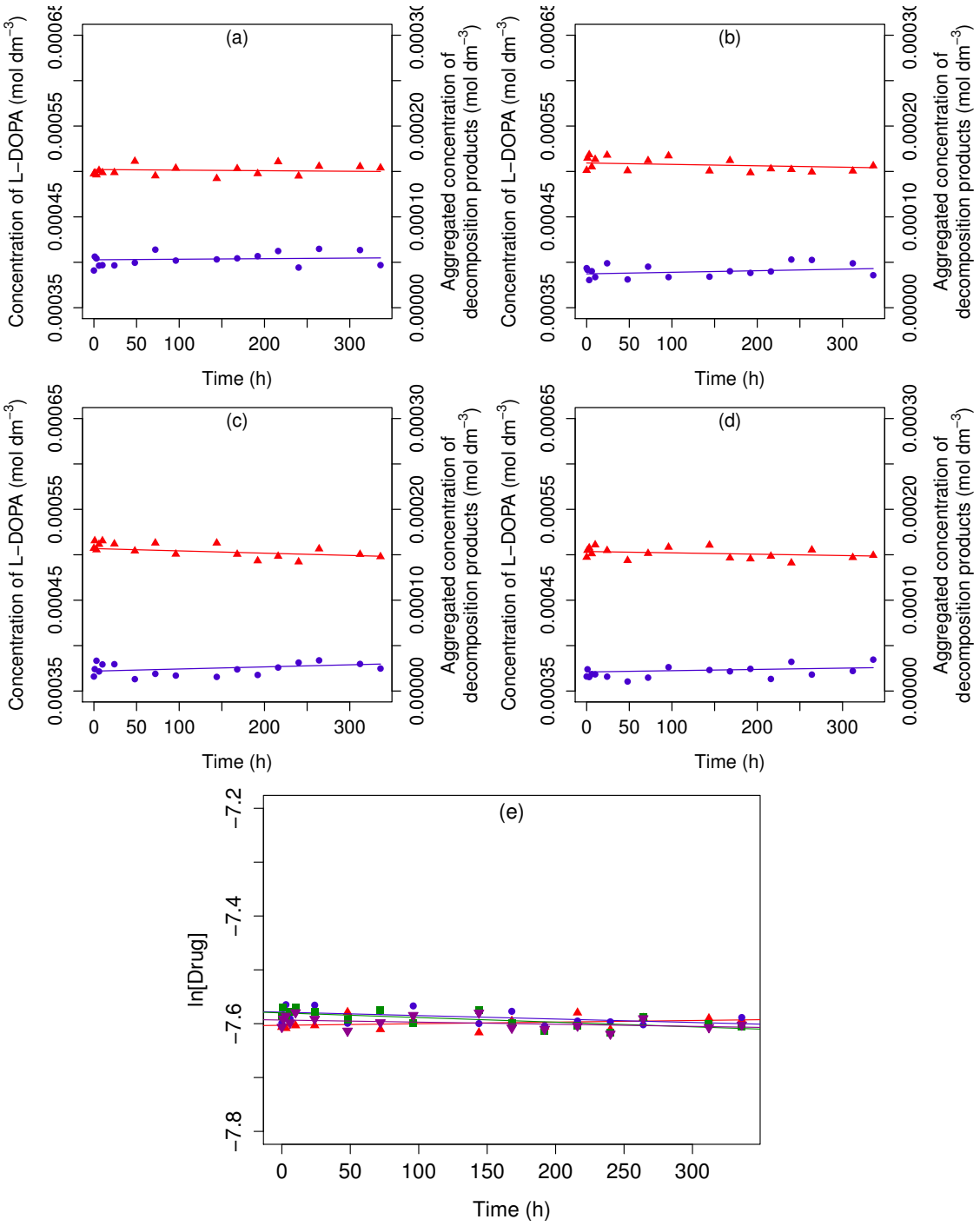


Figure B.10: The decomposition profiles of L-DOPA in solution at (a) room temperature, (b) 40 °C, (c) 80 °C, and (d) under exposure to ultraviolet radiation, detailing the concentrations of L-DOPA (▲) and the aggregated concentrations of the decomposition products (●). Also (e) ln[L-DOPA] plotted as a function of time for the four experiments: room temperature (▲), 40 °C (●), 80 °C (■) and UV radiation (▼).

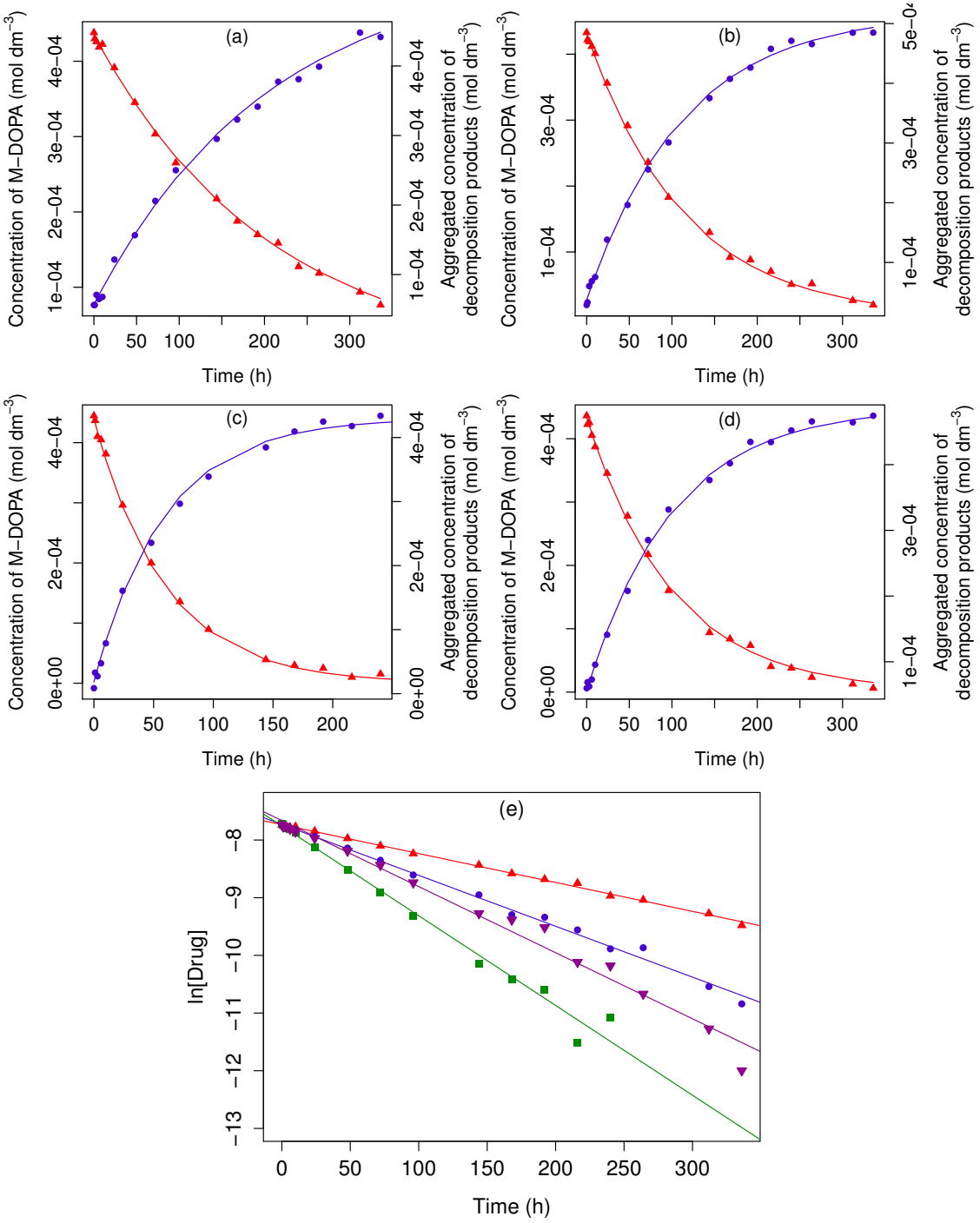


Figure B.11: The decomposition profiles of MgAl-MDOPA$_{IE}$ in aqueous suspension at (a) room temperature, (b) 40 °C, (c) 80 °C, and (d) under exposure to ultraviolet radiation, detailing the concentrations of M-DOPA (▲) and the aggregated concentrations of the decomposition products (●). Also (e) ln[M-DOPA] plotted as a function of time for the four experiments: room temperature (▲), 40 °C (●), 80 °C (■) and UV radiation (▼).

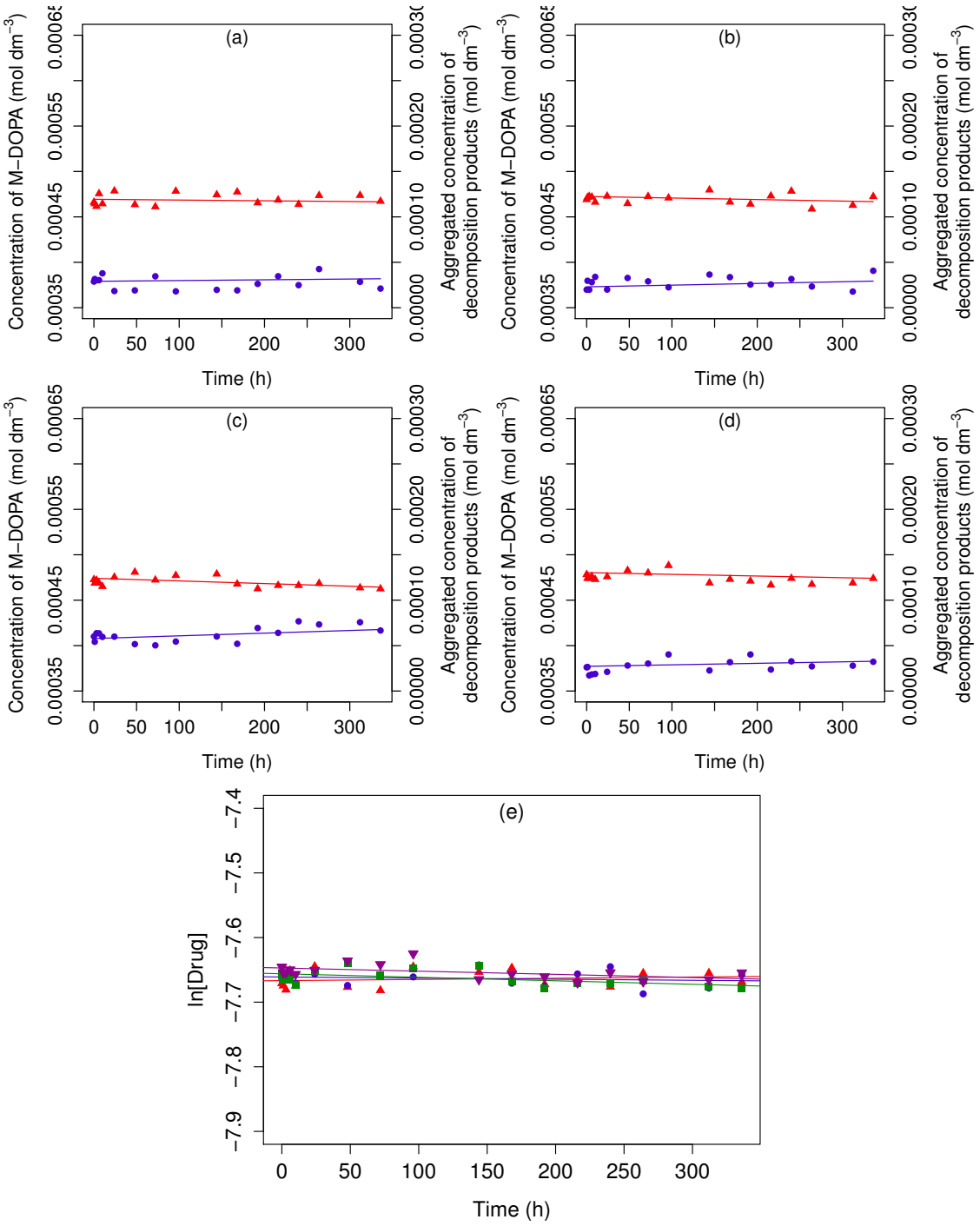


Figure B.12: The decomposition profiles of M-DOPA in solution at (a) room temperature, (b) 40 °C, (c) 80 °C, and (d) under exposure to ultraviolet radiation, detailing the concentrations of M-DOPA (▲) and the aggregated concentrations of the decomposition products (●). Also (e) ln[M-DOPA] plotted as a function of time for the four experiments: room temperature (▲), 40 °C (●), 80 °C (■) and UV radiation (▼).

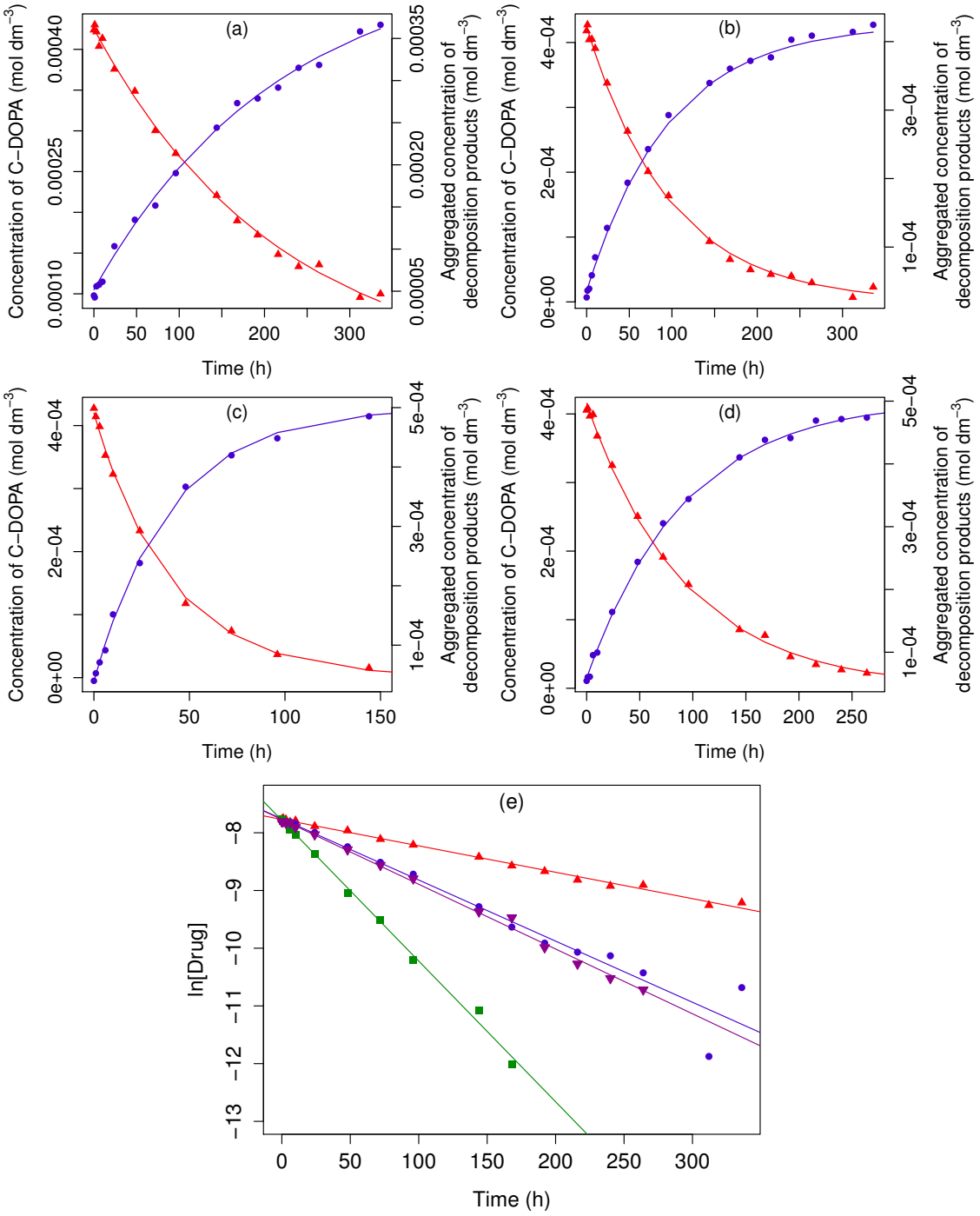


Figure B.13: The decomposition profiles of MgAl-CDOPA$_{IE}$ in aqueous suspension at (a) room temperature, (b) 40 °C, (c) 80 °C, and (d) under exposure to ultraviolet radiation, detailing the concentrations of C-DOPA (▲) and the aggregated concentrations of the decomposition products (●). Also (e) ln[C-DOPA] plotted as a function of time for the four experiments: room temperature (▲), 40 °C (●), 80 °C (■) and UV radiation (▼).

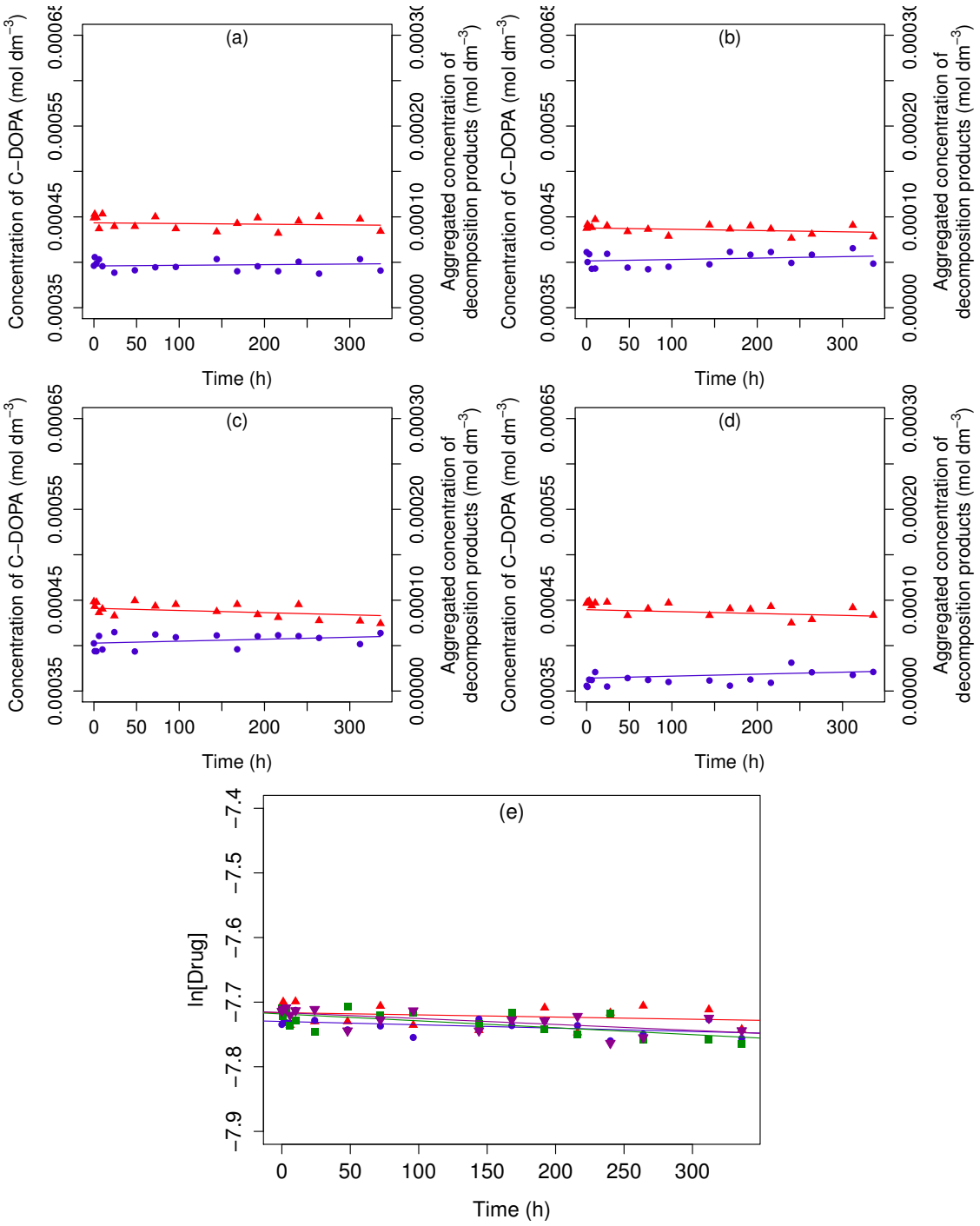


Figure B.14: The decomposition profiles of C-DOPA in solution at (a) room temperature, (b) 40 °C, (c) 80 °C, and (d) under exposure to ultraviolet radiation, detailing the concentrations of C-DOPA (▲) and the aggregated concentrations of the decomposition products (●). Also (e) ln[C-DOPA] plotted as a function of time for the four experiments: room temperature (▲), 40 °C (●), 80 °C (■) and UV radiation (▼).

C Supporting data for Chapter 4

C.1 Lattice parameters and interlayer distances for all nanohybrids containing β-cyclodextrins and β-cyclodextrin–drug complexes

Table C.1: The lattice parameters and interlayer distances for all LDH nanohybrids containing β-cyclodextrins and β-cyclodextrin–drug inclusion complexes of the form MgAl-⟨Cyclodextrin⟩⟨Drug⟩, calculated from the (110) and (003) Bragg reflections observed in their powder XRD patterns.

Cyclodextrin	Drug	Cell parameters (Å)		Interlayer
		a	c	distance (Å)
β-CMCD[P1]	-	3.041	74.52	20.04
	CIN	3.040	75.52	20.37
	TST	3.040	75.93	20.51
β-CMCD[P2]	-	3.042	70.85	18.82
	CIN	3.035	73.16	19.59
	TST	3.037	73.74	19.78
β-CMCD[P3]	-	3.042	69.92	18.51
	CIN	3.036	72.77	19.46
	TST	3.037	73.44	19.68
	CPZ	3.036	73.89	19.83
	PMZ	3.034	74.54	20.05
	IMI	3.033	73.54	19.71
	AMI	3.036	74.84	20.15
β-CMCD[P4]	-	3.042	68.41	18.00
	CIN	3.036	71.57	19.06
	TST	3.035	73.24	19.61
	CPZ	3.041	73.49	19.70
β-CMCD[P5]	-	3.039	66.96	17.52
	CIN	3.035	70.50	18.70
	TST	3.034	71.30	18.97
	CPZ	3.036	73.23	19.61
β-CMCD[P6]	-	3.036	65.31	16.97
	CIN	3.031	69.64	18.41
	TST	3.035	71.34	18.98
	CPZ	3.036	72.25	19.28

Continued on following page ...

... Continued from previous page.

Cyclodextrin	Drug	Cell parameters (Å)		Interlayer
		a	c	distance (Å)
β-CMCD[P6]	PMZ	3.034	71.88	19.16
	IMI	3.039	72.49	19.36
	AMI	3.038	73.31	19.64
β-CMCD[P7]	-	3.031	63.88	16.49
	CIN	3.034	67.16	17.59
	TST	3.039	69.16	18.25
	CPZ	3.036	70.54	18.71
β-CMCD[P8]	-	3.035	62.23	15.94
	CIN	3.037	66.87	17.49
	TST	3.039	68.37	17.99
	CPZ	3.034	70.74	18.78
β-CMCD[P9]	-	3.035	61.99	15.86
	CIN	3.030	66.20	17.27
	TST	3.034	66.42	17.34
	CPZ	3.037	70.26	18.62
	PMZ	3.035	70.51	18.70
	IMI	3.038	69.58	18.39
	AMI	3.032	71.27	18.96
β-CMCD[C2]	-	3.035	64.77	16.79
	CIN	3.034	67.24	17.61
	TST	3.031	71.21	18.94
	CPZ	3.038	72.91	19.50
	PMZ	3.030	73.61	19.74
	IMI	3.036	71.70	19.10
	AMI	3.032	72.66	19.42
β-SBECD	-	3.029	57.08	14.23
	CIN	3.031	67.96	17.85
	TST	3.037	65.41	17.00
	CPZ	3.032	69.25	18.28
	PMZ	3.036	67.70	17.77
	IMI	3.037	68.80	18.13
	AMI	3.029	71.17	18.92

C.2 Correlation coefficients of modelled drug release kinetics of β-cyclodextrin–drug containing nanohybrids

Table C.2: Evaluation of different kinetic models of drug release from LDH nanohybrids containing β-cyclodextrin–drug inclusion complexes of the form MgAl-⟨Cyclodextrin⟩⟨Drug⟩ using correlation coefficients, r^2. Highlighted figure indicates closest fit for each release profile.

Cyclodextrin	Drug	Model correlation coefficient, r^2				
		Avrami–Erofe'ev	Elovich	Simple first order	Modified Freundlich	Parabolic diffusion
release in pH 2.0 *buffer*						
β-CMCD[P1]	CIN	0.640	0.629	0.271	0.619	0.792
	TST	0.667	0.606	0.210	0.632	0.708
β-CMCD[P5]	CIN	0.714	0.575	0.170	0.658	0.684
	TST	0.805	0.792	0.283	0.794	0.863
	CPZ	0.601	0.537	0.138	0.615	0.734
β-CMCD[P9]	CIN	0.780	0.633	0.192	0.877	0.695
	TST	0.816	0.720	0.223	0.881	0.734
	CPZ	0.590	0.555	0.195	0.602	0.886
β-CMCD[C2]	CIN	0.703	0.707	0.264	0.683	0.842
	TST	0.870	0.791	0.256	0.895	0.799
	CPZ	0.569	0.480	0.110	0.646	0.698
β-SBECD	CIN	0.660	0.598	0.168	0.717	0.763
	TST	0.558	0.503	0.144	0.476	0.665
	CPZ	0.672	0.569	0.163	0.733	0.697
release in pH 4.0 *buffer*						
β-CMCD[P1]	CIN	0.731	0.677	0.298	0.728	0.797
	TST	0.432	0.427	0.103	0.399	0.665
β-CMCD[P5]	CIN	0.784	0.674	0.216	0.843	0.770
	TST	0.779	0.701	0.277	0.792	0.818
	CPZ	0.563	0.476	0.137	0.643	0.669
β-CMCD[P9]	CIN	0.916	0.887	0.464	0.905	0.830
	TST	0.785	0.672	0.216	0.855	0.716
	CPZ	0.859	0.758	0.240	0.886	0.781
β-CMCD[C2]	CIN	0.497	0.483	0.159	0.498	0.777
	TST	0.580	0.476	0.135	0.656	0.674
	CPZ	0.535	0.433	0.145	0.603	0.624
β-CMCD[S]	CIN	0.788	0.831	0.400	0.721	0.846
	TST	0.870	0.776	0.325	0.925	0.761
	CPZ	0.819	0.759	0.236	0.885	0.799

Continued on following page . . .

. . . Continued from previous page.

Cyclodextrin	Drug	Model correlation coefficient, r^2				
		Avrami–Erofe'ev	Elovich	Simple first order	Modified Freundlich	Parabolic diffusion
		release in pH 7.0 *buffer*				
β-CMCD[P1]	CIN	0.518	0.519	0.137	0.496	0.778
	TST	0.515	0.438	0.108	0.618	0.677
β-CMCD[P2]	CIN	0.713	0.618	0.154	0.868	0.717
	TST	0.750	0.659	0.181	0.831	0.747
β-CMCD[P3]	CIN	0.807	0.720	0.221	0.878	0.747
	TST	0.835	0.783	0.219	0.902	0.798
	CPZ	0.837	0.816	0.297	0.830	0.835
	PMZ	0.736	0.647	0.178	0.840	0.730
	IMI	0.716	0.626	0.166	0.821	0.709
	AMI	0.787	0.708	0.210	0.852	0.804
β-CMCD[P4]	CIN	0.815	0.784	0.216	0.926	0.833
	TST	0.850	0.812	0.241	0.963	0.822
	CPZ	0.885	0.818	0.266	0.965	0.799
β-CMCD[P5]	CIN	0.886	0.868	0.275	0.959	0.851
	TST	0.903	0.881	0.286	0.951	0.841
	CPZ	0.924	0.895	0.337	0.929	0.854
β-CMCD[P6]	CIN	0.933	0.920	0.336	0.949	0.855
	TST	0.968	0.950	0.404	0.917	0.871
	CPZ	0.909	0.883	0.329	0.944	0.882
	PMZ	0.943	0.908	0.332	0.946	0.860
	IMI	0.962	0.936	0.382	0.959	0.869
	AMI	0.928	0.898	0.343	0.944	0.884
β-CMCD[P7]	CIN	0.964	0.963	0.420	0.961	0.884
	TST	0.968	0.966	0.420	0.964	0.889
	CPZ	0.944	0.934	0.363	0.985	0.867
β-CMCD[P8]	CIN	0.991	0.990	0.546	0.901	0.896
	TST	0.967	0.984	0.513	0.813	0.874
	CPZ	0.972	0.974	0.412	0.935	0.873
β-CMCD[P9]	CIN	0.978	0.987	0.531	0.906	0.881
	TST	0.977	0.983	0.571	0.862	0.900
	CPZ	0.986	0.986	0.488	0.940	0.897
	PMZ	0.986	0.989	0.499	0.905	0.892
	IMI	0.986	0.985	0.535	0.918	0.897
	AMI	0.975	0.983	0.460	0.922	0.891
β-CMCD[C2]	CIN	0.946	0.924	0.379	0.953	0.897
	TST	0.948	0.936	0.352	0.988	0.874
	CPZ	0.920	0.897	0.324	0.923	0.854

Continued on following page . . .

. . . Continued from previous page.

Cyclodextrin	Drug	Model correlation coefficient, r^2				
		Avrami–Erofe'ev	Elovich	Simple first order	Modified Freundlich	Parabolic diffusion
release in pH 7.0 *buffer*						
β-CMCD[C2]	PMZ	0.841	0.808	0.264	0.924	0.830
	IMI	0.940	0.893	0.331	0.951	0.857
	AMI	0.911	0.875	0.334	0.946	0.872
β-SBECD	CIN	0.983	0.975	0.626	0.881	0.899
	TST	0.973	0.971	0.588	0.868	0.891
	CPZ	0.971	0.968	0.596	0.861	0.888
	PMZ	0.989	0.987	0.572	0.911	0.893
	IMI	0.990	0.988	0.560	0.902	0.896
	AMI	0.978	0.971	0.639	0.865	0.907

C.3 Rate constants for drug release from β-cyclodextrin–drug containing nanohybrids

Table C.3: Rate constants, k_F, for drug release from β-cyclodextrin–drug containing nanohybrids in acid buffers, calculated from the modified Freundlich model.

Drug	Buffer	Release rate constant, $k_F \times 10^{-3}$ (s^{-1})				
	pH	CMCD[P1]	CMCD[P5]	CMCD[P9]	CMCD[C2]	SBECD
CIN	2.0	10.8	10.5	4.55	7.52	5.46
	4.0	6.33	4.26	5.83	12.0	5.23
TST	2.0	5.95	6.13	3.95	2.65	10.9
	4.0	12.3	5.61	3.94	7.89	4.43
CPZ	2.0	-	8.47	8.94	5.23	6.05
	4.0	-	7.10	3.29	8.89	3.19

Table C.4: Rate constants, k_F, for drug release from β-cyclodextrin–drug containing nanohybrids in pH 7.0 buffer, calculated from the modified Freundlich model.

Drug	Release rate constant, $k_F \times 10^{-3}$ (s^{-1})										
	[P1]	[P2]	[P3]	[P4]	[P5]	[P6]	[P7]	[P8]	[P9]	[C2]	SBECD
CIN	7.78	4.17	2.44	2.28	1.77	1.47	1.47	1.26	1.30	1.48	1.27
TST	6.80	4.12	2.75	2.18	1.92	1.40	1.42	1.18	1.27	1.57	1.25
CPZ	-	-	4.09	2.56	2.26	1.88	1.66	1.33	1.30	2.25	1.24
PMZ	-	-	4.23	-	-	1.61	-	-	1.35	2.39	1.30
IMI	-	-	4.06	-	-	1.63	-	-	1.34	1.80	1.22
AMI	-	-	3.76	-	-	1.78	-	-	1.30	2.08	1.27

D Supporting data for Chapter 5

D.1 FTIR spectra of composites

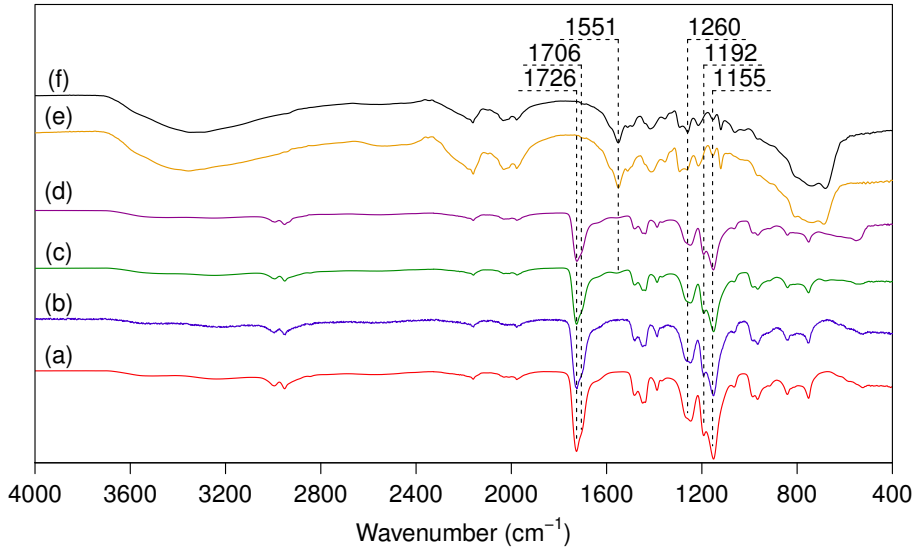


Figure D.1: The FTIR spectra of (a) Eud-S, (b) Eud-S{L-DOPA}, (c) Eud-S{MgAl-LDOPA}, (d) Eud-S{MgFeAl-LDOPA}, (e) MgAl-LDOPA and (f) MgFeAl-LDOPA.

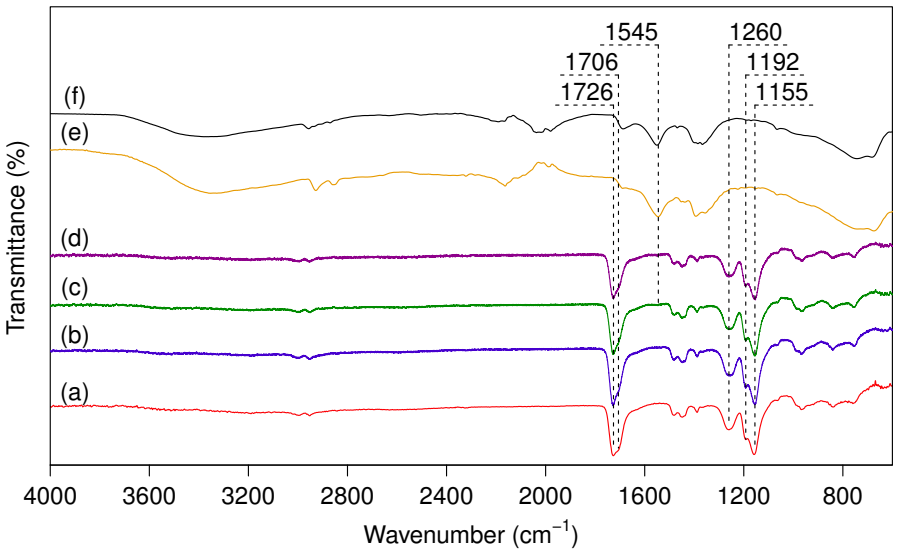


Figure D.2: The FTIR spectra of (a) Eud-L, (b) Eud-L{GBP}, (c) Eud-L{MgAl-GBP}, (d) Eud-L{MgAl-PGB}, (e) MgAl-GBP and (f) MgAl-PGB.

D.2 Correlation coefficients of kinetic models fitted to drug release profiles of composites

Table D.1: Evaluation of different kinetic models of drug release from composites containing GBP, PGB and L-DOPA using correlation coefficients, r^2. Highlighted figure indicates closest fit for each release profile.

Sample	Buffer pH	Model correlation coefficient, r^2				
		Avrami–Erofe'ev	Elovich	Simple first order	Modified Freundlich	Parabolic diffusion
Eud-L{MgAl-GBP}	2.0	0.625	0.733	0.259	0.735	0.911
	4.0	0.934	0.950	0.480	0.949	0.915
	7.0	0.840	0.865	0.716	0.501	0.914
Eud-S{MgAl-GBP}	2.0	0.327	0.311	0.144	0.310	0.911
	4.0	0.782	0.852	0.487	0.851	0.920
	7.0	0.870	0.805	0.814	0.628	0.907
Eud-L{MgAl-PGB}	2.0	0.511	0.668	0.198	0.671	0.910
	4.0	0.958	0.970	0.534	0.967	0.913
	7.0	0.916	0.930	0.652	0.541	0.892
Eud-S{MgAl-PGB}	2.0	0.294	0.284	0.302	0.283	0.915
	4.0	0.803	0.820	0.612	0.818	0.920
	7.0	0.958	0.840	0.719	0.691	0.904
Alg{MgAl-LDOPA}	2.0	0.895	0.905	0.254	0.902	0.858
	4.0	0.940	0.948	0.306	0.913	0.907
	7.0	0.935	0.962	0.327	0.934	0.904
Alg{MgFeAl-LDOPA}	2.0	0.949	0.945	0.339	0.945	0.893
	4.0	0.939	0.942	0.334	0.921	0.901
	7.0	0.981	0.972	0.413	0.894	0.902
Eud-L{MgAl-LDOPA}	2.0	0.824	0.837	0.220	0.883	0.870
	4.0	0.911	0.927	0.284	0.982	0.868
	7.0	0.962	0.965	0.430	0.946	0.908
Eud-L{MgFeAl-LDOPA}	2.0	0.651	0.649	0.145	0.696	0.795
	4.0	0.921	0.940	0.308	0.975	0.864
	7.0	0.958	0.990	0.399	0.921	0.887
Eud-S{MgAl-LDOPA}	2.0	0.872	0.879	0.251	0.950	0.878
	4.0	0.982	0.978	0.536	0.918	0.885
	7.0	0.997	0.977	0.532	0.839	0.896
Eud-S{MgFeAl-LDOPA}	2.0	0.852	0.848	0.232	0.975	0.813
	4.0	0.979	0.970	0.587	0.878	0.902
	7.0	0.984	0.983	0.513	0.859	0.884

D.3 Reaction parameters for drug release from composites, obtained from kinetic models

Table D.2: Values of the rate constants, k_r, and reaction exponents, n, for the release of GBP and PGB in pH 4 and pH 7 buffers from Eud composites, as determined by the Avrami–Erofe'ev model.

Sample	Buffer pH	Rate constant, $k_r \times 10^{-4}$ (s^{-1})	Reaction exponent, n
Eud-L{MgAl-GBP}	4.0	0.344	0.151
	7.0	1.955	0.244
Eud-S{MgAl-GBP}	4.0	0.182	0.338
	7.0	1.727	0.209
Eud-L{MgAl-PGB}	4.0	0.415	0.110
	7.0	2.312	0.109
Eud-S{MgAl-PGB}	4.0	0.305	0.214
	7.0	1.013	0.110

Table D.3: Values of the rate constants, k_{EA} and k_F, and reaction exponents, n, for the release of L-DOPA from Alg and Eud–LDH composites in buffers of varying pH, as determined by the Avrami–Erofe'ev and modified Freundlich models.

Sample	Buffer	Reaction	Rate constants, $\times 10^{-3}$ (s^{-1})	
	pH	exponent, n	k_{EA}	k_F
Alg{MgAl-LDOPA}	2.0	0.300	0.427	0.708
	4.0	0.318	0.156	1.801
	7.0	0.271	0.105	1.591
Alg{MgFeAl-LDOPA}	2.0	0.311	0.769	1.288
	4.0	0.227	0.107	1.764
	7.0	0.106	0.093	1.500
Eud-L{MgAl-LDOPA}	2.0	0.312	5.093	0.014
	4.0	0.124	2.554	0.074
	7.0	0.148	1.850	0.135
Eud-L{MgFeAl-LDOPA}	2.0	0.364	3.579	0.040
	4.0	0.187	3.362	0.045
	7.0	0.150	2.332	0.103
Eud-S{MgAl-LDOPA}	2.0	0.180	3.543	0.036
	4.0	0.167	2.327	0.083
	7.0	0.133	1.833	0.152
Eud-S{MgFeAl-LDOPA}	2.0	0.439	4.759	0.013
	4.0	0.184	3.046	0.054
	7.0	0.166	1.984	0.150

D.4 Decomposition plots of composites containing L-DOPA

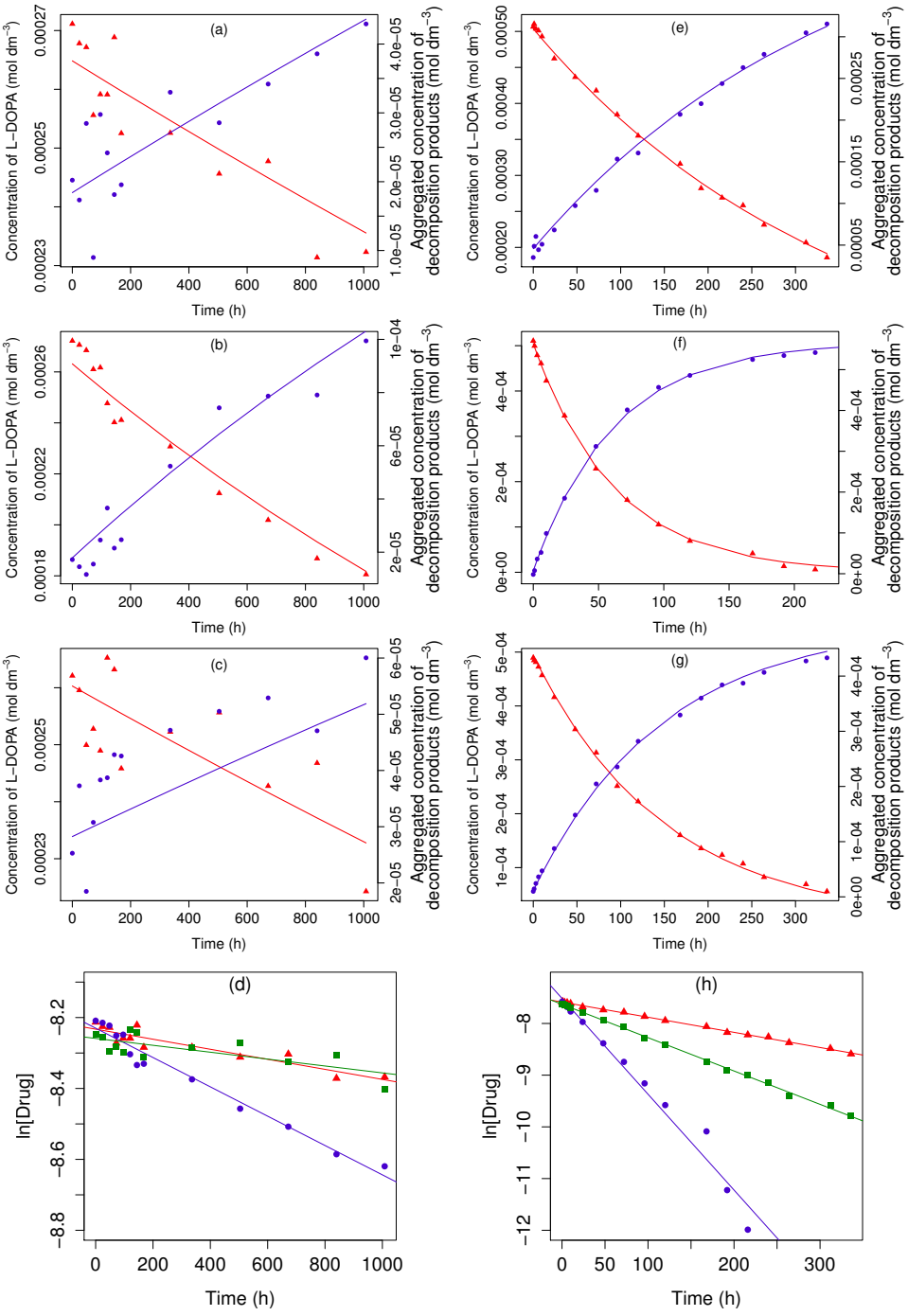


Figure D.3: The decomposition profiles of Alg{MgAl-LDOPA} in dry conditions at (a) room temperature, (b) 80 °C, and (c) under exposure to UV radiation, and in aqueous suspension at (e) room temperature, (f) 80 °C, and (g) under exposure to UV radiation, detailing the concentrations of L-DOPA (▲) and the aggregated concentrations of the decomposition products (●). Also (d) (dry) and (h) (wet) ln[L-DOPA] plotted as a function of time for the six experiments: room temperature (▲), 80 °C (●), and UV radiation (■).

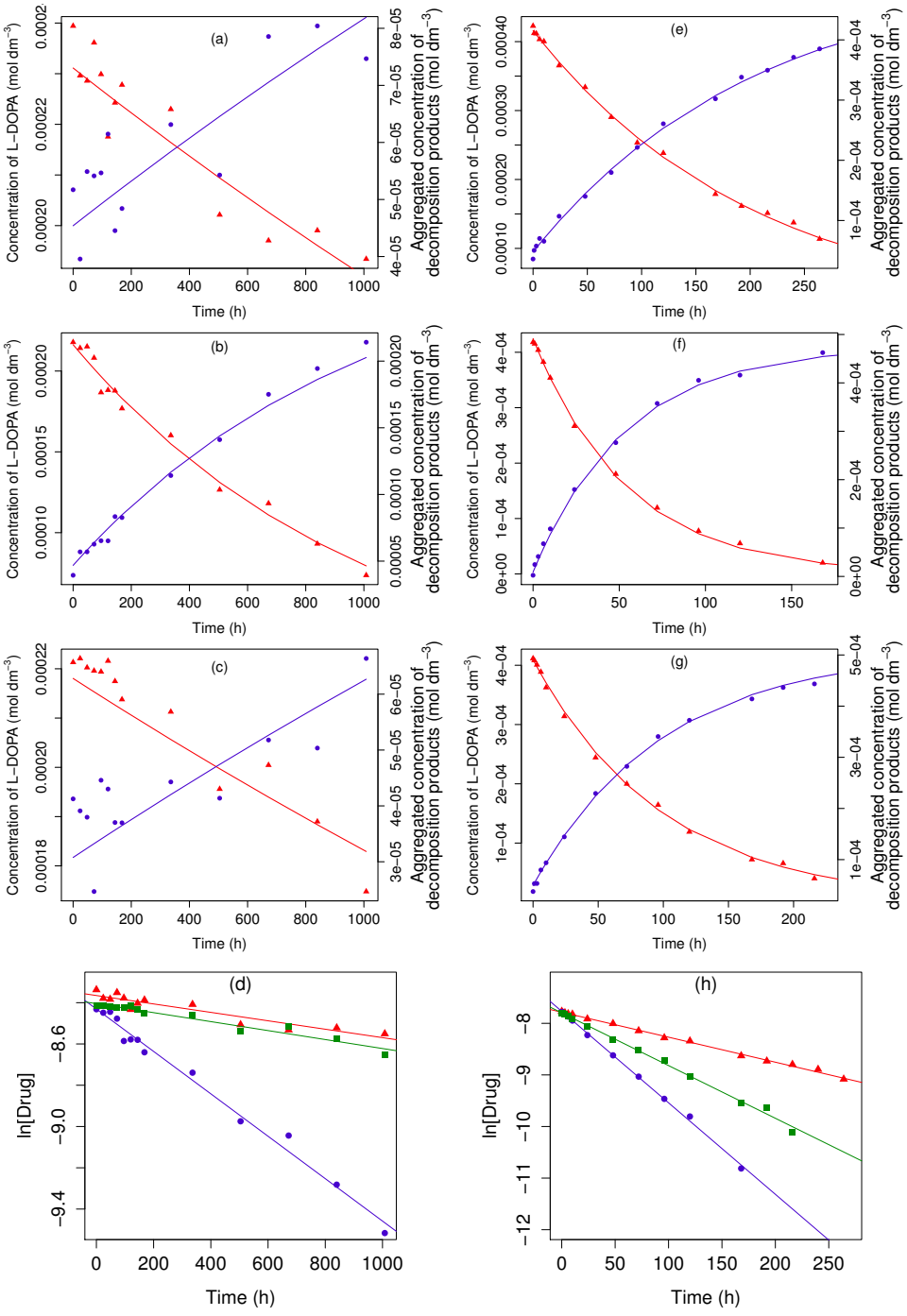


Figure D.4: The decomposition profiles of Alg{MgFeAl-LDOPA} in dry conditions at (a) room temperature, (b) 80 °C, and (c) under exposure to UV radiation, and in aqueous suspension at (e) room temperature, (f) 80 °C, and (g) under exposure to UV radiation, detailing the concentrations of L-DOPA (▲) and the aggregated concentrations of the decomposition products (●). Also (d) (dry) and (h) (wet) ln[L-DOPA] plotted as a function of time for the six experiments: room temperature (▲), 80 °C (●), and UV radiation (■).

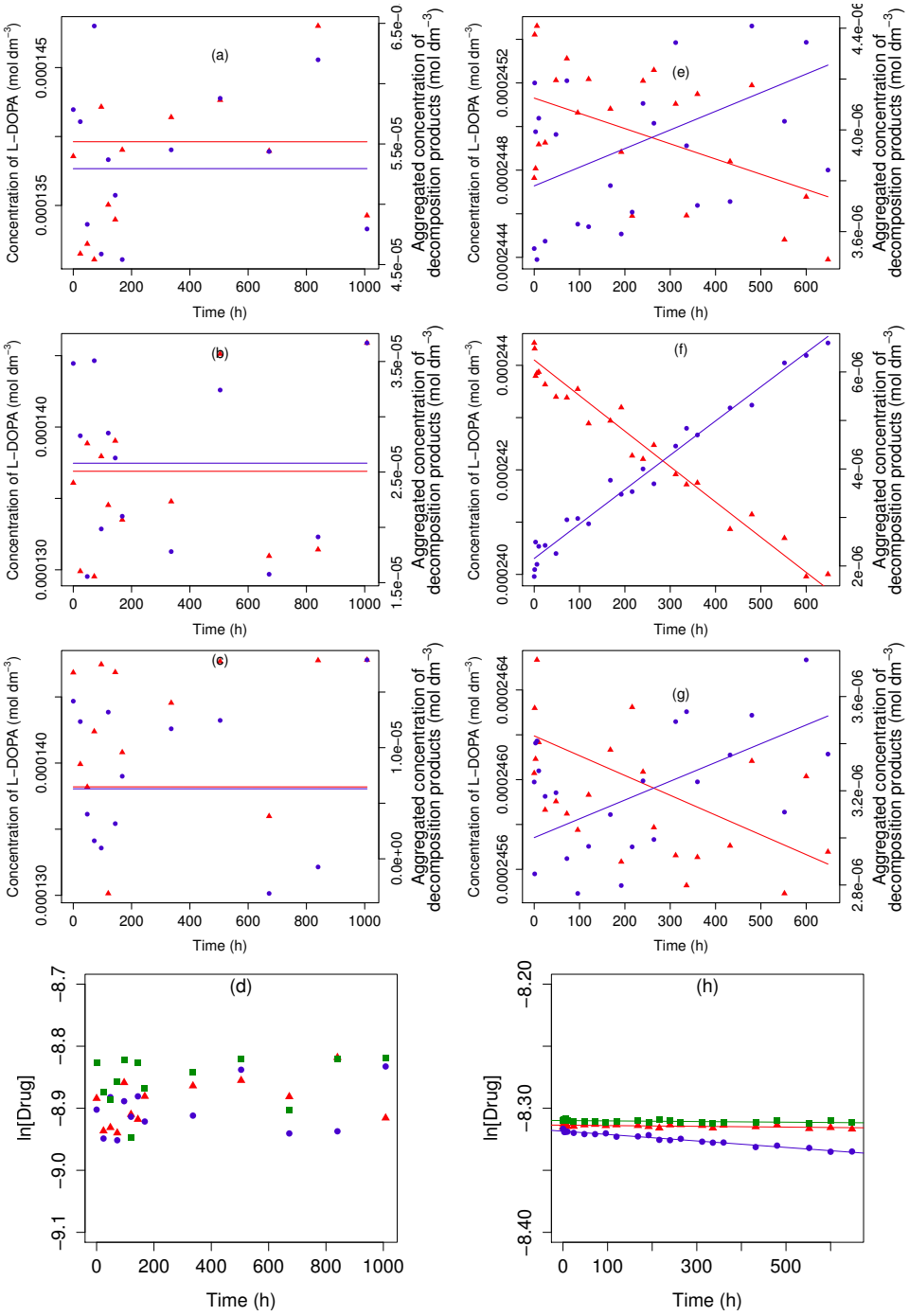


Figure D.5: The decomposition profiles of Eud-L{MgAl-LDOPA} in dry conditions at (a) room temperature, (b) 80 °C, and (c) under exposure to UV radiation, and in aqueous suspension at (e) room temperature, (f) 80 °C, and (g) under exposure to UV radiation, detailing the concentrations of L-DOPA (▲) and the aggregated concentrations of the decomposition products (●). Also (d) (dry) and (h) (wet) ln[L-DOPA] plotted as a function of time for the six experiments: room temperature (▲), 80 °C (●), and UV radiation (■).

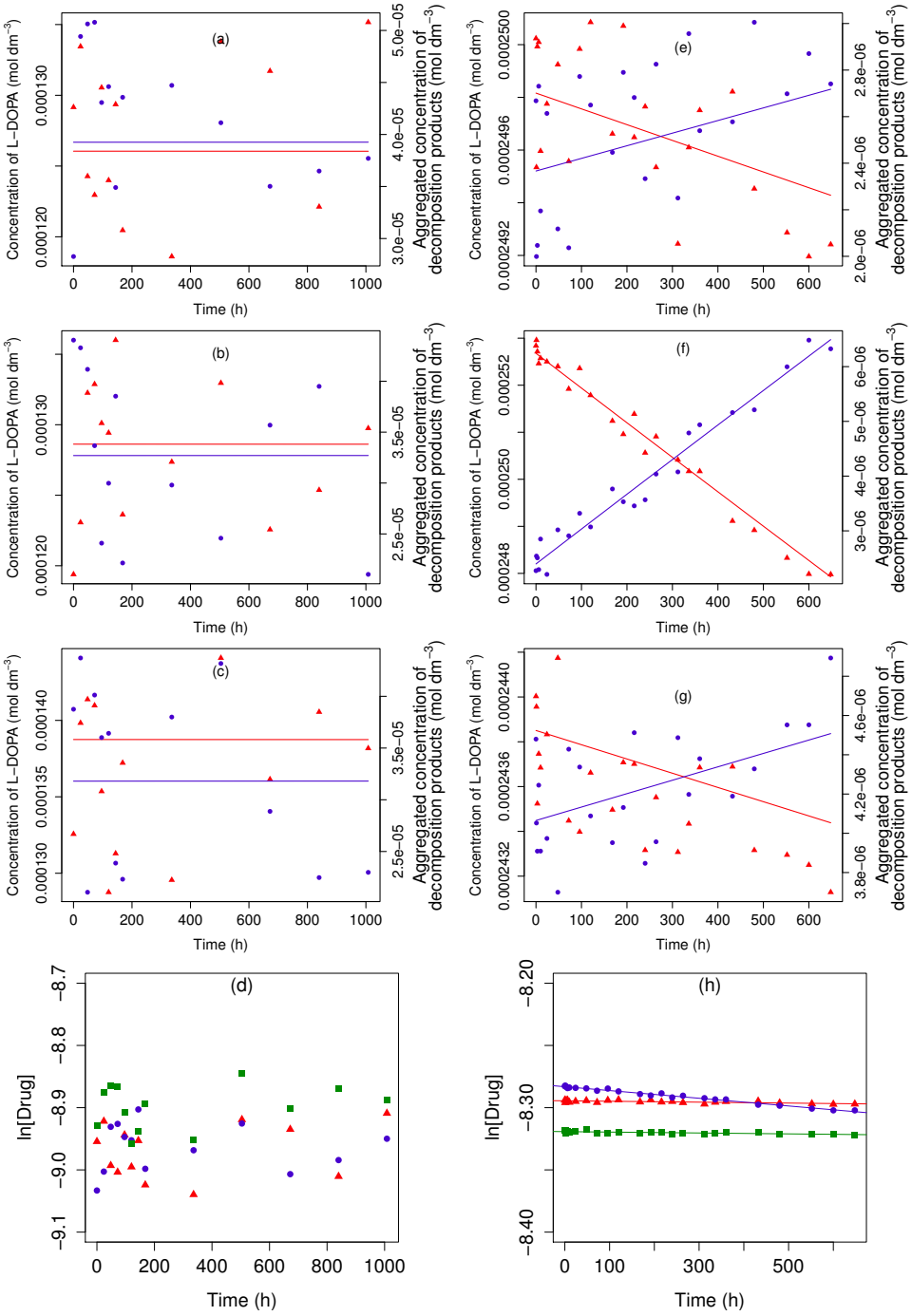


Figure D.6: The decomposition profiles of Eud-L{MgFeAl-LDOPA} in dry conditions at (a) room temperature, (b) 80 °C, and (c) under exposure to UV radiation, and in aqueous suspension at (e) room temperature, (f) 80 °C, and (g) under exposure to UV radiation, detailing the concentrations of L-DOPA (▲) and the aggregated concentrations of the decomposition products (●). Also (d) (dry) and (h) (wet) ln[L-DOPA] plotted as a function of time for the six experiments: room temperature (▲), 80 °C (●), and UV radiation (■).

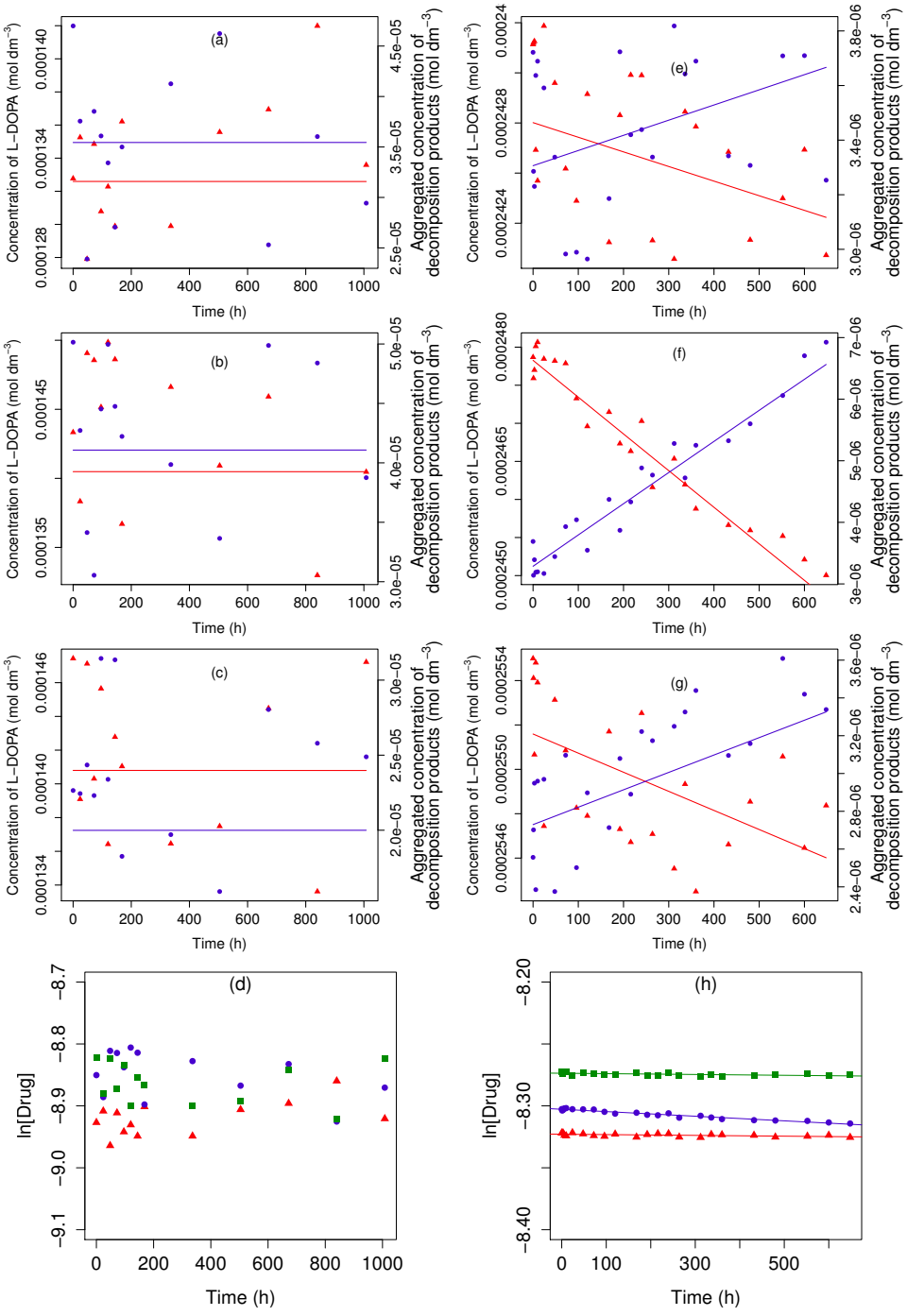


Figure D.7: The decomposition profiles of Eud-S{MgAl-LDOPA} in dry conditions at (a) room temperature, (b) 80 °C, and (c) under exposure to UV radiation, and in aqueous suspension at (e) room temperature, (f) 80 °C, and (g) under exposure to UV radiation, detailing the concentrations of L-DOPA (▲) and the aggregated concentrations of the decomposition products (●). Also (d) (dry) and (h) (wet) ln[L-DOPA] plotted as a function of time for the six experiments: room temperature (▲), 80 °C (●), and UV radiation (■).

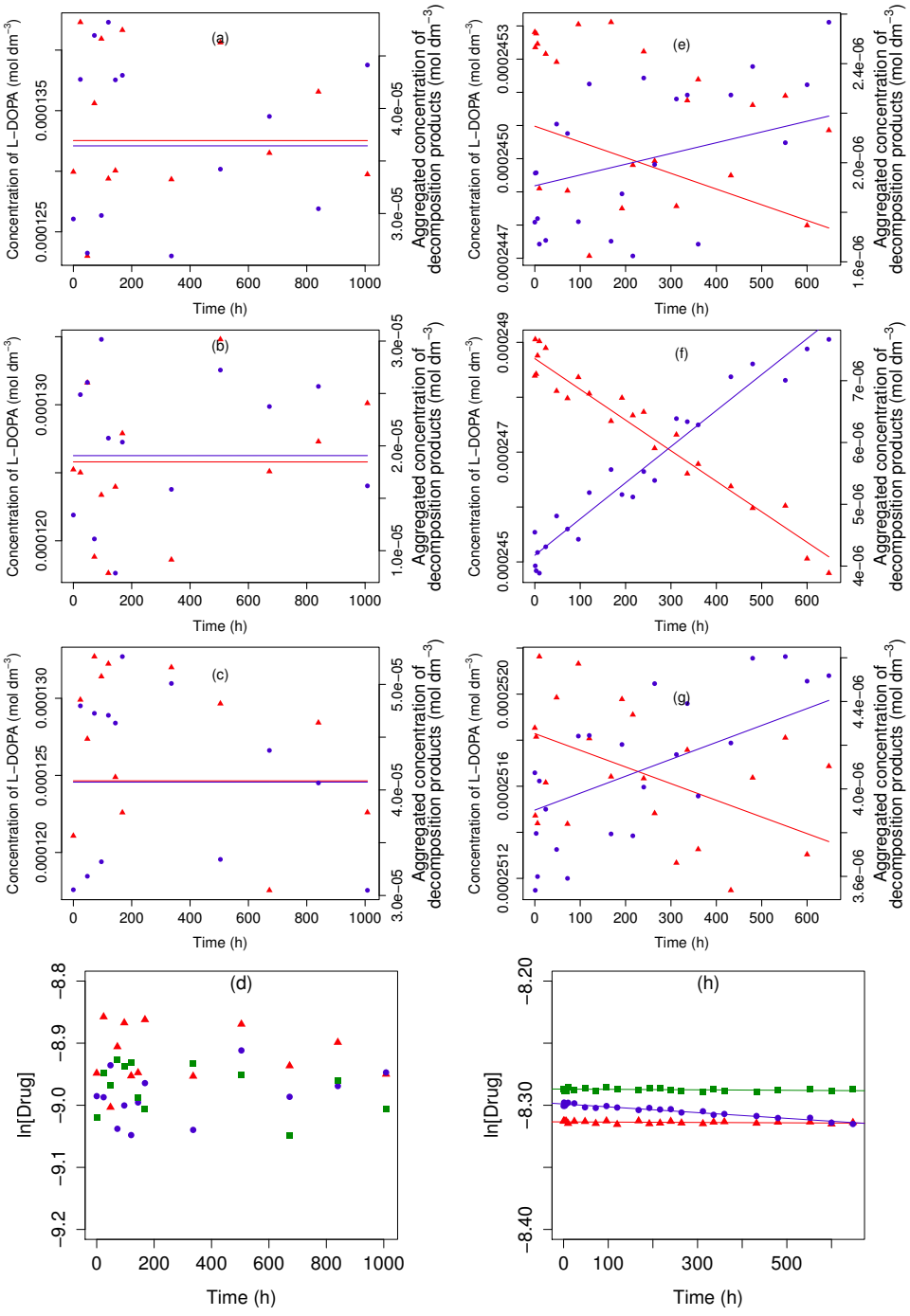


Figure D.8: The decomposition profiles of Eud-S{MgFeAl-LDOPA} in dry conditions at (a) room temperature, (b) 80 °C, and (c) under exposure to UV radiation, and in aqueous suspension at (e) room temperature, (f) 80 °C, and (g) under exposure to UV radiation, detailing the concentrations of L-DOPA (▲) and the aggregated concentrations of the decomposition products (●). Also (d) (dry) and (h) (wet) ln[L-DOPA] plotted as a function of time for the six experiments: room temperature (▲), 80 °C (●), and UV radiation (■).